COORDINATED CONTROL OF ACTIVE SAFETY SYSTEMS FOR MULTI-TRAILER ARTICULATED HEAVY VEHICLES

BY

SHENJIN ZHU

A Thesis

Submitted to the School of Graduate Studies

in Partial Fulfillment of the Requirements

for the Degree of

Doctor of Philosophy

in Mechanical Engineering

Faculty of Engineering and Applied Science

University of Ontario Institute of Technology

Oshawa, Ontario, Canada, 2016

Doctor of Philosophy (2016) University of Ontario Institute of Technology

(Mechanical Engineering) Oshawa, Ontario

TITLE: Coordinated Control of Active Safety Systems for Multi-trailer Articulated Heavy Vehicles

AUTHOR: Shenjin Zhu, M.A.Ss in Mechanical Engineering

(McMaster University)

SUPERVISOR: Professor Dr. Yuping He

Professor Dr. Jing Ren

NUMBER OF PAGES: XVIII, 232

To my wife Jinbo Zhang,

my parents in-law,

my son Jason Zhu and

my daughter Cathy Zhu.

Their encouragement and support

made this opportunity possible.

Acknowledgements

I would like to express my sincerest gratitude to my supervisors, Dr. Yuping He and Dr. Jing Ren, whose continuous encouragement, motivation, guidance and support from the initial to the final level enabled me to develop an understanding of the vehicle dynamics subject. I am heartily thankful to Dr. Yuping He and Dr. Jing Ren for being patient, inspiring to keep me going during the years of this research.

I thank Dr. Thomas Hu for his continuous support on our parallel computing system. I also thank Mr. Armin Sobhani, and Mr. James Desjardins at SHARCNET for their support on collecting simulation data.

I thank my fellow graduate students Dr. MD. Manjural Islam, Mr. Qiushi Wang, Mr. Tao Sun, Mr. Zhituo Ni, Mr. Chen He, Mr. Eungkil Lee, Mr. Jindong Cai for the support they provided during this research.

I thank for Dr. Bruce Minaker for providing the EOM software package for modeling of vehicle systems.

Financial support of this research by the Natural Science and Engineering Research Council of Canada (NSERC), Canadian Foundation for Innovation (CFI) is greatly acknowledged.

Abstract

To improve the directional performance of multitrailer articulated heavy vehicles (MTAHVs), the model-based active safety systems, including the active trailer steering, trailer differential braking and the active roll control are developed. The active safety systems are integrated and coordinated for optimal overall performance. The coordinated control system is designed in a modular, hierarchical and multilevel approach. At the upper level, a moment controller is designed to stabilize the yaw and the roll dynamics. At the intermediate level, an allocator is designed to distribute the demanded moments to the actuating systems. At the lower level, the active suspension system realizes the demanded roll moment, and the active trailer steering and the trailer differential braking share the demanded yaw moment. The directional performance of the MTAHV with the coordinated control system is evaluated in closed-loop simulations. A unified driver model for road vehicles is developed to 'drive' the vehicle in the closed-loop simulations. Considering the characteristics of the single unit and the multiunit vehicle drivers, a set of design parameters are introduced to govern the characteristics of the driver model to mimic human drivers in driving single unit and multiunit road vehicles, especially to simulate MTAHV drivers' driving performance under a high-speed evasive and a low-speed path-following maneuvers, respectively. The directional performance of the MTAHV with the coordinated control system and the driver model may be valuated and optimized using a genetic algorithm with the performance measures in the time-domain and the frequency-domain, thanks to the introduction of the automated frequency response measuring method (AFRM) into the articulated heavy vehicle dynamics. The proposed design methods/techniques and findings derived from the research will contribute to the advancement of active safety systems for MTAHVs.

Table of Contents

List of Figures

List of Tables

Chapter 1 Introduction

1.1 Multi-trailer Articulated Heavy Vehicles

Multi-trailer articulated heavy vehicles (MTAHVs) demonstrate significant economic and environmental benefits. It is shown that compared with an articulated heavy vehicle (AHV) with a single trailer, a tractor/two-trailer combination can improve fuel economy, and reduce greenhouse gas emissions by approximately one-third, in addition to the benefits of congestion reduction, infrastructure protection, and savings on maintenance and driver costs. MTAHVs have potentials to save up to $320 million, including 70 million liters fuel yearly in Ontario, Canada (LCVP, 2011). An investigation of economic efficiency of long combination vehicle (LCVs) in Alberta, Canada declares that the application of MTAHVs in Alberta has resulted in 80% decrease in the mileage travelled by heavy commercial vehicles, 40% saving for shippers, 32% cut on fuel consumption, and 40% reduction on pavement wear (Woodrooffe and Ash, 2001). A British research claims that raising the maximum truck weight from 41 to 44 tons has generated significant economic and environmental benefits (McKinnon, 2005). The research in Texas, USA has predicted that allowing operation of MTAHVs would save the Texas shippers $374 million to $1.9 billion a year (Bienkowski and Walton, 2011). A case study has demonstrated that the application of MTAHVs connecting the Chinese Gulan Intermodal Container Depot with seaports would induce 36.2% vehicle mileage reduction, 17.1% transport cost decline, 22.7% less fuel consumption and CO2 emission (Nagl, 2007).

However, the poor directional performance of MTAHVs restricts their wide applications. In Ontario, Canada, MTAHVs are only allowed to operate on the designated freeway networks and approved municipal roads, carrying gross vehicle weight (GVW) not greater than that of a

conventional tractor/trailer and running at night time to ensure road safety (LCVP, 2011). Concerning safety and pavement damage, the Intermodal Surface Transportation Efficiency Act, USA, has frozen the MTAHV use on the federal highway system since 1991 (Adams et al, 2012). To promote further utilization of LCVs, the safety concerns have to be eased through exploiting technical solutions.

The main disadvantages of MTAHVs including pavement and road infrastructure damage, traffic congestion and road safety hazard (Grislis, 2010) are directly associated with their main features: heavy weight, poor manoeuvrability, and low stability. Heavy weights are responsible for pavement damage. A heaviest MTAHV has an equivalent impact of 2000 cars on road (Grislis, 2010). The greatest impact of MTAHVs on road and bridge is directly related to the maximum single axle load which may be mitigated by raising the amount of axles employed. Thus, MTAHVs with multiple axles can be made less aggressive than traditional tractor/trailer combinations.

Poor manoeuvrability causes large off-tracking when a MTAHV corners on urban roads. The road infrastructure designed for traditional tractor/trailer with limited radii of curves and narrow traffic lanes may not well accommodate the manoeuvring characteristics of MTAHVs. Damage of vehicles, road shoulders, curbs, and roadside signs may take place. Poor manoeuvrability is also responsible for urban road and two-lane highway congestion (Grislis, 2010).

Low stability of MTAHVs creates safety hazards on road. It can lead to roll and lateral unstable modes. Particularly, MTAHVs tend to rollover when negotiating tight curves at high speeds due to high center of gravity (CG) and relatively narrow track width. The static rollover threshold is a basic measure of roll stability (Winkler, 2000). Rollover thresholds are well above 1.0 g (g is the gravitational acceleration constant) for most of passenger cars, 0.8 g-1.2 g for light trucks, vans and SUVs, and well below 0.5 g for fully loaded MTAHVs. The lateral acceleration in normal

cornering can easily exceed the rollover threshold of MTAHVs and result in rollover accidents. Roll stability is strongly dependent on the frequency content of manoeuvres (Winkler, 2000).

The lateral unstable modes of MTAHVs manifest jackknife or trailer swing. Various factors may contribute to jackknife, including poor inertial characteristics, bad timing braking or steering (Chen and Hsu, 2008), brake failure, improper braking and poor road conditions (Bouteldja and Cerezo, 2011), and excessive speed on low frictional road. The lateral performance measures for lateral dynamics of MTAHVs include rearward amplification (RWA), off-tracking, and yaw damping (Kharrazi, 2012).

1.2 Manoeuvrability and Stability of MTAHVs

Manoeuvrability and stability are intrinsic characteristics of moving objects. A motion has to be controllable and stable for practical applications. A MTAHV should perform a maneuver with adequate stability.

The correlations exist among the manoeuvrability, stability and the degrees of freedom (DOF) of a moving object. A unicycle has five DOF per unit, and demonstrates the best manoeuvrability and the poorest stability. From a bicycle to a passenger car, the reduced DOF has degraded the manoeuvrability and improved the stability. The same trend exists when transition from trucks to tractor/semitrailers (TSTs) and to MTAHVs. A larger number of DOF results in better manoeuvrability and poorer stability, and vice versa (Fancher, et al, 1984). The manoeuvrability is positively, and the stability negatively correlated with the number of DOF. The removal of roll DOF at pintle-hitch couplings in an A-train would reduce the RWA ratio from around 2 to under 1.5 (Winkler, 2000).

The manoeuvrability and stability of MTAHVs may be improved by introducing external yaw and/or roll moments. The moments generated by passive trailer steering systems improve the

manoeuvrability at the cost of the stability of MTAHVs (Fancher, and Winkler, 2007, Odhams, et al, 2010). Active yaw and/or roll moments generated by active safety systems (ASSs), e.g., active trailer steering (ATS), trailer differential braking (TDB), and active roll control (ARC) can improve both the manoeuvrability and stability. The active steering (Mokhiamar and Abe, 2002, Fukao, et al, 2004), differential braking (Barbarisi, et al, 2009, Hancock, et al, 2005, Jo, et al, 2008), and the ARC (Yim, et al, 2011, Du and Zhang, 2008) have been developed for passenger cars. The application of ASSs in MTAHVs (Palkovics and Fries, 2001, MacAdam, and Hagan, 2002) is relatively limited.

Two requirements to make a MTAHV safe are appropriate technical parameters and proper driving (Grislis, 2010). The safety performance study in Alberta, Canada shows that the special operation permit program has made the MTAHVs 5 times safer than the TSTs (Woodrooffe, et al, 2004). Road safety is an outcome of the driver-vehicle-road interactions. The ASS design is to construct controller/controllers to work with the driver and the road.

The Multidisciplinary Vehicle Systems Design Laboratory (MVSDL) at University of Ontario Institute of Technology (UOIT) has conducted several initial works on the ASSs for MTAHVs. The MVSDL has developed an automated design synthesis method (ADS) for ATS systems (Islam et al, 2010, He et al, 2010, Oberoi and He, 2011, Oberoi et al, 2011, He and Islam, 2012, Islam et al, 2012). In this method, the vehicle modeling, ATS controller construction, performance evaluation and the design variable search are conducted simultaneously at the early design stages of AHVs. The MVSDL has developed a driver-software-in-the-loop (DSIL) real time simulation platform (Ding and He, 2012). The DSIL platform is a virtual testing tool equipped with fully configurable virtual vehicles, road conditions, test procedures, manoeuvres, interfacable software and hardware. The MVSDL has conducted comparative studies on the ASSs of articulated vehicles

for improving stability in time and frequency analysis (Islam et al, 2010, Shamim et al, 2011, Ding et al, 2011, Islam and He, 2011). The MVSDL has developed a multilevel design synthesis (MDS) method for mechatronic vehicles with integrated control systems (ICSs) (He, 2008). The MDS uses the decomposition-synthesis approach. Large systems are partitioned disciplinarily into multi-level sub-systems for analysis. The design variables, criteria and the constraints are formulated and solved at the subsystem level. The information is shared and the optimization is conducted in the top-down and the bottom-up fashions. The optimization process is terminated when all the parties receive their acceptable solutions.

1.3 Limitations of the Existing ASSs and the Design Methods

There are several limitations on the existing ASSs and the design methods. The stability of AHVs has long been studied without considering the driver. The driver may play a destabilizing part on the vehicle systems (Plochl, and Edelmann, 2007). The driver models (Cheng, and Cebon, 2007, He et al 2010, He and Islam, 2012, Islam, Ding and He, 2012) in the closed-loop simulations are mainly adapted from those designed for passenger cars without considering the unique dynamic features of MTAHVs. A driver model by Ding and He (2012), based on the motion cues from the trailing units, does not provide anticipative results. The current ASSs (Aurell and Edund, 1989, Eisele and Peng, 2000, Jujnovich and Cebon, 2002, Wu and Lin, 2003, Rangavaj and Tsao, 2007, Oudghiri et al, 2007, He et al, 2010, Islam et al, 2010, Oberoi and He, 2011, Gu and Yang, 2011, Oberoi et al, 2011, Ding and He, 2011, He and Islam, 2012, and Islam et al, 2012) have not adequately addressed the driver-vehicle-road (DVR) interactions.

The integration of ATS, ARC and TDB for MTAHVs has not been adequately investigated, in spite of the extensive research of the integrated control for single unit vehicles, e.g., He (2008), ATS (Rangavaj and Tsao, 2007, Kharrazi et al, 2010, Islam et al, 2010) and the TDB (MacADAM,

and Hagan, 2002, Zong et al, 2011) on MTAHVs. The robustness of the ASSs on parametric uncertainties and un-modeled dynamics has not been fully investigated.

1.4 Research Objectives

The proposed research will develop new coordinated ASSs for MTAHVs. The MVSDL's previous work will be extended to MTAHVs considering the interactions of driver and vehicle. The following objectives are to be achieved.

1.4.1 Integrated Control of the ATS, ARC and the TDB

The ATS, ARC and the TDB will be integrated to accommodate various operating conditions of MTAHVs on road. The previous ATS, ARC and TDB technologies for AHVs will be extended to MTAHVs. The proposed integrated control systems (ICSs) will have a hierarchical architecture, performing ATS, TDB and ARC coordination, and actuator manipulation in the MDS framework.

1.4.2 Development of a Driver Model for MTAHVs

A driver model will be developed for MTAHVs. The model will capture the unique features of MTAHV drivers and perceive the motion cues of all vehicle units. The designed model will be responsible for the closed-loop simulations in this research.

1.4.3 Development of the Innovative Design Methods for ASSs

The ultimate research goal is to develop a multilevel design optimization method (MDO) for the ASSs of MTAHVs. The MDO is an extension of the MDS for mechatronic vehicles with the ICS. The MDO should be innovative, effective and robust, considering the parametric uncertainties, un-modeled dynamics, and the driver skills.

1.5 Methodology

The following design methodology will be applied during the development of the ASSs for MTAHVs.

1.5.1 Integrated Control of the ATS, TDB, and the ARC

The TDB is effective in improving stability of MTAHVs (Palkovics et al, 1999, Eisele and Peng, 2000), and can curtail jackknife and trailer swing on the low frictional road and prevent rollover on the high frictional road.

The MTAHVs demonstrate worse manoeuvrability compared with the conventional AHVs. Poor manoeuvrability raises concerns for the safety and the highway infrastructure damage (Rangavaj, and Tsao, 2007) and promotes the accident rate on road (Jason et al, 1998). The ATS systems can significantly improve the manoeuvrability of MTAHVs (Rangavaj, and Tsao, 2007, He et al, 2010, Islam et al, 2010, He and Islam, 2012, Islam, Ding, and He, 2012).

By integration in one MTAHV, the ATS and the TDB can compensate each other. The proposed coordinated ASS will have a hierarchical architecture, consisting of three levels. The virtual control is determined at the upper level, and allocated at the intermediate level. The actuators are manipulated at the bottom level. The hierarchical ICS is optimized iteratively.

1.5.2 Validation of the ICS Using Numerical Simulations

The designed ICS will be validated by using numerical simulations, including the driver model validation, ASS validation, driver/vehicle interaction examination, and the MDO development.

1) Driver Model Validation. A driver model will be designed and simulated in the Matlab/Simulink under the specified test manoeuvres.

2) ASS Validation. The ICS is assessed under various cases: the baseline, ATS, ARC, TDB, and their integration. In these cases, the ICS will be evaluated in the directional performance measures of the MTAHV through benchmark comparisons.

3) Development of Innovative Design Methods for the ASSs. A MDO method will be developed for the design of ASSs for MTAHVs based on the MVSDL's previous work. A multilevel evaluation framework is proposed correspondingly. The MTAHV driver model and the ICS are designed and evaluated independently. The coordination of the ICS, driver model and MTAHV is optimized at the upper level and evaluated overall considering the control allocation and the realization in the multilevel approach.

1.6 Major Contributions of This Research

1) A unified driver model has been developed for road vehicles including single-unit passenger cars, SUVs, and light trucks and multi-unit heavy commercial vehicles.

2) An automated frequency response measuring technique (AFRM) has been introduced to acquire frequency response of the nonlinear vehicle models automatically. The on-line application of the AFRM makes the frequency-domain design optimization of active safety systems (ASSs) for articulated heavy vehicles feasible.

3) The functionality of the software package, EoM (Equation of Motion), has been extended from originally generating linear models of multi-body dynamic systems for stability analysis and control design to currently formulating nonlinear models for dynamics simulation by replacing the linear tire models with the nonlinear ones, e.g., the Dugoff and the Magic tire models.

4) A coordinated control scheme, considering the active trailer steering (ATS), trailer differential braking (TDB), and the active roll control (ARC), for the multi-trailer articulated heavy vehicles (MTAHVs) has been developed in a multi-level/modular approach. A side-slip angle based

allocation algorithm is proposed to coordinate the functionality of the ATS and the TDB subsystems.

1.7 Organization of the Thesis

This thesis is organized as follows. An extensive literature review on the directional performance of MTAHVs, driver models, and ASSs is presented in Chapter 2. Vehicle modeling and validation are provided in Chapter 3. In Chapter 4, the lateral dynamic analysis of AHVs in the frequency-domain is conducted with the introduction of the automated frequency measuring technique. A unified lateral preview driver model for road vehicles is designed in Chapter 5. The integrated control system for MTAHVs is formulated considering the ATS, TDB and the ARC in Chapter 6. Robust active steering systems for AHVs are studied in Chapter 7. An investigation of test maneuvers for determining rearward amplification of MTAHVs is conducted in Chapter 8. Finally, conclusions are drawn in Chapter 9.

Chapter 2 Literature Review

2.1 Directional Performance of MTAHVs

A MTAHV consists of a tractor and two or more trailers connected to each other at articulation points using mechanical couplings, such as pintle hitches, 5th wheels, etc. (Fancher and Winkler, 2007). MTAHVs are increasingly used on highways across Canada due to economic and environmental benefits (OLCV, 2009). The complex configurations and large sizes of MTAHVs lead to poor manoeuvrability and low stability.

The manoeuvrability is associated with the kinematic characteristics of MTAHVs. The performance measures for manoeuvrability of MTAHVs include low-speed off-tracking, frontal swing, tail swing, and steering tire friction demand in a low speed cornering (NRTC, 2001). The off-tracking is defined as the maximum offset between the paths of the tractor front axle center and the trailer rearmost axle center under low-speed cornering maneuvers, and is attributed to the inherent factors and external conditions. The low-speed off-tracking is dependent on the geometric parameters of MTAHVs and the manoeuvers conducted (Fancher et al, 1984, CDT, 1984, Erkert et al, 1989, Cheng and Huang, 2011). The low-speed off-tracking causes extra road space consumption (Fancher and Winkler, 2007). Poor maneuverability of MTAHVs may disrupt traffic flow (CTSWS, 2000).

Due to multiple unit configurations, MTAHVs exhibit unique dynamic features. The lateral stability of MTAHVs is an important research topic in road vehicle lateral dynamics. The performance measures to evaluate the lateral stability involve static rollover threshold, transient off-tracking, rearward amplification (RWA), and yaw damping (Fancher and Winkler, 2007). Poor stability may lead to unstable motion modes, including jackknifing, trailer swing and rollover

(Islam et al, 2012, He et al, 2010), causing serious accidents. Every year, approximately 120,000 injuries and 5000 fatalities are related to AHVs (CTAA, 2010), amongst them, 23.1% involving fatality and 28% causing incapacitating injury (USDT, 2005). Heavy commercial vehicles are overrepresented in fatal accidents (Kharrazi, 2012). Correlations exist between AHV accident rates and maneuvers (Jason et al, 1998, CTSWS, 2000, Kharrazi, 2012).

Manoeuvrability and lateral stability have contradictory requirements on the vehicle system parameters (Fancher and Winkler, 2007). For instance, shorter trailer wheelbase and more articulation joints would improve manoeuverability, but deteriorate stability of the AHV. Adequately addressing the trade-off relationship between manoeuvrability and lateral stability is a challenging task facing designers and researchers.

2.2 Active Control of MTAHVs

To date, extensive research and experiments have been conducted to solve the trade-off design problem of MTAHVs. Since 1980s, weights and dimensions of MTAHVs have been the research topics of the vehicle system dynamists around the world. The passive vehicle system parameters cannot fully accommodate the contradictory requirements from manoeuvrability and lateral stability under various operating conditions. Active control techniques may provide promising solutions to this conflicting MTAHV design problem. The past two decades have witnessed the advancement of active control of AHVs (Lam, 1988, Fancher and Winkler, 2007).

2.2.1 Control Strategies

The control strategies are defined as the selection and application of mechanisms of MTAHVs to realize the active control functionalities. The steering control, braking control, suspension control, and the active roll control are the commonly used control strategies for improving the dynamic performance of AHVs.

2.2.1.1 Active Steering Control

Today's steer-by-wire control systems are evolved from traditional mechanical steering linkages, speed-dependent four-bar steering mechanisms (Bozeman and Drench, 1998), the software-implementation of mechanical controllers using virtual sensors and actuators (Jujnovich and Cebon, 2002, Fancher and Winkler, 2007), and the strategic transition from mechanical manipulation to modern steer-by-wire implementation (Fletcher et al, 2006). Since then, active steering has been widely investigated to improve the manoeuvrability (Cheng and Cebon, 2007, Rangavajhula and Tsao, 2008, Cheng et al, 2011), lateral stability (Islam et al, 2012, Kharrazi et al, 2012, Ding et al, 2013), and the trade-off between manoeuverability and lateral stability (He and Islam, 2012, Tabatabaei Oreh et al, 2012, and Tabatabaei Oreh et al, 2012a). The geometrical steering control systems (Percy and Spark, 2012, Percy and Spark, 2012a) translate the operator's command on the leading unit to the wheel and hitch angles on the trailing units, aimed at reducing the low-speed scuffing and off-tracking of the trailer wheels.

2.2.1.2 Differential Braking Control

Differential braking (DB) techniques used on AHVs are developed from traditional pneumatic systems (Palkovics and Fries, 2001). In the differential braking system, the electronics are utilized to fulfill measurement, signal transmission, and control, and the hydraulics and pneumatics are kept as energy sources. The differential braking control systems provide several benefits such as being more compact, easier to control, faster response, safer performance and present platforms for future functionality expansion. The DB control strategy has been applied to AHVs to improve lateral stability (Elwell and Kimbrough, 1993, Petersen et al, 1998, Fancher et al, 1998, MacAdam et al, 2000, Eisele and Peng, 2000, Stevenson and Ridley, 2005, Azad et al, 2006, Zhou and Zhang,

2012), and prevent jackknife (Chen and Hsu, 2008, Hac et al, 2009, Chen and Shieh, 2010, Zong et al, 2011).

2.2.1.3 Active Suspension Control

Active suspension systems can be used to improve the ride quality and roll stability of AHVs. The commonly used methods including control of the damping coefficients of dampers or directly manipulating the vertical forces using hydraulic or electric actuators. Yi and Hedrick (1989) evaluated the active/semi-active suspensions of tractor/semitrailer combinations on the damage of pavement and achieved reduction on the pavement degradation by the modulation of semi-active shock absorbers. Chen et al (2008) presented fuzzy-logic-control based air suspensions for improving ride comfort and road friendliness of truck by actively adjusting the damping coefficients of semi-active suspensions. Sulaiman et al (2012) investigated the semi-active suspension systems in the improvement of ride quality and road holding of heavy vehicles. Chen et al (2013) compared two multi-axle heavy truck suspension control strategies on a functional virtual prototype model in terms of road friendliness and ride comfort.

2.2.1.4 Active Roll Control

Extensive research may be found in the field of active roll control for AHVs. Miege and Cebon (2005) investigated the benefits of active anti-roll bar systems for improving roll stability of an experimental tractor/semitrailer combination. Jeppesen and Cebon (2009) considered the observer-based fault detection in the active roll control of a tractor/semitrailer combination. Huang et al (2012) used an active anti-roll-bar manipulation for rollover prevention of AHVs with multiple-rollover-index minimisation.

2.2.2 Reference Generation

Reference tracking is a common practice in the active control of MTAHVs. The reference, which demonstrates desired performance properties of the vehicle, is first generated. The performance measures of the vehicle are then forced by a controller (or controllers) to track the reference. There are two types of commonly used methods to generate the reference: 1) reference model simulation; and 2) direct measurement or observation of the vehicle.

2.2.2.1 Reference Model Simulation

The model matching approach has been widely applied to control systems design. A reference model, which provides the desired performance, is first designed. Then a controller is constructed to track the response of the reference model. Two types of reference models, namely, kinematic and dynamic models, are employed. In the kinematic model, a MTAHV may be modeled using geometric relationships (Odhams et al, 2010, Percy and Spark, 2012, Jujnovich and Cebon, 2013). The tractor, trailers, axles, and the wheels are modeled as links connected with joints. The low-speed performance measures of the vehicle are forced to match the response of a geometric model.

The dynamic model matching is usually used in the control of MTAHVs in high-speed operations. A linear dynamic model may be adopted as a reference model. Using the dynamic model matching, the active steering system forces the vehicle to follow the simulated steady-state response of the virtual dynamic model (Palkovics, 1992, Palkovics et al, 1994, Gianone et al, 1995). A sliding mode control system tracks the desired states of the simulated x_d -generator (Misawa, 1997). A path-following control system traces the response of the simulated first-order differential equation planner (Fancher et al, 1998). The reference trajectories are obtained by observing the states of a simulated, LQR compensated model using the Kalman filter (Miege and

Cebon, 2005). The philosophy of the loop transfer recovery (LTR) (Doyle and Stein, 1979, Sampson, 2000) may also be ascribed to the dynamic model matching.

The zero-state-following is a principle utilized in the regulation systems. The variable(s) or state(s) of interest are forced by linear quadratic regulators (LQRs) to approach zero. The application of the zero-state-following can be found in the planar dynamics attenuation (El-Gindy et al, 2001), multiple-rollover-index minimisation (Huang et al, 2012), and the manoeuvrability/stability improvement (Cheng, and Cebon, 2007, Rangavajhula et al, 2008, Hac et al, 2009, He et al, 2010, Ding et al , 2011, Islam et al, 2012, He and Islam, 2012).

2.2.2.2 Direct Measurement or Observation

In a path-following maneuver, the trajectory of a lead point is required for the follow point to track (Jujnovich and Cebon, 2013). This trajectory may be directly measured or observed. Cheng and Cebon (2008) proposed an active trailer steering strategy to improve roll stability of AHVs; two points on the semitrailer, the articulation point and the end point of the semitrailer, are selected; an optimal controller is designed to make the end point to track the articulation point. As the reference, the articulation point trajectory is observed by using the Kalman filter. The strategy of utilizing the direct measurements (or observation) as the reference trajectories is adopted by Chen and Tomizuka (2000), Cheng et al (2011), Cheng, Roebuck, Odhams and Cebon, (2011), Islam and He, (2011).

2.2.3 Control Algorithms

Among the active control systems of AHVs, the linear quadratic regulator (LQR) is the most popular algorithm (Cheng, and Cebon, 2007, He, 2008, Islam et al, 2010, Islam et al, 2010a, He et al, 2010, Ding and He, 2011, Islam and He, 2011, Ding et al, 2011, Ding and He, 2012, Islam et al, 2012, He and Islam, 2012, Tabatabaei Oreh et al, 2012, Tabatabaei Oreh et al, 2012a, Ding et

al, 2013). The proportional-integral-derivative controller (PID) is the second most frequently used algorithm (Hata et al, 1989, Notsu et al, 1991, Lin et al, 1996, Fancher et al, 1998, Miege and Cebon, 2005a, Odhams et al, 2010, Jujnovich and Cebon, 2013). Few attempts can be found in the sliding mode control (Acarman and Ozguner, 2003, Imine et al, 2012) and the fuzzy logic control (Tanka and Takahiro, 1997, Ding et al, 2011, Tabatabaei Oreh et al, 2012, 2012a) of AHVs.

2.3 Models of MTAHVs

The introduction of active control systems into the dynamics of AHVs has changed the role of AHV modeling (Fancher and Winkler, 2007). Currently, there are three classes of models, namely, control-oriented models, dynamics models and general purpose models, available (Fancher and Winkler, 2007). The models of AHVs are problem-dependent involving approximations, assumptions, simplifications and complexity associated with accuracy and precision.

The control-oriented models are used to generate commands for manipulating control elements in the control systems. There are kinematic and dynamic control models available in the literature. The kinematic control models are built on the kinematic relationship of physical structures without considering the system dynamics, and thus limit their applicability to manoeuvrability improvement (Odhams et al, 2010, Percy and Spark, 2012, Percy and Spark, 2012a, Jujnovich and Cebon, 2013).

There are two kinds of commonly used dynamic control-oriented models, namely, yaw-plane and yaw-roll. The dynamic control-oriented models may be linear or nonlinear dependent on the objectives of the control systems. The yaw-plane models are widely used in the active control systems for improving the directional performance of AHVs (Palkovics et al, 1994, Islam and He, 2008, Chen and Hsu, 2008, Chen and Shieh, 2010, Liu, 2007, He et al, 2010, He and Islam, 2012, Ding et al, 2012, Tabatabaei Oreh et al, 2012).

The yaw-roll control models consider more DOF than that of the corresponding yaw-plane models and are appropriate for roll motion control (Kharrazi et al, 2010, Kharrazi et al, 2012), roll stability enhancement (Miege and Cebon, 2005, Cheng and Cebon, 2008, Cheng et al, 2011), and rollover prevention (Huang et al, 2012). The decoupled yaw-roll model, consisting of yaw dynamics and roll dynamics models in series, is applicable to rollover warning (Chen and Peng, 2005). The simple roll-plane models are also used in active roll control (Miege and Cebon, 2005a), and lateral load transfer estimation (Kamnik et al, 2003).

The dynamics models are used to simulate tire and vehicle dynamics. With the fidelity as primary concern, the dynamics models should describe the system dynamics with sufficient accuracy and precision. The commonly used dynamics models cover nonlinear yaw-plane, yaw-roll, and yaw-roll-pitch dynamics of AHVs.

The nonlinear dynamics models are usually employed when advanced dynamics models built with multi-body dynamics software package are unavailable. In common practice, a nonlinear dynamics model is first constructed using physical laws or the Lagrange method, and then linearized at certain operation point. A controller is constructed with the linearized model and validated with the nonlinear dynamics model simulation, e.g., in jackknife prevention (Chen and Hsu, 2008), directional performance enhancement (Kharrazi et al, 2010, Kharrazi et al, 2012), and directional characteristics improvement (Tabatabaei Oreh et al, 2012, Tabatabaei Oreh et al, 2012a).

Several multibody dynamics software packages, such as ADAMS, TruckSim and ArcSim, are available for building complex dynamics models of AHVs with high fidelity, accuracy and precision. A comprehensive 77-DOF 3D dynamics model of a tractor/semitrailer combination in ADAMS was employed to validate a partial feedback linearization controller (Fletcher et al, 2006).

A TruckSim model of the fully laden CVDC (Cambridge Vehicle Dynamics Consortium) tractor/semitrailer combination was used to test the virtual driver steering strategy (Cheng and Cebon, 2008). The TruckSim models were applied to validate the active safety systems of AHVs (Ding et al, 2012, Sulaiman et al, 2012, He et al, 2013). The CASCADE (a vehicle simulation system) model was used to evaluate the lateral load transfer coefficient estimation method (Kamnik et al, 2003). An ArcSim model was applied to assess the performance of the time-to-rollover metric computation (Chen and Peng, 2005).

The general purpose models are used to simulate the entire driving process, include the models of sensors, actuators, driving environment, tire road interfaces (NTC, 2005), aerodynamic disturbance (Palkovics et al, 1994) and drivers. Driver models mainly infer to the mathematical representation of driver's path-following control behaviour.

2.4 Driver Models

Following the introduction of active control systems into the vehicle dynamics, driver models have served the analysis and synthesis of the performance and stability of vehicle systems for over decades. Since its origination in 1950s, research on understanding and modeling of drivers' behaviours has never stagnated. Today, driver modeling has covered a broad topic.

Based on control functionalities, driver models are classified into longitudinal dynamics control driver models, lateral dynamics control driver models, and combined lateral/longitudinal control driver models (MacAdam, 2003).

Depending on the objects focused, driver models are categorized into vehicle-focused driver models, driver-focused driver models, driver/vehicle combination-focused driver models and environment/traffic-focused driver models (Plochl and Edelmann, 2007).

Driver models are organized in terms of model formulations, decision making process, response and reaction time determination, steering dynamics performance index construction and driver model parameter identification (Taheri, 2014).

The aforementioned driver models are mainly focused on single unit vehicles, and with only feedback motion cues from single units. This approach is appropriate for passenger cars, SUVs, and trucks. The following listed articles launched strategic attempts of driver model construction with all unit motion cue feedback.

The AHV-based driver models defined on the lateral positions and orientations of the trailing units showed oscillatory behaviour (Yang et al, 2003, Ding and He, 2012). Further investigation of the AHV driver models (Yang et al, 2003) showed that the lateral position and heading angle of the lead unit was the fundamental motion cue, and the driver model structure with the fundamental motion cue plus the lateral acceleration of the lead unit, articulation rate and roll angle of the trailing unit provided the best composite performance. Liu (2007) constructed an AHV driver model using full state feedback with a constant physiological time delay in the LQR framework.

2.5 Automated Design Synthesis

The automated design synthesis (ADS) uses the decomposition-synthesis approach in solving problems in a large and complex system. The ADS was systematically investigated in the virtual development of ground vehicle suspensions (He and McPhee, 2007). The ADS was also applied to ATS design for AHVs (He and Islam, 2012) in a way that the design variables of the AHV were optimized in a single loop.

Chapter 3 Vehicle Modeling

3.1 Introduction

MTAHVs have multiple unit configurations and large sizes, and demonstrate poor low-speed manoeuvrability and low high-speed stability (Fancher and Winkler, 2007). The Australia performance-based standards (PBSs) for articulated heavy vehicles (AHVs) specify the swept path, frontal swing, and the tail swing to measure low-speed manoeuvrability (Edgar, 2004). A unified measure for manoeuvrability, i.e., path-following off-tracking (PFOT), defined as the maximum radial offset between the path of the tractor's front axle center and that of the rearmost trailer's rear axle center under a given PFOT test maneuver, is well accepted (He and Islam, 2012, Islam, Ding and He, 2012). The PBSs suggest the static rollover threshold, rearward amplification (RWA), and the yaw damping coefficient as the measures of high-speed stability (Edgar, 2004). The RWA, defined as the ratio of the peak lateral acceleration at the rearmost trailer's CG to that of the tractor under a lane-change maneuver, is applied as a unified measure for high-speed stability (He and Islam, 2012, Islam, Ding and He, 2012).

To address the inherent drawbacks such as poor low-speed manoeuvrability and low high-speed stability and improve the directional performance of MTAHVs, the effect of variations in size and weight on stability and maneuverability has been investigated (Ervin et al, 1983), various innovative passive mechanisms such as mechanical couplings (Winkler et al, 1986) and steering axles (Jujnovich and Cebon, 2002) have been invented, and achieved limited benefits due to the conflicting requirements of manoeuvrability and stability.

To alleviate the limitations, various active safety systems (ASSs) such as active trailer steering (ATS), trailer differential braking (TDB) and active roll control (ARC) systems have been proposed

(He et al, 2016) and achieved promising improvement in both manoeuvrability and stability. The ATS improves MTAHVs' maneuverability and lateral stability in the low and high-speed operational modes, respectively (Rangavajhula and Tsao, 2007, Kharazi et al, 2012, Kharazi, et al, 2013). The ARC tilts the trailers of MTAHVs to the inside of a corner to raise the static rollover threshold and reduce the lateral load transfer for AHVs (Sampson and Cebon, 1998, Miege and Cebon, 2005, and Huang et al, 2012). The TDB system, through right or left side braking, generates yaw torques for suppressing rearward amplification of trailers for AHVs (Ervin, et al, 1998, Fancher et al, 1998, and MacAdam and Hagan, 2002).

Unfortunately, no one ASS can solve all lateral dynamics problems of MTAHV alone. The ATS, ARC, and the TDB systems may coexist in a MTAHV. The combination of the ATS, TDB and ARC without coordination may produce adverse interference and degrade the overall performance of MTAHV-ASS systems. An integration of the ATS, TDB and ARC may be inevitable. Recently, to enhance the directional performance of MTAHVs, an integration of the ATS, TDB, and ARC, has been investigated (Islam et al, 2012, Islam et al, 2013, Islam and He, 2013). However, the applicability and contribution of the individual ASSs and the coordination of the ASSs have not been adequately addressed.

The key components of ASSs are model-based controllers. Thus, simple and accurate models of MTAHVs are essential. Different ASSs may have different objectives and working ranges with respect to lateral acceleration for them to perform effectively (He et al, 2016). The ATS, ARC and TDB are effective at the lateral acceleration levels of 0-0.3g, 0.3-0.6g and 0.2-0.7g, respectively. For an ATS system to enhance maneuverability and stability in the 0-0.3g lateral acceleration range, a linear yaw-plane model of MTAHV with linear tire models may be sufficient. For the formulation of the ARC system in the range of 0.3-0.6g, the focus of the model is mainly put on

the prediction of roll dynamics considered in a linear range, a linear yaw-roll model may be competent. When design the TDB system to stabilize the lateral dynamics of MTAHV under extreme operating conditions of lateral acceleration 0.3-0.7g, considering the effect of longitudinal speed reduction and addressing the saturation property of pneumatic tires, a nonlinear yaw-plane model, considering the longitudinal, lateral and yaw dynamics and applying nonlinear tire models for predicting the lateral tire forces, may be indispensable.

For the purpose of ASS design, optimization and coordination for MTAHVs, Islam et al (2014) have studied multiple MTAHV models. However, their work is limited to linear models; the saturation property of pneumatic tires is not addressed; the presented models may be effective for design of ATS and ARC; the performance of TDB based on these linear models may be compromised; and due to their simplicity, these models may not be suitable for simulating vehicle dynamics.

Numerical simulations play increasingly important role in the MTAHV dynamics. To simulate the MTAHV dynamics, dynamics models with sufficient levels of accuracy and fidelity are imperative. To incorporate with the ATS, the dynamics model shall be capable of providing lateral dynamic performance measures, such as yaw rates and side-slip angles of all vehicle units. To evaluate the effectiveness of the ARC system, the performance measures such as the static rollover threshold of MTAHV and lateral load transfer ratios of individual axles are required. To assess the performance of the TDB system, the performance measures of lateral, yaw and longitudinal dynamics and the combined nonlinear longitudinal and lateral characteristics of pneumatic tires are required.

In this chapter, modelling of a tractor/semitrailer and a B-train double is conducted. The tractor/semitrailer is modelled with a three DOF linear yaw-plane model, a three DOF nonlinear yaw-plane model, and a twenty-one DOF TruckSim model. The linear yaw-plane model is used to design

a linear sliding mode active steering controller and a mu-synthesis active steering controller. The nonlinear yaw-plane model is utilized to formulate a nonlinear sliding mode active steering controller. The TruckSim model is applied to simulate the tractor/semitrailer dynamics. A linear yaw-plane model, a linear yaw-roll model, and a nonlinear yaw-plane model of the B-train double are derived using the Newtonian mechanics. The linear yaw-plane model is intended for use in an ATS and a sliding mode preview driver model design. The linear yaw-roll model is expected to construct an ARC system and an integrated control system considering the ATS, TDB and ARC. The nonlinear yaw-plane model will be used to formulate a TDB system. The nonlinear yaw-roll model is generated using the EoM software package (Minaker and Rieveley, 2010, Minaker and Rieveley, 2013) to simulate the dynamics of MTAHV. To verify the feasibility and applicability, the yaw-plane model, linear yaw-roll model, nonlinear yaw-plane model and the nonlinear EoM yaw-roll model are validated with a TruckSim model in various lateral acceleration conditions. To disclose the essential difference between the linear and nonlinear models, the linear yaw-plane and yaw-roll models are compared with the nonlinear yaw-plane and yaw-roll models under a high lateral acceleration manoeuvre to justify the allocation of the models to the ASSs.

3.2 Modeling of a Tractor/Semitrailer

3.2.1 Three DOF Linear Yaw-Plane Model

The tractor/semitrailer combination consists of a tractor with two axles and a semitrailer with a single axle, and the tractor and semitrailer are connected with a fifth wheel. As shown in Figure 3.1, the vehicle system is telescoped laterally and each axle set is denoted by one wheel. Based on the body-fixed coordinate systems $x_1 - y_1$ and $x_2 - y_2$ for the tractor and semitrailer, respectively, the governing equations of motion for the model can be derived (Eills, 1969). The motions

considered are the tractor side-slip angle, β_1, tractor yaw rate, $\dot{\psi}_1$, and articulation angle, $\Delta\psi$, between the tractor and semitrailer. In this model, the aerodynamic forces, the rolling and pitching motions, and the longitudinal forces between tire and road are ignored. To derive the vehicle model, the following assumptions have been made: (1) the forward speed U remains constant; (2) the tractor's front wheel steer angle δ_{1f} is small; (3) the articulation angle $\Delta\psi$ is small; (4) all products of variables, i.e., all second order terms of small variations, are ignored; and (5) the lateral tire force $F_i, i = 1,2,3$ is a linear function of the tire side-slip angle α_i, i = 1,2,3.

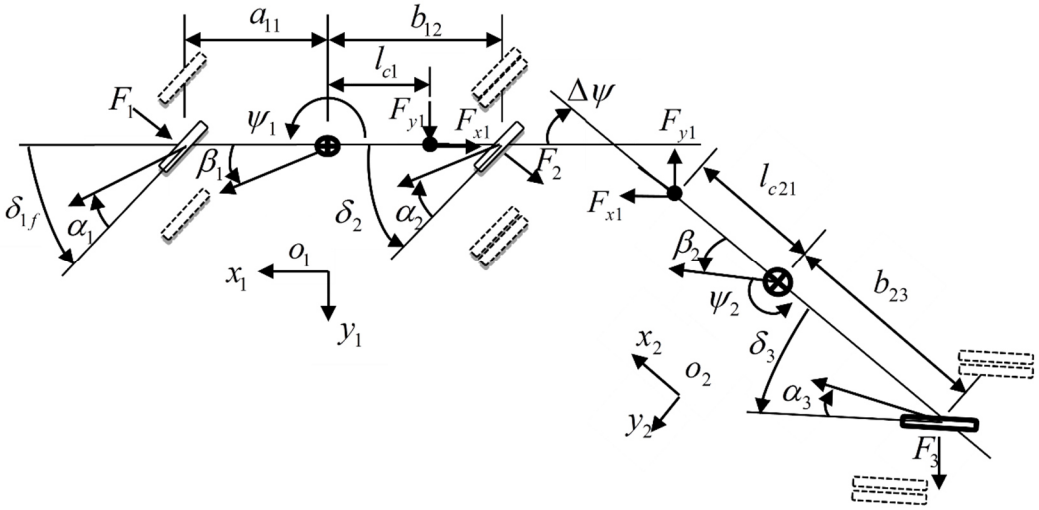

Figure 3.1 Yaw-plane model of the tractor/semitrailer combination

From the Newton's law of dynamics, the equations of motion for the tractor are

$$m_1 U_1 \left(\dot{\psi}_1 + \dot{\beta}_1\right) = F_1 + F_2 + F_{y1} \tag{3.1a}$$

$$I_{zz1}\ddot{\psi}_1 = F_1 a_{11} - F_2 b_{12} - F_{y1} l_{c1} \tag{3.1b}$$

The equations of motion for the semitrailer are

$$m_2 U_2 (\dot{\psi}_2 + \dot{\beta}_2) = F_3 - F_{y1} + \Delta\psi \cdot F_{x1} \tag{3.2a}$$

$$I_{zz2}\ddot{\psi}_2 = -F_3 b_{23} - F_{y1} l_{c21} + \Delta\psi \cdot F_{x1} l_{c21} \tag{3.2b}$$

As shown Figure 3.1, the following kinematic relations hold,

$$\alpha_1 = \beta_1 + \left(\frac{a_{11}}{U_1}\right)\dot{\psi}_1 - \delta_{1f},\ \alpha_2 = \beta_1 - \left(\frac{b_{12}}{U_1}\right)\dot{\psi}_1 - \delta_2 \tag{3.3a}$$

$$\alpha_3 = \beta_1 - \Delta\psi - \frac{l_{c21} + b_{23} + l_{c1}}{U_1}\dot{\psi}_1 - \frac{l_{c21} + b_{23}}{U_2}\Delta\dot{\psi} - \delta_3 \tag{3.3b}$$

$$\beta_2 = \beta_1 - \Delta\psi - \frac{l_{c1} + l_{c21}}{U_1}\dot{\psi}_1 - \frac{l_{c21}}{U_2}\Delta\dot{\psi},\ \Delta\psi = \psi_2 - \psi_1 \tag{3.3c}$$

where $\Delta\psi$ is defined as the articulation angle between the tractor and the trailer. The reader is referred to (Eills, 1969) for the details about the derivation of the above kinematic relations. The lateral tire forces are determined using the linear tire model as

$$F_1 = -C_{f11}\alpha_1,\ F_2 = -C_{r12}\alpha_2,\ F_3 = -C_{r23}\alpha_3 \tag{3.4}$$

where C_{f11}, C_{r12} and C_{r23} are the total cornering stiffness of the tires on the tractor front axle, tractor rear axle, and the semitrailer axle, respectively. Eliminating the coupling forces from Equations (3.1) and (3.2) and combining with Equations (3.3) and (3.4) leads to the three DOF linear yaw-plane model expressed as

$$\mathbf{M}\dot{\mathbf{x}} = \mathbf{P}\mathbf{x} + \mathbf{H}_1\delta_{1f} + \mathbf{H}_2\delta_2 + \mathbf{H}_3\delta_3 \tag{3.5}$$

where system matrices $\mathbf{M}$, $\mathbf{P}$, $\mathbf{H}_1$, $\mathbf{H}_2$ and $\mathbf{H}_3$ are given in Appendix A, and the state vector is defined as

$$\mathbf{x} = \begin{bmatrix}\dot{\psi}_1 & \Delta\dot{\psi} & \beta_1 & \Delta\psi\end{bmatrix}^T \tag{3.6}$$

The state-space form of Equation (3.5) can be rewritten as

$$\dot{\mathbf{x}} = \mathbf{A}\mathbf{x} + \mathbf{B}_1\delta_{1f} + \mathbf{B}_2\delta_2 + \mathbf{B}_3\delta_3 \tag{3.7}$$

where $\mathbf{A}=\mathbf{M}^{-1}\mathbf{P}$, $\mathbf{B}_1=\mathbf{M}^{-1}\mathbf{H}_1$, $\mathbf{B}_2=\mathbf{M}^{-1}\mathbf{H}_2$, $\mathbf{B}_3=\mathbf{M}^{-1}\mathbf{H}_3$. The output is defined as the lateral accelerations at the CG of the tractor and the CG of the semitrailer, i.e., $\mathbf{y}=[\ddot{y}_1 \quad \ddot{y}_2]^T$. Hence, the output equation is derived as

$$\mathbf{y}=\mathbf{C}\mathbf{x}+\mathbf{D}_1\delta_{1f}+\mathbf{D}_2\delta_2+\mathbf{D}_3\delta_3 \tag{3.8}$$

where the matrices $\mathbf{C}$, $\mathbf{D}_1$, $\mathbf{D}_2$ and $\mathbf{D}_3$ are offered in Appendix A. The notation and nominal values of the parameters of the tractor/semitrailer are provided in Table A1 in Appendix A. The tire cornering stiffness coefficients are identified using the TruckSim model to be introduced.

3.2.2 Three DOF Nonlinear Yaw Plane Model

The three DOF nonlinear yaw-plane model can be obtained by replacing the linear tire model in Equation (3.4) with the magic formula (Pacejka, 2005). The state-space equation of the nonlinear yaw plane model is derived as

$$\dot{\mathbf{x}}=\mathbf{A}_{nl}\mathbf{x}+\mathbf{B}_{nl}F,\ \mathbf{y}=\mathbf{C}_{nl}\mathbf{x}+\mathbf{D}_{nl}F \tag{3.9}$$

where $\mathbf{A}_{nl}=\mathbf{M}^{-1}\mathbf{P}_{nl}$, $\mathbf{B}_{nl}=\mathbf{M}^{-1}\mathbf{H}_{nl}$, and the system matrices $\mathbf{C}_{nl}$, $\mathbf{D}_{nl}$, $\mathbf{M}$, $\mathbf{P}_{nl}$, $\mathbf{H}_{nl}$ are given in Appendix A; and the lateral tire force vector $F=[F_1 \quad F_2 \quad F_3]^T$ is calculated as

$$F_i=D_i\sin\left(C_i\arctan\left\{B_i\alpha_i-E_i\left[B_i\alpha_i-\arctan\left(B_i\alpha_i\right)\right]\right\}\right),\ i=1,2,3 \tag{3.10}$$

where $B_i, C_i, D_i,$ and E_i are the magic formula parameters (Pacejka, 2005) tuned to match the responses of the nonlinear yaw-plane model with the TruckSim tractor/semitrailer model.

3.2.3 TruckSim Model

The TruckSim software package is based on a symbolic multibody program, VehicleSim (VS) Lisp, to generate equations of motion for 3 dimensional multibody vehicle systems (MSC, 2014, Islam, et al., 2015). As shown in Figure 3.2, the configuration of the tractor/semitrailer

combination is defined as "*S_S+S"*, where "*S"* indicates a solid axle, an underscore "_" a separation of axle groups, a "+" a fifth wheel connecting two vehicle units. Thus, as the configuration indicated, the tractor/semitrailer combination consists of a 2 solid-axle tractor having one front axle and one rear axle, and one semitrailer having one solid axle.

Figure 3.2 TruckSim model of the tractor/semitrailer combination

The VS Lisp takes an input as the description of the AHV configuration mostly in geometric terms, e.g., body DOF, point locations, directions of force vectors, etc. (MSC, 2014). With the configuration information, the VS Lisp derives equations of motion in terms of ordinary differential equations (ODEs), and generates computer source code (C or Fortran) to solve them.

The TruckSim software package involves the following three relevant elements: 1) VS browser, 2) TruckSim databases, and 3) VS solver. The VS browser is a graphical user interface (GUI), which serves as the primary interface to the TruckSim. The TruckSim databases are used to select vehicle configuration templates (e.g., *S_S+S,* for which the ODEs are generated by the VS Lisp), and define system parameters, tire-road interactions, test maneuvers, etc. The VS solver is utilised to solve relevant governing equations of motion of the vehicle model and execute the

defined dynamic simulations. The VS browser can be used to allow other applications, e.g., a design optimization defined in MATLAB, access to the TruckSim databases via an interface.

In the TruckSim model, the nonlinear dynamics of the pneumatic tires, suspension systems, and mechanical joints, etc., are taken into account. For a nonlinear vehicle model, the motions considered are as follows. Each of the sprung masses is considered as a rigid body with six DOF, namely lateral, longitudinal, vertical, pitch, roll and yaw. The fifth wheel is modeled as a ball-joint, about which roll, yaw, and pitch motions are allowed. Each axle is treated as a beam axle that can roll and bounce with respect to the sprung mass to which it is attached. Each wheel is modeled with a spinning DOF. Thus, the tractor/semitrailer combination has been modeled as a twenty-one DOF nonlinear model using the TruckSim software.

3.2.4 Validation of the Tractor/Semitrailer Models

3.2.4.1 Model Validation in the Time-Domain

The yaw-plane models are first validated with the TruckSim model in the time-domain to gain composite information of the models under a specified maneuver. The single cycle sine wave lateral acceleration test (SCSLA) specified in SAE J2179 (SAE, 1993) with the desired trajectory shown in Figure 3.3, is conducted. The desired trajectory is integrated up from a 0.15g amplitude SCSLA. The driver model provided in the TruckSim is employed to 'drive' the virtual tractor/semitrailer and the yaw-plane models. The design parameters of the driver model, e.g., preview time and time lag, are manipulated in a way that the lateral acceleration response of the tractor mimics the designated lateral acceleration as close as possible while the trajectory of tractor CG remains in the $\pm 150mm$ tolerance from the desired one. The lateral accelerations of the tractor and semitrailer of all models are shown in Figure 3.4. The nonlinear yaw-plane model has achieved better agreement with the TruckSim model, especially on the semitrailer unit.

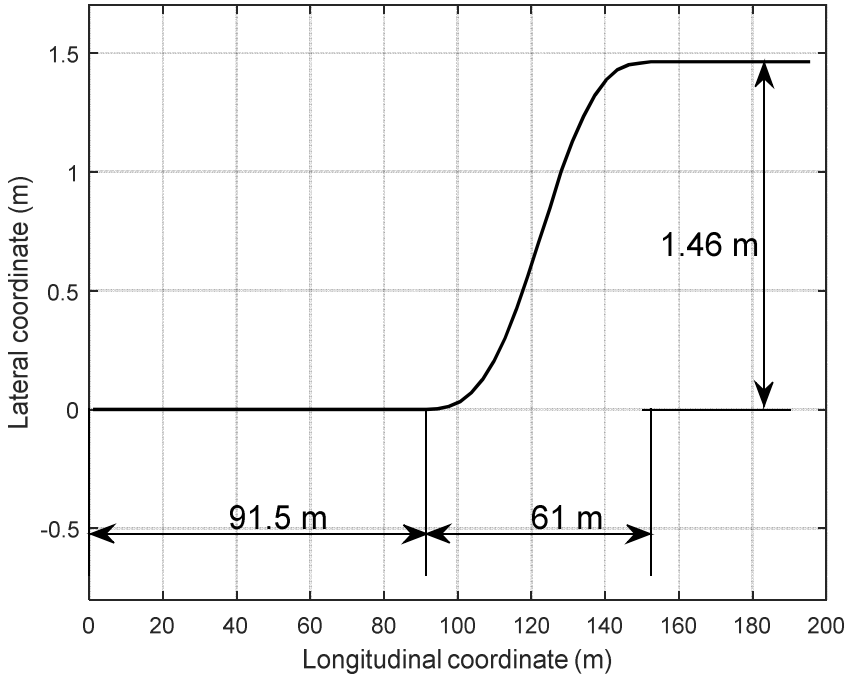

Figure 3.3 Desired trajectory of the CG of the tractor under the SCSLA maneuver

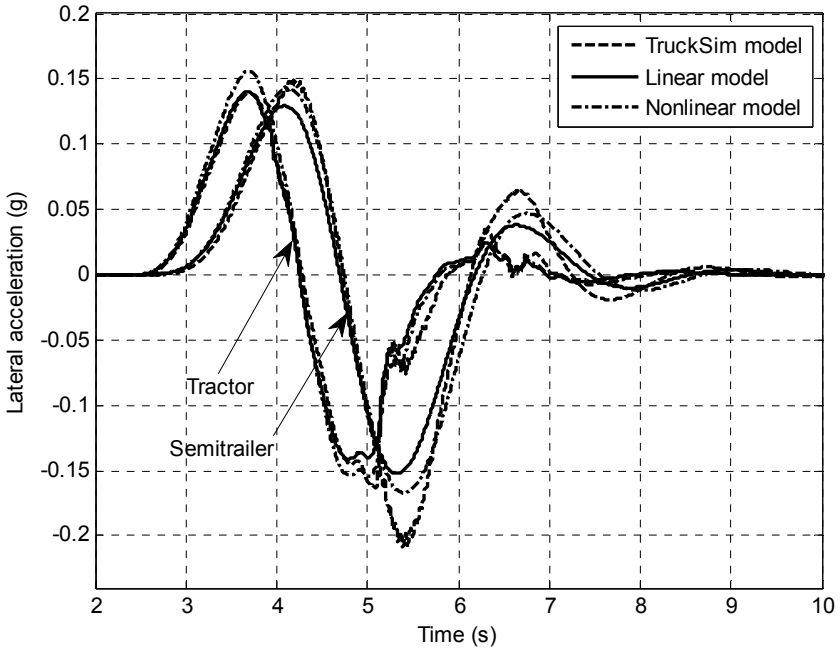

Figure 3.4 Time histories of lateral accelerations of the linear, nonlinear and TruckSim tractor/semitrailer models under the SCSLA maneuver

3.2.4.2 Frequency Analysis of the Tractor/Semitrailer Models

To validate the linear and nonlinear yaw-plane models in the frequency-domain, the magnitude responses acquired using the automated frequency response measuring technique (AFRM) are compared with that of the TruckSim model in the frequency range of 0 to 1 Hz, inspired by previous works (Ervin and MacAdam, 1982 and ISO, 2000). The AFRM will be introduced in Chapter 4. The tractor/semitrailer models are excited using the multi-cycle sine wave steer input (MCSSI) in the continuous mode to minimize transient effect (Zhu et al, 2016).

Figure 3.5 shows the RA (rearward amplification ratio in lateral acceleration) frequency functions of the tractor/semitrailer models. Figure 3.6 shows the frequency functions of the gain between the tractor lateral acceleration and the steering wheel angle, and Figure 3.7 the frequency functions of the gain between the semitrailer lateral acceleration and the steering wheel angle. The frequency analysis results disclose that the simple three DOF yaw-plane models only catch the main trend of the directional response of the complex twenty-one DOF nonlinear TruckSim model; the time-domain validated models cannot guarantee good agreement in a frequency range of interest; and the yaw plane models used to design ASSs are subjected to model inaccuracy and un-modeled dynamics. This inaccuracy and un-modeled dynamics may be mainly induced by large amount of approximations, reduced DOF, neglected nonlinearities, and unconsidered load shifting. The model inaccuracy and un-modeled dynamics identified are main concern of capability of the model-based ASSs to be designed and motivated us to investigate robust ASSs in Chapter 7.

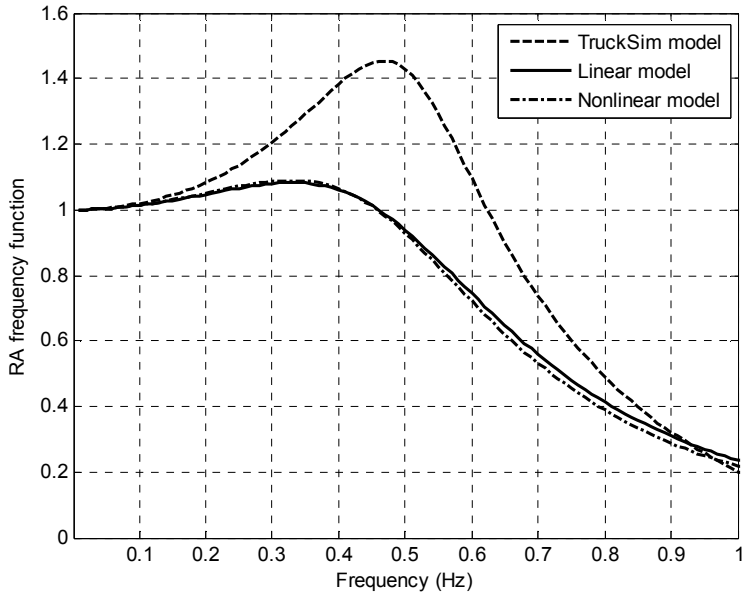

Figure 3.5 RA frequency functions of the TruckSim, linear, and the nonlinear tractor/semitrailer models

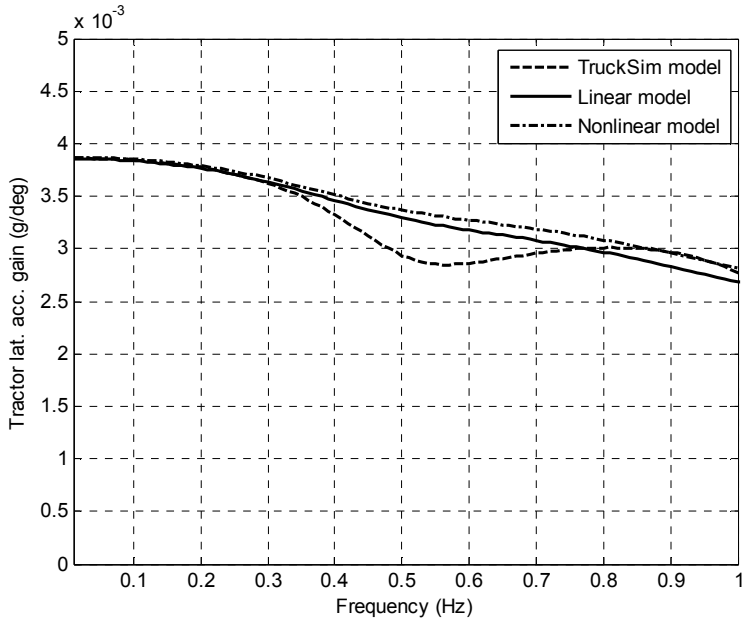

Figure 3.6 Frequency functions of the gain between the tractor lateral acceleration and the steering wheel angle of the TruckSim, linear and the nonlinear tractor/semitrailer models

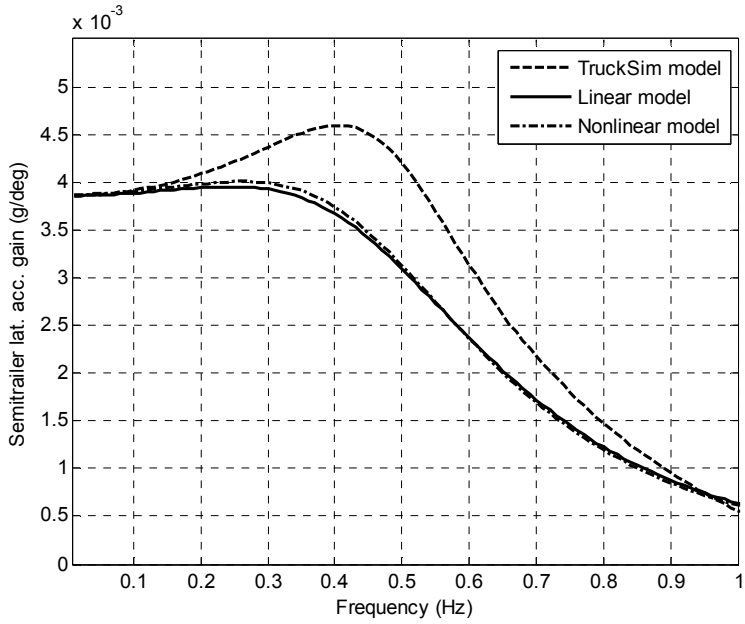

Figure 3.7 Frequency functions of the gain between the semitrailer lateral acceleration and the steering wheel angle of the TruckSim, linear the nonlinear tractor/semitrailer models

3.3 Modeling of the B-train Double

3.3.1 Vehicle Modeling Using the Newtonian Mechanics

In this section, a linear yaw-plane model, a linear yaw-roll model, and a nonlinear yaw-plane model of the B-train double are generated using the Newtonian mechanics (Lin, 1994, Sampson, 2000 and Cheng, 2009). The notation and nominal values of the parameters of the B-train double models are provided in Appendix B.

3.3.1.1 The Coordinate Systems

The linear yaw-plane model, linear yaw-roll model, and the nonlinear yaw-plane model are considered in the SAE coordinate system (Gillespie, 1992). Figure 3.8 shows the B-train double with the inertia and the body-fixed coordinate systems. In the linear yaw-roll model, the B-train double is modeled with six rigid bodies, namely, the sprung masses and unsprung masses of the tractor, 1st and the 2nd semitrailers. The three axles on each unit are lumped into a rigid-body, i.e.,

the unsprung, based on the experimental results on the TruckSim model of the B-train double. Figure 3.9 shows the axle roll angle time histories of the TruckSim model under a single cycle sine wave steer input. The roll angles of the nine axles are clustered quite well in three groups which suggests to model the three axles of each unit as a rigid-body.

In the linear yaw-roll model, the sprung masses are connected to the corresponding unsprung masses with torsional springs of constant stiffness and damping coefficients. The unsprung masses hold constant roll stiffness in the range of roll motion. The three sprung masses are connected with two fifth-wheels, which restrict relative translational and pitch motions of the adjacent units, allow relative yaw motion, and govern relative roll with springs of constant roll stiffness. An inertia coordinate system $(OXYZ)$, which is fixed on the ground, works as a basic reference frame. Three body-fixed coordinate systems, $(o_1x_1y_1z_1)$, $(o_2x_2y_2z_2)$ and $(o_3x_3y_3z_3)$ as shown in Figure 3.8 are employed with the corresponding x-axis coincident with the roll axis and the origin under the CG of whole mass of the corresponding unit.

In the linear or nonlinear yaw-plane model, the B-train double is modeled with three rigid bodies, namely, the tractor, 1st and 2nd semitrailer. The roll dynamics is not considered. The two adjacent vehicle units are connected with a fifth-wheel, restricting relative translational, roll and pitch motions and allowing the freedom of relative yaw.

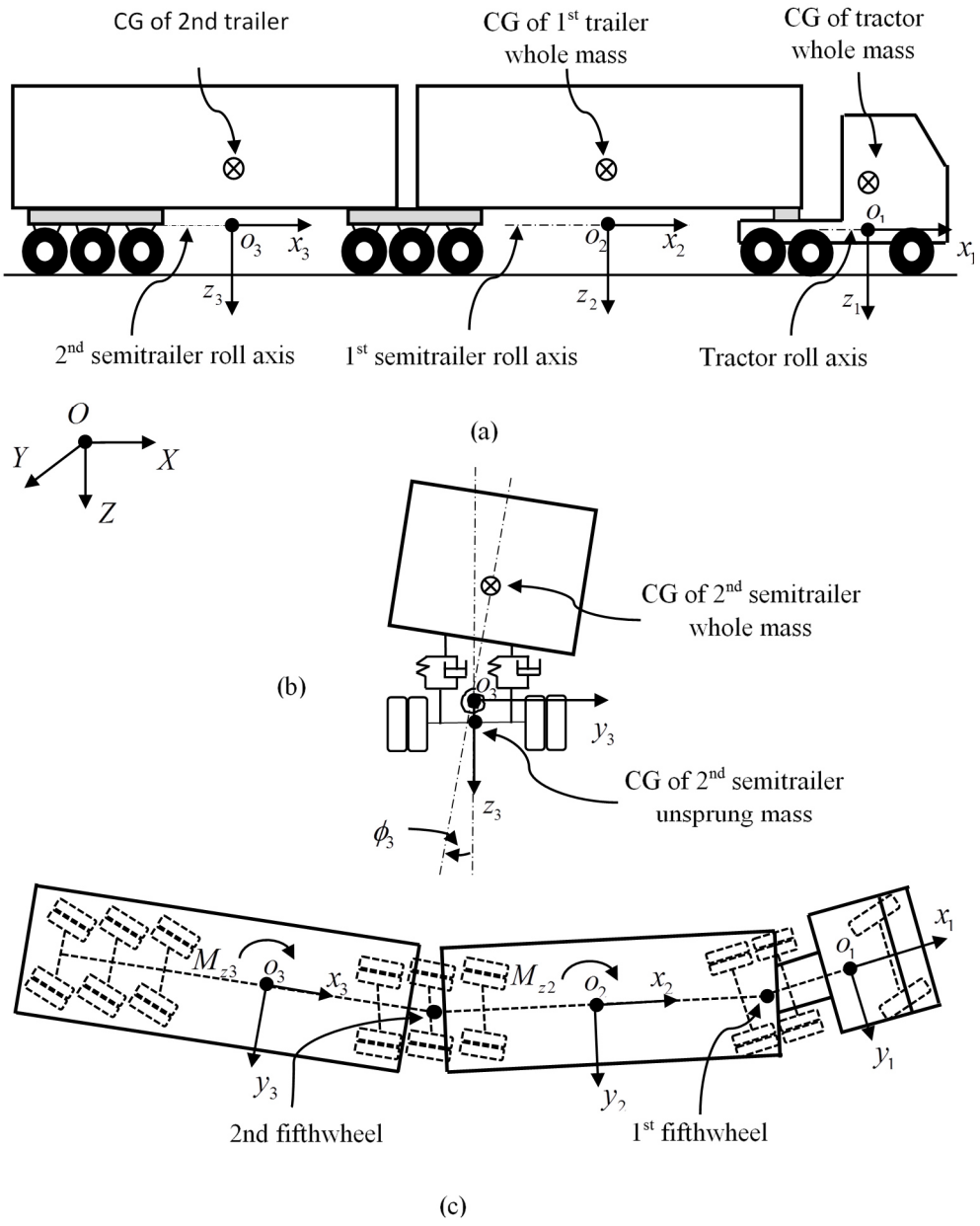

Figure 3.8 Yaw-roll model of a B-train double with the inertia and vehicle fixed coordinate systems: (a) side view, (b) rear view, and (c) top view

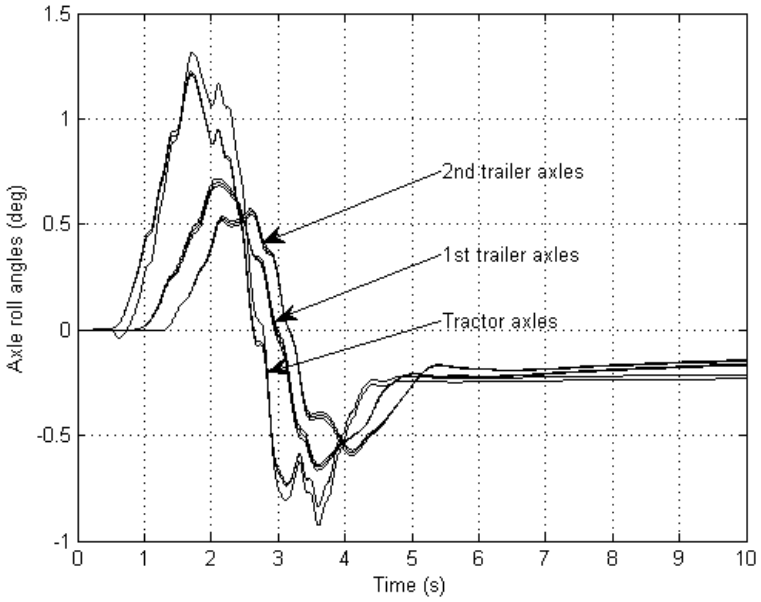

Figure 3.9 Axle roll angles of the TruckSim model of the B-train double under a 0.4 Hz single cycle sine wave steer input

In the linear yaw-plane model, the B-train double is modeled with four DOF including the yaw and lateral motion of the tractor, yaw motions of the 1st and 2nd semitrailers. In the nonlinear yaw-plane model, the B-train double is modeled with five DOF including longitudinal, lateral and yaw motions of the tractor and yaw motions of the 1st and 2nd semitrailers. The motions considered in the linear and nonlinear yaw-plane models are located at the CGs of the whole masses of the vehicle units. The variables of motion in the linear/nonlinear yaw-plane models are denoted in a state vector

$$\mathbf{x} = \begin{bmatrix} \beta_1 & \dot{\psi}_1 & \beta_2 & \dot{\psi}_2 & \beta_3 & \dot{\psi}_3 \end{bmatrix}^T \Big/ \begin{bmatrix} U & \beta_1 & \dot{\psi}_1 & \beta_2 & \dot{\psi}_2 & \beta_3 & \dot{\psi}_3 \end{bmatrix}^T \tag{3.11}$$

In the linear yaw-roll model, the B-train double is modeled with ten DOF including the yaw and lateral motion of the tractor sprung mass, yaw motions of the 1st and 2nd semitrailer sprung masses, and the roll motions of the six rigid-bodies. The lateral and yaw motions considered are

located at the CGs of the whole mass of the tractor, 1st and the 2nd semitrailers, and the variables of motions are denoted in the state vector

$$\mathbf{x} = \left[\phi_1 \quad \dot{\phi}_1 \quad \beta_1 \quad \dot{\psi}_1 \quad \phi_2 \quad \dot{\phi}_2 \quad \beta_2 \quad \dot{\psi}_2 \quad \phi_3 \quad \dot{\phi}_3 \quad \beta_3 \quad \dot{\psi}_3 \quad \phi_{t1} \quad \dot{\phi}_{t1} \quad \phi_{t2} \quad \dot{\phi}_{t2} \quad \phi_{t3} \quad \dot{\phi}_{t3} \right]^T \quad (3.12)$$

3.3.1.2 Kinematical Constraint Equations

The equations of motion of the B-train double consists of kinematical constraint equations induced by the fifth-wheels and dynamic equations responding to external forces and moments. The kinematical constraints can be modeled through the coordinate transformation of the velocities at the fifth-wheels using the rotational kinematics (Hibbeler, 2007). The velocities of the tractor, 1st and the 2nd semitrailers at the 1st and 2nd coupling points denoted in the respective body-fixed coordinate systems are converted into the inertia coordinate system to be comparable.

The velocities of the tractor and the 1st semitrailer at the 1st coupling point in the linear yaw-roll model given in the tractor-fixed coordinate system $\left(o_1 x_1 y_1 z_1\right)$, and the 1st semitrailer-fixed coordinate system $\left(o_2 x_2 y_2 z_2\right)$ are, respectively:

$${}^{yr}\vec{V}_1^1 = U\vec{i}_1 + \left[V_1 + \left(h_{c1} - h_{r1} \right) \dot{\phi}_1 - l_{c1} \dot{\psi}_1 \right] \vec{j}_1 \quad (3.13a)$$

$${}^{yr}\vec{V}_2^1 = U\vec{i}_2 + \left[V_2 + \left(h_{c2} - h_{r2} \right) \dot{\phi}_2 + l_{c21} \dot{\psi}_2 \right] \vec{j}_2 \quad (3.13b)$$

Note that the superscript and the subscript of a velocity represents the coupling point and the body-fixed coordinate system, respectively. The velocities of the 1st and 2nd semitrailers at the 2nd coupling point in the yaw-roll model given in the 1st semitrailer-fixed coordinate system $\left(o_2 x_2 y_2 z_2\right)$ and 2nd semitrailer-fixed coordinate system $\left(o_3 x_3 y_3 z_3\right)$ are:

$${}^{yr}\vec{V}_2^2 = U\vec{i}_2 + \left[V_2 + \left(h_{c2} - h_{r2} \right) \dot{\phi}_2 - l_{c22} \dot{\psi}_2 \right] \vec{j}_2 \quad (3.14a)$$

$$^{yr}\vec{V}_3^2 = U\vec{i}_3 + \left[V_3 + \left(h_{c3} - h_{r3}\right)\dot{\phi}_3 + l_{c3}\dot{\psi}_3\right]\vec{j}_3 \tag{3.14b}$$

In the yaw-plane model, similarly, the velocities of the tractor and 1st semitrailer at the 1st coupling point given in the tractor-fixed coordinate system $\left(o_1x_1y_1\right)$ and the 1st semitrailer-fixed coordinate system $\left(o_2x_2y_2\right)$ are, respectively:

$$^{yp}\vec{V}_1^1 = U\vec{i}_1 + \left(V_1 - l_{c1}\dot{\psi}_1\right)\vec{j}_1 \tag{3.15a}$$

$$^{yp}\vec{V}_2^1 = U\vec{i}_2 + \left(V_2 + l_{c21}\dot{\psi}_2\right)\vec{j}_2 \tag{3.15b}$$

The velocities of the 1st and 2nd semitrailers at the 2nd coupling point given in the 1st semitrailer-fixed coordinate system $\left(o_2x_2y_2\right)$ and 2nd semitrailer-fixed coordinate system $\left(o_3x_3y_3\right)$ are respectively:

$$^{yp}\vec{V}_2^2 = U\vec{i}_2 + \left(V_2 - l_{c22}\dot{\psi}_2\right)\vec{j}_2 \tag{3.16a}$$

$$^{yp}\vec{V}_3^2 = U\vec{i}_3 + \left(V_3 + l_{c3}\dot{\psi}_3\right)\vec{j}_3 \tag{3.16b}$$

The velocities at the coupling points represented in the yaw-plane model are basically the same as those represented in the yaw-roll model but with the roll-associated terms removed or set to zero due to the negligence of the roll dynamics.

The velocities of different unit at the same coupling point should be equal when represented in the same coordinate system, i.e., the inertia coordinate system $\left(OXYZ\right)$. Converting the coordinates in the body-fixed coordinate systems into the inertia coordinate system $\left(OXYZ\right)$ using the rotational kinematics are explained in detail by Jazar (2011), and applied by Lin (1994) to derive the kinematic constraint for a tractor/semitrailer. When conducting the conversion, the rotation angles and lateral velocities are assumed small. The cosine and sine of the rotation angle

approximately equals one and the angle itself, respectively. The product terms between the rotation angles and lateral velocities are ignored.

For the yaw-roll model, conversions about the yaw and the roll axis are conducted and the sequence of conversion has no effect. For the yaw-plane model, only one conversion about the yaw-axis is conducted. Converting the velocities at the 1st coupling point in the tractor-fixed coordinate systems $(o_1 x_1 y_1 z_1)$ of the yaw-roll model and $(o_1 x_1 y_1)$ of the yaw-plane model are given respectively:

$$ {}^{yr}_{O}\vec{V}_1^1 = \begin{bmatrix} \cos\psi_1 & -\sin\psi_1 & 0 \\ \sin\psi_1 & \cos\psi_1 & 0 \\ 0 & 0 & 1 \end{bmatrix} \begin{bmatrix} 1 & 0 & 0 \\ 0 & \cos\phi_1 & -\sin\phi_1 \\ 0 & \sin\phi_1 & \cos\phi_1 \end{bmatrix} {}^{yr}\vec{V}_1^1 = \begin{bmatrix} U\vec{I} \\ \left[U\psi_1 + V_1 + (h_{c1} - h_{r1})\dot{\phi}_1 - l_{c1}\dot{\psi}_1\right]\vec{J} \\ V_1\phi_1\vec{K} \end{bmatrix} \tag{3.17a} $$

$$ {}^{yp}_{O}\vec{V}_1^1 = \begin{bmatrix} \cos\psi_1 & -\sin\psi_1 & 0 \\ \sin\psi_1 & \cos\psi_1 & 0 \\ 0 & 0 & 1 \end{bmatrix} {}^{yp}\vec{V}_1^1 = \begin{bmatrix} U\vec{I} \\ (U\psi_1 + V_1 - l_{c1}\dot{\psi}_1)\vec{J} \\ 0\vec{K} \end{bmatrix} \tag{3.17b} $$

All other coordinates are converted in the same manner. By setting the velocities at the same coupling point equal, the kinematic constraints for the yaw-roll model and the yaw-plane model are derived, respectively, as

$$ \dot{\beta}_1 - \dot{\beta}_2 + \frac{h_{cr1}}{U}\ddot{\phi}_1 - \frac{l_{c1}}{U}\ddot{\psi}_1 - \frac{h_{cr2}}{U}\ddot{\phi}_2 - \frac{l_{c21}}{U}\ddot{\psi}_2 + \dot{\psi}_1 - \dot{\psi}_2 = 0 \tag{3.18a} $$

$$ \dot{\beta}_2 - \dot{\beta}_3 + \frac{h_{cr2}}{U}\ddot{\phi}_2 - \frac{l_{c22}}{U}\ddot{\psi}_2 - \frac{h_{cr3}}{U}\ddot{\phi}_3 - \frac{l_{c3}}{U}\ddot{\psi}_3 + \dot{\psi}_2 - \dot{\psi}_3 = 0 \tag{3.18b} $$

$$ \dot{\beta}_1 - \frac{l_{c1}}{U}\ddot{\psi}_1 - \dot{\beta}_2 - \frac{l_{c21}}{U}\ddot{\psi}_2 + \dot{\psi}_1 - \dot{\psi}_2 = 0 \tag{3.18c} $$

$$\dot{\beta}_2 - \frac{l_{c22}}{U}\ddot{\psi}_2 - \dot{\beta}_3 - \frac{l_{c3}}{U}\ddot{\psi}_3 + \dot{\psi}_2 - \dot{\psi}_3 = 0 \tag{3.18d}$$

3.3.1.3 Linear Yaw-roll, Linear Yaw-plane, and Nonlinear Yaw-plane Models

1) Linear Yaw-Roll Model

For simplicity, the following assumptions are made for the linear yaw-roll and yaw-plane models: 1) the forward speed of the vehicle is fixed; 2) the longitudinal, vertical and the pitch dynamics are ignored; 3) the wheel dynamics are negligible; 4) the articulation angles and the side-slip angles are small; and 5) the aerodynamics are ignored. The linear tire models are applied for the linear yaw-roll model. The dynamic equations of the linear yaw-roll model are derived using the three-dimensional kinetics (Hibbeler, 2007). Taking the tractor sprung mass as an example, in three-dimensional rotation in the tractor-fixed coordinate system $(o_1 x_1 y_1 z_1)$, the general equations of rotation are given by:

$$\begin{aligned}\left[I_{sxx1} + \left(h_{s1} - h_{r1}\right)^2 m_{s1}\right]\ddot{\phi}_1 - \left(I_{syy1} - I_{szz1}\right)\dot{\theta}_1\dot{\psi}_1 - I_{sxy1}\left(\ddot{\theta}_1 - \dot{\psi}_1\dot{\phi}_1\right) - I_{syz1}\left(\dot{\theta}_1^2 - \dot{\psi}_1^2\right) \\ - I_{szx1}\left(\ddot{\psi}_1 + \dot{\phi}_1\dot{\theta}_1\right) = \sum M_{x1}\end{aligned} \tag{3.19a}$$

$$I_{syy1}\ddot{\theta}_1 - \left(I_{szz1} - I_{sxx1}\right)\dot{\psi}_1\dot{\phi}_1 - I_{syz1}\left(\ddot{\psi}_1 - \dot{\phi}_1\dot{\theta}_1\right) - I_{szx1}\left(\dot{\psi}_1^2 - \dot{\phi}_1^2\right) - I_{sxy1}\left(\ddot{\phi}_1 + \dot{\theta}_1\dot{\psi}_1\right) = \sum M_{y1} \tag{3.19b}$$

$$I_{szz1}\ddot{\psi}_1 - \left(I_{sxx1} - I_{syy1}\right)\dot{\phi}_1\dot{\theta}_1 - I_{szx1}\left(\ddot{\phi}_1 - \dot{\theta}_1\dot{\psi}_1\right) - I_{sxy1}\left(\ddot{\phi}_1^2 - \omega\dot{\theta}_1^2\right) - I_{syz1}\left(\ddot{\theta}_1 + \dot{\psi}_1\dot{\phi}_1\right) = \sum M_{z1} \tag{3.19c}$$

where $\sum M_{x1}$, $\sum M_{y1}$, $\sum M_{z1}$ denotes, respectively, the external roll, pitch, and yaw moments, I_{sxy1} the roll-pitch product of inertia, I_{syy1} the pitch moment of inertia, I_{syz1} the pitch-yaw product of inertia, and $\dot{\theta}_1$ the pitch rate of the tractor sprung mass. Note in the subscripts, s denotes the sprung mass, and 1 the 1st unit, i.e., the tractor. Taking into consideration the neglected pitch dynamics,

and the lateral symmetry of the sprung mass of the tractor results in $I_{sxy1} = I_{syz1} = \dot{\theta}_1 = 0$. Thus only the 1st and 3rd equations in (3.19) remain and are simplified to:

$$\left[I_{sxx1} + \left(h_{s1} - h_{r1} \right)^2 m_{s1} \right] \ddot{\phi}_1 - I_{szx1} \ddot{\psi}_1 = \sum M_{x1} \tag{3.20a}$$

$$I_{szz1} \ddot{\psi}_1 - I_{szx1} \ddot{\phi} = \sum M_{z1} \tag{3.20b}$$

Equation (3.20) governs the roll and yaw dynamics of the tractor sprung mass and serves as a template for building up the equations of rotational motion for all the rigid bodies considered. Also note that the sprung and unsprung masses of one vehicle unit share approximately the same yaw motion and thus are lumped into a whole unit with a single yaw dynamics equation.

Applying Equation (3.20) and translational dynamics, the governing equations of motion of the tractor in the linear yaw-roll model are given as

$$m_1 U \left(\dot{\beta}_1 + \dot{\psi}_1 \right) = -m_{s1} \left(h_{s1} - h_{r1} \right) \ddot{\phi}_1 + Y_{\beta_1} \beta_1 + Y_{\dot{\psi}_1} \dot{\psi}_1 + Y_{\delta_{11}} \delta_{11} + F_{cy1} \tag{3.21a}$$

$$-I_{sxz1} \ddot{\phi}_1 + I_{zz1} \ddot{\psi}_1 = N_{\beta_1} \beta_1 + N_{\dot{\psi}_1} \dot{\psi}_1 - l_{c1} F_{cy1} + N_{\delta_{11}} \delta_{11} \tag{3.21b}$$

$$\begin{aligned} &\left[I_{sxx1} + \left(h_{s1} - h_{r1} \right)^2 m_{s1} \right] \ddot{\phi}_1 - I_{sxz1} \ddot{\psi}_1 = m_{s1} g \left(h_{s1} - h_{r1} \right) \phi_1 - m_{s1} U \left(h_{s1} - h_{r1} \right) \left(\dot{\beta}_1 + \dot{\psi}_1 \right) \\ &+ \left(K_{r1f} + K_{r1r} \right) \left(\phi_{t1} - \phi_1 \right) + \left(L_{r1f} + L_{r1r} \right) \left(\dot{\phi}_{t1} - \dot{\phi}_1 \right) - K_{12} \left(\phi_1 - \phi_2 \right) + F_{cy1} h_{cr1} + M_{x1f} + M_{x1r} \end{aligned} \tag{3.21c}$$

$$\begin{aligned} &\left[I_{u1xx} + \left(h_{r1} - h_{u1} \right)^2 m_{u1} \right] \ddot{\phi}_{t1} - I_{u1xz} \ddot{\psi}_1 = -h_{r1} \left(Y_{\beta_1} \beta_1 + Y_{\dot{\psi}_1} \dot{\psi}_1 + Y_{\delta_{11}} \delta_{11} \right) - \left(K_{t1f} + K_{t1r} \right) \phi_{t1} \\ &\quad - m_{u1} U \left(h_{u1} - h_{r1} \right) \left(\dot{\beta}_1 + \dot{\psi}_1 \right) + m_{u1} g \left(h_{u1} - h_{r1} \right) \phi_{t1} - \left(K_{r1f} + K_{r1r} \right) \left(\phi_{t1} - \phi_1 \right) \\ &\quad - \left(L_{r1f} + L_{r1r} \right) \left(\dot{\phi}_{t1} - \dot{\phi}_1 \right) - M_{x1f} - M_{x1r} \end{aligned} \tag{3.21d}$$

The governing equations of the 1st semitrailer in the linear yaw-roll model are provided as

$$m_2 U \left(\dot{\beta}_2 + \dot{\psi}_2 \right) = -m_{s2} \left(h_{s2} - h_{r2} \right) \ddot{\phi}_2 + Y_{\beta_2} \beta_2 + Y_{\dot{\psi}_2} \dot{\psi}_2 - F_{cy1} + F_{cy2} \tag{3.22a}$$

$$-I_{sxz2} \ddot{\phi}_2 + I_{zz2} \ddot{\psi}_2 = N_{\beta_2} \beta_2 + N_{\dot{\psi}_2} \dot{\psi}_2 - l_{c21} F_{cy1} - l_{c22} F_{cy2} + M_{z2} \tag{3.22b}$$

$$\begin{aligned}&\left[I_{sxx2}+\left(h_{s2}-h_{r2}\right)^2 m_{s2}\right]\ddot{\phi}_2-I_{sxz2}\ddot{\psi}_2=m_{s2}g\left(h_{s2}-h_{r2}\right)\phi_2-m_{s2}U\left(h_{s2}-h_{r2}\right)\left(\dot{\beta}_2+\dot{\psi}_2\right)\\&-K_{r2}\left(\phi_2-\phi_{t2}\right)-L_{r2}\left(\dot{\phi}_2-\dot{\phi}_{t2}\right)-K_{12}\left(\phi_2-\phi_1\right)-K_{23}\left(\phi_2-\phi_3\right)-F_{cy1}h_{cr2}+F_{cy2}h_{cr3}+M_{x2}\end{aligned} \tag{3.22c}$$

$$\begin{aligned}&\left[I_{u2xx}+\left(h_{u2}-h_{r2}\right)^2 m_{u2}\right]\ddot{\phi}_{t2}-I_{u2xz}\ddot{\psi}_2=-h_{r2}\left(Y_{\beta 2}\beta_2+Y_{\dot{\psi}_2}\dot{\psi}_2\right)-K_{t2}\phi_{t2}\\&-m_{u2}U_2\left(h_{u2}-h_{r2}\right)\left(\dot{\beta}_2+\dot{\psi}_2\right)+m_{u2}g\left(h_{u2}-h_{r2}\right)\phi_{t2}-K_{r2}\left(\phi_{t2}-\phi_2\right)-L_{r2}\left(\dot{\phi}_{t2}-\dot{\phi}_2\right)-M_{x2}\end{aligned} \tag{3.22d}$$

The governing equations of the 2nd semitrailer in the linear yaw-roll model are derived as

$$m_3U\left(\dot{\beta}_3+\dot{\psi}_3\right)=-m_{s3}\left(h_{s3}-h_{r3}\right)\ddot{\phi}_3+Y_{\beta_3}\beta_3+Y_{\dot{\psi}_3}\dot{\psi}_3-F_{cy2} \tag{3.23a}$$

$$-I_{sxz3}\ddot{\phi}_3+I_{zz3}\ddot{\psi}_3=N_{\beta_3}\beta_3+N_{\dot{\psi}_3}\dot{\psi}_3-l_{c3}F_{cy2}+M_{z3} \tag{3.23b}$$

$$\begin{aligned}&\left[I_{xx3}+\left(h_{s3}-h_{r3}\right)^2 m_{s3}\right]\ddot{\phi}_3-I_{sxz3}\ddot{\psi}_3=m_{s3}g\left(h_{s3}-h_{r3}\right)\phi_3-m_{s3}U\left(h_{s3}-h_{r3}\right)\left(\dot{\beta}_3+\dot{\psi}_3\right)\\&\quad-K_{r3}\left(\phi_3-\phi_{t3}\right)-L_{r3}\left(\dot{\phi}_3-\dot{\phi}_{t3}\right)-K_{23}\left(\phi_3-\phi_2\right)-F_{cy2}h_{cr3}+M_{x3}\end{aligned} \tag{3.23c}$$

$$\begin{aligned}&\left[I_{u3xx}+\left(h_{u3}-h_{r3}\right)^2 m_{u3}\right]\ddot{\phi}_{t3}-I_{u3xz}\ddot{\psi}_3=-h_{r3}\left(Y_{\beta_3}\beta_3+Y_{\dot{\psi}_3}\dot{\psi}_3\right)-K_{t3}\phi_{t3}\\&-m_{u3}U_3\left(h_{u3}-h_{r3}\right)\left(\dot{\beta}_3+\dot{\psi}_3\right)+m_{u3}g\left(h_{u3}-h_{r3}\right)\phi_{t3}-K_{r3}\left(\phi_{t3}-\phi_3\right)-L_{r3}\left(\dot{\phi}_{t3}-\dot{\phi}_3\right)-M_{x3}\end{aligned} \tag{3.23d}$$

In Equations (3.21)-(3.23), the partial derivatives of the lateral forces and yaw moments with respect to the side-slip angle, yaw rate, and the steering angle(s), also be applicable for the linear yaw-plane model, are defined as

$$N_{\beta_1}=a_{11}C_1-b_{12}C_2-b_{13}C_3,\ N_{\beta_2}=-b_{24}C_4-b_{25}C_5-b_{26}C_6,\ N_{\beta_3}=-b_{37}C_7-b_{38}C_8-b_{39}C_9 \tag{3.24a}$$

$$N_{\dot{\psi}_1}=\frac{a_{11}^2C_1+b_{12}^2C_2+b_{13}^2C_3}{U},\ N_{\dot{\psi}_2}=\frac{b_{24}^2C_4+b_{25}^2C_5+b_{26}^2C_6}{U},\ N_{\dot{\psi}_3}=\frac{b_{37}^2C_7+b_{38}^2C_8+b_{39}^2C_9}{U} \tag{3.24b}$$

$$N_{\delta_{11}}=-a_1C_1 \tag{3.24c}$$

$$Y_{\beta_1}=C_1+C_2+C_3,\ Y_{\beta_2}=C_4+C_5+C_6,\ Y_{\beta_3}=C_7+C_8+C_9 \tag{3.24d}$$

$$Y_{\dot{\psi}_1}=\frac{a_{11}C_1-b_{12}C_2-b_{13}C_3}{U},\ Y_{\dot{\psi}_2}=\frac{-b_{24}C_4-b_{25}C_5-b_{26}C_6}{U},\ Y_{\dot{\psi}_3}=\frac{-b_{37}C_7-b_{38}C_8-b_{39}C_9}{U} \tag{3.24e}$$

$$Y_{\delta_{11}} = -C_1 \tag{3.24f}$$

The state-equation of the linear yaw-roll model is obtained by eliminating the lateral coupling forces in Equations (3.21)-(3.23), and rearranging with Equations (3.18a) and (3.18b):

$$\dot{\mathbf{x}} = \mathbf{A}\mathbf{x} + \mathbf{B}_{dd}\delta_{11} + \mathbf{B}\mathbf{u} \tag{3.25a}$$

$$\mathbf{y} = \mathbf{C}\mathbf{x} + \mathbf{D}_{dd}\delta_{11} + \mathbf{D}\mathbf{u} \tag{3.25b}$$

where $\mathbf{A} = -\mathbf{M}^{-1}\mathbf{N}$, $\mathbf{B}_{dd} = -\mathbf{M}^{-1}\mathbf{Q}$, $\mathbf{B} = \begin{bmatrix}\mathbf{B}_{Mz} & \mathbf{B}_{Mx}\end{bmatrix}$, $\mathbf{B}_{Mx} = -\mathbf{M}^{-1}\mathbf{R}$, $\mathbf{B}_{Mz} = -\mathbf{M}^{-1}\mathbf{W}$, $\mathbf{u} = \begin{bmatrix}M_{z2} & M_{z3} & M_{x1f} & M_{x1r} & M_{x2} & M_{x3}\end{bmatrix}^T$, $\mathbf{x} = \begin{bmatrix}\mathbf{x}_1 & \mathbf{x}_2 & \mathbf{x}_3 & \mathbf{x}_t\end{bmatrix}^T$, $\mathbf{x}_1 = \begin{bmatrix}\phi_1 & \dot{\phi}_1 & \beta_1 & \dot{\psi}_1\end{bmatrix}$, $\mathbf{x}_2 = \begin{bmatrix}\phi_2 & \dot{\phi}_2 & \beta_2 & \dot{\psi}_2\end{bmatrix}$, $\mathbf{x}_3 = \begin{bmatrix}\phi_3 & \dot{\phi}_3 & \beta_3 & \dot{\psi}_3\end{bmatrix}$, $\mathbf{x}_t = \begin{bmatrix}\phi_{t1} & \dot{\phi}_{t1} & \phi_{t2} & \dot{\phi}_{t2} & \phi_{t3} & \dot{\phi}_{t3}\end{bmatrix}$, $\mathbf{y} = \begin{bmatrix}a_{y1} & a_{y2} & a_{y3} & \phi_1 & \phi_{t1} & \phi_2 & \phi_{t2} & \phi_3 & \phi_{t3}\end{bmatrix}^T$ and matrices $\mathbf{C}$, $\mathbf{D}$, $\mathbf{D}_{dd}$, $\mathbf{M}$, $\mathbf{N}$, $\mathbf{Q}$, $\mathbf{R}$ and $\mathbf{W}$ are given in Appendix C.

2) Linear Yaw-Plane Model

In the linear yaw-plane model of the B-train double, the roll and pitch-dynamics are not considered. The dynamic equations consist of the governing equations for lateral, and yaw dynamics of the tractor, and yaw dynamics of the 1st and the 2nd semitrailers. The dynamic equations of the yaw-plane model can be obtained by removing roll dynamic equations from the yaw-roll model. The dynamic equations of the linear yaw-plane model of the tractor are given by:

$$m_1 U\left(\dot{\beta}_1 + \dot{\psi}_1\right) = Y_{\beta_1}\beta_1 + Y_{\dot{\psi}_1}\dot{\psi}_1 + Y_{\delta_{11}}\delta_{11} + F_{cy1} \tag{3.26a}$$

$$I_{zz1}\ddot{\psi}_1 = N_{\beta_1}\beta_1 + N_{\dot{\psi}_1}\dot{\psi}_1 - l_{c1}F_{cy1} + N_{\delta_{11}}\delta_{11} \tag{3.26b}$$

The dynamic equations of the linear yaw-plane model of the 1st semitrailer are derived as:

$$m_2 U\left(\dot{\beta}_2 + \dot{\psi}_2\right) = Y_{\beta_2}\beta_2 + Y_{\dot{\psi}_2}\dot{\psi}_2 + Y_{\delta_4}\delta_4 + Y_{\delta_5}\delta_5 + Y_{\delta_6}\delta_6 - F_{cy1} + F_{cy2} \tag{3.27a}$$

$$I_{zz2}\ddot{\psi}_2 = N_{\beta_2}\beta_2 + N_{\dot{\psi}_2}\dot{\psi}_2 - l_{c21}F_{cy1} - l_{c22}F_{cy2} + N_{\delta_4}\delta_4 + N_{\delta_5}\delta_5 + N_{\delta_6}\delta_6 + M_{\gamma_2} \tag{3.27b}$$

The dynamic equations of the linear yaw-plane model of the 2nd semitrailer are provided by:

$$m_3 U\left(\dot{\beta}_3 + \dot{\psi}_3\right) = Y_{\beta_3}\beta_3 + Y_{\dot{\psi}_3}\dot{\psi}_3 + Y_{\delta_7}\delta_7 + Y_{\delta_8}\delta_8 + Y_{\delta_9}\delta_9 - F_{cy2} \tag{3.28a}$$

$$I_{zz3}\ddot{\psi}_3 = N_{\beta_3}\beta_3 + N_{\dot{\psi}_3}\dot{\psi}_3 - l_{c3}F_{cy2} + N_{\delta_7}\delta_7 + N_{\delta_8}\delta_8 + N_{\delta_9}\delta_9 + M_{\gamma_3} \tag{3.28b}$$

The state-equation of the linear yaw-plane model can be obtained by eliminating the lateral coupling forces from Equations (3.26)-(3.28) and rearranging with the constraint equations (3.18c) and (3.18d):

$$\dot{\mathbf{x}}_p = \mathbf{A}_p\mathbf{x}_p + \mathbf{C}_p\delta_{11} + \mathbf{B}_p\mathbf{u}_s + \mathbf{B}_m\mathbf{u}_M \tag{3.29}$$

where $\mathbf{A}_p = -\mathbf{J}^{-1}\mathbf{K}$, $\mathbf{C}_p = -\mathbf{J}^{-1}\mathbf{L}$, $\mathbf{B}_p = -\mathbf{J}^{-1}\mathbf{T}$, $\mathbf{B}_m = -\mathbf{J}^{-1}\mathbf{V}$, $\mathbf{x}_p = \begin{bmatrix}\beta_1 & \dot{\psi}_1 & \beta_2 & \dot{\psi}_2 & \beta_3 & \dot{\psi}_3\end{bmatrix}^T$ with $\mathbf{u}_s = \begin{bmatrix}\delta_4 & \delta_5 & \delta_6 & \delta_7 & \delta_8 & \delta_9\end{bmatrix}^T$, $\mathbf{u}_M = \begin{bmatrix}M_{\gamma_2} & M_{\gamma_3}\end{bmatrix}^T$, and $\mathbf{J}$, $\mathbf{K}$, $\mathbf{L}$, $\mathbf{T}$ and $\mathbf{V}$ are given in Appendix D.

3) Non-linear Yaw-Plane Model

The linear yaw-roll model and the linear yaw-plane model may be effective in the design of active roll control system and active trailer steering system, respectively, under low to middle range lateral acceleration conditions, due to the application of linear tire models. Under high lateral acceleration conditions, the pneumatic tire forces may saturate and cannot be predicted accurately with linear tire models. When designing a trailer differential braking system to stabilize the vehicle under high lateral acceleration condition, a nonlinear yaw-plane model is preferred in which the saturation property of pneumatic tires is clearly addressed.

In this section, a five DOF nonlinear yaw-plane model, considering the longitudinal, lateral and the yaw dynamics of the tractor, the yaw dynamics of the 1st and the 2nd semitrailers, is derived.

For simplicity, the following assumptions are made: (1) the side-slip angles, steering angle of the tractor front axle, and the articulation angles are small; (2) the longitudinal speeds of the vehicle units are equal; (3) the product of small variables are negligible; (4) the pitch and roll motions are not considered; (5) the wheel dynamics are neglected; (6) the axles other than the front axle of the tractor are non-steerable; and (7) the differential braking is only conducted on the trailing units. The longitudinal dynamics are considered and controlled by a longitudinal driver model; and the lateral tire forces are modeled with the Magic tire model (Pacejka, 2005). For the left and right tires on an axle, the following relationships hold, i.e., $F_{xi} = F_{xil} + F_{xir}$, $F_{yi} = F_{yil} + F_{yir}$, $i = 1,2\cdots,9$. Using the Newtonian mechanics, the equations of motion of the tractor are derived as

$$m_1\left(\dot{U} - U\beta_1\dot{\psi}_1\right) = F_{x1} + F_{x2} + F_{x3} + F_{cx1} - f_r m_1 g \tag{3.30a}$$

$$m_1 U\left(\dot{\beta}_1 + \dot{\psi}_1\right) = F_{y1} + F_{y2} + F_{y3} + F_{cy1} \tag{3.30b}$$

$$I_{zz1}\ddot{\psi}_1 = a_{11}F_{y1} - b_{12}F_{y2} - b_{13}F_{y3} - l_{c1}F_{cy1} \tag{3.30c}$$

The equations of motion of the 1st semitrailer are given as

$$m_2\left(\dot{U} - U\beta_2\dot{\psi}_2\right) = F_{x4} + F_{x5} + F_{x6} - F_{cx1} + F_{cx2} - f_r m_2 g \tag{3.31a}$$

$$m_2 U\left(\dot{\beta}_2 + \dot{\psi}_2\right) = F_{y4} + F_{y5} + F_{y6} - F_{cy1} + F_{cy2} \tag{3.31b}$$

$$I_{zz2}\ddot{\psi}_2 = -b_{24}F_{y4} - b_{25}F_{y5} - b_{26}F_{y6} - l_{c21}F_{cy1} - l_{c22}F_{cy2} + M_{yb2} \tag{3.31c}$$

where $M_{yb2} = \frac{d_2}{2}\left(F_{x4l} - F_{x4r}\right) + \frac{d_2}{2}\left(F_{x5l} - F_{x5r}\right) + \frac{d_2}{2}\left(F_{x6l} - F_{x6r}\right)$. The equations of motion of the 2nd semitrailer are provided as

$$m_3\left(\dot{U} - U\beta_3\dot{\psi}_3\right) = F_{x7} + F_{x8} + F_{x9} - F_{cx2} - f_r m_3 g \tag{3.32a}$$

$$m_3 U\left(\dot{\beta}_3 + \dot{\psi}_3\right) = F_{y7} + F_{y8} + F_{y9} - F_{cy2} \tag{3.32b}$$

$$I_{zz3}\ddot{\psi}_3 = -b_{37}F_{y7} - b_{38}F_{y8} - b_{39}F_{y9} - l_{c3}F_{cy2} + M_{\gamma b3} \tag{3.32c}$$

where $M_{\gamma b3} = \frac{d_3}{2}\left(F_{x7l} - F_{x7r}\right) + \frac{d_3}{2}\left(F_{x8l} - F_{x8r}\right) + \frac{d_3}{2}\left(F_{x9l} - F_{x9r}\right)$. Since the wheel dynamics are much faster than the vehicle dynamics (Chung and Yi, 2006), the wheel torque balance can be written as

$$0 = \frac{1}{2}T_d - K_b P_i - r_w F_{xi}, i = 2l, 2r, 3l, 3r \tag{3.33a}$$

$$0 = -K_b P_i - r_w F_{xi}, i = 1l, 1r, 4l, \cdots, 9r \tag{3.33b}$$

Combining Equations (3.30) to (3.32), canceling the coupling forces and rearranging with Equations (3.18c) and (3.18d) give

$$\begin{aligned}\dot{U} = &\frac{m_1}{m_1+m_2+m_3}U\beta_1\dot{\psi}_1 + \frac{m_2}{m_1+m_2+m_3}U\beta_2\dot{\psi}_2 + \frac{m_3}{m_1+m_2+m_3}U\beta_3\dot{\psi}_3 + \frac{T_d}{r_w\left(m_1+m_2+m_3\right)} \\ &- \frac{K_b}{r_w\left(m_1+m_2+m_3\right)}\sum_{i=4l}^{9r}P_i - f_r g\end{aligned} \tag{3.34a}$$

$$\dot{\mathbf{x}}_p = \mathbf{A}_n\mathbf{x}_p + \mathbf{B}_F\mathbf{u}_F + \mathbf{B}_M\mathbf{u}_M \tag{3.34b}$$

where $\mathbf{A}_n = \mathbf{J}^{-1}\mathbf{K}_n$, $\mathbf{B}_F = \mathbf{J}^{-1}\mathbf{L}_n$, $\mathbf{B}_M = \mathbf{J}^{-1}\mathbf{R}_n$, and matrix $\mathbf{J}$ is given in Appendix D, and matrices $\mathbf{K}_n$, $\mathbf{L}_n$, $\mathbf{R}_n$ are provided in Appendix E, $\mathbf{u}_M = \begin{bmatrix} M_{\gamma b2} & M_{\gamma b3} \end{bmatrix}^T$, and $\mathbf{u}_F = \begin{bmatrix} F_{y1} & F_{y2} & F_{y3} & F_{y4} & F_{y5} & F_{y6} & F_{y7} & F_{y8} & F_{y9} \end{bmatrix}^T$. The lateral tire forces can be generated using the Magic tire model (Pacejka, 2005) with the side-slip angles calculated as

$$\begin{cases} \alpha_1 = \delta_{11} - \beta_1 - \frac{a_{11}}{U}\dot{\psi}_1, \alpha_2 = \frac{b_{12}}{U}\dot{\psi}_1 - \beta_1, \alpha_3 = \frac{b_{13}}{U}\dot{\psi}_1 - \beta_1, \alpha_4 = \frac{b_{24}}{U}\dot{\psi}_2 - \beta_2, \alpha_5 = \frac{b_{25}}{U}\dot{\psi}_2 - \beta_2, \\ \alpha_6 = \frac{b_{26}}{U}\dot{\psi}_2 - \beta_2, \alpha_7 = \frac{b_{37}}{U}\dot{\psi}_3 - \beta_3, \alpha_8 = \frac{b_{38}}{U}\dot{\psi}_3 - \beta_3, \alpha_9 = \frac{b_{39}}{U}\dot{\psi}_3 - \beta_3 \end{cases} \tag{3.35}$$

With Equation (3.33), the external yaw-moment in the second equation of (3.34) can be represented in terms of the brake pressures of the semitrailer wheels as

$$M_{\gamma b2}=\frac{d_2K_b}{2r_w}\left(\sum_{i=4}^{6}P_{bir}-\sum_{i=4}^{6}P_{bil}\right),\ M_{\gamma b3}=\frac{d_3K_b}{2r_w}\left(\sum_{i=7}^{9}P_{bir}-\sum_{i=7}^{9}P_{bil}\right) \tag{3.36}$$

Assuming that the brake pressures on the same side of a semitrailer are equal, i.e., $P_{4l}=P_{5l}=P_{6l}$, $P_{4r}=P_{5r}=P_{6r}$, $P_{b7l}=P_{b8l}=P_{b9l}$, $P_{b7r}=P_{b8r}=P_{b9r}$. The brake pressures required to realize the yaw moments are determined as

$$P_{4l}=P_{5l}=P_{6l}=-\frac{2r_w}{3d_2K_b}M_{\gamma 2},\ for\ M_{\gamma 2}<0,\ \ P_{4r}=P_{5r}=P_{6r}=\frac{2r_w}{3d_2K_b}M_{\gamma 2},\ for\ M_{\gamma 2}>0 \tag{3.37a}$$

$$P_{7l}=P_{8l}=P_{9l}=-\frac{2r_w}{3d_3K_b}M_{\gamma 3},\ for\ M_{\gamma 3}<0,\ \ P_{7r}=P_{8r}=P_{9r}=\frac{2r_w}{3d_3K_b}M_{\gamma 3},\ for\ M_{\gamma 3}>0 \tag{3.37b}$$

3.3.2 Vehicle Modeling Using the EoM Software Package

In this section, a nonlinear EoM yaw-roll model of the B-train double is generated automatically using the EoM software package (Minaker and Rieveley, 2013) in the ISO coordinate system (HeiBing and Ersoy, 2011). The variables of the EoM model are converted into the SAE coordinate system to make the models comparable. The EoM software package is developed by the Vehicle Dynamics and Control Research Group at the University of Windsor. The EoM can be used to generate linear equations of motion for three-dimensional dynamic systems, composed of rigid bodies coupled with flexible or rigid connectors. The mathematical formulation of a linear model is well documented by Minaker and Rieveley (2010). The EoM can run in Matlab/Octave. The EoM requires the configuration of a system in an input file, defining the system elements such as bodies, connectors, loads, actuators, and sensors, and automatically exports the state-space equation of the system. One of the contributions of this research is to extend the functionality of

the EoM software package to generate nonlinear models of multi-body dynamic systems, especially MTAHVs.

The EoM yaw-roll model of the B-train double is formulated with six rigid bodies as listed in Table F1 in Appendix F with eleven DOF including longitudinal, lateral, yaw and roll DOF for the tractor sprung mass, yaw and roll DOF for the 1st and 2nd semitrailer, roll DOF for the tractor, the 1st and 2nd semitrailer unsprung masses, plus eighteen (18) wheel spinning DOF. In the EoM model, the motion of each rigid body is modeled with twelve variables including three positions, three orientations and their first-order time derivatives. For a system of 6-rigid bodies, the state vector is defined as

$$\mathbf{x} = \begin{bmatrix} \mathbf{p}_1 & \mathbf{p}_2 & \cdots & \mathbf{p}_6 & \dot{\mathbf{p}}_1 & \dot{\mathbf{p}}_2 & \cdots & \dot{\mathbf{p}}_6 \end{bmatrix}^T,\ \mathbf{p}_i = \begin{bmatrix} x_i & y_i & z_i & \phi_i & \theta_i & \psi_i \end{bmatrix}, i = 1,2,\cdots,6 \quad (3.38)$$

where $\mathbf{p}_i$ contains the positions and orientations of the rigid body B_i. The whole list of the state variables of the EoM yaw-roll model of the B-Train Double is illustrated in Table F1 in Appendix F.

3.3.2.1 Linear EoM Yaw-roll Model

Manually modeling of a MTAHV is a tedious and error-prone process. Computer codes are preferred to solve this kind of problems. The automatic generation of nonholonomic equations of motion proposed by Minaker and Rieveley (2010) is suitable for modeling the vehicle dynamics for stability analysis and control design purposes. This method has been originally coded in the EoM software package for automatic generation of linear equations for multibody dynamic systems. A linear yaw-roll model using linear tire models of the B-train double can be represented in a general form (Minaker and Rieveley, 2010) as

$$\dot{\mathbf{z}} = \mathbf{A}\mathbf{z} + \mathbf{B}\mathbf{u},\ \ \mathbf{x} = \mathbf{R}\mathbf{z} \quad (3.39)$$

where, the state vector $\mathbf{x}$ is defined in Equation (3.38), $\mathbf{z}$ the generalized state vector, $\mathbf{u}$ the applied time-varying loads, and $\mathbf{R}$ the orthogonal complement matrix of the state vector. The process matrix $\mathbf{A}$ and the input matrix $\mathbf{B}$ are given by:

$$\mathbf{A} = -\left[\mathbf{L}^T \begin{bmatrix} \mathbf{I} & \mathbf{0} \\ \mathbf{0} & \mathbf{M} \end{bmatrix} \mathbf{R}\right]^{-1} \mathbf{L}^T \begin{bmatrix} \mathbf{V} & -\mathbf{I} \\ \mathbf{K} & \mathbf{C} \end{bmatrix} \mathbf{R}, \quad \mathbf{B} = \left[\mathbf{L}^T \begin{bmatrix} \mathbf{I} & \mathbf{0} \\ \mathbf{0} & \mathbf{M} \end{bmatrix} \mathbf{R}\right]^{-1} \mathbf{L}^T \begin{bmatrix} \mathbf{0} \\ \mathbf{I} \end{bmatrix} \tag{3.40}$$

where $\mathbf{C}$ is the damping matrix, $\mathbf{I}$ the identity matrix, $\mathbf{K}$ the stiffness matrix, $\mathbf{L}$ the orthogonal complement matrix of the constraints and $\mathbf{M}$ the mass matrix, and $\mathbf{V}$ the linearization matrix of the kinematical differential equations. For the detailed formulation of Equation (3.39), interested readers can refer to the paper (Minaker and Rieveley, 2010).

3.3.3.2 Nonlinear EoM Yaw-Roll Model

1) Magic Tire Model

Generally, the linear tire model used in the linear EoM yaw-roll model may not effectively reflect the saturation effect of pneumatic tires. The Magic formula tire model can describe the dynamic characteristics of pneumatic tires under combined side-slip and longitudinal-slip (Bakker et al, 1987, and Pacejka, 2005). With the distributed normal load, a spinning wheel receives a resistant rotating moment. This resistant moment can be converted to a longitudinal resistant force which is negatively added to the longitudinal force generated by the pneumatic tire. The longitudinal resistant force may be modeled as a proportional term of the normal load. With the Magic formula tire model, also taking account the longitudinal resistance, the longitudinal and lateral forces of the i^{th} tire may be calculated, ignoring camber influence, as

$$\begin{cases} F_{xi} = D_{xi}\sin\left[\mathrm{C}_{xi}\arctan\left(B_{xi}\phi_{xi}\right)\right] - f_r F_{zi} \\ F_{yi} = D_{yi}\sin\left[C_{yi}\arctan\left(B_{yi}\phi_{yi}\right)\right] \\ \phi_{xi} = \left(1-E_{xi}\right)\sigma_i + \left(E_{xi}/B_{xi}\right)\arctan\left(B_{xi}\sigma_i\right) \\ \phi_{yi} = \left(1-E_{yi}\right)\alpha_i + \left(E_{yi}/B_{yi}\right)\arctan\left(B_{yi}\alpha_i\right) \end{cases} \quad for\ i = 1l, 1r, 2l, \cdots, 9r \tag{3.41}$$

where the coefficients B_{xi}, C_{xi}, D_{xi}, E_{xi}, B_{yi}, C_{yi}, D_{yi}, E_{yi} are polynomials of the normal force of the i^{th} tire (dual tire).

When calculating the normal forces of the wheels, the tandem group on the tractor and the tridem groups on the semitrailers are simplified as single axles at the longitudinal centers of the groups, e.g., $b_1 = \frac{b_{12}+b_{13}}{2}$, $b_2 = \frac{b_{24}+b_{25}+b_{26}}{3}$, $b_3 = \frac{b_{37}+b_{38}+b_{39}}{3}$, $b_{1s} = \frac{b_{12s}+b_{13s}}{2}$, $b_{2s} = \frac{b_{24s}+b_{25s}+b_{26s}}{3}$, and $b_{3s} = \frac{b_{37s}+b_{38s}+b_{39s}}{3}$, for simplicity. Considering the lateral, longitudinal, and the roll load transfers, the normal forces of the wheels are determined (He et al, 2006) as

$$F_{z1l} = \frac{1}{2}\frac{b_1 m_1 g}{a_{11}+b_1} - \frac{1}{2}\frac{h_{cg1}m_1 a_{x1}}{a_{11}+b_1} + \frac{a_{y1}}{d_{11}}\left(\frac{m_{1s}b_{1s}h_{r1}}{a_{11}+b_1} + \frac{b_{1s}m_{1u}h_{u1}}{a_{11}+b_1}\right) - \frac{1}{d_{11}}\left(K_{r1f}\phi_1 + L_{r1f}\dot{\phi}_1\right) \tag{3.42a}$$

$$F_{z1r} = \frac{1}{2}\frac{b_1 m_1 g}{a_{11}+b_1} - \frac{1}{2}\frac{h_{cg1}m_1 a_{x1}}{a_{11}+b_1} - \frac{a_{y1}}{d_{11}}\left(\frac{m_{1s}b_{1s}h_{r1}}{a_{11}+b_1} + \frac{b_{1s}m_{1u}h_{u1}}{a_{11}+b_1}\right) + \frac{1}{d_{11}}\left(K_{r1f}\phi_1 + L_{r1f}\dot{\phi}_1\right) \tag{3.42b}$$

$$\begin{aligned} F_{z2l} = F_{z3l} = {} & \frac{1}{4}\frac{a_{11}m_1 g}{a_{11}+b_1} + \frac{1}{4}\frac{h_{cg1}m_1 a_{x1}}{a_{11}+b_1} + \frac{1}{4}\left(\frac{b_2 m_2 g}{a_2+b_2} - \frac{h_{cg2}m_2 a_{x2}}{a_2+b_2}\right) \\ & + \frac{1}{2}\frac{a_{y1}}{d_1}\left(\frac{m_{1s}a_{1s}h_{r1}}{a_{11}+b_1} + \frac{a_{1s}m_{1u}h_{u1}}{a_{11}+b_1}\right) - \frac{1}{2}\frac{1}{d_1}\left(K_{r1r}\phi_1 + L_{r1r}\dot{\phi}_1\right) \end{aligned} \tag{3.42c}$$

$$\begin{aligned} F_{z2r} = F_{z3r} = {} & \frac{1}{4}\frac{a_{11}m_1 g}{a_{11}+b_1} + \frac{1}{4}\frac{h_{cg1}m_1 a_{x1}}{a_{11}+b_1} + \frac{1}{4}\left(\frac{b_2 m_2 g}{a_2+b_2} - \frac{h_{cg2}m_2 a_{x2}}{a_2+b_2}\right) \\ & - \frac{1}{2}\frac{a_{y1}}{d_1}\left(\frac{m_{1s}a_{1s}h_{r1}}{a_{11}+b_1} + \frac{a_{1s}m_{1u}h_{u1}}{a_{11}+b_1}\right) + \frac{1}{2}\frac{1}{d_1}\left(K_{r1r}\phi_1 + L_{r1r}\dot{\phi}_1\right) \end{aligned} \tag{3.42d}$$

$$F_{z4l}=F_{z5l}=F_{z6l}=\frac{1}{6}\frac{a_2m_2g}{a_2+b_2}+\frac{1}{6}\left(\frac{b_3m_3g}{a_3+b_3}-\frac{h_{cg3}m_3a_{x3}}{a_3+b_3}\right)+\frac{1}{6}\frac{h_{cg2}m_2a_{x2}}{a_2+b_2}+\frac{1}{3}\frac{a_{y2}}{d_2}\left(h_{r2}m_{2s}+h_{u2}m_{2u}\right)-\frac{1}{3}\frac{1}{d_2}\left(K_{r2}\phi_2+L_{r2}\dot{\phi}_2\right) \tag{3.42e}$$

$$F_{z4r}=F_{z5r}=F_{z6r}=\frac{1}{6}\frac{a_2m_2g}{a_2+b_2}+\frac{1}{6}\left(\frac{b_3m_3g}{a_3+b_3}-\frac{h_{cg3}m_3a_{x3}}{a_3+b_3}\right)+\frac{1}{6}\frac{h_{cg2}m_2a_{x2}}{a_2+b_2}-\frac{1}{3}\frac{a_{y2}}{d_2}\left(h_{r2}m_{2s}+h_{u2}m_{2u}\right)+\frac{1}{3}\frac{1}{d_2}\left(K_{r2}\phi_2+L_{r2}\dot{\phi}_2\right) \tag{3.42f}$$

$$F_{z7l}=F_{z8l}=F_{z9l}=\frac{1}{6}\frac{a_3m_3g}{a_3+b_3}+\frac{1}{6}\frac{h_{cg3}m_3a_{x3}}{a_3+b_3}+\frac{1}{3}\frac{a_{y3}}{d_3}\left(h_{r3}m_{3s}+h_{u3}m_{3u}\right)-\frac{1}{3}\frac{1}{d_3}\left(K_{r3}\phi_3+L_{r3}\dot{\phi}_3\right) \tag{3.42g}$$

$$F_{z7r}=F_{z8r}=F_{z9r}=\frac{1}{6}\frac{a_3m_3g}{a_3+b_3}+\frac{1}{6}\frac{h_{cg3}m_3a_{x3}}{a_3+b_3}-\frac{1}{3}\frac{a_{y3}}{d_3}\left(h_{r3}m_{3s}+h_{r3}m_{3u}\right)+\frac{1}{3}\frac{1}{d_3}\left(K_{r3}\phi_3+L_{r3}\dot{\phi}_3\right) \tag{3.42h}$$

The tire sideslip angles are determined as

$$\alpha_{1l}=\alpha_{1r}=\alpha_1=\delta_{11}-\frac{\dot{y}_{t1}-h_{u1}\dot{\phi}_{t1}+a_{11u}\dot{\psi}_{t1}}{U},\quad \alpha_{2l}=\alpha_{2r}=\alpha_2=-\frac{\dot{y}_{t1}-h_{u1}\dot{\phi}_{t1}-b_{12u}\dot{\psi}_{t1}}{U} \tag{3.43a}$$

$$\alpha_{3l}=\alpha_{3r}=\alpha_3=-\frac{\dot{y}_{t1}-h_{u1}\dot{\phi}_{t1}-b_{13u}\dot{\psi}_{t1}}{U},\quad \alpha_{4l}=\alpha_{4r}=\alpha_4=\delta_4-\frac{\dot{y}_{t2}-h_{u2}\dot{\phi}_{t2}+d_x\dot{\psi}_{t2}}{U} \tag{3.43b}$$

$$\alpha_{5l}=\alpha_{5r}=\alpha_5=\delta_5-\frac{\dot{y}_{t2}-h_{u2}\dot{\phi}_{t2}}{U},\quad \alpha_{6l}=\alpha_{6r}=\alpha_6=\delta_6-\frac{\dot{y}_{t2}-h_{u2}\dot{\phi}_{t2}-d_x\dot{\psi}_{t2}}{U} \tag{3.43c}$$

$$\alpha_{7l}=\alpha_{7r}=\alpha_7=\delta_7-\frac{\dot{y}_{t3}-h_{u3}\dot{\phi}_{t3}+d_x\dot{\psi}_{t3}}{U},\quad \alpha_{8l}=\alpha_{8r}=\alpha_8=\delta_8-\frac{\dot{y}_{t3}-h_{u3}\dot{\phi}_{t3}}{U} \tag{3.43d}$$

$$\alpha_{9l}=\alpha_{9r}=\alpha_9=\delta_9-\frac{\dot{y}_{t3}-h_{u3}\dot{\phi}_{t3}-d_x\dot{\psi}_{t3}}{U} \tag{3.43e}$$

where $\delta_4,\cdots,\delta_9$ are the active steering angles generated by the active trailer steering system. The tire longitudinal slip ratios are determined as

$$\sigma_i = \begin{cases} \dfrac{r_w\dot{\theta}_{wi} - U}{r_w\dot{\theta}_{wi}}, \textit{when accelerating} \\ \dfrac{r_w\dot{\theta}_{wi} - U}{U}, \textit{when braking} \end{cases}, i = 1l, 1r, 2l, 2r, \cdots, 9l, 9r \tag{3.44}$$

The wheel dynamics are determined, using the linear tire model, as

$$\begin{cases} \dot{\omega}_{wi} = \dfrac{1}{4I_{wi}} T_d - \dfrac{K_{bi}}{I_{wi}} P_{bi} - \dfrac{C_{\sigma i} r_w^2 \omega_{wi}}{I_{wi} \max\left(r_w\omega_{wi}, U\right)} + \dfrac{C_{\sigma i} r_w U}{I_{wi} \max\left(r_w\omega_{wi}, U\right)}, i = 2l, 2r, 3l, 3r \\ \dot{\omega}_{wi} = -\dfrac{K_{bi}}{I_{wi}} P_{bi} - \dfrac{C_{\sigma i} r_w^2 \omega_{wi}}{I_{wi} \max\left(r_w\omega_{wi}, U\right)} + \dfrac{C_{\sigma i} r_w U}{I_{wi} \max\left(r_w\omega_w, U\right)}, i = 1l, 1r, 4l, \cdots, 9r \end{cases} \tag{3.45}$$

2) Nonlinear EoM Yaw-roll Model

The EoM software package was originally designed to automatically generate linear models of nonholonomic multi-body dynamic systems. When used for MTAHVs, the small-angle and small-slip-ratio assumptions have been made for generating linear models. These assumptions are valid under normal highway operation condition. However, under extreme driving conditions, for example, driving with high accelerations, the side-slip angles and the longitudinal slip ratios of tires may become large and the tire forces may saturate. An effective approach to tackle the saturation effect of the pneumatic tires is to use a nonlinear tire model, e.g., the Magic tire model (Bakker et al, 1987, and Pacejka, 2005). In this research, the functionality of the EoM software package is extend to generate nonlinear models of non-holonomic multibody dynamic systems. The linear EoM model of the B-train double may be extended to a nonlinear model when replacing the linear tire model with the nonlinear Magic tire model.

The linear tire forces are fed into the linear model through the dampers laterally and longitudinally connecting the tires with the ground. The damping coefficients of the dampers consist of the cornering stiffness and longitudinal slip coefficients. Considering a pneumatic tire

in a linear operating range, the product of the cornering stiffness and the side-slip angle is the lateral tire force and the product of the longitudinal slip ratio and the longitudinal slip coefficient is the longitudinal tire force. The lateral and longitudinal tire forces are contained in the damping matrix $\mathbf{C}$ in Equation (3.40). By setting the cornering stiffness and the longitudinal slip coefficients to unity in the input configuration file, the damping matrix $\mathbf{C}$ contains only the side-slip angles and the longitudinal slip ratios and is denoted as $\mathbf{C}_{unity}$. To expose the linear tire model and further replace it with the Magic tire model, a matrix reformulation is conducted as

$$\begin{bmatrix} \mathbf{V} & -\mathbf{I} \\ \mathbf{K} & \mathbf{C}_{unity} \end{bmatrix} = \begin{bmatrix} \mathbf{V} & -\mathbf{I} \\ \mathbf{K} & \mathbf{C}_{unity} - \Theta \end{bmatrix} + \begin{bmatrix} \mathbf{0} & \mathbf{0} \\ \mathbf{0} & \Theta \end{bmatrix} \tag{3.46}$$

where Θ is the damping matrix formulated on the deflection matrix and the diagonal matrix containing the cornering stiffness and the longitudinal slip ratios. Figure 3.10 shows the block diagram of the EoM vehicle model with matrix reformulation, clearly demonstrating the formulation of the tire forces and the resulted moments, where matrices $\mathbf{A}_1$ and $\mathbf{A}_2$ are formulated as

$$\mathbf{A}_1 = -\left[\mathbf{L}^T \begin{bmatrix} \mathbf{I} & \mathbf{0} \\ \mathbf{0} & \mathbf{M} \end{bmatrix} \mathbf{R}\right]^{-1} \mathbf{L}^T \begin{bmatrix} \mathbf{V} & -\mathbf{I} \\ \mathbf{K} & \mathbf{C} - \Theta \end{bmatrix}, \mathbf{A}_2 = -\left[\mathbf{L}^T \begin{bmatrix} \mathbf{I} & \mathbf{0} \\ \mathbf{0} & \mathbf{M} \end{bmatrix} \mathbf{R}\right]^{-1} \mathbf{L}^T \tag{3.47}$$

For the EoM yaw-roll model of the B-train double, the input to the tire model is the state vector defined in Equation (3.38). By using the state variables, the side-slip angles and slip-ratios are formulated using Equations (3.43) and (3.44), respectively. The outputs of the tire models feed the rigid bodies with the tire forces. These bodies include the unsprung masses of the vehicle units which receive lateral and longitudinal tire forces. The state variables employed are limited only to

those contributing to the side-slip angles and longitudinal slip-ratios as listed in Equations (3.43) and (3.44).

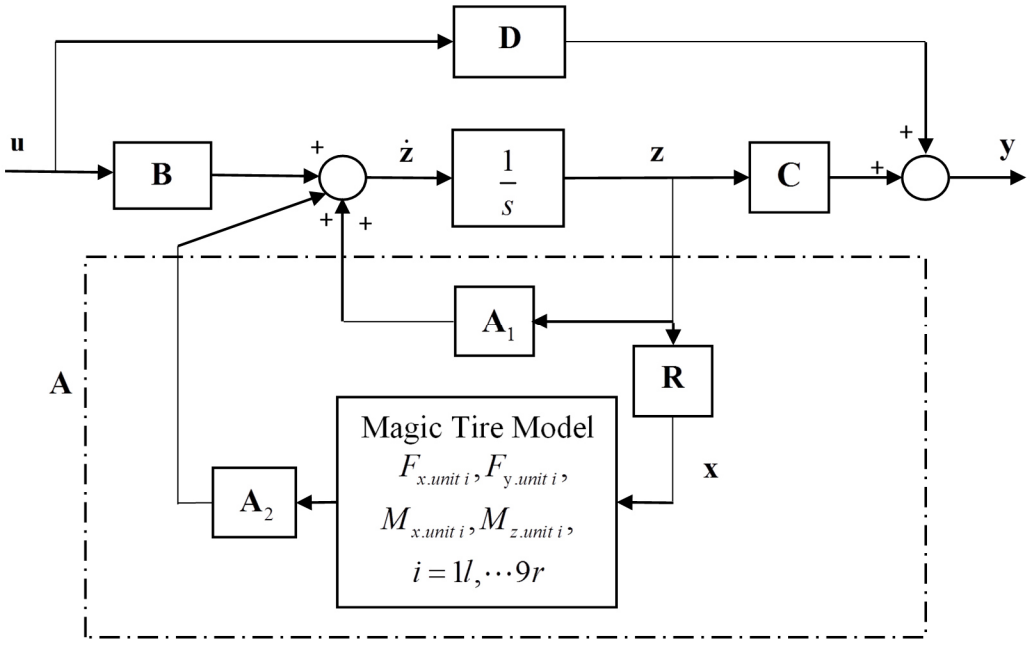

Figure 3.10 Block diagram of the EoM model with the matrix decomposition

Interestingly, the outputs of the tire models enter the EoM model as the forms of external forces (lateral or longitudinal) and moments (roll, and yaw) in a sequence exactly same as that of the variables employed for the side-slip angles and slip-ratios appearing in the state vector. For example, the calculation of the side-slip angle of the tire on the first rear axle of the tractor in Equation (3.43), $\alpha_2 = -\frac{\dot{y}_{t1} - h_{u1}\dot{\phi}_{t1} - b_{12u}\dot{\psi}_{t1}}{U}$, employs the state variables $\dot{y}_{t1}$, $\dot{\phi}_{t1}$, and $\dot{\psi}_{t1}$ in the sequence, 44-46-48, in the state vector as shown in Table F1; for the tractor unsprung mass B2, the resulted lateral force F_{yt1}, roll moment M_{xt1}, and yaw moment M_{zt1} to the tractor unsprung mass due to the side-slip angle α_2 are organized in the same sequence, 44-46-48, in the external force vector to the EoM model. Considering the wheel steering effects, the longitudinal and the

lateral forces, the roll and the yaw moments to the unsprung masses (B2, B4, and B4) are determined as

$$\begin{cases} F_{xt1}=\sum_{i=1l}^{3r}F_{xi},\ F_{yt1}=\sum_{i=1l}^{3r}F_{yi},\ M_{xt1}=h_{u1}F_{yt1} \\ M_{zt1}=\frac{d_{11}}{2}\left(F_{x1r}-F_{x1l}\right)+\frac{d_1}{2}\left(F_{x2r}+F_{x3r}-F_{x2l}-F_{x3l}\right)+a_{11u}\left(F_{y1l}+F_{y1r}\right) \\ \quad -b_{12u}\left(F_{y2l}+F_{y2r}\right)-b_{13u}\left(F_{y3l}+F_{y3r}\right) \end{cases} \tag{3.48a}$$

$$\begin{cases} F_{xt2}=\sum_{i=4l}^{6r}F_{xi},\ F_{yt2}=\sum_{i=4l}^{6r}F_{yi},\ M_{xt2}=h_{u2}F_{yt2}, \\ M_{zt2}=\frac{d_2}{2}\sum_{i=4}^{6}\left(F_{xir}-F_{xil}\right)+d_x\left(F_{y4l}+F_{y4r}\right)-d_x\left(F_{y6l}+F_{y6r}\right) \end{cases} \tag{3.48b}$$

$$\begin{cases} F_{xt3}=\sum_{i=7l}^{9r}F_{xi},\ F_{yt3}=\sum_{i=7l}^{9r}F_{yi},\ M_{xt3}=h_{u3}F_{yt3} \\ M_{zt3}=\frac{d_3}{2}\sum_{i=7}^{9}\left(F_{xir}-F_{xil}\right)+d_x\left(F_{y7l}+F_{y7r}\right)-d_x\left(F_{y9l}+F_{y9r}\right) \end{cases} \tag{3.48c}$$

The complete list of the state variables employed for the tire model and the resulted external forces (moments) to the EoM model is illustrated in Table F2 in Appendix F. With the side-slip angles and slip-ratios in Equations (3.43) and (3.44), to obtain a nonlinear EoM model, the linear tire model is simply replaced with the magic tire model. Introducing the nonlinear tire model into the EoM model is a significant step expanding the functionality of the EoM software package.

To improve the roll dynamics of the vehicle units, direct roll moments $M_x=\begin{bmatrix}M_{x1f} & M_{x1r} & M_{x2} & M_{x3}\end{bmatrix}^T$ as in Equation (3.25) are applied through the tractor front suspension with M_{x1f}, tractor rear suspension group with M_{x1r}, 1st semitrailer suspension group with M_{x2}, and the 2nd semitrailer suspension group with M_{x3}. In the EoM model, these active roll moments are distributed on the tractor, 1st and the 2nd semitrailer units as action-reaction moment

pairs between respective sprung mass and unsprung mass bodies ($M_{x1f}+M_{x1r}, -M_{x1f}-M_{x1r}$), ($M_{x2}, -M_{x2}$), and ($M_{x3}, -M_{x3}$), respectively, as modeled similarly in the linear yaw-roll model in Equations (3.21)-(3.23). The active roll moments are added to the internal action-reaction roll-moment pair within the vehicle units. The modified roll moments are determined as

$$\begin{cases} M_{x1} = M_{x1f} + M_{x1r}, M_{xt1} = h_{u1}F_{yt1} - M_{x1f} - M_{x1r}, \\ M_{xt2} = h_{u2}F_{yt2} - M_{x2}, M_{xt3} = h_{u3}F_{yt3} - M_{x3} \end{cases} \tag{3.49}$$

3.3.4 Validation of the B-train Double Models

3.3.4.1 Model Validation at a Low Lateral Acceleration

The nonlinear EoM yaw-roll model, linear yaw-plane model, linear yaw-roll model and the nonlinear yaw-plane model of the B-train double are first validated using the TruckSim model at a low lateral acceleration operation. Since the linear tire models match the magic tire models well in a linear region at low lateral acceleration operation, it is expected that the nonlinear EoM yaw-roll model, linear yaw-plane model, linear yaw-roll model, and the nonlinear yaw plane model may provide good agreement with the TruckSim model at a low lateral acceleration operation. A high-speed open-loop single lane change (SLC) maneuver is used to create a low lateral acceleration scenario. The models are excited using a 0.4 Hz single cycle sine wave tractor front wheel steer angle input. The amplitude of the input and the forward speed of the vehicle are manipulated to investigate the RWA property of the B-train double, simulated with the linear and the nonlinear models.

Figure 3.11 shows the time history of the tractor front wheel steer angle with amplitude of 1.79 deg. Figure 3.12 and Figure 3.13 shows the time histories of yaw-rate of the vehicle units, and lateral acceleration at the CGs of the tractor, 1st and the 2nd semitrailer of the EoM yaw-roll model, TruckSim model, linear yaw-roll model, and the nonlinear yaw-plane model of the B-train double,

respectively. Figure 3.14 shows the roll angles of the sprung masses of the vehicle units of the nonlinear EoM yaw-roll model, TruckSim model, and the linear yaw-roll model of the B-train double. Excellent match has been achieved on the lateral dynamics by the nonlinear EoM yaw-roll model, TruckSim model, linear yaw-plane model, linear yaw-roll model, and the nonlinear yaw-plane model and on the roll dynamics by the nonlinear EoM yaw-roll model, TruckSim model and the linear yaw-roll model.

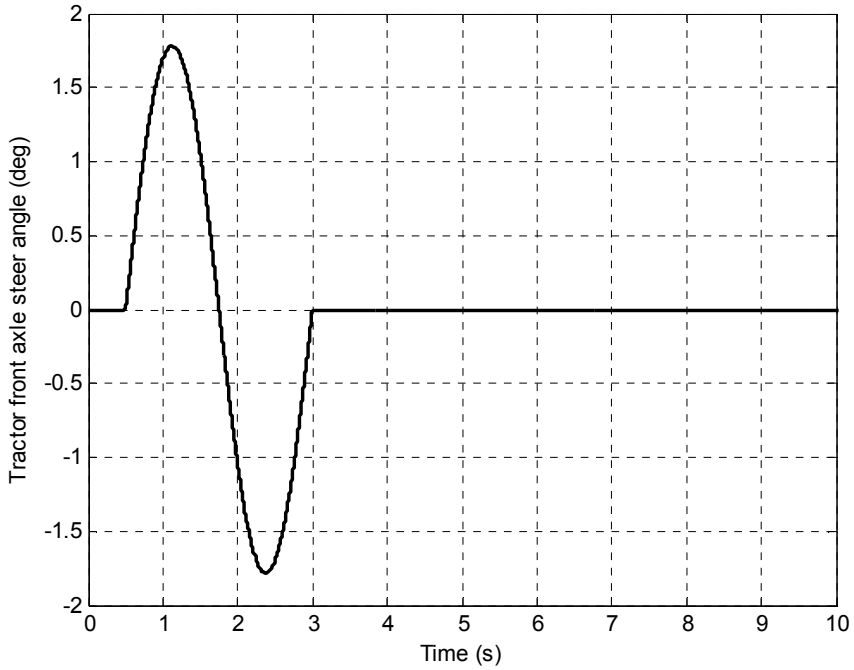

Figure 3.11 Tractor front wheel steer angle input for the single lane change maneuver

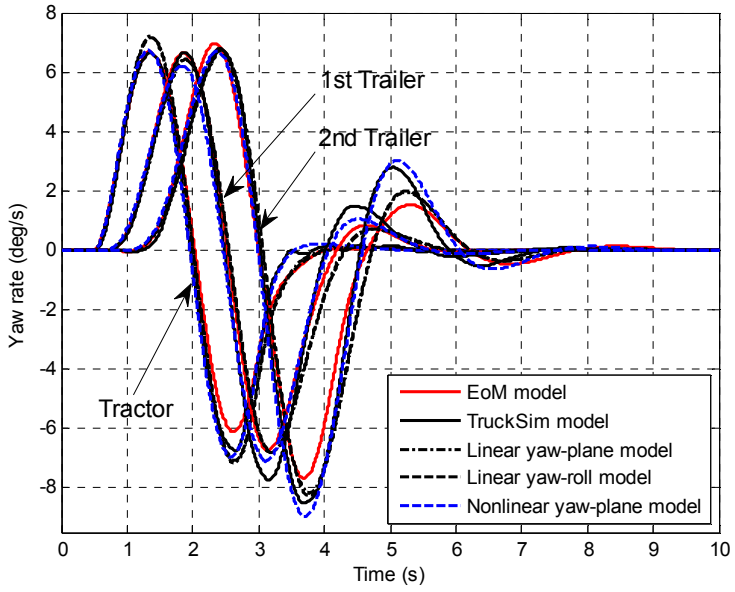

Figure 3.12 Yaw rates of the EoM yaw-roll model, TruckSim model, linear yaw-plane model, linear yaw-roll model and the nonlinear yaw-plane model of the B-train double under the low lateral acceleration SLC maneuver at forward speed $U = 110$ km/h

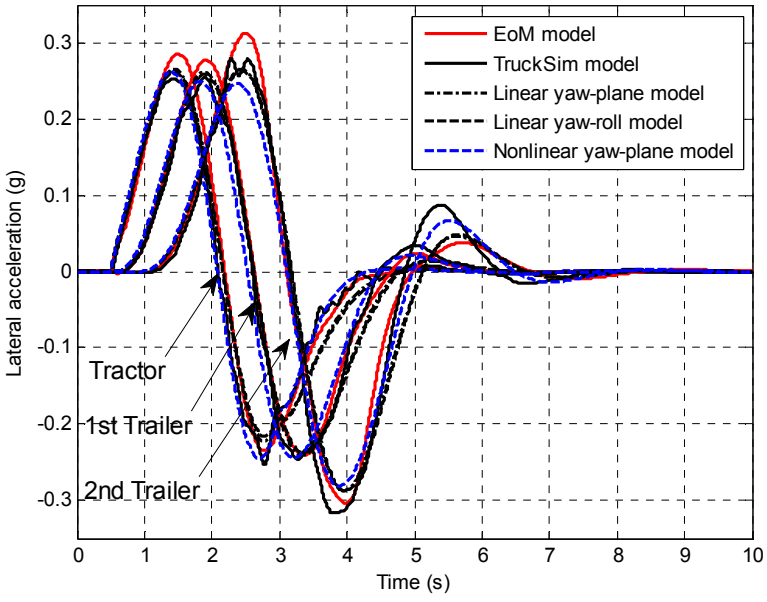

Figure 3.13 Lateral accelerations of the nonlinear EoM yaw-roll model, TruckSim model, linear yaw-plane model, linear yaw-roll model and the nonlinear yaw-plane model under the low lateral acceleration SLC maneuver at forward speed $U = 110$ km/h

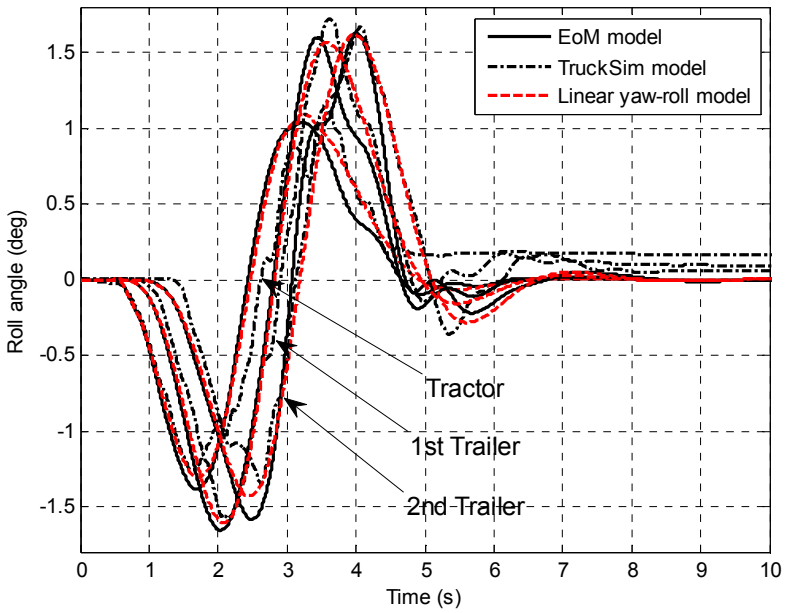

Figure 3.14 Roll angles the sprung masses of the nonlinear EoM yaw-roll model, TruckSim model, and the linear yaw-roll model under the low lateral acceleration SLC maneuver at forward speed $U = 110$ km/h

Figure 3.15 shows the normal forces of the wheels of the B-train double simulated using the TruckSim model and the nonlinear EoM yaw-roll model under the low lateral acceleration SLC maneuver of forward speed $U = 110$ km/h. Note that the front, 1st rear and the 2nd rear axle of the tractor is denoted as axle 1, axle 2, axle 3; the front, middle, and the rear axle of the 1st semitrailer as axle 4, axle 5, and axle 6; and the front, middle, and the rear axle of the 2nd semitrailer as axle 7, axle 8, and axle 9, respectively. Excellent agreement has been achieved by the TruckSim model and the nonlinear EoM yaw-roll model. It can be observed that, for the TruckSim and the EoM yaw-roll model, the wheels on the 1st semitrailer take the highest amount of normal forces within all the wheels; the left wheels of the 2nd semitrailer have their minimal normal forces closest to zero and 2nd semitrailer may be the first unit to roll over if continuing increasing lateral acceleration of the vehicle; and the 2nd semitrailer has more severe load transfer than other units. The load

transfer under the SLC maneuver verifies the observations on the lateral dynamics shown in Figures 3.12-3.13 and indicates the rearward amplification (RWA) phenomenon.

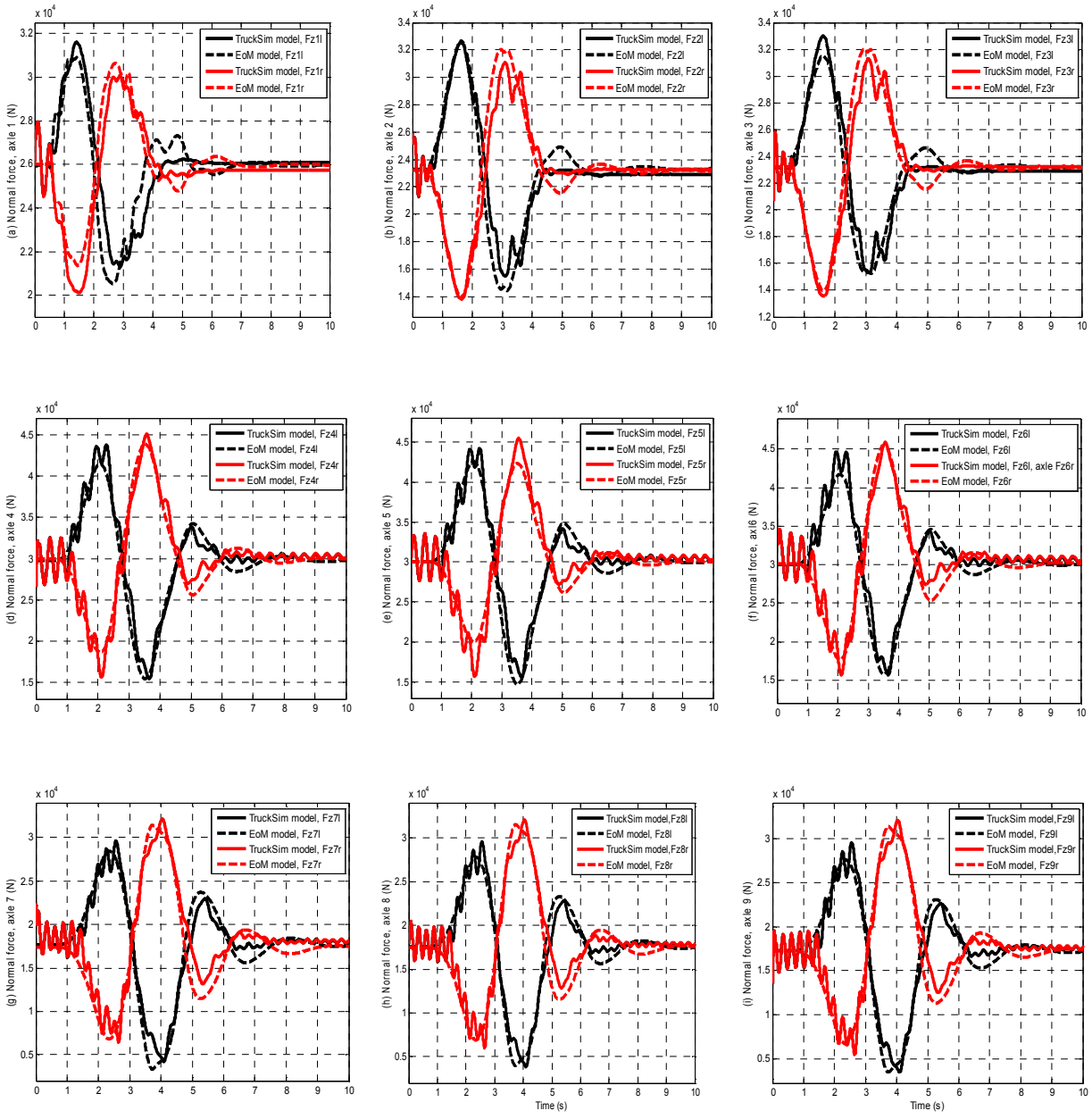

Figure 3.15 Normal forces of the wheels of the B-train double simulated using the TruckSim model and the nonlinear EoM yaw-roll model under the SLC maneuver of forward speed U =110 km/h showing the load transfers on: (a) axle 1, (b) axle 2, (c) axle 3, (d) axle 4, (e) axle 5, (f) axle 6, (g) axle 7, (h) axle 8, and (i) axle 9

Figure 3.16 and Figure 3.17 shows respectively the time history of the forward speed, and the total drive torque distributed on the drive wheels of the tractor of the B-train double simulated using the TruckSim and the nonlinear EoM yaw-roll model under the low lateral acceleration SLC maneuver of forward speed $U = 110$ km/h. Good match has been achieved by both models. The TruckSim model has slightly faster response and more transient drop on the forward speed. The drive torque of the TruckSim model shown in Figure 3.17 also demonstrates faster response and more quickly converges to the steady value, which interprets the evolution of the forward speed in Figure 3.16. Comparatively, the drive torque of the nonlinear EoM yaw-roll model is larger than that of the TruckSim model in time integration sense, which results in less forward speed drop and crosses over the forward speed of the TruckSim model in the period from 15 to 50s.

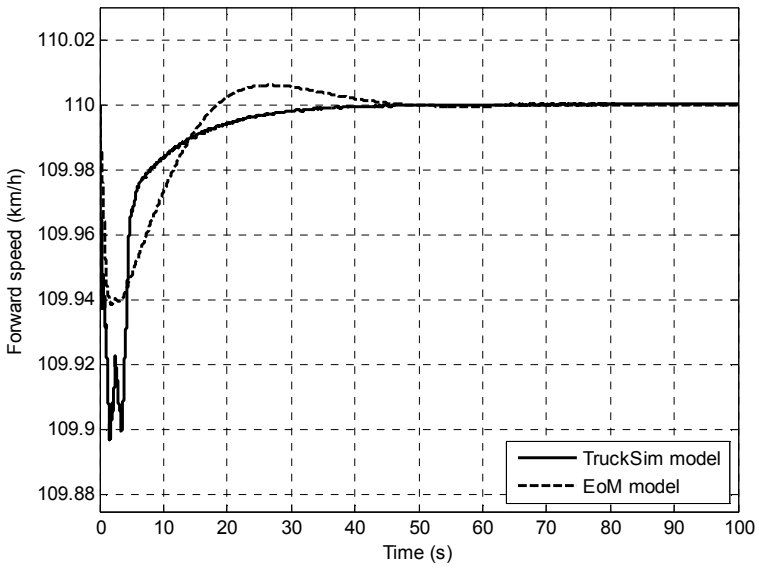

Figure 3.16 Forward speed of the B-train double simulated using the TruckSim and the nonlinear EoM yaw-roll model under the low lateral acceleration SLC maneuver of the nominal forward speed $U = 110$ km/h

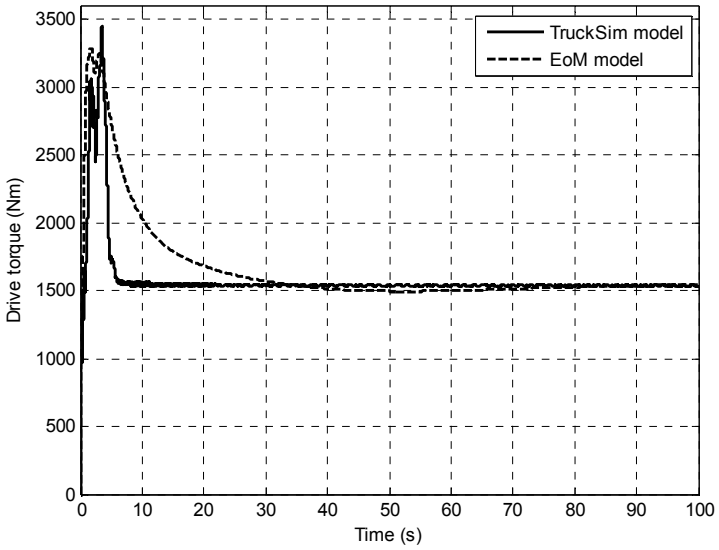

Figure 3.17 Total drive torque for the drive wheels of the tractor of the B-train double simulated using the TruckSim and the nonlinear EoM yaw-roll model under the low lateral acceleration SLC maneuver at forward speed $U = 110$ km/h

Figures 3.18 and 3.19 shows respectively the time histories of the yaw-rate and lateral acceleration of the B-train double simulated using the nonlinear EoM yaw-roll model, TruckSim model, linear yaw-plane model, linear yaw-roll model, and the nonlinear yaw-plane model under the low lateral acceleration SLC maneuvers indicating the dependence of RWA on the vehicle forward speed. Note that in each sub-figure, three groups of timely distributed curves from left to right denote the performance measures of the tractor, 1st and the 2nd semitrailers, respectively. With a low vehicle forward speed, the rear units (the 1st and 2nd semitrailers) yield lower yaw rate, lateral acceleration and better stability than the tractor. Following the increase of the forward speed, responses of the yaw-rate and lateral acceleration of the rear units starts to grow over that of the tractor, gradually demonstrates the RWA property, improves in maneuverability and degrades in stability.

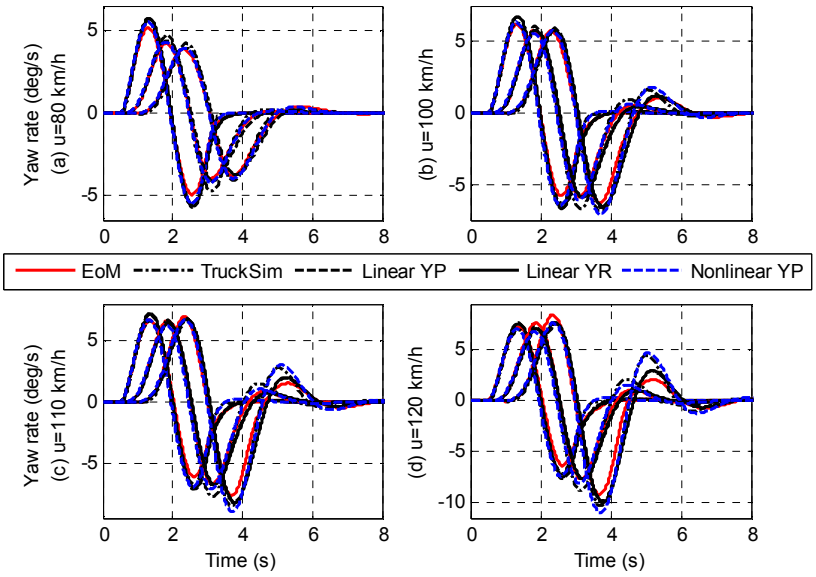

Figure 3.18 Yaw rates of the B-train double models under the SLC maneuvers showing the forward speed dependence of the RWA property: (a) $U = 80$ km/h, (b) $U = 100$ km/h, (c) $U = 110$ km/h, and (d) $U = 120$ km/h

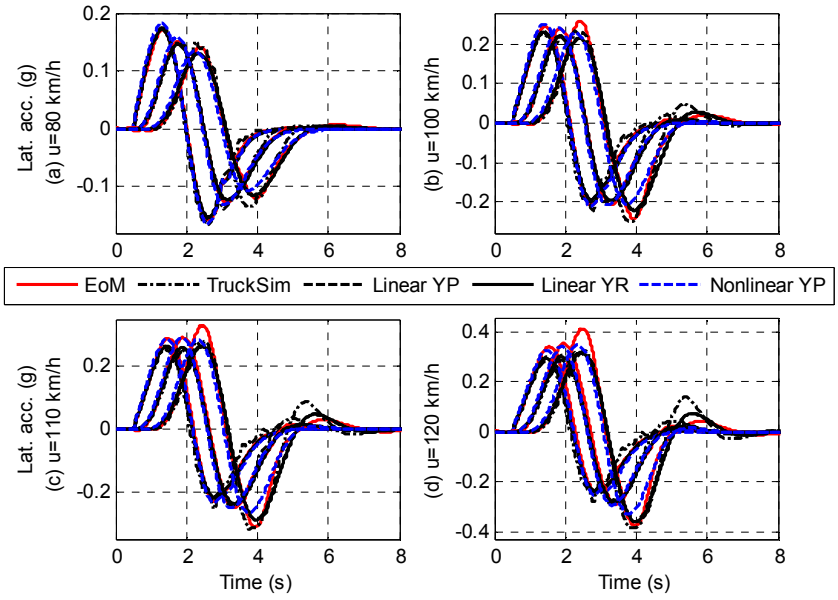

Figure 3.19 Lateral accelerations of the B-train double models under the low lateral acceleration SLC maneuvers showing the forward speed dependence of the RWA property: (a) $U = 80$ km/h, (b) $U = 100$ km/h, (c) $U = 110$ km/h, and (d) $U = 120$ km/h

3.3.4.2 Model Validation at a High Lateral Acceleration Operation

At high lateral acceleration operations, the pneumatic tire forces may saturate. The linear tire models used in the linear yaw-plane model, and the linear yaw-roll model may not effectively predict the saturation property. The prediction capabilities of the linear models may be compromised and questionable. In the following high lateral acceleration operation simulations, the performance measures in yaw-rate and lateral acceleration of the B-train double simulated using the nonlinear EoM yaw-roll model, TruckSim model, linear yaw-plane mode, linear yaw-roll model, and the nonlinear yaw-plane model are compared. In all the models considered, the linear yaw-plane model, and the linear yaw-roll model use linear tire models and are deemed as linear models. The nonlinear EoM model, TruckSim model, and the nonlinear yaw-plane model apply the Magic tire models and are ascribed to nonlinear models. To achieve a high lateral acceleration, a 0.4 Hz single cycle sine wave steer angle of amplitude of 3.58 deg for the tractor front axle is used to excite the B-train double simulated using the linear and nonlinear models.

Figure 3.20 shows the yaw-rate time histories of the B-train double simulated using the nonlinear EoM model, TruckSim model, linear yaw-plane model, linear yaw-roll model and the nonlinear yaw-plane model under the high lateral acceleration SLC maneuver. Note that in the figure, three groups of timely distributed curves from left to right denote the performance measures of the tractor, 1st and the 2nd semitrailers, respectively. The nonlinear yaw-plane model provides a closer match with the nonlinear EoM yaw-roll model in the yaw-rate measure than the linear yaw-plane and the linear yaw-roll models. Compared with the other nonlinear models, the TruckSim model demonstrates heavier asymmetry with respect to the time axis on the 1st and the 2nd semitrailers, but matches the nonlinear EoM yaw-roll model and the nonlinear yaw-plane very well in the amplitude-sense. The linear yaw-plane and linear yaw-roll models match each other

well on all units due to the application of the same linear tire models. The difference made by different kinds of tire models is evident under this high lateral acceleration operation.

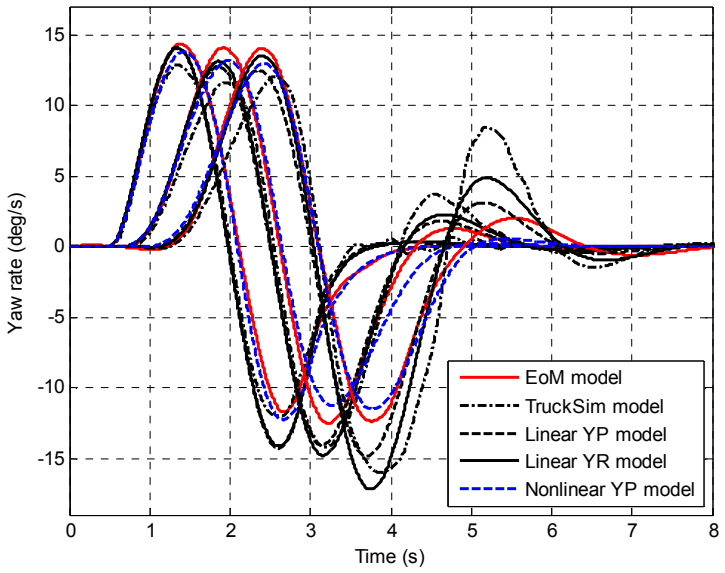

Figure 3.20 Yaw-rates of the B-train double models under the high lateral acceleration SLC maneuver at forward speed $U = 110$ km/h

Figure 3.21 shows the lateral acceleration time histories of the B-train double simulated using the nonlinear EoM yaw-roll model, TruckSim model, linear yaw-plane model, linear yaw-roll model, and the nonlinear yaw-plane model under the high lateral acceleration SLC maneuver of forward speed $U = 110$ km/h. Note that in the figure, three groups of timely distributed curves from left to right denote the performance measures of the tractor, 1st and the 2nd semitrailers, respectively. Excellent match has been achieved by the nonlinear EoM yaw-roll model, TruckSim model, and the nonlinear yaw-plane model, except that on the 2nd semitrailer, TruckSim model demonstrates heavier asymmetry with respect to the time axis than those of other nonlinear models. The linear yaw-plane model and the linear yaw-roll model match each other very well.

The difference made by the tire models (linear and nonlinear) on the lateral acceleration measures demonstrated by the linear and nonlinear models are apparent. This fact suggests that the linear models using the linear tire models are not sufficient for predicting the vehicle performance under a high lateral acceleration operation condition. The prediction capability of the nonlinear models including the nonlinear EoM yaw-roll model, TruckSim model and the nonlinear yaw-plane model for the performance of the B-train double under high lateral acceleration operation conditions is verified.

The insightful findings in the model validation at low and high lateral acceleration operation conditions build the foundation in the allocation of the vehicle models to the ASSs (active safety systems) design, optimization and coordination in the following research, i.e., the linear yaw-plane model is for the ATS, linear yaw-roll model for the ARC and the nonlinear yaw-plane model for the TDB.

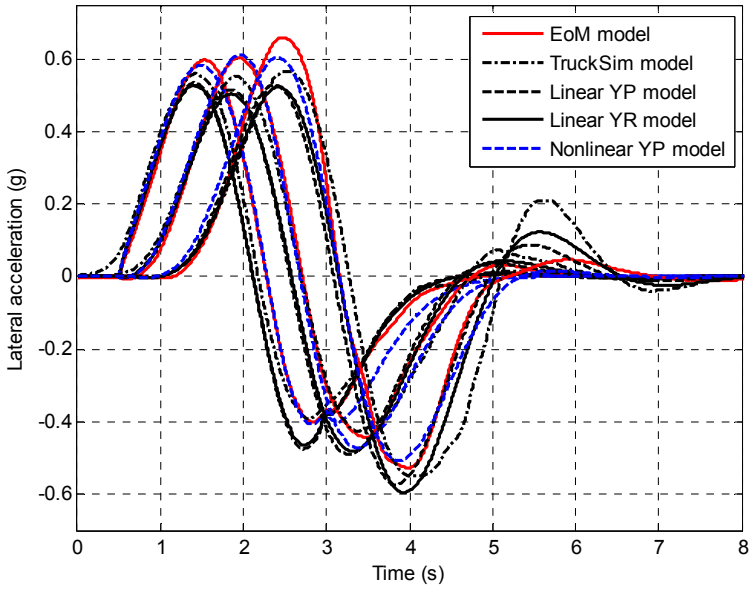

Figure 3.21 Lateral accelerations of the B-train double models under the high lateral acceleration SLC maneuver at forward speed $U = 110$ km/h

3.4 Summary

In order to design, optimize, and coordinate active safety systems (ASSs) for tractor/semitrailer combination and multi-trailer articulated heavy vehicles (MTAHVs), a linear yaw-plane model and a nonlinear yaw-plane model of the tractor/semitrailer, a linear yaw-plane model, a linear yaw-roll model, a nonlinear yaw-plane model, and a nonlinear EoM yaw-roll model have been derived and validated using the TruckSim models. All the models demonstrate the forward-speed-dependent property in rearward amplification. The linear models and the nonlinear models present lateral acceleration dependence property in predicting capability. At low lateral acceleration operation, the linear yaw-plane model, linear yaw-roll model, nonlinear yaw-plane model, nonlinear EoM yaw-roll model and the TruckSim model produce close match in predicting the performance of the B-train double. At high lateral acceleration operations, the linear yaw-plane model matches the linear yaw-roll very well; the nonlinear EoM yaw-roll model, nonlinear yaw-plane model and the TruckSim model yield close prediction capability; and the linear models separate themselves from the nonlinear ones clearly due to the application of different kinds of tire models.

The simulation results at low and high lateral acceleration operations suggest the following allocations of the models to the active safety system design for MTAHVs: 1) the linear yaw-plane model, effective in the low lateral acceleration range of 0-0.3g, is used to design the active trailer steering system to improve maneuverability and stability at low lateral acceleration operation; 2) the linear yaw-roll model, with main focus on predicting the roll dynamics, is applied to construct the active roll control system to stabilize the MTAHV in the medium lateral acceleration range of 0.2 to 0.6g; 3) the nonlinear yaw-plane model, sufficient in predicting the lateral dynamics of MTAHVs at high lateral acceleration operation, is employed to derive the trailer differential

braking system for stabilizing the MTAHV at the high lateral acceleration range from 0.3-0.7g; and 4) the nonlinear EoM yaw-roll model, which considers the longitudinal, lateral and roll dynamics of the MTAHV and the saturation property of the tire dynamics, is suitable for simulating the vehicle dynamics.

Chapter 4 Articulated Heavy Vehicle Lateral Dynamic Analysis Using an Automated Frequency Response Measuring Technique

4.1. Introduction

An articulated heavy vehicle (AHV) consists of a towing unit, namely tractor or truck, and one or multiple trailing units, called trailers. The adjacent units are connected at articulation points using mechanical couplings, e.g., dollies, fifth wheels, pintle hitches, etc. Due to multi-unit configurations, AHVs exhibit a unique dynamic phenomenon, i.e., rearward amplification (RWA), in which the rearmost unit experiences an amplified lateral acceleration with respect to that achieved at the tractor or truck (Fancher and Winkler, 2007). It is reported that the static rollover threshold of AHVs, expressed as lateral acceleration in gravitational acceleration (g), can be as low as 0.25g (Winkler, 2000). Lightly damped yaw responses of trailing units may easily precipitate rollover of the rearmost trailer (Winkler et al., 1983, Kang and Deng, 2007). RWA is of critical importance to the directional performance of AHVs. The RWA ratio, defined as the ratio of the peak lateral acceleration at the rearmost trailer's center of gravity (CG) to that of the leading unit (Fancher and Winkler, 2007), is often used as an important performance measure for assessing the lateral stability of AHVs (El-Gindy et al., 2001).

It is difficult for a driver to sense the motions of trailers, because his/her perception is based mainly on the response of the tractor (or truck) rather than the trailer(s) (Palkovics and Fries, 2001). Articulation joint(s) and tractor cab suspension isolate the driver from the trailer motions. AHVs may exhibit an exaggerated response of the rearward units (i.e., RWA) when performing a lane-change maneuver. The rearmost trailer is usually the first unit to rollover, and by the time the driver

realizes what is happening, it is too late to take corrective action. It is shown that only a minority of rollovers could be avoided with a warning device, and approximately half of the rollovers are not preventable by driver's action alone (Winkler et al., 1983, Palkovics and Fries, 2001). In order to attenuate rearward amplification tendencies in AHVs, a variety of potential solutions have been investigated. The effect of variations in size and weight constraints on the stability of AHVs was investigated (Ervin et al., 1983). Various types of coupling mechanisms, e.g., the modified A-dollies and B-dollies, were proposed for reducing the RA tendencies of AHVs (Winkler et al., 1986). The improvement of the lateral stability of AHVs achieved by the aforementioned solutions is limited, since these passive mechanisms cannot accommodate varied operating conditions, e.g., vehicle forward speed, trailer payload, and radius of road curvature (Fancher and Winkler, 2007). To address the limitations of the passive mechanisms, over the past two decades various active safety systems, including trailer differential braking (MacAdam and Hagan, 2002) and active trailer steering (Rangavajhula and Tsao, 2007), have been investigated to suppress the unwanted trailer yaw motions in AHVs.

Because of the cost and safety concerns, it may not be practical to conduct field or road tests to examine the directional performance of AHVs with or without the above active safety systems during concept design phases. Numerical simulation, thus, may be more practical in certain situations (Islam et. al., 2012). To determine the directional performance envelope of an AHV without active safety system, numerical optimization was conducted by searching optimal passive design variables; in the design synthesis, the lateral stability evaluations were conducted, based on numerical simulations of a nonlinear TruckSim AHV model (He, et al., 2013). To determine the optimal directional performance of an AHV with an active safety system, linear-model-based design optimization was performed by finding optimal passive and active design variables (He and

Islam, 2012). In the design optimization, a linear vehicle model was used for deriving the optimal controller for the ASS; and the optimal passive design variables for the mechanical trailer system and the optimal active design variables for the optimal controller were identified simultaneously in a single design process.

In the aforementioned design optimizations, the evaluations of the RWA ratio were based on the time-domain simulations of either a linear or a nonlinear AHV model. It is disclosed that the RWA ratio of an AHV is strongly dependent on steering input frequency (Ervin and MacAdam, 1982, Fancher, 1982). One of the distinguished features of dynamic response analysis in the frequency-domain is data reduction, i.e., a large number of time-domain samples are replaced by a small number of spectral lines (Pintelon at el., 1994). To comprehensively evaluate the lateral stability of an AHV, the lateral dynamic analysis over a frequency band of interest is necessary. In the case of a linear AHV model, the lateral dynamic analysis in the frequency-domain can be easily implemented using the transfer function method. However, in the case of a nonlinear AHV model, in order to achieve the required dynamic responses over a frequency band, numerous simulations in the time-domain have to be conducted in a tedious and time consuming process.

To date, there are a number of commercial multibody dynamic packages, e.g., ADAMS, DADS, TruckSim, etc., available for deriving sophisticated nonlinear AHV models for time-domain numerical simulations with high fidelity. However, these nonlinear AHV models are not suitable, instead, manually derived linear AHV models through very tedious, difficult, time-consuming, and error-prone process (Kortum, 1993) are required, for performing frequency response analysis. Recently, a spectrum-analyzer-based automated frequency response measuring (AFRM) tool is offered in Matlab, which acquires the frequency response of a second-order system driven by a complex sinusoidal signal (MathWorks, 2014). It is expected that the integration of

the AFRM tool with a multibody AHV model may be a useful method for achieving a relevant lateral dynamic response over a frequency band of interest. Conventionally, a linear and a nonlinear AHV model are usually compared and validated using only time-domain simulations due to the difficulty for directly obtaining the frequency responses of the nonlinear model (Islam et al., 2015). The AFRM tool may also provide an alternative way to compare and validate a nonlinear vehicle model with the corresponding linear model using frequency-domain simulations. Most importantly, the on-line application of the AFRM makes the frequency domain design optimization of ASSs for AHVs feasible.

This chapter examines the feasibility and effectiveness of incorporating the AFRM capabilities in multibody AHV models for the frequency-domain lateral dynamic analysis. The emphasis is placed on examining the applicability of the AFRM technique for linear systems. To demonstrate the effectiveness of the AFRM technique, it is applied to acquire the frequency responses in terms of the lateral accelerations of both the tractor and trailer using the linear yaw-plane and nonlinear TruckSim models of the tractor/semitrailer combination. The respective frequency responses are compared with those derived using a chirp signal (or swept-sine) steer input method, the transfer function method, and time-domain simulations of the linear and the nonlinear models. The frequency responses acquired using the AFRM technique from the three DOF linear and the twenty-one DOF nonlinear models are compared. A frequency response function (FRF) of the RWA ratio has been determined using the AFRM method. The FRF of RWA ratios in a frequency band of interest have been compared with those obtained using the single sine-wave steer input procedure recommended by ISO14791 (ISO, 2000). With the aid of the AFRM technique, the frequency-domain parametric analysis of the nonlinear TruckSim model is also conducted.

4.2 Automated Frequency Response Measuring Technique

Figure 4.1 shows the incorporation of the automated frequency response measuring (AFRM) capabilities (MathWorks, 2014) in the nonlinear TruckSim model for the lateral dynamic analysis in frequency-domain. The combined AFRM-TruckSim system consists of a signal generator, a system/plant (e.g., the nonlinear TruckSim model) to be examined, a spectrum analyzer and a data processor. The signal generator and the spectrum analyzer are coded with the state-flow programming language in Simulink. The data processing is conducted in Matlab. The system to be examined can be a linear or nonlinear dynamic system model, or a physical system. In this research, the system to be investigated is either the 3-DOF linear yaw-plane model coded in Simulink or the twenty one DOF nonlinear TruckSim model of the tractor/semitrailer combination derived in Chapter 3. In the case of the TruckSim model, the AFRM tool is interfaced with TruckSim software using an S-function, which enables the data communications between Simulink and TruckSim, and dynamically links TruckSim software as a subroutine of Matlab.

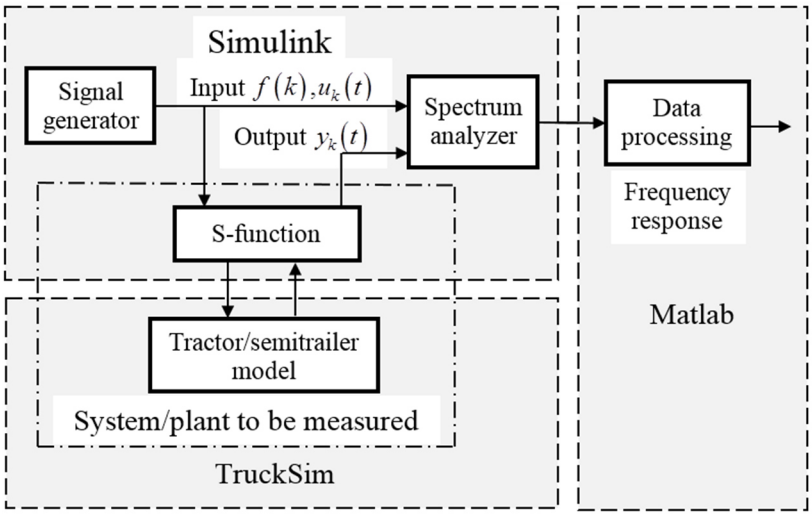

Figure 4.1 Schematic representation of the incorporation of the AFRM tool in the nonlinear TruckSim model

In the signal generator, the frequency band of input signal to be generated is determined by the bandwidth of the system to be examined. To properly excite the dynamics of the system, the frequency band of the input is selected at least one decade over the bandwidth of the system, and the frequency characteristics of the steering action of a human driver should also be considered. The frequency band is discretized with a frequency interval Δf . The selection of Δf is a trade-off solution between the smoothness of frequency-response curve and the length of test time. If a smaller Δf is selected, we may achieve a smoother frequency-response curve at the expense of longer test time. In this research, the frequency interval is selected as $\Delta f = 0.01$ Hz, and the frequency band is chosen as 0.0 ~ 1.0 Hz based on previous studies (Ervin and MacAdam, 1982, ISO, 2000). The input signal in the time-domain can be expressed as

$$u_k(t) = A\sin\left(2\pi f(k)t\right), \quad k = 1,2,3,..., \quad t \in \left(0, nT(k)\right) \tag{4.1}$$

where $f(k) = k\Delta f$, the k^{th} frequency, $T(k) = \dfrac{1}{f(k)}$ the period of the k^{th} sine-wave, n is an integer representing the number of cycles of the sine-wave with a specified frequency $f(k)$, and A is the amplitude of the sine-wave. Direct application of sine-waves as the steer input avoids time-consuming process of Fourier transform, and facilitates the validation of the AFRM technique using the manual measurement method. The number of cycles, n, is selected as small as possible to shorten the length of test time, while n should also be large enough to suppress the transient effect. Here n takes the value of 1 in order to achieve a compromised solution.

In this research, the objective is to examine the applicability of the AFRM technique for linear systems, and to use this method to extract the linearized characteristics in the frequency-domain from a nonlinear system. The amplitude of the input signal must be restricted below a limit in order to not excite nonlinear dynamics of the system. It should be noted that the applicability of the

AFRM technique for nonlinear systems will be investigated by the authors in a subsequent research.

In the spectrum analyzer, the magnitude and phase responses are acquired over a range of frequency. The frequency responses are kept unchanged in the given cycle(s) of a sine-wave until the frequency has been updated. At the k^{th} frequency, the magnitude and phase responses are computed as

$$M_k(t)\big|_{t\in(0,nT(k))} = \frac{magnitude\left(y_{k-1}(t)\big|_{t\in(0,nT(k-1))}\right)}{magnitude\left(u_{k-1}(t)\big|_{t\in(0,nT(k-1))}\right)} \tag{4.2a}$$

$$P_k(t)\big|_{t\in(0,nT(k))} = \frac{\pi}{2} - angle\left(y_{k-1}(t)\big|_{t\in(0,nT(k-1))}\right) \tag{4.2b}$$

Hence, the magnitude and phase curves from the spectrum analyzer are stair functions of time, which are called time-domain frequency data. During the data processing, the frequency responses are obtained by removing the repeated frequency data points from the time-domain data.

4.3 Verification of the AFRM Technique

In this section, the applicability of the AFRM technique for linear vehicle systems is examined through the following steps:

1) Comparison of the AFRM technique against other methods. In the case of the three DOF linear yaw-plane model, the simulation results based on the AFRM technique are compared with those using the transfer function method; in the case of the twenty one DOF nonlinear TruckSim model, the simulation results derived using the AFRM technique are compared against with those based on a chirp signal (or swept-sine) steer input method and a manual measurement approach.

2) Comparison of the linear and nonlinear models using time-domain simulations. In order to examine the degree of agreement between the linear and nonlinear models, the time-domain simulation results derived from the linear and nonlinear models under an emulated low lateral acceleration single-lane change maneuver are compared.
3) Comparison of the linear and nonlinear models using frequency-domain simulations. Under the condition that the amplitude of the steering input signal is strictly restricted to ensure not to excite the nonlinear dynamic characteristics of the nonlinear model, the linear and nonlinear models' frequency responses based on the AFRM technique are compared.

4.3.1 Comparison of the AFRM Technique against other Methods

The effectiveness of the AFRM technique is verified: 1) with the frequency responses achieved using the transfer functions (TF) of the linear model, 2) with the frequency responses achieved using the chirp signal steer input method based on the TruckSim model, and 3) the numerical results based on the time-domain simulations of the TruckSim model.

Table 4.1 Tire cornering stiffness coefficients of the validated linear model

C_{f11} (N/rad)	C_{r12} (N/rad)	C_{r23} (N/rad)
242,597	578,760	554,484

Table 4.2 RWA ratios measured using the AFRM and TF methods

Frequency (Hz)	0.2	0.8
RWA ratio with AFRM	1.060 (point A in Figure 4(a))	0.758 (point B in Figure 4(a))
RWA ratio with TF	1.068 (point A in Figure 4(a))	0.724 (point B in Figure 4(a))
Relative error* (%)	-0.75 (point C in Figure 4(b))	4.70 (point D in Figure 4(b))

*The relative error is defined as the ratio of the difference between the results based on the AFRM technique and the transfer function (TF) method to that based on the TF method.

Figure 4.2 illustrates the linear model's frequency responses in terms of RWA ratio derived using the AFRM and the TF methods when the tire cornering stiffness coefficients take the values listed in Table 4.1. Table 4.2 offers the numerical results at points A and B in Figure 4.2(a) and at points C and D in Figure 4.2(b). Note that points C and D in Figure 4.2(b) correspond to points A and B in Figure 4.2(a), respectively. It is indicated that within the frequency range of 0.01~1.0 Hz, the maximum relative error of the RWA ratio acquired by the AFRM tool with respect to the RWA ratio calculated by the TF method is 4.72% at the frequency of 0.76 Hz. Figure 4.3 shows the phase responses of the linear model achieved using the AFRM and TF methods. In the case of the linear model, the benchmark shown in Figures 4.2, 4.3, and Table 4.2 demonstrates an excellent agreement between the AFRM and TF methods.

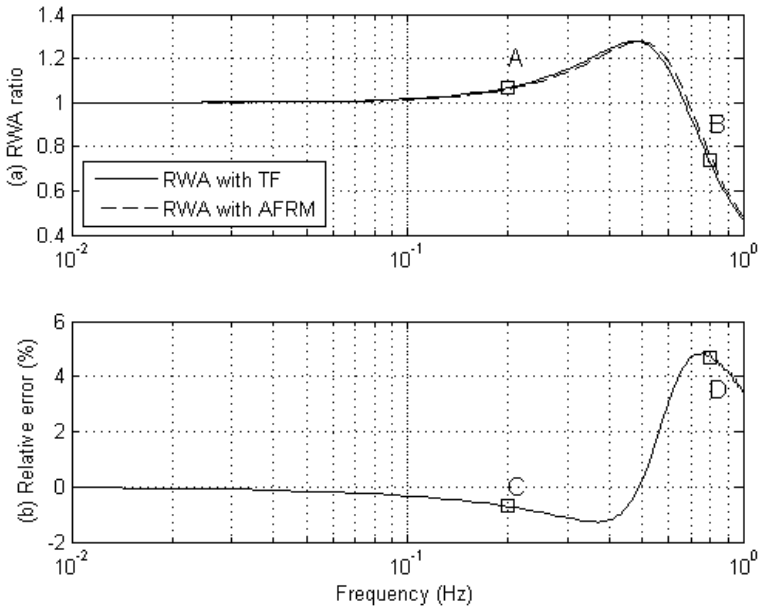

Figure 4.2 Linear vehicle model's magnitude response in terms of RWA ratio: (a) RWA ratio versus frequency, (b) the relative error of the RWA ratio achieved using the AFRM approach with respect to the RWA ratio derived using the transfer function method

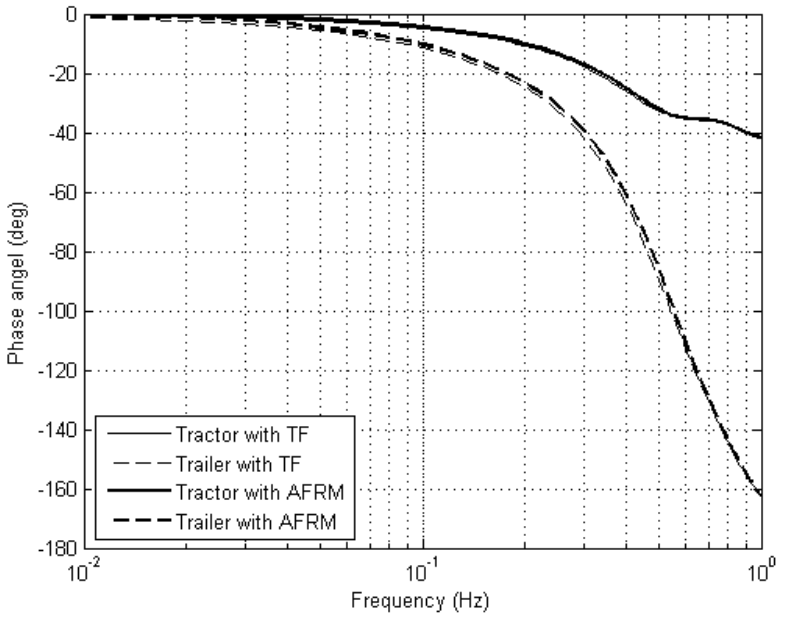

Figure 4.3 Linear vehicle model's phase responses achieved using the AFRM and TF methods

Figure 4.4 shows the TruckSim model's frequency responses, showing the lateral acceleration response of each vehicle unit to the tractor steer input. The frequency responses are obtained using the AFRM technique, the chirp signal (or swept-sine) steer input method (Gloth and Sinapius, 2004), and the manual measurement based on the time-domain numerical simulations of the TruckSim model. Table 4.3 lists the lateral acceleration gains at the selected frequencies derived using the three methods, the relative errors between the frequency responses obtained using the AFRM technique and the chirp signal steer input method, and the relative errors between the frequency responses acquired with the AFRM technique and the manual measurement approach. Note that in the case of the chirp signal steer input method, the linear sweep approach is applied, the steer input amplitude is 0.86°, the start frequency $f_0 = 0.01$ Hz, the end frequency $f_e = 1.0$ Hz, the time, T, sweeps from f_0 to f_e is 180 seconds, and the frequency responses are acquired using fast Fourier transform.

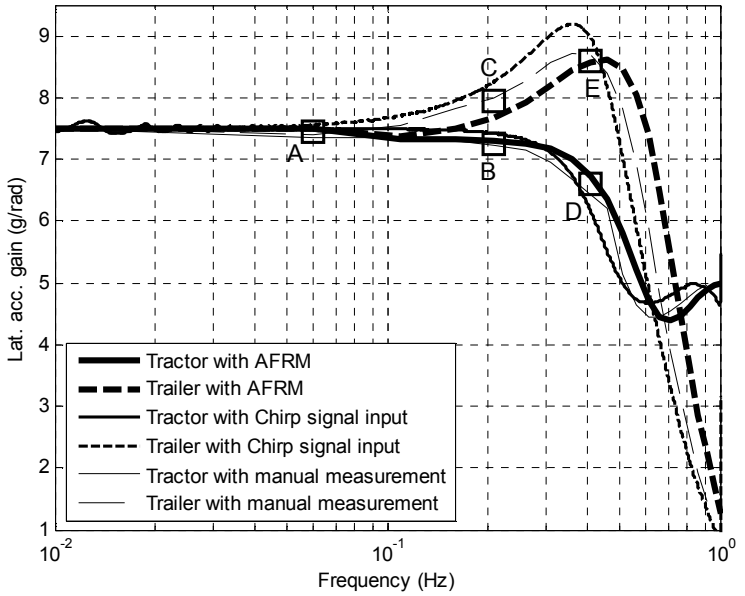

Figure 4.4 TruckSim model's frequency responses of the lateral acceleration for each vehicle unit to tractor front wheel steer input

Table 4.3 Lateral acceleration gains (at the selected points shown in Figure 4.4) acquired using the AFRM and manual measurement methods

Methods			AFRM	Chirp signal input		Manual measurement	
Point	Frequency (Hz)	Vehicle Unit	Gain (g/rad)	Gain (g/rad)	Relative error*	Gain (g/rad)	Relative Error#
A	0.06	Tractor	7.51	7.49	-0.27%	7.38	-1.73%
		Trailer	7.51	7.56	0.67%	7.41	-1.33%
B	0.21	Tractor	7.30	7.42	1.64%	7.25	-0.68%
C	0.21	Trailer	7.70	8.27	7.4%	8.0	3.9%
D	0.41	Tractor	6.75	6.15	-8.9%	6.42	-4.9%
E	0.41	Trailer	8.59	8.88	3.38%	8.70	1.28%

*The relative error is defined as the ratio of the difference between the gain based on the chirp method and the AFRM method to that based on the AFRM method.
#The relative error is defined as the ratio of the difference between the gain based on the manual measurement and the AFRM method to that based on the AFRM method.

As shown in Figure 4.4 and Table 4.3, the comparison of the lateral acceleration responses based on the AFRM, the chirp signal input, and the manual measurement methods indicates that the three approaches achieve a very good agreement. It has been observed that the AFRM method is sensitive to the asymmetry of the sinusoidal responses of the TruckSim model. The asymmetric

sinusoidal responses will decrease the measurement accuracy of the AFRM method. The asymmetry of time-domain lateral acceleration responses of AHVs was reported in past researches (Ervin and MacAdam, 1982).

The aforementioned comparisons indicate that: (1) in the case of the linear vehicle model, the results achieved using the AFRM technique is very close to those of the TF method, and the relative error between the two methods is less than 5.0%; and (2) in the case of the nonlinear vehicle model, if symmetric sinusoidal responses of a nonlinear vehicle model can be achieved, the AFRM technique, the chirp signal input method, and the manual measurement based on the time-domain simulation of the nonlinear vehicle model can reach a very good agreement. Moreover, compared with the chirp signal steer input method, the AFRM technique has the distinguished features as follows: 1) in the AFRM method, the system/plant concerned is excited using pure sinusoids; 2) the discrete Fourier transform (DFT) is conducted using correlation which is technically less demanding and easier to manage than the fast Fourier transform (FFT) used for the modal analysis with the chirp signal inputs or random signal excitations; 3) only the time-domain signals of the current frequency (single frequency) are processed in the DFT for computing the frequency response function (FRF); 4) there is no high-frequency filtering, no window weighting, and no spectrum averaging processes necessary, and, thus, less possibility of information loss; and 5) verification of the effectiveness of the AFRM method by using manual measurement is straightforward.

4.3.2 Comparison of Linear and Nonlinear Models Using Time-Domain Simulations

Table 4.1 and Table A1 (in Appendix A) provide the system parameters for the linear model validated using the TruckSim model. The parameters listed in Table A1 are also used for the TruckSim model. The other related parameters can be obtained in (Sampson, 2002).

In order to examine the dynamic behaviors of the linear and nonlinear vehicle models under typical SLC maneuvers, numerical simulations in time-domain have been conducted. Figure 4.5 shows the time history of tractor front wheel steer angle input, i.e., a 0.1 Hz single cycle sine-wave with amplitude of 1.5^o, and Figure 4.6 the time histories of the lateral acceleration for each vehicle unit based on the linear and nonlinear models. Figures 4.7 and 4.8 show the time histories of the lateral acceleration for each vehicle unit of the two vehicle models excited with 0.4 and 0.8 Hz inputs of 1.5^o amplitude, respectively. Table 4.4 provides the lateral acceleration values at each vehicle unit's CG at the selected points on the curves shown in Figure 4.8.

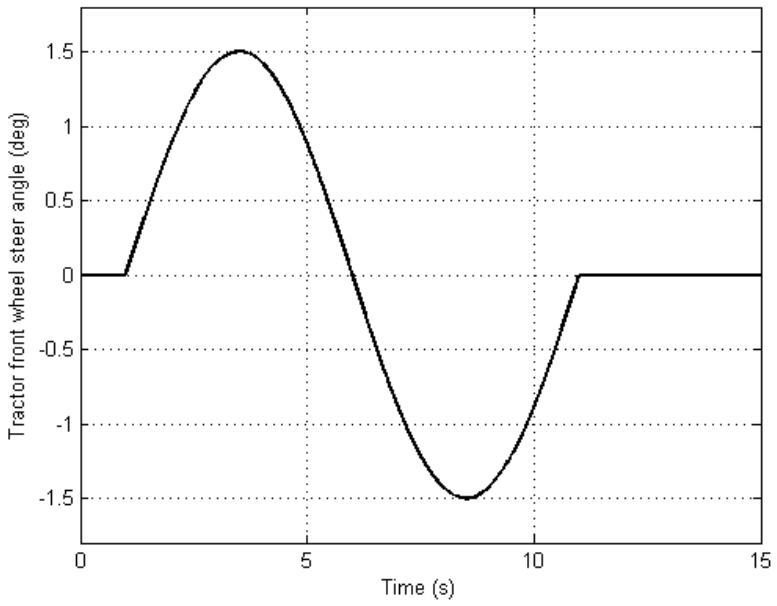

Figure 4.5 Time history of the tractor front wheel steer angle input (a single sine-wave with an amplitude of 1.5 deg and a frequency of 0.1 Hz)

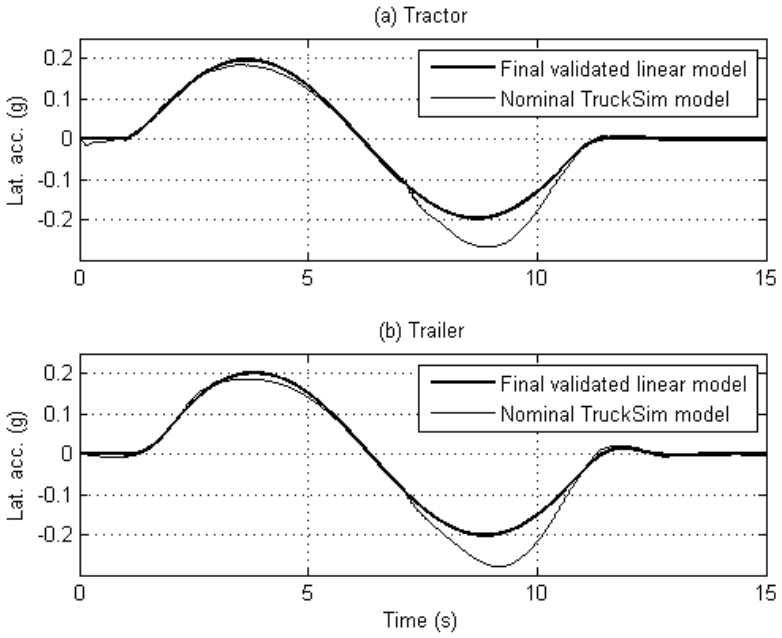

Figure 4.6 Lateral accelerations for the vehicle under a sine-wave steer angle input of the tractor front wheel with an amplitude of 1.5o and a frequency of 0.1 Hz at a forward speed of 150 km/h: (a) lateral acceleration at the tractor CG, and (b) lateral acceleration at the trailer CG

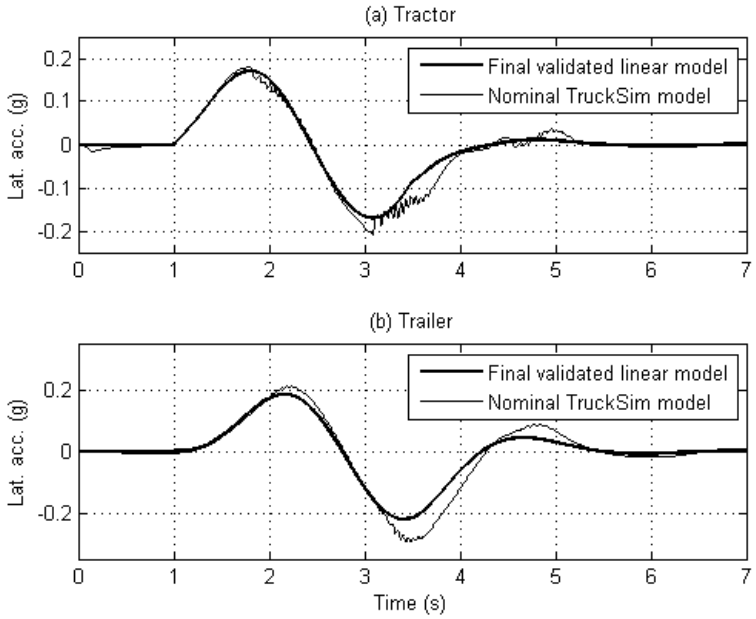

Figure 4.7 Lateral accelerations of the vehicle under a sine-wave steer angle input of the tractor front wheel with an amplitude of 1.5o and a frequency of 0.4 Hz at a forward speed of 150 km/h: (a) lateral acceleration at the tractor CG, and (b) lateral accelerate at the trailer CG

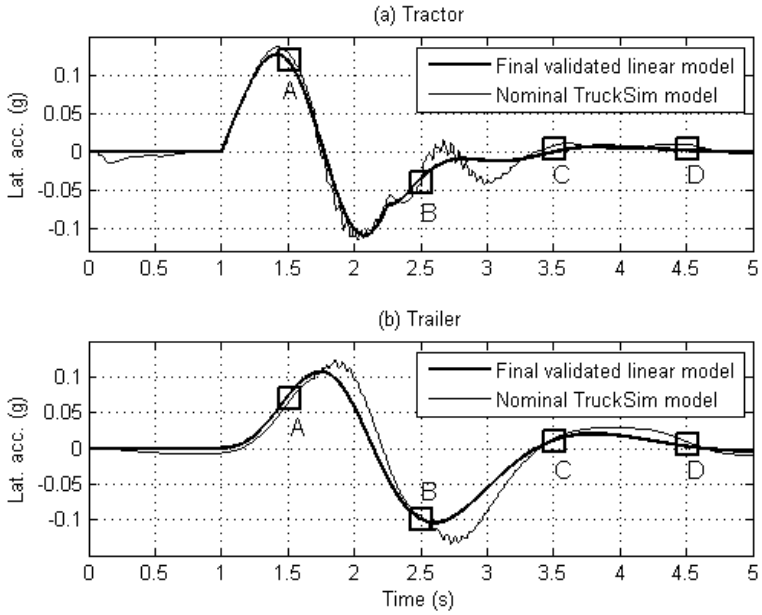

Figure 4.8 Lateral accelerations of the vehicle under a sine-wave steer angle input of the tractor front wheel with an amplitude of 1.5o and a frequency of 0.8 Hz at a forward speed of 150 km/h: (a) lateral acceleration at the tractor CG, and (b) lateral acceleration at the trailer CG

Table 4.4 Lateral acceleration of vehicle units at the selected points on the curves in Figure 4.8

	Point A		Point B		Point C		Point D	
	Tractor	Trailer	Tractor	Trailer	Tractor	Trailer	Tractor	Trailer
Lateral acceleration (linear model) (g)	0.115	0.075	-0.035	-0.101	0	0.012	0.001	0.002
Lateral acceleration (TruckSim model) (g)	0.127	0.065	-0.038	-0.095	0.007	0.014	0.009	0.009
Error* (g)	-0.012	0.010	0.003	-0.006	-0.007	-0.002	-0.008	-0.007
Time (s)	1.51		2.51		3.51		4.51	

*Error is defined as the difference between the lateral acceleration based on the linear model and that based on the TruckSim model

Based on the time-domain numerical simulation results shown in Table 4.4 and in Figures 4.6, 4.7, and 4.8, the following observations have been made: (1) under low lateral acceleration (less than 0.3g) maneuvers, the linear and nonlinear models reach a very good agreement, consistent with the conclusion made in (Islam et al., 2015); (2) the extent of the agreement between the simulation results based on the two models is frequency dependent; and (3) under a given single cycle sine-wave front wheel steer angle input, the time history of the lateral acceleration for each

vehicle unit of the linear model is also approximately symmetric sine-wave, while that of the nonlinear model is a distorted sine-wave, asymmetric with respect to the time axis.

To further investigate the time-domain lateral dynamic behaviors of the linear and nonlinear vehicle models, numerical simulations under a variable frequency sine-wave steer angle input of the tractor front wheel have been conducted. The tractor front wheel steer angle input is made using the signal generator shown in Figure 4.1. At each frequency, a single cycle sine-wave steer angle signal, with frequency varying from 0.01 to 1.0 Hz with an interval of 0.05 Hz and amplitude of 1.72^{o}, is generated to excite the lateral dynamics responses of the linear and nonlinear models. The vehicle forward speed maintains constant at 150 km/h.

Simulation results shown in Figures 4.9 and 4.10 clearly illustrate that the lateral acceleration responses of the TruckSim model to the variable frequency sine-wave steer angle input are deformed sine-waves, asymmetric with respect to the time-axis. This observation is consistent with the disclosed phenomenon introduced previously in the case of the single cycle sine-wave steer angle input.

This asymmetry is detrimental to the performance of the AFRM method. To mitigate and avoid negative impact of the asymmetry on the accuracy of the frequency response acquisition using the AFRM method, an offset time-axis is introduced in such a way that the asymmetric dynamic responses of the nonlinear vehicle model are symmetric with respect to the offset axis. In the research, the offset axis is used when the AFRM method is utilized to acquire the frequency responses of the TruckSim model.

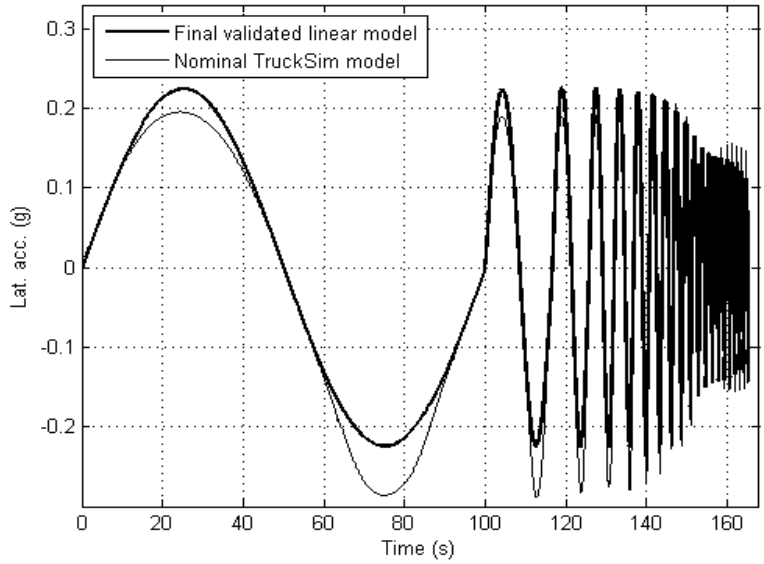

Figure 4.9 Tractor lateral accelerations under the variable frequency sine-wave steer angle input of the tractor front wheel

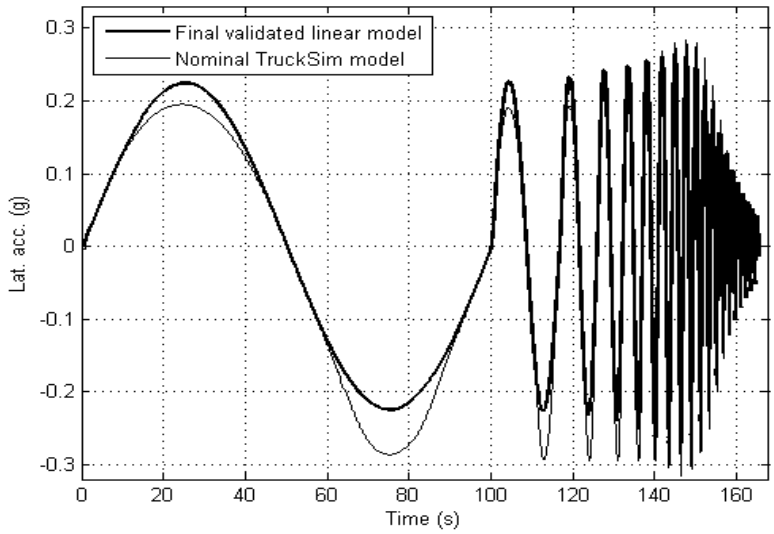

Figure 4.10 Trailer lateral accelerations under the variable frequency sine-wave steer angle input of the tractor front wheel

4.3.3 Comparison of Linear and Nonlinear Models Using Frequency-Domain Simulations

In order to further examine the performance of the AFRM technique, this frequency response acquiring method is applied to compare the lateral acceleration responses of the linear and nonlinear models, which have been validated using the time-domain numerical simulations described in Section 4.3.2. Figure 4.11 shows the linear and nonlinear models' frequency responses obtained using the AFRM method, showing the lateral acceleration response of each vehicle unit to the tractor front wheel steer angle input. Table 4.5 lists the lateral acceleration gains at the selected frequencies and the relative errors between the frequency responses of the two vehicle models.

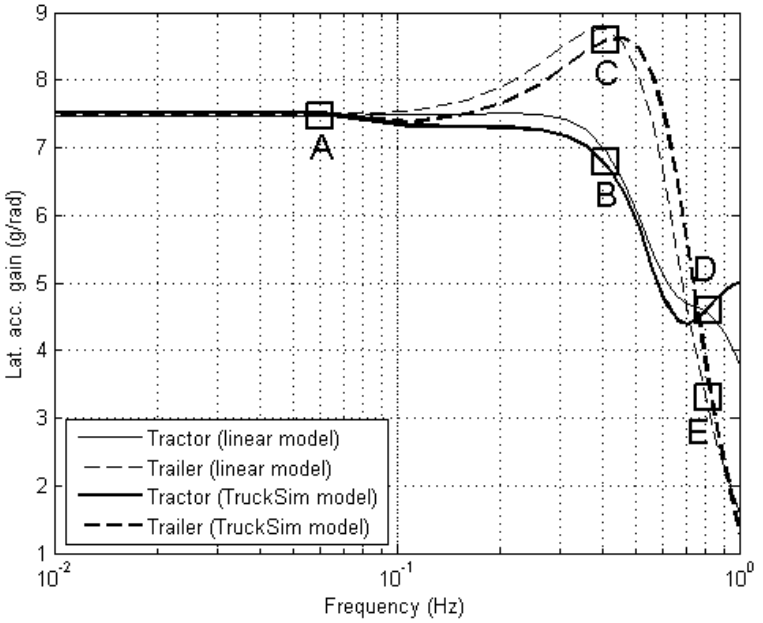

Figure 4.11 Frequency responses of the linear and TruckSim models showing the lateral acceleration response of each vehicle unit to the tractor front wheel steer input

Simulation results shown in Figure 4.11 and in Table 4.5 illustrate that within the selected frequency range, the linear and nonlinear vehicle models achieve a good agreement. Moreover, the degree of the agreement between the frequency-domain simulation results based on the two models is frequency dependent, which confirms the observation discussed previously in Section 4.3.2.

Table 4.5 Lateral acceleration gains (at the selected points shown in Figure 4.11) measured using the AFRM method

	A		B	C	D	E
Vehicle unit	Tractor	Trailer	Tractor	Trailer	Tractor	Trailer
TruckSim model (g/rad)	7.508	7.505	6.737	8.579	4.623	3.592
Linear model (g/rad)	7.478	7.481	6.958	8.755	4.545	3.138
Relative error*(%)	-0.4	-0.32	3.28	2.05	-1.69	-12.64
Frequency (Hz)	0.06		0.41		0.81	

*The relative error is defined as the difference between the results based on the linear model and the TruckSim model to that of the TruckSim model

The above analysis indicates that the AFRM method may provide an alternative way to acquire the FRF of the RWA ratio for AHVs. It should be noted that when used to acquire the frequency responses of a nonlinear system model, the AFRM technique is to extract the linear dynamic characteristics of the nonlinear model. In the application of the AFRM method, the amplitude of the input signal should be strictly restricted to ensure not to excite the nonlinear dynamic characteristics.

4.4 Determination of the RWA Ratio Recommended by ISO14791

In order to determine the RWA ratio of AHVs, ISO14791 recommends three different test procedures (ISO, 2000): 1) pseudo-random steer input, 2) single sine-wave steer input, and 3) single sine-wave lateral acceleration input. For the pseudo-random input procedure, the maximum lateral acceleration of the first vehicle unit should be restricted below a limit level in such a way that all vehicle units are keep within the linear regime (ISO, 2000). This method may achieve a

complete representation of the frequency dependency of the RWA ratio in the frequency-domain. The second test procedure is an open-loop SLC maneuver under a full period sinusoidal steer input applied to the steering wheel. The third test procedure is a closed-loop SLC maneuver, under which the first unit follows a predefined trajectory at a constant vehicle forward speed. Both the second and third test procedures can provide only a RWA ratio for a given frequency, at which the specified lane-change is performed.

For the pseudo-random input test procedure, stochastic excitation signals are applied to acquire the frequency response function (FRF) of the RWA ratio over a wide frequency band. It is reported that several waveforms are available to excite a given system in order to determine the required FRFs, and the most common types of waveforms are harmonic excitation, e.g., discretely stepped sine, period excitation like multi-sine, transient excitation like chirp signal (or sinusoidal sweeps), and random excitation (Gloth and Sinapius, 2004). As shown in Figure 4.4, both the AFRM approach and the chirp signal input method can be used to acquire the FRFs of the lateral acceleration of each vehicle unit of the TruckSim model, and the results based on the two methods reach a very good agreement. This implies that, similar to the pseudo-random steer input test procedure recommended by ISO14791, the AFRM method may also be effectively used to determine the FRF of the RWA ratio for AHVs. Actually, the FRF of the RWA ratio for the three DOF linear model has already been acquired using the AFRM technique as shown in Figure 4.2(a).

It has been validated that for an AHV, at a given frequency, the RWA ratio determined under the closed-loop SLC maneuver and the ratio evaluated using the FRF derived under the pseudo-random steer input test procedure should research an excellent agreement (Aurell and Koppenaal, 1998). Similarly, it is expected that for the three DOF linear model, at a given frequency, the RWA ratio based on the AFRM technique and the open-loop SLC maneuver recommended by ISO14791

should achieve a good agreement. In order to elucidate this issue, we correlate the simulation results based on the AFRM technique introduced in Section 4.3.1 and those achieved using the time-domain simulations described in Section 4.3.2. Actually, results shown in Figures 4.6, 4.7, and 4.8 are achieved under the emulated open-loop single SLC maneuvers recommended by ISO14791, i.e., the single sine-wave steer input, at frequency of 0.1, 0.4, and 0.8 Hz, respectively. With the time-domain results shown in Figures 4.6, 4.7, and 4.8, the linear model's RWA ratios at frequency of 0.1, 0.4, and 0.8 Hz can be determined and the corresponding values are listed in Table 4.6. With the FRF for the linear vehicle model based on the AFRM technique shown in Figure 4.2(a), the RWA ratios at the frequency of 0.1, 0.4, and 0.8 Hz can also be determined, and the corresponding values are listed in Table 4.6. An observation of the results shown in Table 4.6 discloses that the maximum relative error (absolute value) between the results based on the two methods is 9.38%, the open-loop SLC maneuver recommended by ISO14791 and the AFRM method achieve a very good agreement. The benchmark of the simulation results listed in Table 4.6 is consistent with the aforementioned expectation.

Table 4.6 Linear model's RWA ratios determined under the open-loop SLC maneuver recommended by ISO14791 and the RWA ratios achieved using the AFRM technique

	RWA ratio at 0.1 Hz	RWA ratio at 0.4 Hz	RWA ratio at 0.8 Hz
Single sine-wave input	1.023	1.189	0.842
AFRM technique	1.013	1.229	0.763
Relative error*	-0.99%	3.36%	-9.38%

*The relative error is defined as the ratio of the difference between the results based on the AFRM technique and the single sine-wave steer input method to that based on the single sine-wave steer input method.

4.5 Parametric Analysis based on the Frequency Responses of the TruckSim Model

In order to demonstrate other applications of the AFRM method to the lateral dynamic analysis of the tractor/semitrailer combination, parametric analysis based on the frequency responses of the

TruckSim model has been conducted. Figure 4.12 illustrates the frequency response of the TruckSim model, showing the effect of the trailer mass moment of inertia (I_{zz2}) on the lateral acceleration response of each vehicle unit to the tractor front wheel steer angle input. It is observed that the variation of I_{zz2} has negligible influence on the lateral acceleration gain of the tractor and trailer within the low frequency range of 0.01 to 0.1 Hz. In the case of the tractor, the lateral acceleration gain increases with the mass moment of inertia in the frequency range of 0.2 to 0.8 Hz. In the case of the trailer, increasing I_{zz2} leads to the increase of the peak value of the lateral acceleration gain in the frequency range of 0.05 to 0.5 Hz, while the increase of I_{zz2} results in the increase of the slope for dropping the lateral acceleration gain in the frequency band of 0.5 to 1.0 Hz.

Figure 4.13 offers the frequency response of the TruckSim model, illustrating the impact of the longitudinal distance between the trailer CG to the fifth wheel (l_{c21}) on the lateral acceleration response of each vehicle unit to the tractor front wheel steer angle input. A close observation of Figure 4.13 indicates that increasing l_{c21} results in shifting up the lateral acceleration gain of the tractor and trailer up to the frequency of 0.37 Hz and 0.5 Hz, respectively. In the case of the trailer, within the frequency range of 0.5 to 1.0 Hz, the higher the value of l_{c21}, the larger the slope of dropping the lateral acceleration gain. In the case of the tractor, within the high frequency range of 0.37 to 1.0 Hz, the effect of l_{c21} varies: first the increase of the parameter will speed up the drop of the lateral acceleration gain, then the increase of the parameter will shift up the gain.

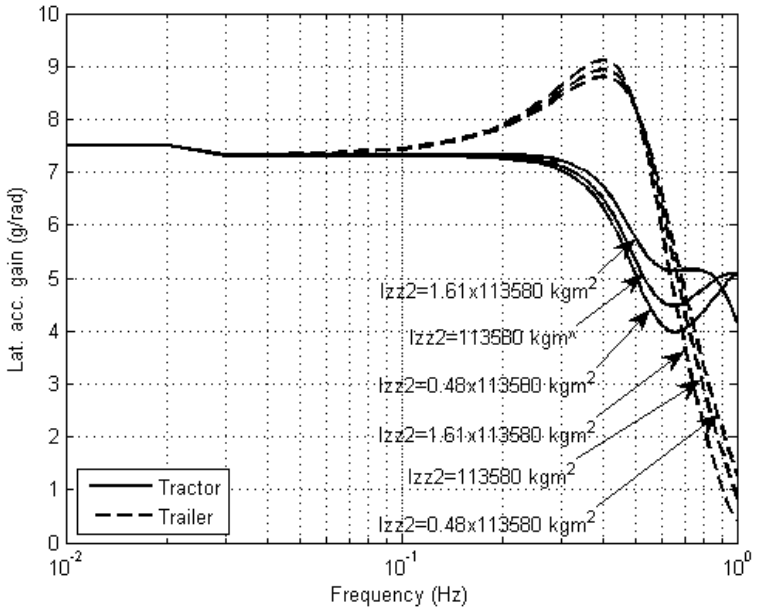

Figure 4.12 Frequency response of the TruckSim model showing the effect of the trailer mass moment of inertia (Izz2) on the lateral acceleration response of each vehicle unit to the tractor front wheel steer angle input

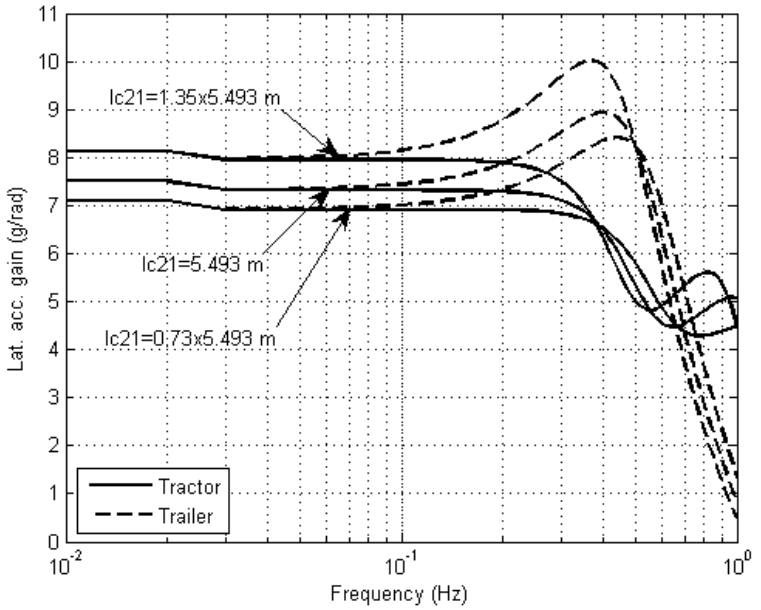

Figure 4.13 Frequency response of the TruckSim model showing the effect of the longitudinal distance between the trailer CG to the fifth wheel (lc21) on the lateral acceleration response of each vehicle unit to the tractor front wheel steer angle input

Figure 4.14 shows the effect of the trailer mass, m_2, on the frequency responses of the lateral accelerations of the vehicle units. At the low frequency up to 0.6 Hz, increasing the trailer mass leads to shifting down the frequency responses of the both units. Within the frequency range of 0.6 to 1.0 Hz, when the trailer mass is larger than the nominal value, the following observations can be made: 1) the frequency response of the tractor starts to move up with the increase of the frequency; and 2) the increase of the trailer mass makes the frequency response of the tractor move up earlier and faster. On the other hand, within the frequency range of 0.6 to 1.0 Hz, if the trailer mass is smaller than the nominal value, the frequency response of the tractor decreases with the increase of the frequency. In the case of the trailer, within the frequency range of 0.6 to 1.0 Hz, the frequency response of the trailer drops monotonously with the increase of the frequency; the increase of the parameter will speed up the drop of the frequency response.

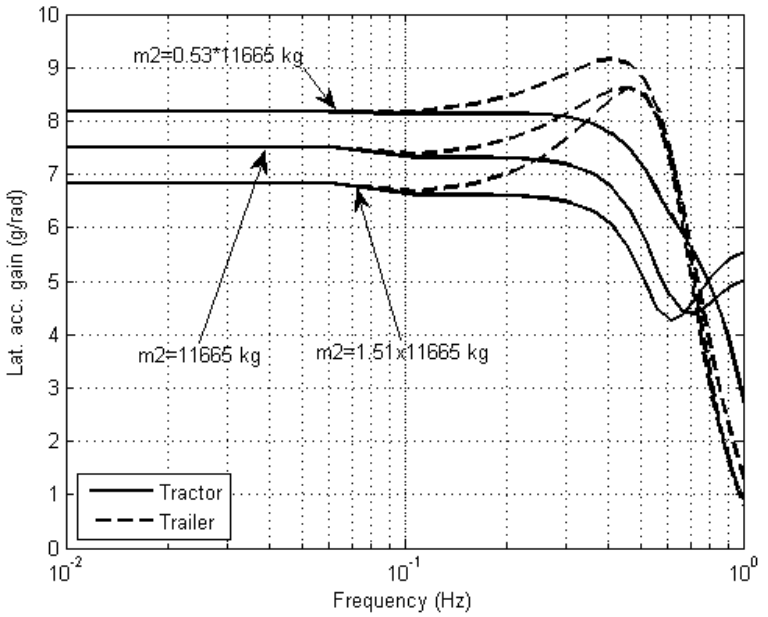

Figure 4.14 Frequency response of the TruckSim model showing the effect of the trailer mass on the lateral acceleration response of each vehicle unit to the tractor front wheel steer angle input

The above parametric analysis shows that the trailer parameters, i.e., trailer mass moment of inertia (I_{zz2}), trailer mass (m_2), and the longitudinal distance between the trailer CG to the fifth wheel (l_{c21}), have impacts on the lateral acceleration of the tractor and the trailer. All the three parameters are directly related to the trailer payload, which is randomly varied depending on operating conditions. In the trailer lateral dynamic control system design, the uncertainties of these parameters and their impacts on the lateral dynamics of the AHV should be considered in order to improve the robustness of the active safety system.

The above case studies indicate that the integration of the AFRM method and the multibody vehicle model can be used to acquire the required frequency responses over the frequency band of interest. Moreover, the combination of the AFRM method with the AHV model provides an effective tool to conduct lateral dynamic analysis and directional performance evaluation, in particular, through parametric studies based on frequency-domain numerical simulations. By means of using the AFRM technique, the distinguished feature of frequency response analysis in data reduction, i.e., a large number of time-domain samples being replaced by a small number of spectral lines, can be realized and fully utilized. The data reduction of frequency response analysis with respect to time response analysis is of significant importance for directional performance optimization of AHVs due to computational efficiency improvement.

4.6 Summary

This chapter proposes a method for articulated heavy vehicle (AHV) lateral dynamic analysis using frequency-domain simulations by means of integrating an automated frequency response measuring (AFRM) technique with a multibody AHV model. The feasibility and effectiveness of the proposed method for linear systems has been demonstrated by way of comparing the AFRM

technique with three different approaches: 1) the chirp signal (or swept-sine) steer input method, 2) the transfer function method based on a linear AHV model, and 3) the manual measurement built upon the time-domain simulations of the corresponding nonlinear AHV model, i.e., the TruckSim model. In order to avoid exciting nonlinear dynamics of the TruckSim model, the amplitude of the variable frequency sine-wave steer input of the AFRM method must be restricted below a limit. With the aid of the AFRM technique, the linear dynamic characteristics can be extracted from the corresponding nonlinear AHV model. Thus, the proposed method provides an alternative approach to the validation of the linear dynamic characteristics of a nonlinear AHV model using the corresponding linear model based on frequency-domain simulations. The AFRM method can be used to acquire the frequency response function (FRF) of the rearward amplification (RWA) ratio, the resulting FRF has been validated using the simulation results derived from an emulated single sing-wave steer input test procedure recommended by ISO14791. With the AFRM technique, multibody AHV models can be directly used to conduct parametric analysis in the frequency-domain, which provides a valuable tool for the design analysis of AHVs for improving directional performance. Compared with the chirp signal (or swept-sine) input excitation method for modal identification, the AFRM technique is more computationally efficient with less information loss during the data processing. With the proposed AFRM tool, the frequency response of the RWA measure over a specified frequency band can be acquired in such a way that the vehicle steer input signal generation, AHV model simulation, and the FRF acquisition can be implemented through an automatic process executed on a computer. Therefore, the AFRM technique provides an ideal tool for the design optimization of AHVs based on frequency response analysis in order to effectively improve the lateral stability.

It is observed that the time history of the lateral acceleration response of the nonlinear AHV model to a variable frequency sine-wave steer angle input of the tractor front wheel is a deformed sine-wave, which is asymmetric with respect to the time-axis. This asymmetry is detrimental to the performance of the AFRM method. To mitigate the negative impact of the asymmetry on the accuracy of the frequency response measurement of the AFRM method, an offset time-axis may be introduced in such a way that the asymmetric dynamic responses of the nonlinear vehicle model are symmetric with respect to the offset axis.

The applicability of the AFRM technique for nonlinear systems will be investigated using nonlinear dynamic analysis techniques, e.g., the describing function method, in the near future. For example, under given conditions it is possible to use describing functions to predict the response of certain nonlinear systems to purely sinusoidal excitation. It is expected that insightful findings will be disclosed in the subsequent research on examining the feasibility and effectiveness of the AFRM technique for nonlinear systems.

Chapter 5 A Unified Lateral Preview Driver Model for Road Vehicles

5.1 Introduction

To date, closed-loop driver/vehicle simulations have been widely used for design and development of vehicle systems and, in particular, driver assistance systems (Horiuchi and Yuhara, 2000, Islam et al, 2012, MacAdam, 1980, MacAdam, 1981, MacAdam, 2003, Peng, 2002, Plochl and Edelmann, 2007, Ungoren and Peng, 2005, and Yang et al, 2001). In order to perform closed-loop driver/vehicle simulations, we have to model and simulate driver behaviours. In 1980, MacAdam generated an optimal preview driver model (MacAdam, 1981), which has been implemented in commercial software packages, CarSim and TruckSim, for closed-loop simulations of both Single-Unit Vehicles (SUVs) and Multi-Unit Vehicles (MUVs) (MacAdam, 1980). The driver model was derived by minimizing a cost function, which was defined as a mean squared lateral position error between a predicted lateral position and a target lateral position. Experimental and simulation results based on the driver model demonstrate that driver steering control under path-following maneuvers can be accurately simulated as a time-delayed optimal preview control process (MacAdam, 1981). In 2005, Ungoren and Peng generalized the MacAdam's driver model by introducing an additional weighed yaw error in the cost function (Ungoren and Peng, 2005). In the generalized driver model, a parameter is tunable to assign relative importance of lateral position and yaw error in the cost function to be minimized, which permits the driver model to have additional flexibility to simulate different driver behaviours. The aforementioned two driver models were generated based on SUVs (MacAdam, 1980, Ungoren and Peng, 2005), and the vast

majority of driver models reported in the literature have also been derived for SUVs (MacAdam, 2003, Plochl and Edelmann, 2007, and Yang et al, 2001). Fewer SUV-based driver models have been applied to closed-loop simulations for articulated heavy vehicles (AHVs), and these driver models use control schemes based on lateral position error and/or yaw error of the leading unit alone (Islam et al, 2012, MacAdam, 1980). These SUV-based driver models may not well mimic the driving performance characteristics of human drivers for AHVs and, in particular, Multi-Trailer Articulated Heavy Vehicles (MTAHVs).

The dynamics of MTAHVs differs significantly from that of SUVs. Due to MTAHVs' multi-unit configurations, large sizes, and high centers of gravity (CGs), these large vehicles show poor maneuverability and low lateral stability (Wang and He, 2016). MTAHVs exhibit unstable motion modes, e.g., jack-knifing and trailer swing, which could cause fatal accidents. MTAHVs may display an exaggerated lateral motions of the rearward units when executing evasive maneuvers (Winkler, 2001). The rearmost trailing unit is usually the first one to rollover and by the time the driver realizes what is occurring, it is generally too late for him/her to take corrective action. The maneuverability of MTAHVs may be well represented with the performance measure of path-following off-tracking (PFOT), which is defined as the maximum radial offset between the path of the leading unit's front axle center and that of the rearmost trailing unit's rear axle center under a specified path-following maneuver; the lateral stability of MTAHVs could be effectively evaluated with the indicator of rearward amplification (RWA), which is specified as the ratio of the peak lateral acceleration at the rearmost trailing unit's CG to that of the leading unit under an obstacle avoidance lane-change maneuver (Islam et al, 2012). Driving MTAHVs, which exhibit the above unique dynamic characteristics, may pose stringent requirements on the drivers in the aspects of training, experience and driving skills. For an AHV and, especially, a MTAHV, the

various motion state variables of the trailing units could affect the driving behavior of the driver. However, very few driver models have been reported in the literature to simulate the driving performance characteristics of drivers for AHVs and, in particular, MTAHVs, considering perception of motions of both leading and trailer units (MacAdam, 2003, Plochl and Edelmann, 2007, and Yang et al, 2001).

In 2001, Yang et al proposed a driver model for tractor/semitrailer combinations (Yang, 1999, Yang et al, 2001, and Yang et al, 2002). The driver model is featured with multi-loop structure, which incorporates the path preview, low and high frequency compensatory gains and time delays, and prediction of tractor lateral acceleration, articulation rate and the trailer sprung mass roll angle. The effect of the driver model parameters of reaction time, preview distance, and compensatory gain on the directional performance of the tractor/semitrailer combination was examined using closed-loop simulations under an obstacle avoidance maneuver. In 2007, Liu also proposed a driver model for tractor/semitrailer combinations, in which the steering angle is determined by the feedback of the tractor and trailer instantaneous states with a time delay (Liu, 2007). The feedback gains were derived by minimizing a predefined cost function, and sensitivity analysis on the feedback gains were carried out using numerical simulations. However, the tractor/semitrailer driver model does not differentiate the perceived motion states of the leading and trailing units. In reality, it may be difficult for a human driver to fully sense the trailer motions, as the driver's perception is based mainly on the leading unit response rather than the trailer(s) (Palkovics and Fries, 2001). Articulation joint(s) and the tractor cab suspensions may isolate the human driver from trailing units' motions. In 2012, Ding and He reported a driver model for tractor/semitrailer combinations in order to differentiate the perceived motion states of the leading and trailing units and examine the corresponding effect on the directional performance of the tractor/semitrailer

(Ding and He, 2012). Unfortunately, the driving performance characteristics of the driver model was not adequately investigated. In recent years, closed-loop simulation of MTAHVs has been applied to the design and development of active safety systems for MTAHVs (Ding et al, 2013). However, to the best of the authors' knowledge, there is no any driver model dedicated to MTAHVs reported in the literature.

This chapter proposes a unified driver model, which considers the dynamic characteristics of both SUVs and MUVs, and thus can be applied to closed-loop simulations of each type of vehicles by selecting appropriate parameter values of the driver model. The unified driver model is designed using a sliding mode control (SMC) technique. The SMC-based preview driver model distinguishes itself from conventional driver models with the following features: 1) by means of the SMC controller design, the 'driver' steering angle is determined considering the lateral position and yaw errors of all the leading and trailing units of MTAHVs; 2) a set of tunable parameters are specified to assign relative weights to the lateral position and yaw errors of the leading and trailing units, which differentiate the perceived motion states of the leading and trailing units; 3) the SMC-based driver model is designed with two modes, namely, stability- and path-following-oriented, which may be used to simulate MTAHV drivers' driving performance under a high-speed evasive and a low-speed path-following maneuver, respectively; and 4) the SMC-based preview driver model can simulate performance characteristics for drivers of both SUVs and MUVs, and this model turns into the MacAdam optimal preview driver model if a control parameter takes the value of infinity. Without loss of generality, the SMC-based preview driver model is derived based on a B-Train Double represented by a four degrees of freedom (DOF) linear yaw-plane model presented previously in Chapter 3. In order to examine the performance of the SMC-based preview driver model, closed-loop simulations under an evasive maneuver are conducted via the integration of

the driver model and the nonlinear EoM yaw-roll B-Train Double model developed in a multibody dynamic package, EoM (Minaker and Rieveley, 2010, Minaker and Rieveley, 2013) presented also in Chapter 3. The distinguished features of the SMC-based preview driver model are demonstrated via benchmark numerical simulations.

5.2 Four DOF Linear Yaw-plane Model

The four DOF linear yaw-plane model presented in Chapter 3 is applied to design the driver model. Removing the active input terms, the state-space representation of the yaw-plane model of the B-Train Double is re-written as

$$\dot{\mathbf{x}}_p = \mathbf{A}_p \mathbf{x}_p + \mathbf{C}_p \delta_{11} \tag{5.1}$$

where $\mathbf{x}_p = \begin{bmatrix} \beta_1 & \dot{\psi}_1 & \beta_2 & \dot{\psi}_2 & \beta_3 & \dot{\psi}_3 \end{bmatrix}^T$. In the SMC-based preview driver model to be designed in Subsection 5.3, the 'driver' steering angle will be determined by the errors of lateral position and yaw rate of each vehicle unit. Thus, the state-space equation of the yaw-plane model expressed in Equation (5.1) is reformulated as

$$\begin{cases} \dot{\mathbf{x}}_d = \mathbf{A}_d \mathbf{x}_d + \mathbf{B}_d \delta_{11} \\ \mathbf{y} = \mathbf{C}_d \mathbf{x}_d \end{cases} \tag{5.2}$$

where $\mathbf{x}_d = \begin{bmatrix} Y_1 & \psi_1 & v_1 & \dot{\psi}_1 & Y_2 & \psi_2 & v_2 & \dot{\psi}_2 & Y_3 & \psi_3 & v_3 & \dot{\psi}_3 \end{bmatrix}^T$ denotes the resulting state variable vector, $\mathbf{y} = \begin{bmatrix} Y_1 & Y_2 & Y_3 \end{bmatrix}^T$ represents the output vector, Y_1, Y_2 and Y_3 are lateral position of the tractor front axle center, lateral position of the CG of the 1st semitrailer, and lateral position of the CG of the 2nd semitrailer, respectively**.** The matrices $\mathbf{A}_d$, $\mathbf{B}_d$ and $\mathbf{C}_d$ are provided in Appendix G. Note that Y_1, Y_2 and Y_3 are measured in the inertial coordinate system, and they are determined as follows

$$\begin{cases} \dot{Y}_1 = U_1\psi_1 + (v_1 + a_1\dot{\psi}_1) \\ \dot{Y}_2 = U_2\psi_2 + v_2 \\ \dot{Y}_3 = U_3\psi_3 + v_3 \end{cases} \tag{5.3}$$

5.3 SMC-Based Preview Driver Model

As introduced previously, MTAHVs are featured with large sizes, multi-unit vehicle structures, and wide range of trailer payload variations. In closed-loop driver/vehicle system modelling, the aforementioned features of MTAHVs may introduce parametric uncertainties and frequently lead to un-modeled dynamics. It is reported that the main advantages of sliding mode control (SMC) systems are insensitivity to parameter variations, disturbance rejection, and simple design implementation (Young et al, 1999). A SMC-based driver model was proposed for SUVs (Menhour et al, 2010). In this section, a SMC technique is applied to the design of the unified driver model for SUVs and, in particular, for MTAHVs. In the design of the unified driver model, we consider the following two control schemes: 1) Leading Unit Path Tracking (LUPT), and 2) Delayed Leading Unit Lateral Previews (DLULP). In the LUPT scheme design, it is assumed that in order to track a given trajectory under an evasive maneuver, the steering angle of the front wheels of the leading vehicle unit is determined in such a way that the leading unit front axle center is forced to track the target trajectory based on the conventional lateral position preview control concept, while the CGs of the trailing units are tracking the path of the leading unit front axle center. The DLULP scheme is based on the idea that to track the given trajectory, the steering angle of the front wheels of the leading vehicle unit is determined by minimizing the combined lateral position errors of the leading and trailing units based on the conventional lateral preview control concept, and the previewed lateral position for the leading unit with the related time delay is used as the previewed lateral position for the respective trailing unit. The following subsections

introduce the representation of the desired trajectory and vehicle state variables as well as the design of the unified driver model with the LUPT and DLULP schemes.

5.3.1 Desired Trajectory and Predicted Vehicle State Variables

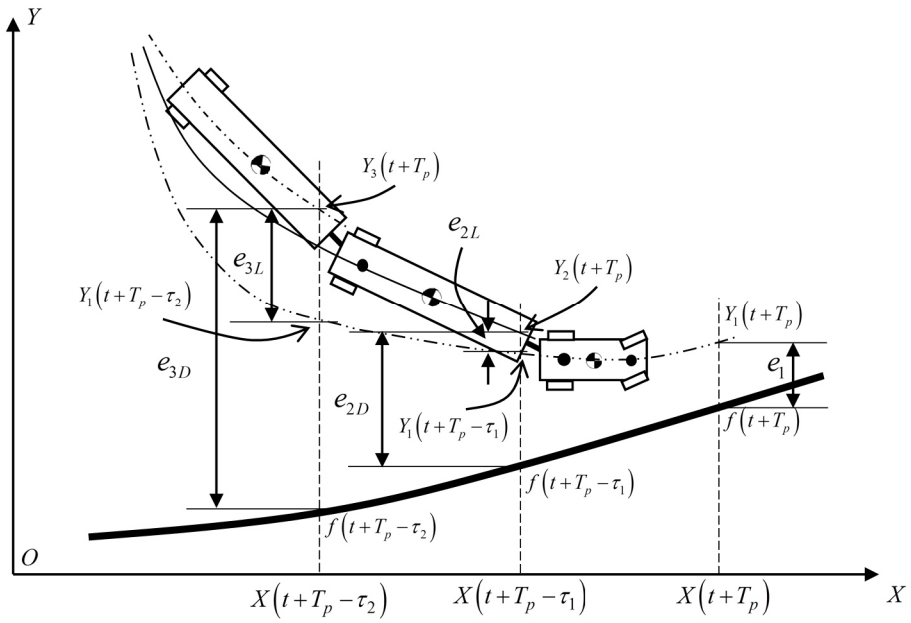

Figure 5.1 Geometry representation of the B-Train Double and desired trajectory

As shown in Figure 5.1, the solid line represents a given desired trajectory in the X-O-Y inertial coordinate system. The desired trajectory determines the relation between the X and Y coordinates of a point of interest on the trajectory. The data of the trajectory may be pre-saved in a lookup table, which is a single-input-single-output system. To determine a target point on the trajectory, the input of the lookup table is the reading of the horizontal coordinate, $X(t)$ and the output is the vertical coordinate, $Y(t)$. Note that for the point $(X(t),Y(t))$ on the trajectory, $Y(t)$ is represented as $f(t)$, which is treated as the previewed lateral position for the driver model. At time instant $t+T_p$, the horizontal coordinate of the tractor front axle center (TFAC) is determined as

$$X(t+T_p) = X(t) + \int_t^{t+T_p} (U - v_1\psi_1)dt \tag{5.4}$$

As seen in Figure 5.1, with the horizontal coordinate of $X\left(t+T_p\right)$, the vertical coordinate of the point on the desired trajectory is $f\left(t+T_p\right)$.

At time instant $t+T_p$, the output and state variables of the linear yaw-plane vehicle model can be predicted based on the state variables at time instant t, $\mathbf{x}_d(t)$, using direct numerical integration of the equation of motions expressed in Equation (5.2) (Ogata, 2010), assumed that the steering angle is constant in the time interval $\left(t,t+T_p\right)$. Note that T_P is the preview interval. The states at time instants $t+T_p$, $t+T_p-\tau_1$ and $t+T_p-\tau_2$ are predicted as

$$\begin{cases} \mathbf{x}_d(t+T_p)=\mathbf{\Phi}(t+T_p,t)\mathbf{x}_d(t)+\mathbf{K}(t+T_p,t)\delta_{11}(t) \\ \mathbf{x}_d(t+T_p-\tau_1)=\mathbf{\Phi}(t+T_p-\tau_1,t)\mathbf{x}_d(t)+\mathbf{K}(t+T_p-\tau_1,t)\delta_{11}(t) \\ \mathbf{x}_d(t+T_p-\tau_2)=\mathbf{\Phi}(t+T_p-\tau_2,t)\mathbf{x}_d(t)+\mathbf{K}(t+T_p-\tau 2,t)\delta_{11}(t) \end{cases} \tag{5.5}$$

where $\mathbf{\Phi}(\eta,\xi)=\mathbf{I}+\sum_{n=1}^{\infty}\frac{\mathbf{A}^n(\eta-\xi)^n}{n!}$ and $\mathbf{K}(\eta,\xi)=\left[\mathbf{I}+\sum_{n=1}^{\infty}\frac{\mathbf{A}^n(\eta-\xi)^n}{(n+1)!}\right]\mathbf{B}(\eta-\xi)$ denote the transition matrix and transition vector, respectively, and $\mathbf{I}$ is the identity matrix, τ_1 and τ_2 represent the time required for the CG of the 1st and the 2nd trailer to travel at the speed of U from their current positions to the corresponding location of the tractor front axle center. The time delays τ_1 and τ_2 can be approximately calculated as

$$\begin{cases} \tau_1=\dfrac{a_1+l_{c1}+l_{c21}}{U} \\ \tau_2=\dfrac{a_1+l_{c1}+l_{c21}+l_{c22}+l_{c3}}{U} \end{cases} \tag{5.6}$$

With Equation (5.5), based on the state variables $\mathbf{x}_d(t)$ and steering angle $\delta_{11}(t)$ at time instant t (determined by Equation (5.2)), the position of the TFAC at time instant $t+T_p$ can be predicted.

5.3.2 LUPT Driver Model

In the design of the driver model based on the LUPT scheme, it is assumed that at time instant of t, the predicted lateral positions of the tractor front axle center, the 1st trailer CG, and the 2nd trailer CG, i.e., $Y_1(t+T_p)$, $Y_2(t+T_p)$ and $Y_3(t+T_p)$ should follow the previewed lateral position for the tractor, the delayed lateral position of the TFAC for the 1st trailer CG, and the delayed lateral position of the TFAC for the 2nd trailer CG, i.e., $f(t+T_p)$, $Y_1(t+T_p-\tau_1)$ and $Y_1(t+T_p-\tau_2)$, respectively. If the lateral position tracking errors for the tractor front axle center, the 1st trailer CG, and the 2nd trailer CG are denoted as e_1, e_{2L} and e_{3L}, respectively, they can be specified as

$$\begin{cases} e_1 = Y_1(t+T_p) - f(t+T_p) \\ e_{2L} = Y_2(t+T_p) - Y_1(t+T_p-\tau_1) \\ e_{3L} = Y_3(t+T_p) - Y_1(t+T_p-\tau_2) \end{cases} \tag{5.7}$$

Considering the interrelation of individual lateral position tracking errors for the three vehicle units, we define a combined lateral position tracking error as

$$e = e_1 + k_1 e_{2L} + k_2 e_{2L} \tag{5.8}$$

where k_1 and k_2 are constants. The sliding surface S in the state space is defined as

$$S = \dot{e} + \kappa_L e \tag{5.9}$$

where κ_L is a positive constant, which is an important driver model parameter that governs the convergence rate of the sliding surface. In order to make the combined tracking error e and its derivative $\dot{e}$ vanish exponentially, the necessary condition is to steer the S variable to zero (Slotine, 1984), that is

$$\dot{e} + \kappa_L e = 0 \tag{5.10}$$

Combining Equations (5.2), (5.5), (5.7), (5.8) and (5.10), taking into account the features of matrix $\mathbf{B}$, i.e., all elements are zeros for rows 1, 5, and 9, and assuming that the steering angle is constant in the time interval $(t, t+T_p)$, lead to the steering angle as

$$\delta_{11}(t) = \frac{\dot{f}(t+T_p) + \kappa_L f(t+T_p) - \left[\mathbf{W}_1\mathbf{\Phi}(t+T_p,t) + \mathbf{W}_2\mathbf{\Phi}(t+T_p-\tau_1,t) + \mathbf{W}_3\mathbf{\Phi}(t+T_p-\tau_2,t)\right]\mathbf{x}(t)}{Den} \tag{5.11}$$

where $\mathbf{W}_1 = \mathbf{A}_d(1,:) + k_1\mathbf{A}_d(5,:) + k_2\mathbf{A}_d(9,:) + \kappa_L\mathbf{C}_d(1,:) + \kappa_L k_1\mathbf{C}_d(2,:) + \kappa_L k_2\mathbf{C}_d(3,:)$,

$\mathbf{W}_2 = -k_1\left[\mathbf{A}_d(1,:) + \kappa_L\mathbf{C}_d(1,:)\right]$, $\mathbf{W}_3 = -k_2\left[\mathbf{A}_d(1,:) + \kappa_L\mathbf{C}_d(1,:)\right]$,

$Den = \mathbf{W}_1\mathbf{K}\left(t+T_p,t\right) + \mathbf{W}_2\mathbf{K}\left(t+T_p-\tau_1,t\right) + \mathbf{W}_3\mathbf{K}\left(t+T_p-\tau_2,t\right)$. Note that $\mathbf{A}_d(i,:)$ and $\mathbf{C}_d(i,:)$ represent the i^{th} row of matrices $\mathbf{A}_d$ and $\mathbf{C}_d$, respectively.

Considering Equation (5.11) and the delay effect of human driver, we can describe the closed-loop system with the LUPT driver model and a vehicle model in terms of the block diagram shown in Figure 5.2. In the closed-loop system, the vehicle dynamics may be simulated with different vehicle models. In this research, the twenty-nine DOF nonlinear EoM yaw-roll model is used to mimic the dynamic of the B-Train Double. As seen in Figure 5.2, the LUPT driver model includes the following parameters: preview time T_p, time lag τ_d, control gain κ_L, and the constants k_1 and k_2.

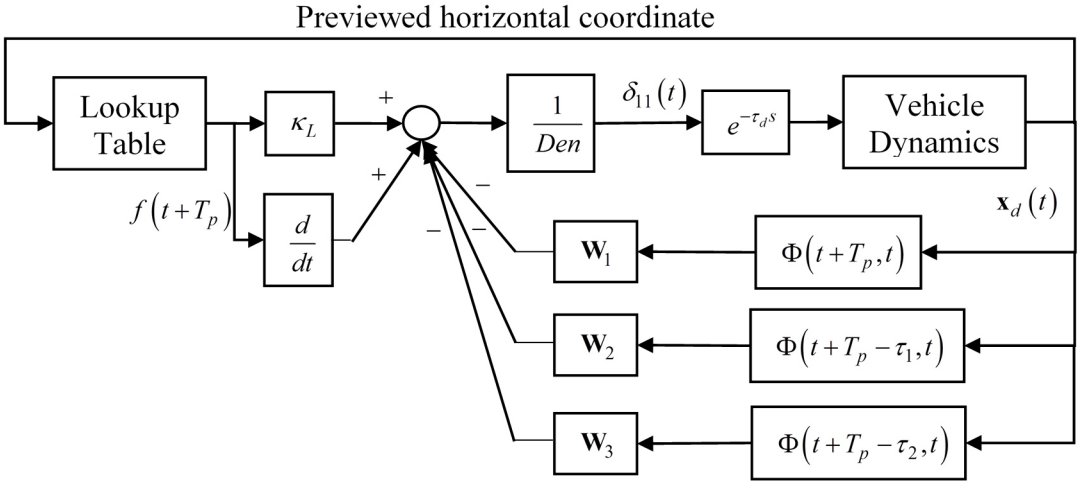

Figure 5.2 Block diagram of the closed-loop system with the LUPT driver and vehicle models

5.3.3 DLULP Driver Model

In the design of the driver model based on the DLULP scheme, it is assumed that at time instant of t, the predicted lateral positions of the tractor front axle center, the 1st trailer CG, and the 2nd trailer CG, i.e., $Y_1(t+T_p)$, $Y_2(t+T_p)$, and $Y_3(t+T_p)$, should follow the previewed lateral position for

the tractor front axle center, the delayed preview of the lateral position of the TFAC for the 1st trailer CG, and the delayed preview of the lateral position of the TFAC for the 2nd trailer CG, i.e., $f(t+T_p)$, $f(t+T_p-\tau_1)$, and $f(t+T_p-\tau_2)$, respectively. As seen in Figure 5.1, if the lateral position tracking errors for the tractor front axle center, the 1st trailer CG, and the 2nd trailer CG are denoted as e_1, e_{2D} and e_{3D}, respectively, they are specified as

$$\begin{cases} e_1 = Y_1(t+T_p) - f(t+T_p) \\ e_{2D} = Y_2(t+T_p) - f(t+T_p-\tau_1) \\ e_{3D} = Y_3(t+T_p) - f(t+T_p-\tau_2) \end{cases} \tag{5.12}$$

Considering the interrelation of individual lateral position tracking errors for the three vehicle units, we define a combined lateral position tracking error as

$$e = e_1 + k_1 e_{2D} + k_2 e_{3D} \tag{5.13}$$

where k_1 and k_2 are constants. The sliding surface S in the state space is defined as

$$S = \dot{e} + \kappa_D e \tag{5.14}$$

where κ_D is a positive constant, which is an important driver model parameter that governs the convergence rate of the sliding surface. In order to make the combined tracking error e and its derivative $\dot{e}$ vanish exponentially, the necessary condition is to steer the S variable to zero, that is

$$\dot{e} + \kappa_D e = 0 \tag{5.15}$$

Combining Equations (5.2), (5.5), (5.12), (5.13) and (5.15), taking into account the features of matrix $\mathbf{B}$, and assuming that the steering angle is constant in the time interval $(t, t+T_p)$, leads to the steering angle as

$$\delta_{11}(t) = \frac{\kappa_D\left[f(t+T_p)+k_1 f(t+T_p-\tau_1)+k_2 f(t+T_p-\tau_2)\right]+\dot{f}(t+T_p)+k_1\dot{f}(t+T_p-\tau_1)+k_2\dot{f}(t+T_p-\tau_2)-\mathbf{W}_1\boldsymbol{\Phi}(t+T_p,t)\mathbf{x}(t)}{\mathbf{W}_1\mathbf{K}(t+T_p,t)} \tag{5.16}$$

where $\mathbf{W}_1 = \mathbf{A}_d(1,:) + k_1\mathbf{A}_d(5,:) + k_2\mathbf{A}_d(9,:) + \kappa_D\mathbf{C}_d(1,:) + \kappa_D k_1\mathbf{C}_d(2,:) + \kappa_D k_2\mathbf{C}_d(3,:)$.

Considering Equation (5.16) and the delay effect of human driver, we can describe the closed-loop system with the DLULP driver model and a vehicle model in terms of the block diagram shown in Figure 5.3. In the closed-loop system, the vehicle dynamics may also be simulated with different vehicle models. In this research, the ten DOF nonlinear yaw-roll model is used to mimic the dynamics of the B-Train Double. As seen in Figure 5.3, the DLULP driver model includes the following parameters: preview time T_p, time lag τ_d, control gain κ_D, and the constants k_1 and k_2.

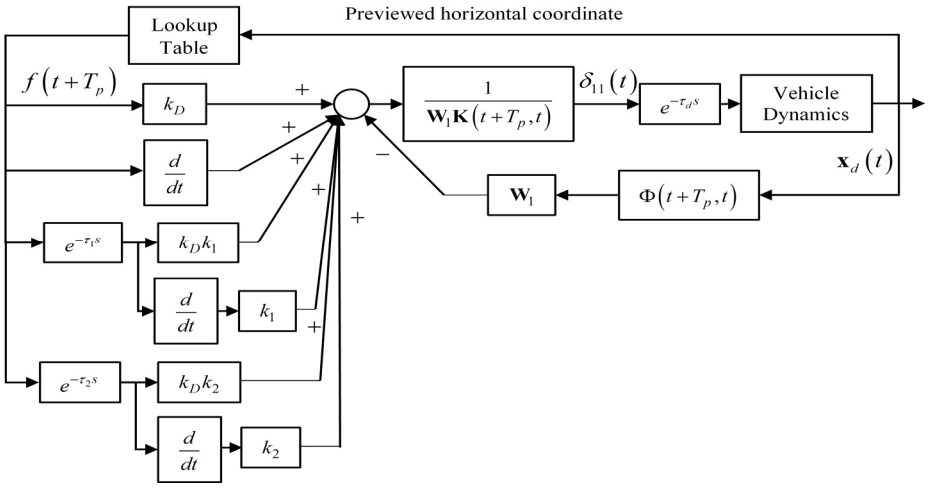

Figure 5.3 Block diagram of the closed-loop system with the DLULP driver and vehicle models

5.4 Driver Model Validation

To compare the proposed LUPT and DLULP driver models with that by MacAdam (MacAdam, 1980, MacAdam, 1981), we will examine and evaluate the closed-loop simulation results of the B-Train Double based on the twenty-nine DOF nonlinear EoM yaw-roll vehicle model and each of these driver models under a single lane-change (SLC) maneuver. The specified SLC trajectory similar to that reported in (MacAdam, 1981) is shown in Figure 5.4. Under the simulated SLC maneuver, the vehicle forward speed maintains constant at 88 km/h, and the corresponding driver model makes the TFAC follow the predefined trajectory (shown in Figure 5.4) as close as possible. The MacAdam driver model was designed considering only the lateral position tracking error of a

Single-Unit Vehicle or a leading vehicle unit of an articulated vehicle. In order to make the simulation results based on the MacAdam driver model comparable with those derived from the proposed driver models, the following prerequisites are made: 1) in the case of Single-Unit Vehicles (SUVs), Equation (5.1) represents a linear SUV model (e.g., bicycle model), and k_1 and k_2 in both Equations (5.11) and (5.16) should take the value of zero, since there exists no trailing vehicle unit in SUVs; 2) in the case of the B-Train Double, only the state variables of the tractor are available for all the driver models, and similarly k_1 and k_2 in both Equations (5.11) and (5.16) should take the value of zero, since no state variables of the trailing units are available for the LUPT and DLULP driver models. Note that for the second prerequisite aforementioned, with k_1 and k_2 taking the value of zero, the LUPT and DLULP driver models will reduce to a same simplified driver model, in which the tractor front-wheel steering angle is determined by the state variables of the tractor only. For the purpose of simplicity, we call the simplified driver model as TO (tractor only) driver model. In the following subsections, we will compare the TO and the MacAdam driver models. Then, the validated TO driver model will be served as a reference to assess the performance of the LUPT and DLULP driver models.

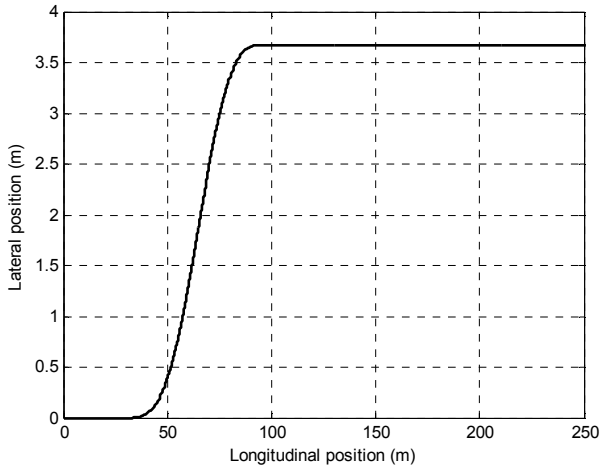

Figure 5.4 Specified trajectory of the SLC maneuver

5.4.1 Comparison of the TO and MacAdam Driver Models

5.4.1.1 Analytical Formulation of the TO Driver Model

For the purpose of simplicity, we will derive the analytical formulation of the TO driver model based on the LUPT driver model. As shown in Equation (5.11), with the second prerequisite aforementioned, the following conditions are true: $k_1 = 0$, $k_2 = 0$, $\mathbf{W}_1 = \mathbf{A}_d(1,:) + \kappa \mathbf{C}_d(1,:)$, $\mathbf{W}_2 = 0$ and $\mathbf{W}_3 = 0$. Subject to the above conditions, Equation (5.11) reduces to

$$\delta_{11}(t) = -\frac{\kappa_L \left(\mathbf{C}_d(1,:)\boldsymbol{\Phi}(t+T_p,t)\mathbf{x}_d(t) - f(t+T_p)\right)}{\left[\mathbf{A}_d(1,:) + \kappa_L \mathbf{C}_d(1,:)\right]\mathbf{K}(t+T_p,t)} - \frac{\left(\mathbf{A}_d(1,:)\boldsymbol{\Phi}(t+T_p,t)\mathbf{x}_d(t) - \dot{f}(t+T_p)\right)}{\left[\mathbf{A}_d(1,:) + \kappa_L \mathbf{C}_d(1,:)\right]\mathbf{K}(t+T_p,t)} \tag{5.17}$$

where the lateral position error and the lateral position error rate are

$$\begin{cases} e_1(t+T_p) = Y_1(t+T_p) - Y_{1d}(t+T_p) = \mathbf{C}_d(1,:)\boldsymbol{\Phi}(t+T_p)\mathbf{x}_d(t) - f(t+T_p) \\ \dot{e}_1(t+T_p) = \dot{Y}_1(t+T_p) - \dot{Y}_{1d}(t+T_p) = \mathbf{A}_d(1,:)\boldsymbol{\Phi}(t+T_p)\mathbf{x}_d(t) - \dot{f}(t+T_p) \end{cases} \tag{5.18}$$

where $Y_1(t+T_p)$ and $Y_{1d}(t+T_p)$ are the predicted and desired (or previewed) lateral positions of the TFAC at time instant $t+T_p$ as shown in Figure 5.1. Essentially, the TO driver model defined in Equation (5.17) is a proportional-derivative controller with the proportional and derivative gains given as

$$\begin{cases} K_p = -\kappa_L \Big/ \left[\mathbf{A}_d(1,:) + \kappa_L \mathbf{C}_d(1,:)\right]\mathbf{K}(t+T_p,t) \\ K_d = -1 \Big/ \left[\mathbf{A}_d(1,:) + \kappa_L \mathbf{C}_d(1,:)\right]\mathbf{K}(t+T_p,t) \end{cases} \tag{5.19}$$

Considering the first equation on Equation (5.3) and assuming that a desired particle is moving along the given trajectory shown in Figure 5.1 at the speed of U_1, we can rewrite the second equation of Equation (5.18) as

$$\dot{e}_1(t+T_p) = \dot{Y}_1(t+T_p) - \dot{Y}_{1d}(t+T_p) = \dot{Y}_1(t+T_p) - \dot{f}(t+T_p) = (v_1 + a_1\dot{\psi}_1) + U_1(\psi_1 - \psi_d) \tag{5.20}$$

where $v_1 + a_1\psi_1$ represents the lateral velocity of the tractor front axle center, ψ_1 the yaw angle of the tractor, and ψ_d is the angle swept from the X axis of the inertial coordinate shown in Figure 5.1 to the velocity of the desired particle, which reaches the point on the trajectory with the horizontal coordinate of $X(t+T_p)$. It is desired that the TFAC can behave as the desired particle, moving along the trajectory at the speed of U_1. Therefore, the term $\psi_1 - \psi_d$ can be treated as the tractor yaw angle error. It is expected that if the vehicle forward speed U_1 or U is large, the rate of change of the lateral position of the TFAC will be proportional to the tractor yaw angle error.

When the control gain κ_L approaches infinity, Equation (5.17) becomes

$$\delta_{11}\big|_{\kappa_L\to\infty}(t) = -\frac{\mathbf{C}_d(1,:)\mathbf{\Phi}(t+T_p,t)\mathbf{x}(t) - f(t+T_p)}{\mathbf{C}_d(1,:)\mathbf{K}(t+T_p,t)} \tag{5.21}$$

which is exactly the same as Equation (10) reported in (MacAdam, 1980). A comparison of Equations (5.17) and (5.21) indicates that with the above second prerequisite, the MacAdam model is a special case of the TO driver model, and the former only considers the lateral position error of the tractor front axle center, while the latter takes into account both the lateral position error and the tractor yaw angle error.

Similarly, with the aforementioned first prerequisite, in the case of SUVs, Equation (5.11) also reduces to Equation (5.17). With the first prerequisite and the control gain κ_L approaching infinity, Equation (5.17) will further reduces to Equation (5.21). This implies that in the case of SUVs, the MacAdam model is also a special case of the LUPT driver model. Note that with the first and second prerequisites, based on the LUPT driver model, the TO model and the MacAdam model are formulated. Similarly, with the first and second prerequisites, based on the DLULP driver model, the TO model and the MacAdam model can also be formulated.

In the case of Single-Unit Vehicles, the applications of the LUPT driver model have already been demonstrated via the closed-loop simulation results based on the driver model and an eight DOF model for a sport utility vehicle (Zhu and He, 2016). This paper focuses on examining the applicability and performance of the proposed LUPT and DLULP driver models for closed-loop simulations of Multi-Unit Vehicles.

5.4.1.2 Simulation Results based on the TO and MacAdam Driver Models

This subsection compares the TO and MacAdam driver models by means of examining the closed-loop simulation results of the B-Train Double under the SLC maneuver with the parameters of preview time (T_p), time lag (τ_d), and control gain (κ_L) taking the values of *1.0 s*, *0.1 s,* and *10*, respectively. Figure 5.5 shows the simulation result in terms of TFAC trajectory, time histories of lateral accelerations at the vehicle unit CGs, time histories of yaw rates of the vehicle units, and time history of tractor front-wheel steering angle.

Closed-loop simulation results shown in Figure 5.5 indicate that the TO and MacAdam driver models achieve an excellent agreement in the directional performance of the B-Train Double under the SLC maneuver. A close observation of Figure 5.5 reveals that compared with the result based on the MacAdam model, the TO driver model uses less steering effort (i.e., smaller peak steering angle of the tractor front-wheel) 'driving' the virtual B-Train Double to complete the SLC maneuver with approximately the same level of path-following off-tracking, but with less peak values of lateral acceleration and yaw rate of the vehicle units. The directional performance improvement is attributed to the tractor yaw angle tracking error control considered in the TO driver model. This observation is consistent with the finding reported in (Ungoren and Peng, 2005).

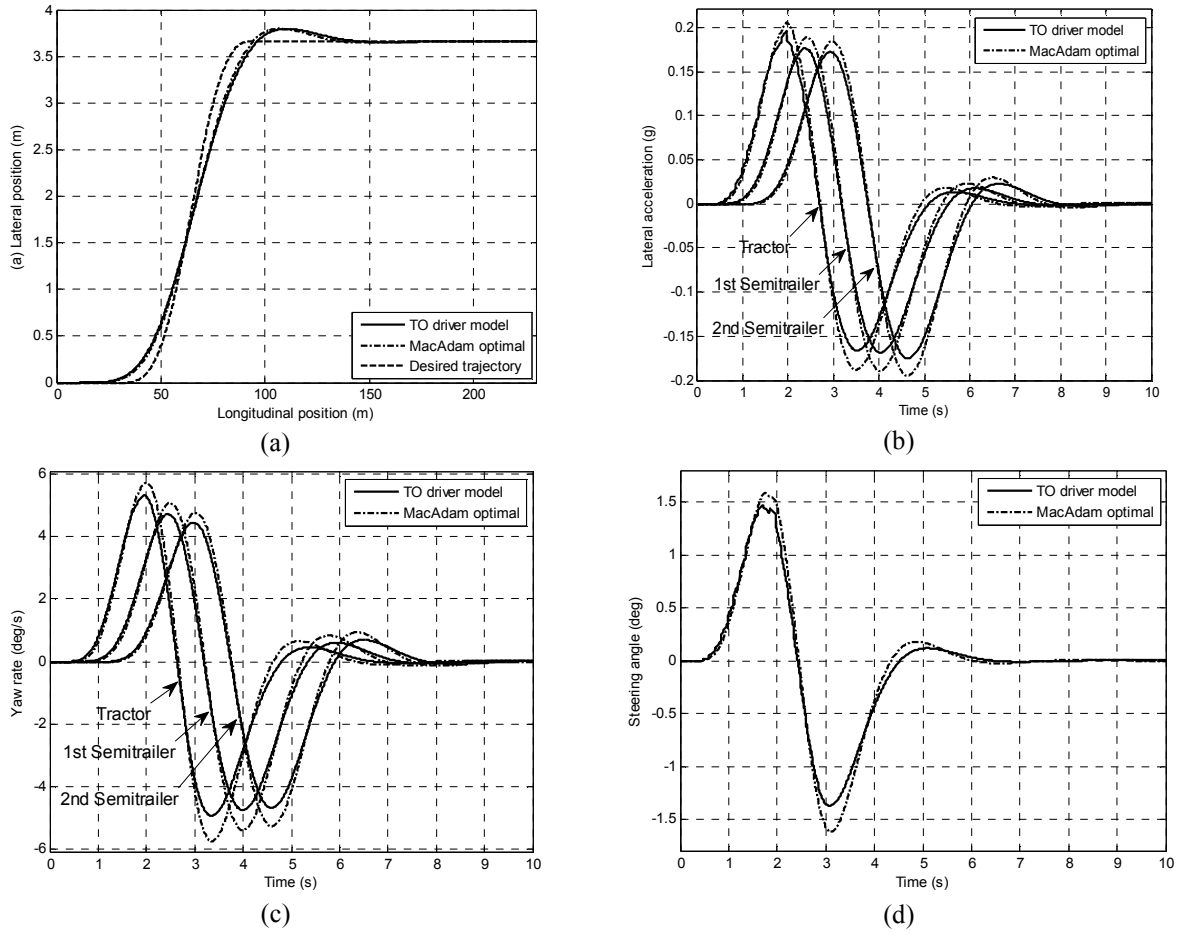

Figure 5.5 Simulation results of the B-Train Double based on the TO and MacAdam driver models under the SLC maneuver: (a) desired trajectory and TFAC path, (b) lateral accelerations at vehicle unit CGs, (c) yaw rates of vehicle units, and (d) tractor front-wheel steering angle

In practical operations of MTAHVs, various uncertainties, e.g., trailer payload variation, may arise. It is required that the driver adaptively drive the MTAHV under varied operating conditions. Thus, a reliable driver model should mimic this driving characteristic of a human driver. In this research, the robust driving performance of the TO driver model is evaluated in terms of the variation of trailer payloads and the change of trailer CG longitudinal positions. As listed in Appendix B, the uncertain masses and the CG longitudinal positions of the 1st and 2nd trailers are modeled as

$$\begin{cases} m_{2.u} = m_2(1 \pm p_{m_2}) \\ m_{3.u} = m_3(1 \pm p_{m_3}) \\ a_{2.u} = a_2(1 \pm p_{a_2}) \\ a_{3.u} = a_3(1 \pm p_{a_3}) \end{cases} \tag{5.22}$$

where $p_{m_2} = p_{m_3} = p_{a_2} = p_{a_3} = 50\%$. Note that the notation of the above parameters is provided in Appendix A. In the simulation, each of the four parameter in Equation (5.22) varies from its nominal value up to relative error of 50%.

To compare the driving performance robustnesses of the TO and MacAdam driver models, Figure 5.6(i) shows the corresponding time histories of lateral position of the TFAC for 100 randomly selected uncertain cases from the variation range defined above, and Figure 5.6(ii) illustrates the respective time histories of the standard deviations of the 100 uncertain cases. A comparison of the results based on the TO and MacAdam driver models indicates that the former exhibits more robust control of the B-Train Double under the SLC maneuver than the latter.

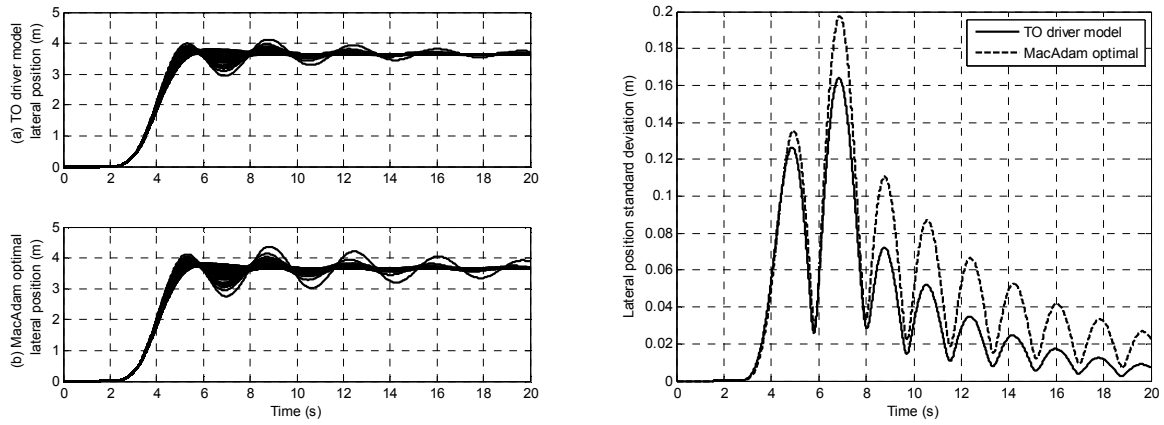

(i) (ii)

Figure 5.6 (i) Time histories of lateral position of the TFAC for 100 uncertain cases based on: (a) TO driver model, and (b) MacAdam driver model; (ii) time histories of the standard deviations of 100 uncertain cases based on the TO and MacAdam driver models

Considering the aforementioned second prerequisite and reviewing Figure 5.2, we deduce that three parameters, i.e. preview time (T_p), time lag (τ_d), and control gain (κ_L), may impose effects on the performance of the TO driver model. In the case of closed-loop simulation for SUVs, the effects

of the parameters of T_p and τ_d of the proposed driver model has been studied and reported in (Zhu and He, 2016). Simulation results indicate that the driver model parameters, T_p and τ_d, can be adjusted to manipulate the trade-off between path-following and stability of the vehicle (MacAdam, 2003, Ogata, 2010). In the rest of the subsection, the effect of κ_L is examined.

As shown in Equation (5.17), κ_L may be viewed as a weighting factor, which imposes a relative weight between the tractor lateral position tracking error control and the tractor yaw angle tracking error control. A larger κ_L assigns a heavier weight on the tractor lateral position tracking error control. It is expected that with the increase of the value of κ_L, the TO driver model becomes closer to that by MacAdam, and once κ_L approaches infinity, the two models will be identical. On the other hand, a smaller κ_L puts a heavier weight on the tractor yaw angle tracking error control. Figure 5.7 shows the simulation result for the tractor of the B-Train Double under the SLC maneuver with the parameter of κ_L for the TO driver model taking the values of *1.0, 10.0 and 100.0*. For the purpose of comparison, the corresponding simulation result based on the MacAdam driver model is also provided in Figure 5.7. Note that for the simulation results illustrated in Figure 5.7, the parameters of T_p and τ_d for the two driver models take the value of *1.0 s* and *0.1 s,* respectively.

As shown in Figure 5.7, with the decrease of the value of κ_L, the over-shoot of the trajectory of the TFAC becomes smaller, the peak values of the tractor yaw rate and lateral acceleration reduce, and the required driver steering effort drops. The simulation results illustrated in Figure 5.7 match the above expectation that with the increase of the value of κ_L, the TO driver model becomes closer to that by MacAdam, and once κ_L approaches infinity, the two models will be identical. Compared with the MacAdam driver model, the tractor yaw rate tracking error control

introduced in the TO driver model makes the directional control of the driver/vehicle combination more stable and more efficient. Numerical simulation results also indicate that with a given value of κ_L for the TO driver model, as the vehicle forward speed (U) increases, the effect of tractor yaw angle tracking error control becomes more obvious. This observation is consistent with the analytical analysis based on Equation (5.20).

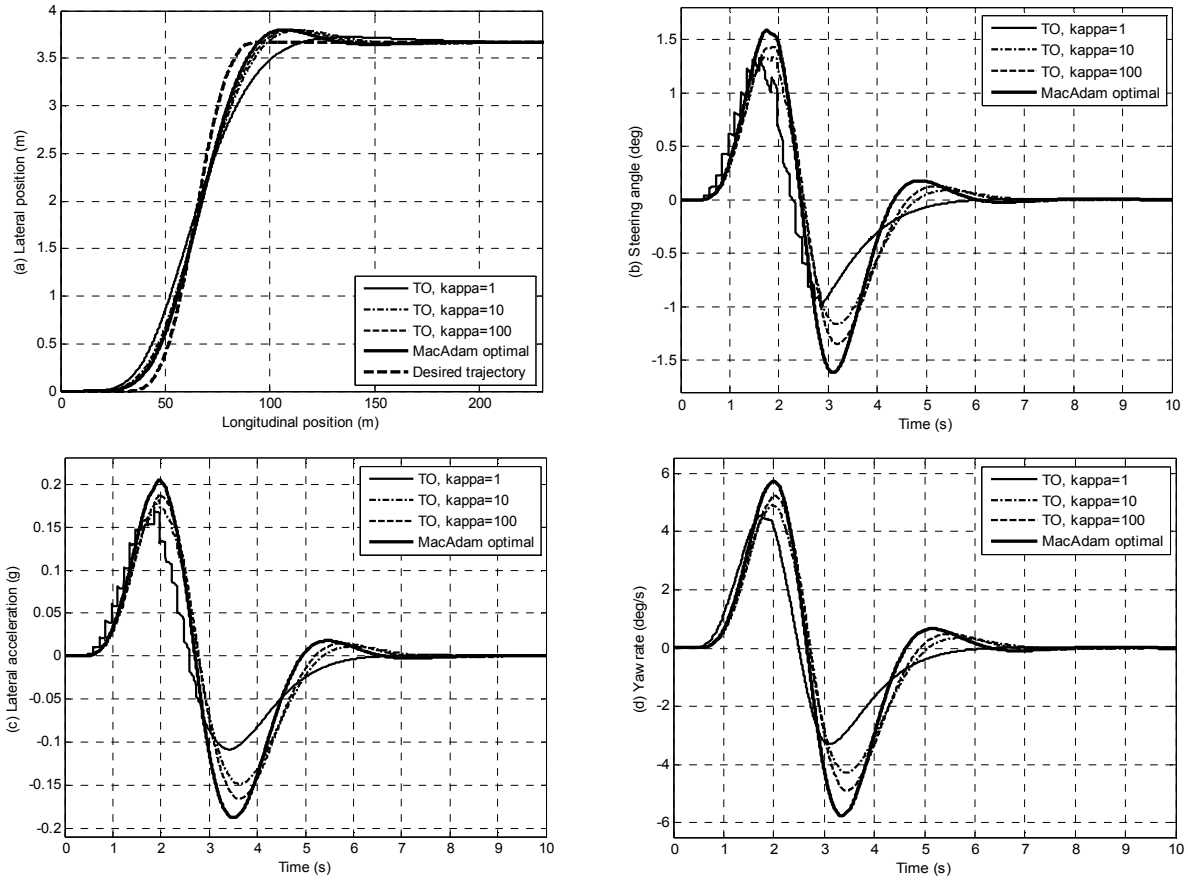

Figure 5.7 Dynamic responses of the tractor of the B-Train Double with the TO or MacAdam driver model under the SLC maneuver: (a) trajectory of the tractor front axle center, (b) time history of tractor front-wheel steering angle, (c) time history of lateral acceleration of the tractor CG, and (d) time history of tractor yaw rate

5.4.2 Comparison of the LUPT and DLULP Driver Models

In Section 5.4.1, the TO driver model is compared against the MacAdam driver model in both analytical and numerical analyses. In the following subsections, the TO driver model serves as a

baseline to evaluate the performance of the LUPT and DLULP driver models when the tracking errors of trailing unit(s) are considered.

5.4.2.1 Simulation Results based on the TO, LUPT and DLULP Driver Models

As shown in Equation (5.8) and (5.13) for the LUPT and DLULP driver model, respectively, the absolute values of k_1 and k_2 may be viewed as the weighting factor for the lateral position tracking error of the 1st and 2nd trailer, respectively. If the absolute value for both k_1 and k_2 is *1.0*, this implies that for either the LUPT or the DLULP driver model, the lateral position tracking errors for all vehicle units are treated equally in determining the tractor front-wheel steering angle. As introduced in Section 5.1, it may be difficult for a human driver to fully sense the trailer motions, as the driver's perception is based mainly on the leading unit response rather than the trailer(s). Articulation joint(s) and the tractor cab suspensions may isolate the human driver from trailing units' motions. Thus, it may be reasonable to impose a constraint on the assigned values for the parameters as $|k_1| < 1.0$ and $|k_2| < 1.0$. Closed-loop simulation based on the yaw-roll vehicle model of the B-Train Double and either the LUPT or the DLULP driver model indicates that to ensure acceptable directional performance of the vehicle, both k_1 and k_2 should take negative values. Note that for the purpose of simplicity, hereafter the TO, LUPT and DLULP driver models are called as TO, L and D mode of the SMC-based driver model, respectively.

Considering the aforementioned factors about the parameters of k_1 and k_2, we assume that for both the L and D modes, $k_1 = -0.6$ and $k_2 = -0.3$. With the above assigned values for k_1 and k_2 as well as $T_p = 1s$, $\tau_d = 0.1s$, and $\kappa_L = \kappa_D = 10$, either the L or the D mode can be combined with the yaw-roll model of the B-Train Double for closed-loop simulation under the SLC maneuver. Figure 5.8 shows the simulation results based on both the L and D modes. For the purpose of comparison, the simulation result based on the TO mode is also provided in the figure.

A close observation of Figure 5.8 discloses that compared the TO mode, the L mode makes the B-Train Double more stable with less steering effort under the SLC maneuver. In comparison with the TO mode, the D mode makes the B-Train Double achieve better path-following performance, especially, in terms of removing the trajectory overshoots of the vehicle units. For the purpose of comparing the TO, L and D modes, Table 5.1 lists performance measures of the B-Train Double with each of the driver modes under the simulated SLC maneuver. As shown in Table 5.1, among the three modes, the D mode achieves the lowest overshoot of the trajectory of each vehicle unit, while the L mode makes each vehicle unit have the smallest average peak lateral acceleration and yaw rate.

Table 5.1 Performance measures of the B-Train Double with the TO/DLULP/LUPT driver model under the SLC maneuver ($k_1 = -0.6, k_2 = -0.3, T_p = 1s, \tau_d = 0.1s, \kappa_L = \kappa_D = 10$)

		TO	DLULP	LUPT
Peak values	$(Y_{1max} - Y_d)$ (m)/overshoot	0.135	0.016	0.164
	$(Y_{2max} - Y_d)$ (m)/overshoot	0.182	0.016	0.204
	$(Y_{3max} - Y_d)$ (m)/overshoot	0.222	0.022	0.238
	$\bar{a}_{y1max}{}^{*}$ (g)	0.165	0.164	0.157
	$\bar{a}_{y2mas}{}^{*}$ (g)	0.158	0.155	0.151
	$\bar{a}_{y3max}{}^{*}$ (g)	0.160	0.155	0.152
	$\overline{\dot{\psi}}_{1max}{}^{*}$ (deg/s)	4.591	4.832	4.339
	$\overline{\dot{\psi}}_{2max}{}^{*}$ (deg/s)	4.292	4.337	4.067
	$\overline{\dot{\psi}}_{3max}{}^{*}$ (deg/s)	4.167	4.136	3.956
Steering angle time integration	$\int_0^t \lvert\delta_{11}(t)\rvert dt$ ** $(\deg \cdot s)$	2.997	2.779	2.893

*The average of the absolute upper and lower peak values of the curve of lateral acceleration or yaw rate of a vehicle unit, which may be used as a stability indicator for the B-Train Double.
**The total area enclosed by the tractor front-wheel steering angle curve (absolute value) and the time axis may be viewed as an indicator for driver steering effort (Wang and He, 2015).

Based on the simulation results shown in Figure 5.8 and Table 5.1, with respect to the TO mode, the L and D mode may be viewed as the stability- and path-following-oriented driver model, respectively. In the following subsection, these two modes are further examined.

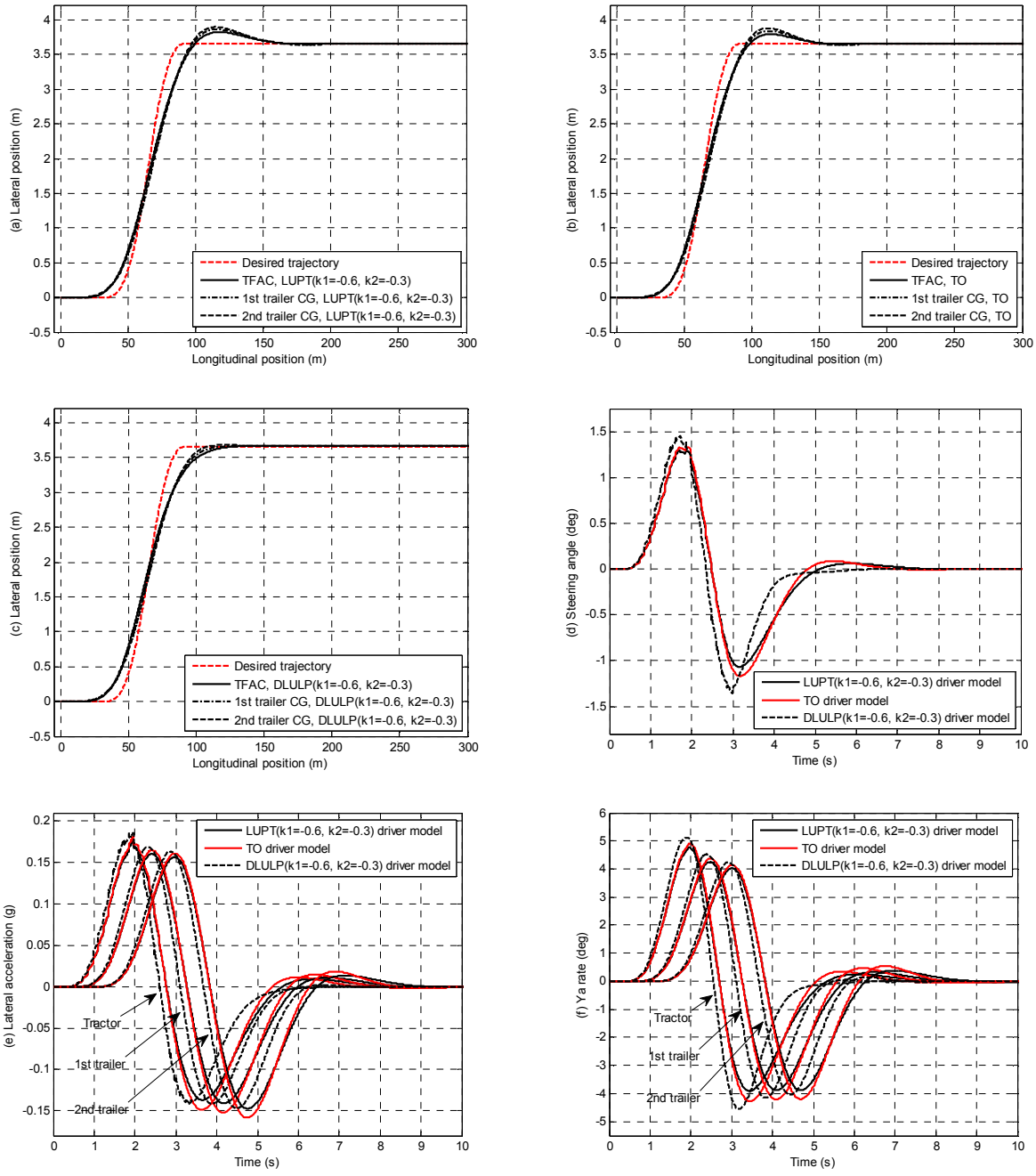

Figure 5.8 Dynamic responses of the virtual B-Train Double with the TO/DLULP/LUPT driver model under the SLC maneuver: (a) trajectory of the vehicle units, LUPT, (b) trajectory of the vehicle units, TO, (c) trajectory of the vehicle units, DLULP, (d) time history of tractor front-wheel steering angle, (e) time histories of lateral acceleration at vehicle unit CGs, and (f) time histories of yaw rate of vehicle units

5.4.2.2 Performance Analysis for the D and L Modes

As shown in Equation (5.7) and (5.12), the main difference between the D and L mode is that the target lateral positions of the trailing units for the D mode are the delayed lateral positions of the desired trajectory, while the target lateral positions of the trailing units for the L mode are the delayed lateral positions of the leading unit. For a closed-loop vehicle directional performance test under a SLC maneuver, the optimal case is that the vehicle unit(s) is viewed as a massless particle moving along the predefined trajectory at a given constant speed (Wang and He, 2016). With the optimal case in mind, for the D mode, the leading unit tracks the motion of the particle, and the trailing units the delayed motions of the particle; similarly, for the L mode, the leading unit tracks the motion of the particle, and the trailing units the delayed motions of the leading unit.

Figure 5.9 shows the time histories of vehicle unit lateral positions and tracking errors of the B-Train Double with either the D or L mode under the SLC maneuver. In the case of the D mode, disregarding the time delays, the time histories of the lateral position tracking error of the three vehicle units show minor differences, as seen in Figure 5.9(b), 5.9(d) and 5.9(f). Accordingly, as shown in Figure 5.9(a), 5.9(c) and 5.9(e), the time histories of the lateral position of the vehicle units have no overshoot and they look the same except for the time delays. In the case of the L mode, the lateral position tracking errors for the trailing units are smaller (compared against the counterparts for the D mode, as shown in Figure 5.9(d) and 5.9(e)). These smaller tracking errors are relative to the respectively delayed lateral position of the tractor, which shows the same level of tracking error as its counterpart for the D mode, as illustrated in Figure 5.9(b). As shown in Figure 5.9(a), 5.9(c) and 5.9(e), in the case of the L mode, the time history of the lateral position of the tractor shows an overshoot, and those of the 1st and 2nd trailers exhibit even larger overshoots

compared against the respectively delayed lateral position of the tractor. Thus, between the D and L modes, the former may achieve better path-following performance.

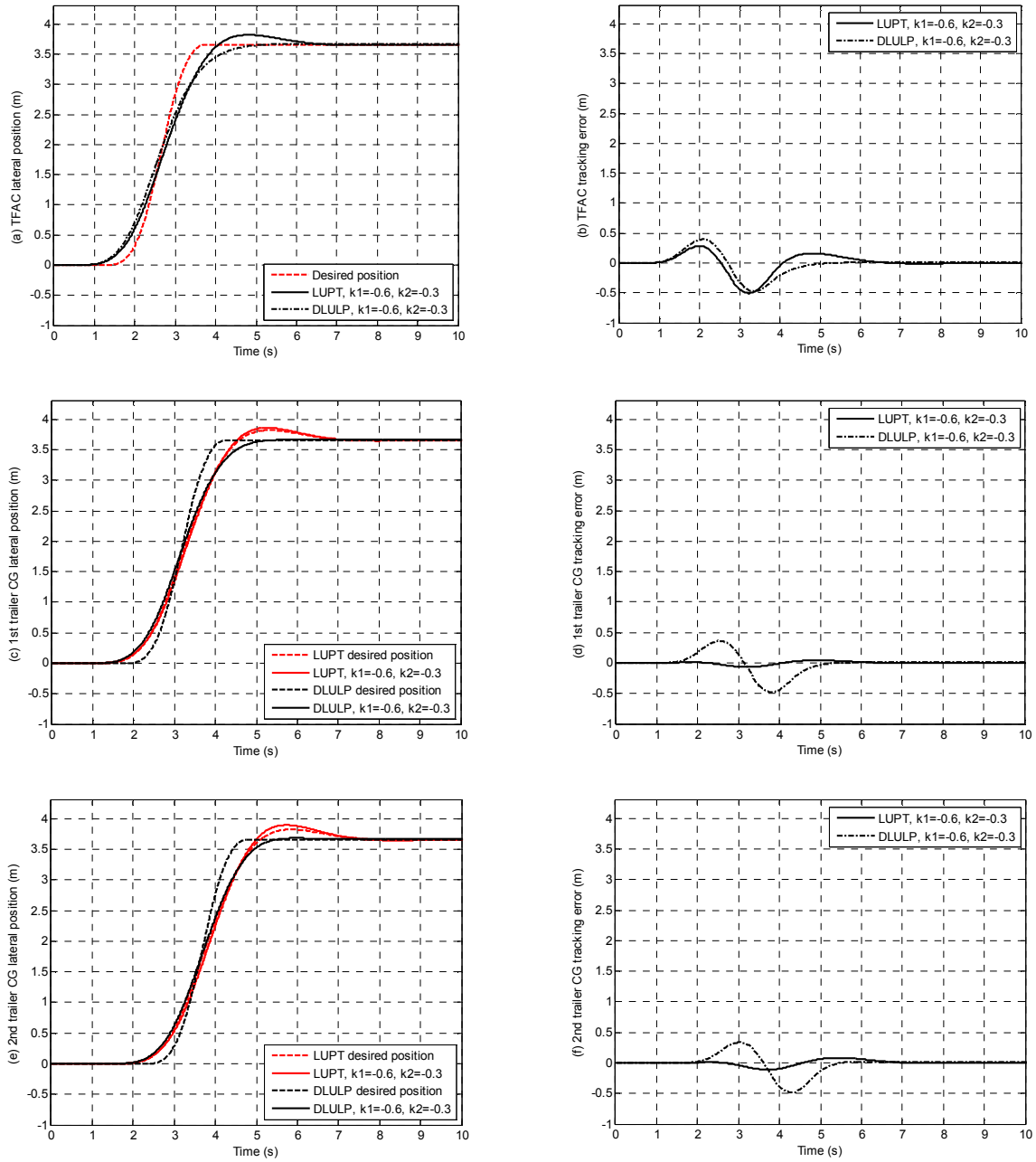

Figure 5.9 Time histories of vehicle unit lateral positions and tracking errors of the B-Train Double with either the D or L mode under the SLC maneuver: (a) TFAC lateral position, (b) TFAC lateral position tracking error, (c) 1st trailer CG lateral position, (d) 1st trailer CG lateral position tracking error, (e) 2nd trailer CG lateral position, and (f) 2nd trailer CG lateral position tracking error

Figure 5.10 shows the time histories of vehicle unit yaw rates and lateral position rate tracking errors of the B-Train Double with either the D or L mode under the SLC maneuver. As shown in Equation (5.20), if the second term on the right-hand side of the equation is dominant, the lateral position rate of the TFAC is proportional to the yaw angle tracking error, i.e., the angle made between the tractor heading and the tangent line at the target point on the desired trajectory. Considering the aforementioned optimal case of a closed-loop vehicle directional performance test under a SLC maneuver, in the case of the D mode, we make the moving directions of the leading and trailing units align with those of the moving particle and delayed moving particles on the desired trajectory. Similarly, in the case of the L mode, the moving direction of the tractor is required to track that of the moving particle on the desired trajectory, while the moving directions of the trailers follow those with respective time delays of the tractor. Compared with the L mode, the steering control of the D mode is more aggressive. As shown in Figure 5.10(b), 5.10(d) and 5.10(f), the time histories of the tractor lateral position rate tracking errors for the D and L modes are close, while tracking errors of the trailers for the D mode are much larger than those for the L mode. The simulation results in vehicle unit position tracking errors are consistent with the above steering control scheme analysis for the two modes. As shown in Figure 5.10(a), 5.10(c) and 5.10(f), compared with the D mode, the conservative steering control of the L mode make the B-Train Double more stable with less peak yaw rate values. Numerical experiments conducted in the research further indicate that to ensure the stability and convergence of the steering control, the maximum absolute values of k_1 and k_2 of the D mode should be constrained below 0.7 for the closed-loop simulation for the B-Train Double, whereas for the L mode, the maximum absolute values of the two parameters may be as high as 1.0.

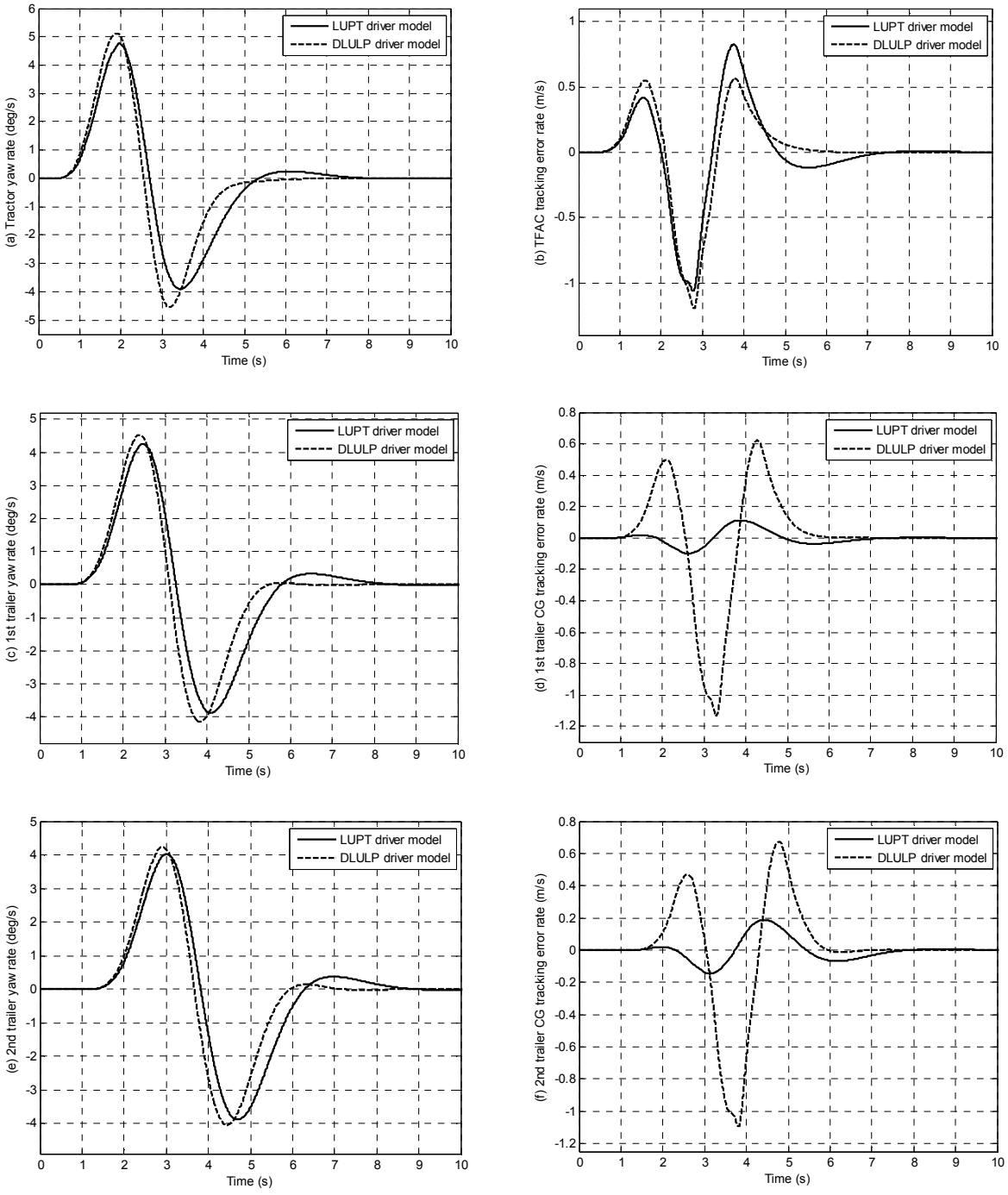

Figure 5.10 Time histories of vehicle unit yaw rates and lateral position rate tracking errors of the B-Train Double with either the D or L mode under the SLC maneuver: (a) tractor yaw rate, (b) TFAC lateral position rate tracking error, (c) 1st trailer yaw rate, (d) 1st trailer CG lateral position rate tracking error, (e) 2nd trailer yaw rate, and (f) 2nd trailer CG lateral position rate tracking error

5.4.2.3 Effects of Trailing Unit Motion Controls on the L Mode Performance

To examine the impact of trailing unit tracking error controls on the SMC-based driver model performance, we take the L mode as an example to conduct numerical analysis. To this end, Table 5.2 defines four cases with different value combination of k_1 and k_2, while other model parameters take the following values: $T_p = 1s, \tau_d = 0.1s$, and $\kappa_L = 10$. In the case of L0 defined in Table 5.2, both k_1 and k_2 take the value of 0.0, and only the tractor tracking errors are considered in determining the TFAC steering angle. Thus, the L0 case corresponds to the TO mode. In the cases of L1, L2 and L3, we consider the tracking errors of both the tractor and 1st trailer, both the tractor and 2nd trailer, and all the vehicle units, respectively. Note that the values of the model parameters are offered in Table 5.2. With the given set of parameter value shown in Table 5.2, the case of L3 is the same as the L mode studied in Subsections 5.4.2.1 and 5.4.2.2. In order to conduct benchmark investigation of the above cases, we conduct closed-loop simulation of the yaw-roll model of the B-Train Double with each of the above mode cases under the SLC maneuver.

For the purpose of the benchmark investigation, we define the L0 case or the TO mode as the baseline case. Table 5.3 lists the relative errors of the case concerned with respect to the L0 case in terms of the average peak values of lateral acceleration at the tractor CG, 1st trailer CG and 2nd trailer CG, the average peak values of yaw rate of the tractor, 1st trailer CG and 2nd trailer CG, as well as the time integration of the tractor front-wheel steering angle. As shown in Table 5.3, in the case of L3, the average peak value of lateral acceleration and yaw rate of each vehicle unit of the B-Train Double may be reduced by approximately 5% and with 3.4% less steering effort with respect to the baseline values. A close observation of the results shown in Table 5.3 discloses the following findings: 1) introducing the lateral position and yaw angle tracking errors of individual trailer contributes to the stability improvement of the B-Train Double with less steering effort; and

2) introducing the lateral position and yaw angle tracking errors of both trailer units further enhances the stability of the MTAHV with even less steering effort.

Table 5.2 Definition of the cases for the L mode with different vehicle unit tracking error controls ($T_p = 1s, \tau_d = 0.1s, and\ \kappa_L = 10$)

	L0	L1	L2	L3
Parameters	$k_1 = 0, k_2 = 0$	$k_1 = -0.6, k_2 = 0$	$k_1 = 0, k_2 = -0.3$	$k_1 = -0.6, k_2 = -0.3$

Table 5.3 Effects of trailing unit tracking error controls on the L mode performance

	$a_{y1}{}^{*}$	$a_{y2}{}^{*}$	$a_{y3}{}^{*}$	$\dot{\psi}_1{}^{*}$	$\dot{\psi}_2{}^{*}$	$\dot{\psi}_3{}^{*}$	$\delta_{11}{}^{**}$
L1	2.63%	2.56%	2.44%	3.28%	2.89%	2.69%	1.20%
L2	2.52%	2.56%	2.51%	2.28%	2.46%	2.49%	2.65%
L3	4.85%	4.43%	5.00%	5.49%	5.24%	5.06%	3.40%

*The relative error is defined as the ratio of the difference between the average peak values of the L0 case and the given case to the average peak value of the L0 case.

**The relative error is defined as the ratio of the difference between the steering angle (absolute value) time integrations of the L0 case and the given case to the steering angle (absolute value) time integration of the L0 case.

5.5 Conclusions

This chapter proposes a unified lateral preview driver model for closed-loop dynamic simulation of road vehicles. In order to design the proposed driver model, a four DOF yaw-plane model for a B-Train Double is applied. The driver model is derived using a sliding mode control technique. To examine the SMC-based driver model, it is integrated with a ten DOF yaw-roll model of the B-Train Double for closed-loop simulation under a single lane-change maneuver.

The SMC-based driver model is validated with the MacAdam optimal preview driver model via both analytical formulation analysis and numerical simulation. Compared with the MacAdam driver model, the proposed one is more flexible to mimic driving performance of a driver under varied operating conditions, e.g., varied vehicle payload, and to simulate a wider range of driver's driving skills by manipulating the relative weight between lateral position and yaw tracking error controls. The SMC-based driver model considers the dynamics features of both Single-Unit

Vehicles and Multi-Unit Vehicles, and thus can be applied to closed-loop simulations of both types of vehicle by selecting appropriate parameter values of the driver model. Given the unique dynamic characteristics of MTAHVs, the SMC-based driver model is designed with two modes, namely, stability- and path-following-oriented. The stability- and path-following-oriented mode may be used to simulate MTAHV drivers' driving performance under a high-speed evasive and a low-speed path-following maneuver, respectively. Tunable parameters are specified to assign relative weights to the lateral and yaw errors of the leading and trailing units, which differentiate the perceived motions states of the leading and trailing units. Introducing trailing units' lateral position and yaw tracking error controls into the proposed driver model contributes to the directional performance improvement of MTAHVs. Numerical simulation demonstrates the applicability and effectiveness of the proposed driver model.

The parameters of the SMC-based driver model are tuned using the trial and error method. Optimization algorithms will be applied to facilitate the finely tuning of the model parameters. The sliding surface design and the stability and convergence of the proposed driver model will be further improved and explored.

Chapter 6 Coordinated Control of Active Safety Systems for Multi-trailer Articulated Heavy Vehicles

6.1 Introduction

The past decade has witnessed the coordinated control in single unit vehicle dynamics. He et al (2006) proposed an integrated control strategy to improve handling and stability, considering active front steering (AFS), and vehicle stability control (VSC). The AFS controller was designed to improve the steerability under low to medium range lateral acceleration operation; and the VSC controller was formulated on the driveline or braking to stabilize the vehicle under high lateral acceleration operation. The AFS and VSC were coordinated using a rule-based integration scheme. Wang and Longoria (2006) investigated a hierarchical coordination of generalized force/moment actuation. A high level controller is formulated to calculate the virtual force. A weighted pseudo-inverse allocation algorithm distributed the virtual force to longitudinal and lateral slips. Tavasoli and Naraghi (2013) presented an integrated VSC scheme in a multistage design approach. A high level controller integrated the steering and braking controllers using the phase-plane method. The control objectives were allocated to steering and braking through solving a minimization problem. Alberding et al (2014) solved a rollover prevention using control allocation by treating the rollover prevention as a constraint in a yaw stabilising differential braking controller. The constraint eliminated the need for a stabilising roll controller and reserved the control authority to the yaw stabilising controller. Binder and Khajepour (2014) coordinated the roll, pitch and vertical dynamics using active and semi-active suspensions. The high level controller calculated the generalized vertical force, pitch and roll moments, each with a nonlinear controller for a single

dynamics. The generalized force/moments were allocated to suspensions using the quadratic programming.

The aforementioned coordinated control systems were designed for single unit vehicles. To the best knowledge of the author, there is no allocation-based coordinated control scheme for MTAHVs yet. In the allocation-based coordinated control framework, a single unit vehicle is commonly modeled with a chassis model and a tire model (Binder and Khajepour, 2014 and Schofield et al, 2006). The chassis model describes the vehicle dynamics and the tire model defines the tire force generation through the tire-road contact patch. The generalized (virtual) force/moment enters the chassis model in a decoupled manner, i.e., each force/moment only affects specific dynamics of the vehicle. A high level controller consists of several controllers, designed for individual dynamics, each described as a single-input-single-output (SISO) system. The generalized forces/moments are distributed to the actuators/effectors using an allocator. The entire process can be conducted in a hierarchical, multilevel, and modular approach. The aforementioned works, in addition to the incorporation of vehicle dynamics control and rollover mitigation (Schofield and Hagglund, 2008), and the control allocation for actuator coordination in heavy vehicles (Tagesson et al, 2009) fall into this category.

Multi-trailer articulated heavy vehicles (MTAHVs) demonstrate poor high-speed stability, which may induce trailer swing, jackknifing and roll-over. Low maneuverability may cause high-speed off-tracking. The stability or maneuverability of a MTAHV may be improved by using ASSs, such as ATS, TDB, and ARC.

Improving the stability or maneuverability of a B-train double using the linear quadratic regulator (LQR) based ASSs has been investigated extensively (Islam, 2013 and He et al, 2016). Unfortunately, their work hasn't adequately addressed the applicability, contribution and

coordination of individual ASSs. In fact, there is no ASS capable of solving all problems of MTAHVs; and the ATS, TDB and ARC may have to coexist. Simple combination of ASSs without coordination may cause interference and degrade overall performance of the MTAHV. The interferences among ASSs could be a safety critical issue (Alberding et al, 2014)

In this research, the coordination of ATS, TDB, and ARC for MTAHVs is considered. A MTAHV has multiple units. The method of coordinated control for single unit vehicles cannot be directly applied to the MTAHVs due to: 1) the MTAHV model is more complex with more generalized forces/moments, 2) the generalized forces/moments enter the model in a coupled manner, 3) one generalized force/moment affects more than one aspect of MTAHV dynamics, and 4) the SISO control systems designed for single unit vehicles are not applicable on the MTAHVs. This research conducts the coordinated control of ASSs for MTAHVs in three modules: 1) the control module; 2) the allocation module; and 3) the realization module. The control module is a direct yaw/roll moment LQR controller. The moment controller is built on a simplified MTAHV model, taking inputs of yaw/roll moments of the vehicle units. The generalized lateral force is made zero, and the longitudinal dynamics is considered exclusively with a longitudinal driver model. The control module is optimized to achieve an optimal trade-off of high-speed maneuverability, lateral, and roll stability.

The allocation module is a task scheduler which allocates the direct moments to individual effectors/actuators, i.e., the roll moment to the ARC actuator and the yaw moment to the ATS and TDB actuators. A side-slip angle based allocation algorithm is developed for the yaw moment allocation in a way that the capability of the ATS is consumed up to its linear limit, before utilizing the TDB. The TDB is restricted to extreme operating conditions in order to minimize its adverse impact on the longitudinal dynamics.

The realization module contains the ARC, ATS and TDB actuators. The ARC realizes the roll moment, and the ATS and TDB share the yaw moment in a way that the ASSs generate pure moments with zero lateral and vertical forces.

6.2 Coordinated Control Design

The coordinated controller of the ASSs of the MTAHV is formulated in three modules: the control module, the allocation module, and the realization module. The individual modules are designed independently, i.e., modification of one without affecting others.

6.2.1 Control Module

The control module is designed using the linear yaw-roll model in Equation (3.25) in Chapter 3, removing the 'disturbance', rewritten as

$$\dot{\mathbf{x}} = \mathbf{A}\mathbf{x} + \mathbf{B}\mathbf{u},\ \mathbf{y} = \mathbf{C}\mathbf{x} + \mathbf{D}\mathbf{u} \tag{6.1}$$

where $\mathbf{u} = \begin{bmatrix} M_{z2} & M_{z3} & M_{x1f} & M_{x1r} & M_{x2} & M_{x3} \end{bmatrix}^T$, $\mathbf{x} = \begin{bmatrix} \mathbf{x}_1 & \mathbf{x}_2 & \mathbf{x}_3 & \mathbf{x}_t \end{bmatrix}^T$ with $\mathbf{x}_1 = \begin{bmatrix} \phi_1 & \dot{\phi}_1 & \beta_1 & \dot{\psi}_1 \end{bmatrix}$, $\mathbf{x}_2 = \begin{bmatrix} \phi_2 & \dot{\phi}_2 & \beta_2 & \dot{\psi}_2 \end{bmatrix}$, $\mathbf{x}_3 = \begin{bmatrix} \phi_3 & \dot{\phi}_3 & \beta_3 & \dot{\psi}_3 \end{bmatrix}$, $\mathbf{x}_t = \begin{bmatrix} \phi_{t1} & \dot{\phi}_{t1} & \phi_{t2} & \dot{\phi}_{t2} & \phi_{t3} & \dot{\phi}_{t3} \end{bmatrix}$, and $\mathbf{y} = \begin{bmatrix} a_{y1} & a_{y2} & a_{y3} & \phi_1 & \phi_{t1} & \phi_2 & \phi_{t2} & \phi_3 & \phi_{t3} \end{bmatrix}^T$. The linear quadratic regulator technique (LQR) (Ogata, 2010) is used to stabilize the yaw and roll dynamics for desired performance. A performance index is formulated as

$$J = \int_0^\infty (\mathbf{y}^T \mathbf{Q} \mathbf{y} + \mathbf{u}^T \mathbf{R} \mathbf{u}) dt \tag{6.2}$$

where $\mathbf{Q} = diag\left(\begin{bmatrix} q_1 & q_2 & q_3 & q_4 & q_5 & q_6 & q_7 & q_8 & q_9 \end{bmatrix}\right)$ and $\mathbf{R} = diag\left(\begin{bmatrix} r_1 & r_2 & r_3 & r_4 & r_5 & r_6 \end{bmatrix}\right)$ are positive-definite symmetric matrices, intended to weight the lateral accelerations of the vehicle units, roll angles of the sprung and unsprung masses, and the direct moment control commands. With the control law $\mathbf{u} = -\mathbf{K}\mathbf{x}$, Equation (6.2) is written as

$$J = \int_0^\infty \left[\mathbf{x}^T \left(\mathbf{C}^T \mathbf{Q} \mathbf{C} + \mathbf{K}^T \mathbf{D}^T \mathbf{Q} \mathbf{D} \mathbf{K} + \mathbf{K}^T \mathbf{R} \mathbf{K} + 2\mathbf{C}^T \mathbf{Q} \mathbf{D} \mathbf{K} \right) \mathbf{x} \right] dt \tag{6.3}$$

The feedback gain matrix $\mathbf{K}$ can be obtained by minimizing the performance index $\mathbf{J}$ with respect to $\mathbf{K}$ by solving a minimization problem with the aid of Matlab software. The design parameters of the control module consist of the weighting factors as

$$P_r = [q_1 \quad q_2 \quad q_3 \quad q_4 \quad q_5 \quad q_6 \quad q_7 \quad q_8 \quad q_9 \quad r_1 \quad r_2 \quad r_3 \quad r_4 \quad r_5 \quad r_6] \tag{6.4}$$

6.2.2 Allocation Module

The allocation module distributes the direct moments to individual actuators. Specifically, the allocation module distributes the roll moments to the ARC actuators, the yaw moments to the ATS and TDB actuators. The capability of the ATS is first consumed up to its linear limit, before applying the TDB to restrain its adverse effect on the longitudinal dynamics. The yaw moments are allocated as follows.

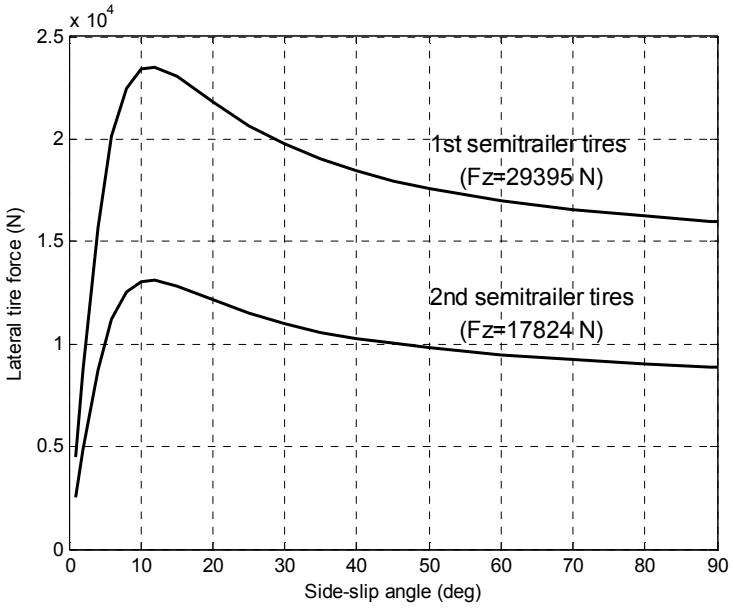

Figure 6.1 Trailer lateral tire forces with respect to corresponding side-slip angles
(The normal load of the each dual-tire of the 1st and 2nd semitrailer is 29395N and 17824 N, respectively)

The linear range side-slip angle thresholds are obtained from the 'experimental' data. Figure 6.1 shows the trailer lateral tire forces (dual tires are treated as single tires) with respect to the side-slip angle, assuming equal normal loads distribution in a tridem group. Within 0-10 deg side-slip angle range, the tires demonstrate approximately linear characteristics. Considering the load transfers, a safety margin of 20% is given, and an 8 deg or 0.14 rad is chosen as the side-slip angle threshold, i.e.,

$$\alpha_{4.thr} = \alpha_{6.thr} = \alpha_{7.thr} = \alpha_{9.thr} = 0.14\ rad \tag{6.5}$$

Table 6.1 Yaw moment allocation using nonlinear programming

Initialize:

$\delta_4(0)=0$, $\delta_6(0)=0$, $\delta_7(0)=0$, $\delta_9(0)=0$

Compute:

For $k=1,2,\cdots$, $\alpha_{40}(k)=\frac{b_{24}}{U}\dot{\psi}_2(k)-\beta_2(k)$, $\alpha_{60}(k)=\frac{b_{26}}{U}\dot{\psi}_2(k)-\beta_2(k)$, $\alpha_{70}(k)=\frac{b_{37}}{U}\dot{\psi}_3(k)-\beta_3(k)$,

$\alpha_{90}(k)=\frac{b_{39}}{U}\dot{\psi}_3(k)-\beta_3(k)$, $\delta_4(k)=-\frac{M_{z2}(k)}{4C_4 d_x\cos\delta_4(k-1)}$, $\delta_6(k)=\frac{M_{z2}(k)}{4C_6 d_x\cos\delta_6(k-1)}$,

$\delta_7(k)=-\frac{M_{z3}(k)}{4C_7 d_x\cos\delta_7(k-1)}$, $\delta_9(k)=\frac{M_{z3}(k)}{4C_9 d_x\cos\delta_9(k-1)}$, $\alpha_4(k)=\delta_4(k)+\alpha_{40}(k)$,

$\alpha_6(k)=\delta_6(k)+\alpha_{60}(k)$, $\alpha_7(k)=\delta_7(k)+\alpha_{70}(k)$, $\alpha_9(k)=\delta_9(k)+\alpha_{90}(k)$

Update:

$$\delta_4(k)=\begin{cases}\delta_4(k)+\left[-\alpha_{4.thr}-\alpha_4(k)\right] for\ \alpha_4(k)<-\alpha_{4.thr}\\ \delta_4(k)-\left[\alpha_4(k)-\alpha_{4.thr}\right] for\ \alpha_4(k)>\alpha_{4.thr}\end{cases},\quad \delta_6(k)=\begin{cases}\delta_6(k)+\left[-\alpha_{6.thr}-\alpha_6(k)\right] for\ \alpha_6(k)<-\alpha_{6.thr}\\ \delta_6(k)-\left[\alpha_6(k)-\alpha_{6.thr}\right] for\ \alpha_6(k)>\alpha_{6.thr}\end{cases}$$

$M_{z2.ATS}(k)=2\delta_4(k)C_4 d_x\cos\left[\delta_4(k-1)\right]-2\delta_6(k)C_6 d_x\cos\left[\delta_6(k-1)\right]$, $M_{z2.TDB}(k)=M_{z2}(k)-M_{z2.ATS}(k)$,

$$\delta_7(k)=\begin{cases}\delta_7(k)+\left[-\alpha_{7.thr}-\alpha_7(k)\right] for\ \alpha_7(k)<-\alpha_{7.thr}\\ \delta_7(k)-\left[\alpha_7(k)-\alpha_{7.thr}\right] for\ \alpha_7(k)>\alpha_{7.thr}\end{cases},\quad \delta_9(k)=\begin{cases}\delta_9(k)+\left[-\alpha_{9.thr}-\alpha 9(k)\right] for\ \alpha 9(k)<-\alpha_{9.thr}\\ \delta_9(k)-\left[\alpha_9(k)-\alpha_{9.thr}\right] for\ \alpha_9(k)>\alpha_{9.thr}\end{cases}$$

$M_{z3.ATS}(k)=2\delta_7(k)C_7 d_x\cos\left[\delta_7(k-1)\right]-2\delta_9(k)C_9 d_x\cos\left[\delta_9(k-1)\right]$, $M_{z3.TDB}(k)=M_{z3}(k)-M_{z3.ATS}(k)$

The passive side-slip angles (without active steering) of the tires on the axles 4, 6, 7, and 9 are denoted as α_{40}, α_{60}, α_{70}, and α_{90}, and calculated using Equation (3.35), respectively. The side-slip angle based yaw moment allocation algorithm using nonlinear programming is listed in Table 6.1.

To ensure overall zero lateral force generation by steering, the wheels on axle 5 and axle 8 are un-steered, and the wheels on axles 4 and 6 and on axles 7 and 9 are steered oppositely.

6.2.3 Realization Module

The realization module contains the ARC, ATS and TDB actuators. In the ARC actuator, the roll moments are realized as action/reaction roll moment pairs between the sprung and unsprung masses of the vehicle units. In the ATS, the yaw moments are realized by using steering angles, assuming linear lateral tire models, for the k^{th} ($k = 1, 2, \cdots$) sampling step, as

$$\begin{aligned} &\delta_4(k) = -\frac{M_{z2.ATS}(k)}{2C_4 d_x \cos\left[\delta_4(k-1)\right]},\ \delta_5(k) = 0,\ \delta_6(k) = \frac{M_{z2.ATS}(k)}{2C_6 d_x \cos\left[\delta_6(k-1)\right]} \\ &\delta_7(k) = -\frac{M_{z3.ATS}(k)}{2C_7 d_x \cos\left[\delta_7(k-1)\right]},\ \delta_8(k) = 0,\ \delta_9(k) = \frac{M_{z3.ATS}(k)}{2C_9 d_x \cos\left[\delta_9(k-1)\right]} \end{aligned},\ for\ k = 1, 2, \cdots \tag{6.6}$$

The lateral forces of the trailer front and rear tires are determined as

$$\begin{cases} F_{yw4l}(k) = F_{yw4r}(k) = -\frac{C_4}{2}\left[\delta_4(k) - \frac{b_{24}}{U}\dot{\psi}_2(k) + \beta_2(k)\right],\ F_{yw6l}(k) = F_{yw6r}(k) = -\frac{C_6}{2}\left[\delta_6(k) - \frac{b_{26}}{U}\dot{\psi}_2(k) + \beta_2(k)\right] \\ F_{yw7l}(k) = F_{yw7r}(k) = -\frac{C_7}{2}\left[\delta_7(k) - \frac{b_{37}}{U}\dot{\psi}_3(k) + \beta_3(k)\right],\ F_{yw9l}(k) = F_{yw9r}(k) = -\frac{C_9}{2}\left[\delta_9(k) - \frac{b_{39}}{U}\dot{\psi}_3(k) + \beta_3(k)\right] \end{cases} \tag{6.7}$$

In the TDB, the yaw moments are realized iteratively. With the allocated yaw moments (leftovers by the ATS), the brake pressures are first determined. Then the longitudinal forces of the trailer front and rear wheels are derived and compared with the available longitudinal forces governed by the friction ellipse (Schofield et al, 2006, Wong, 2008, and Alberding, et al, 2014), and modified accordingly. With the modified longitudinal forces, the brake pressures are re-calculated. The yaw moments are generated as follows, with the steering in Equation (6.6),

$$\begin{aligned} M_{2.TDB}(k) = &\frac{d_2}{2}\left(F_{xw4l} - F_{xw4r}\right)\cos\delta_4(k) + d_x\left(F_{xw4l} + F_{xw4r}\right)\sin\delta_4(k) + \frac{d_2}{2}\left(F_{xw5l} - F_{xw5r}\right) \\ &+ \frac{d_2}{2}\left(F_{xw6l} - F_{xw6r}\right)\cos\delta_6(k) - d_x\left(F_{xw6l} + F_{xw6r}\right)\sin\delta_6(k) \end{aligned} \tag{6.8a}$$

$$M_{3.TDB}(k)=\frac{d_3}{2}\left(F_{xw7l}-F_{xw7r}\right)\cos\delta_7(k)+d_x\left(F_{xw7l}+F_{xw7r}\right)\sin\delta_7(k)+\frac{d_3}{2}\left(F_{xw8l}-F_{xw8r}\right)+\frac{d_3}{2}\left(F_{xw9l}-F_{xw9r}\right)\cos\delta_9(k)-d_x\left(F_{xw9l}+F_{xw9r}\right)\sin\delta_9(k) \tag{6.8b}$$

Considering the fast wheel spinning dynamics (Chung and Yi, 2006), the torque balance of the wheels on the semitrailers is determined as

$$\begin{cases}-K_bP_{4l}(k)-r_wF_{xw4l}(k)=0,-K_bP_{4r}(k)-r_wF_{xw4r}(k)=0,-K_bP_{5l}(k)-r_wF_{xw5l}(k)=0,\\ -K_bP_{5r}(k)-r_wF_{xw5r}(k)=0,-K_bP_{6l}(k)-r_wF_{xw6l}(k)=0,-K_bP_{6r}(k)-r_wF_{xw6r}(k)=0,\\ -K_bP_{7l}(k)-r_wF_{xw7l}(k)=0,-K_bP_{7r}(k)-r_wF_{xw7r}(k)=0,-K_bP_{8l}(k)-r_wF_{xw8l}(k)=0,\\ -K_bP_{8r}(k)-r_wF_{xw8r}(k)=0,-K_bP_{9l}(k)-r_wF_{xw9l}(k)=0,-K_bP_{9r}(k)-r_wF_{xw9r}(k)=0\end{cases} \tag{6.9}$$

Substituting Equation (6.9) into (6.8) gives

$$M_{2.TDB}=\frac{d_2}{2}\frac{K_b}{r_w}\left(P_{4r}-P_{4l}\right)\cos\delta_4-\frac{d_xK_b}{r_w}\left(P_{4l}+P_{4r}\right)\sin\delta_4+\frac{d_2}{2}\frac{K_b}{r_w}\left(P_{5r}-P_{5l}\right)+\frac{d_2}{2}\frac{K_b}{r_w}\left(P_{6r}-P_{6l}\right)\cos\delta_6+\frac{d_xK_b}{r_w}\left(P_{6l}+P_{6r}\right)\sin\delta_6 \tag{6.10a}$$

$$M_{3.TDB}=\frac{d_3}{2}\frac{K_b}{r_w}\left(P_{7r}-P_{7l}\right)\cos\delta_7-\frac{d_xK_b}{r_w}\left(P_{7l}+P_{7r}\right)\sin\delta_7+\frac{d_3}{2}\frac{K_b}{r_w}\left(P_{8r}-P_{8l}\right)+\frac{d_3}{2}\frac{K_b}{r_w}\left(P_{9r}-P_{9l}\right)\cos\delta_9+\frac{d_xK_b}{r_w}\left(P_{9l}+P_{9r}\right)\sin\delta_9 \tag{6.10b}$$

Assuming $P_{4l}=P_{5l}=P_{6l}=P_{IIl}$, $P_{4r}=P_{5r}=P_{6r}=P_{IIr}$, $P_{7l}=P_{8l}=P_{9l}=P_{IIIl}$, $P_{7r}=P_{8r}=P_{9r}=P_{IIIr}$, and considering $\delta_4\approx-\delta_6$, $\delta_7\approx-\delta_9$, Equation (6.10) is rewritten as

$$M_{2.TDB}=\frac{d_2K_b}{r_w}\left(P_{IIr}-P_{IIl}\right)\left(\cos\delta_4+0.5\right)-\frac{2d_xK_b}{r_w}\left(P_{IIl}+P_{IIr}\right)\sin\delta_4 \tag{6.11a}$$

$$M_{3.TDB}=\frac{d_3K_b}{r_w}\left(P_{IIIr}-P_{IIIl}\right)\left(\cos\delta_7+0.5\right)-\frac{2d_xK_b}{r_w}\left(P_{IIIl}+P_{IIIr}\right)\sin\delta_7 \tag{6.11b}$$

The brake pressures can be determined from the yaw moments as

$$P_{IIl}=0,\ P_{IIr}=\frac{r_wM_{2.TDB}}{K_b\left[d_2\left(\cos\delta_4+0.5\right)-2d_x\sin\delta_4\right]},\ for\ M_{2.TDB}>0 \tag{6.12a}$$

$$P_{IIl}=-\frac{r_wM_{2.TDB}}{\left[d_2\left(\cos\delta_4+0.5\right)+2d_x\sin\delta_4\right]K_b},\ P_{IIr}=0,\ for\ M_{2.TDB}<0 \tag{6.12b}$$

$$P_{IIIl}=0,\ P_{IIIr}=\frac{r_w M_{3.TDB}}{K_b\left[d_3\left(\cos\delta_7+0.5\right)-2d_x\sin\delta_7\right]},\ for\ M_{3.TDB}>0 \tag{6.12c}$$

$$P_{IIIl}=-\frac{r_w M_{3.TDB}}{\left[d_3\left(\cos\delta_7+0.5\right)+2d_x\sin\delta_7\right]K_b},\ P_{IIIr}=0,\ for\ M_{3.TDB}<0 \tag{6.12d}$$

The longitudinal forces of the trailer front and rear wheels are determined as

$$F_{xw4l}=\min\left(\frac{K_b}{r_w}P_{IIIl},\ \mu F_{zwIII}\sqrt{1-\left(\frac{F_{yw4l}}{F_{yw4l.max}}\right)^2}\right),\ F_{xw6l}=\min\left(\frac{K_b}{r_w}P_{IIIl},\ \mu F_{zwIII}\sqrt{1-\left(\frac{F_{yw6l}}{F_{yw6l.max}}\right)^2}\right) \tag{6.13a}$$

$$F_{xw4r}=\min\left(\frac{K_b}{r_w}P_{IIIr},\ \mu F_{zwIIIr}\sqrt{1-\left(\frac{F_{yw4r}}{F_{yw4r.max}}\right)^2}\right),F_{xw6r}=\min\left(\frac{K_b}{r_w}P_{IIIr},\ \mu F_{zwIIIr}\sqrt{1-\left(\frac{F_{yw6r}}{F_{yw6r.max}}\right)^2}\right) \tag{6.13b}$$

$$F_{xw7l}=\min\left(\frac{K_b}{r_w}P_{IIIl},\ \mu F_{zwIIIl}\sqrt{1-\left(\frac{F_{yw7l}}{F_{yw7l.max}}\right)^2}\right),F_{xw9l}=\min\left(\frac{K_b}{r_w}P_{IIIl},\ \mu F_{zwIIIl}\sqrt{1-\left(\frac{F_{yw9l}}{F_{yw9l.max}}\right)^2}\right) \tag{6.13c}$$

$$F_{xw7r}=\min\left(\frac{K_b}{r_w}P_{IIIr},\ \mu F_{zwIIIr}\sqrt{1-\left(\frac{F_{yw7r}}{F_{yw7r.max}}\right)^2}\right),F_{xw9r}=\min\left(\frac{K_b}{r_w}P_{IIIr},\ \mu F_{zwIIIr}\sqrt{1-\left(\frac{F_{yw9r}}{F_{yw9r.max}}\right)^2}\right) \tag{6.13d}$$

where μ is the friction coefficient of the tire/road contact patch taking a value of 0.85; $F_{zwIII}=F_{z4l}=F_{z5l}=F_{z6l}$, $F_{zwIIIr}=F_{z4r}=F_{z5r}=F_{z6r}$, $F_{zwIIIl}=F_{z7l}=F_{z8l}=F_{z9l}$ and $F_{zwIIIr}=F_{z7r}=F_{z8r}=F_{z9r}$ are tire normal loads and given in Equation (3.42); and $F_{yw4l.max}$, $F_{yw4r.max}$, $F_{yw6l.max}$, $F_{yw6r.max}$, $F_{yw7l.max}$, $F_{yw7r.max}$, $F_{yw9l.max}$ and $F_{yw9r.max}$ are the maximum lateral tire forces calculated using the magic formula in Equation (3.10). We substitute Equation (6.13) into Equation (6.8) to recalculate the final brake pressures in Equation (6.12) which obey the friction ellipse of the lateral and longitudinal tire forces (Schofield et al, 2006, Wong, 2008, and Alberding, et al, 2014).

6.3 Coordinated Control Optimization

The coordinated ATS, TDB, and ARC are optimized to achieve optimal trade-off of the high-speed maneuverability and stability. The high-speed maneuverability and stability can be described using the rearward amplification (RA) ratio in yaw and roll dynamics. The RA ratio close to 1.0

represents an ideal trade-off of maneuverability and stability. The coordinated control of the ATS, TDB and ARC are optimized to achieve optimal trade-off performance of maneuverability, lateral and roll dynamics.

6.3.1 Test Maneuvers

A standard test maneuver (Preston-Thomas and E-Gindy, 1995, ISO-14791, 2000, and MacAdam and Hagan, 2002) is used to excite RA response. The desired trajectory followed by the tractor front axle center is generated using

$$Y = \frac{\bar{a}_{y1\_ax}}{(2\pi f)^2}\left[2\pi f \frac{X}{U} - \sin\left(2\pi f \frac{X}{U}\right)\right] \tag{6.14}$$

where $\bar{a}_{y1\_ax}$ denotes the amplitude of the single cycle sine wave lateral acceleration input (SCSLA), f the frequency, U the forward speed, and X , Y the longitudinal and lateral position, respectively.

The SMC-based lateral preview driver model is used to 'drive' the virtual vehicle. The design variables of the driver model, together with those of the control module, form the design variable vector of the closed-loop coordinated control system as

$$X = \left[T_p \quad \tau_d \quad \kappa \quad k_1 \quad k_2 \quad q_1 \quad q_2 \quad q_3 \quad q_4 \quad q_5 \quad q_6 \quad q_7 \quad q_8 \quad q_9 \quad r_1 \quad r_2 \quad r_3 \quad r_4 \quad r_5 \quad r_6\right] \tag{6.15}$$

6.3.2 Optimization Process

For a parallel computing system consisting of n workers, there are $n \cdot i$ (i is an integer) populations represented by $n \cdot i$ sets of the design variables $(X_1, X_2, \cdots, X_{n \cdot i})$ in each generation of the genetic algorithm (GA). Each worker is assigned with one computing task by receiving a design variable set. With the variable set, the driver model and the coordinated control system can be formulated, and integrated with the nonlinear EoM yaw-roll B-train double model. A closed-loop

SCSLA maneuver specified in Equation (6.14) is conducted. Upon completion of the simulation, a fitness value is calculated based on the lateral accelerations and roll angles of the active and baseline MTAHV using the CDG technique (Islam, 2013 and He et al, 2016). The fitness value is sent back to the optimizer (the GA). Up receiving all fitness values of the generation, a best value is obtained. The optimizer makes decision based on the termination criterion: 1) the optimization process terminates if the process is converged or the maximum generation has been reached, 2) otherwise a set of $n \cdot i$ population $(X_1, X_2, \cdots, X_{n \cdot i})$ are re-generated and assigned to n workers, and the optimization process continues.

6.4 Simulation Results

To evaluate the applicability, effectiveness, contribution and coordination of the individual ASSs, the MTAHV with the coordinated control system 'driven' by the SMC-based preview driver model is studied under low and high lateral acceleration SCSLA maneuvers with the desired trajectories defined in Figure 6.2. The coordinated ATS, TDB and ARC are compared with the individual ATS and TDB systems.

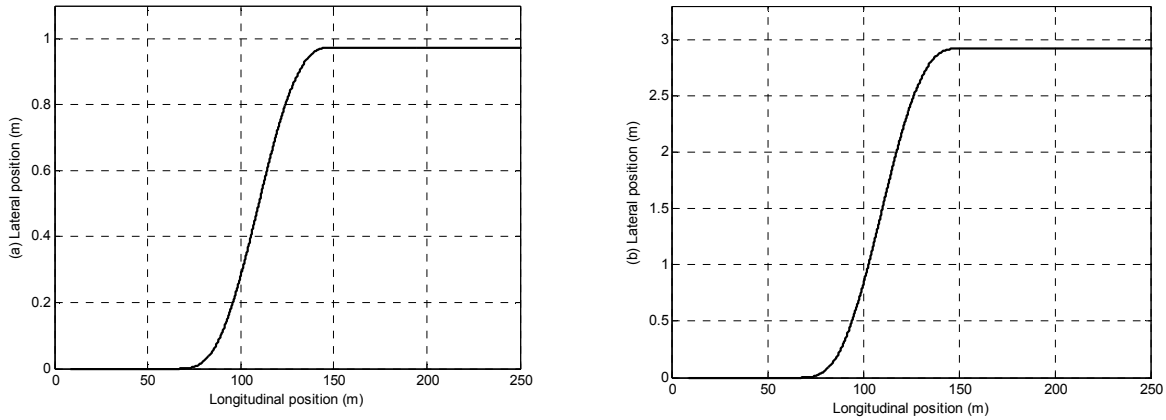

Figure 6.2 Desired trajectory of the tractor front axle center under: (a) a low-g SCSLA maneuver ($a_{y1\_ax} = 0.1$ g, $f = 0.4$ Hz, and $U_1 = 120$ km/h), and (b) a high-g ($a_{y1\_ax} = 0.3$ g, $f = 0.4$ Hz, and $U_1 = 120$ km/h) SCSLA maneuver (based on Equation (6.14))

6.4.1 MTAHV with Pure ATS or TDB

Figure 6.3(a) shows lateral accelerations and Figure 6.3(b) the trailers front and rear wheels side-slip angles of the MTAHV with the ATS under the low-g SCSLA maneuver ($a_{y1\_ax} = 0.1\,g,\ f = 0.4$ *Hz, and* $U_1 = 120$ *km/h*). The ATS has achieved excelled directional performance at the cost of excessive tire side-slip angles, which are larger than the threshold values, exciting the nonlinear tire dynamics. The excessive side-slip angles may be caused: 1) the ATS takes over the full amount of yaw moments required, and 2) only two of the three axles in a tridem group are steered. The ATS is effective only under low level lateral acceleration operations.

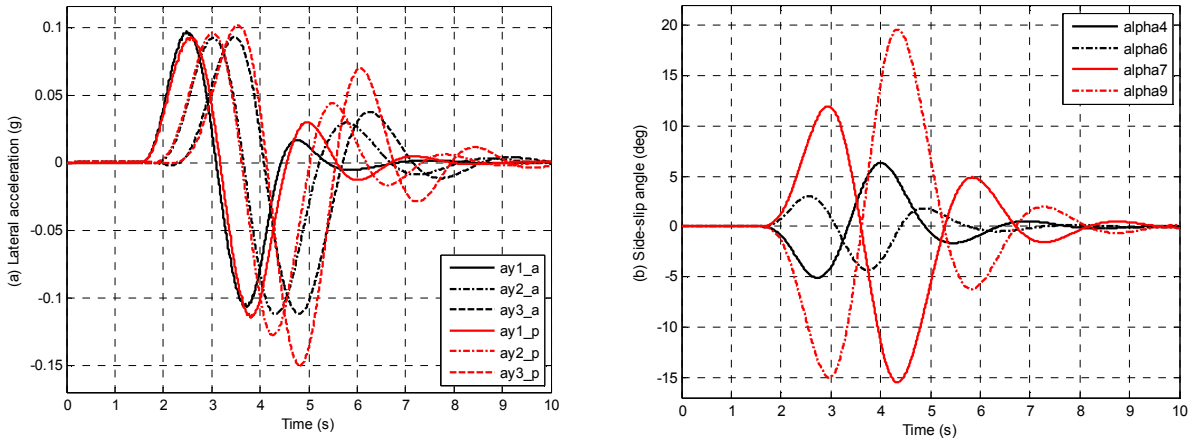

Figure 6.3 Responses of the MTAHV with ATS: (a) lateral acceleration of the vehicle units, (b) side-slip angles of the front and rear wheels of the 1st and 2nd semitrailer

Under high lateral acceleration operations, the ATS may fail to stabilize the vehicle. Figure 6.4 shows the lateral acceleration and the trailer front and rear wheel side-slip angles of the MTAHV with the ATS under the SCSLA maneuver ($a_{y1\_ax} = 0.3\,g,\ f = 0.4$ Hz, *and* $U_1 = 120$ km/h). At the lateral acceleration of 0.3g, the ATS fails to stabilize the MTAHV.

Figure 6.5 shows the lateral accelerations, and Figure 6.6 the brake torques of the trailer left and right wheels of the MTAHV with the TDB under the low and high lateral acceleration SCSLA maneuvers. The TDB successfully stabilize the MTAHV under the low and high lateral

acceleration operations. As shown in Figure 6.6, compared with the low lateral operation case, the brake torques consumed under the high lateral operation are increased. The impact of the brake torques will be investigated with the coordinated control cases in next section. The TDB are effective to stabilize the MTAHV in low and high lateral acceleration operations.

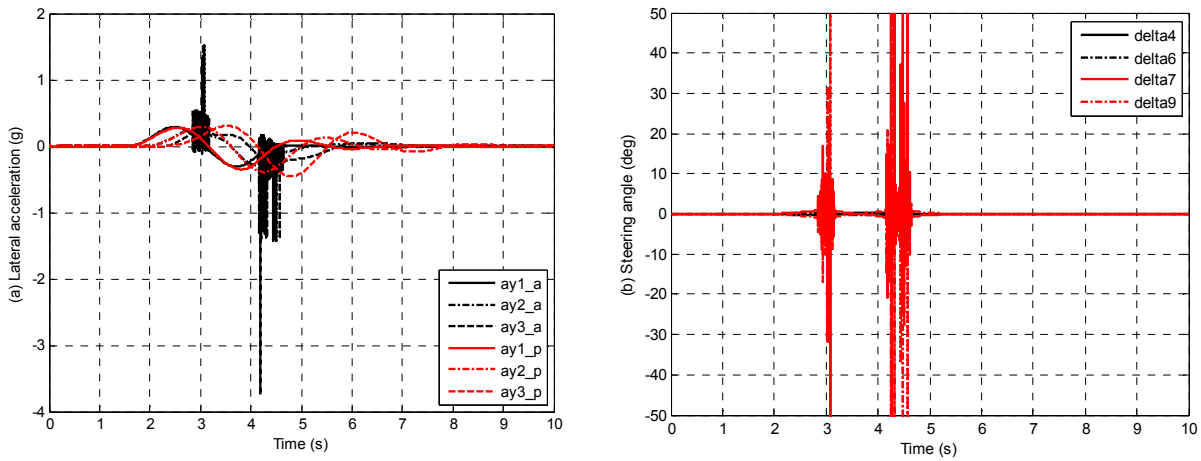

Figure 6.4 Responses of the MTAHV with the ATS under the high lateral acceleration SCSLA maneuver: (a) lateral acceleration, and (b) steering angle of trailer front and rear wheels

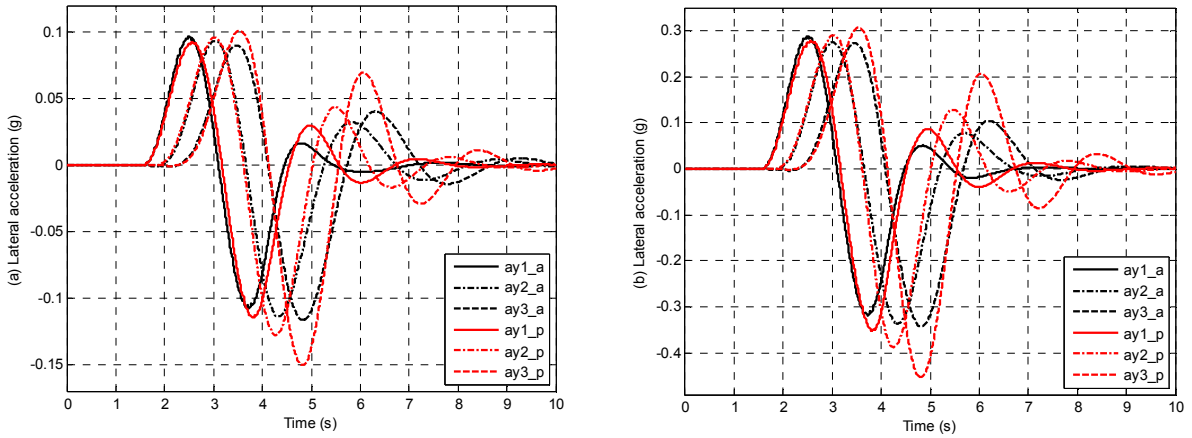

Figure 6.5 Lateral accelerations of the MTAHV with the TDB under the low and high lateral acceleration SCSLA maneuvers: (a) $a_{y1\_ax} = 0.1\,\mathrm{g}$, and (b) $a_{y1\_ax} = 0.3\,\mathrm{g}$

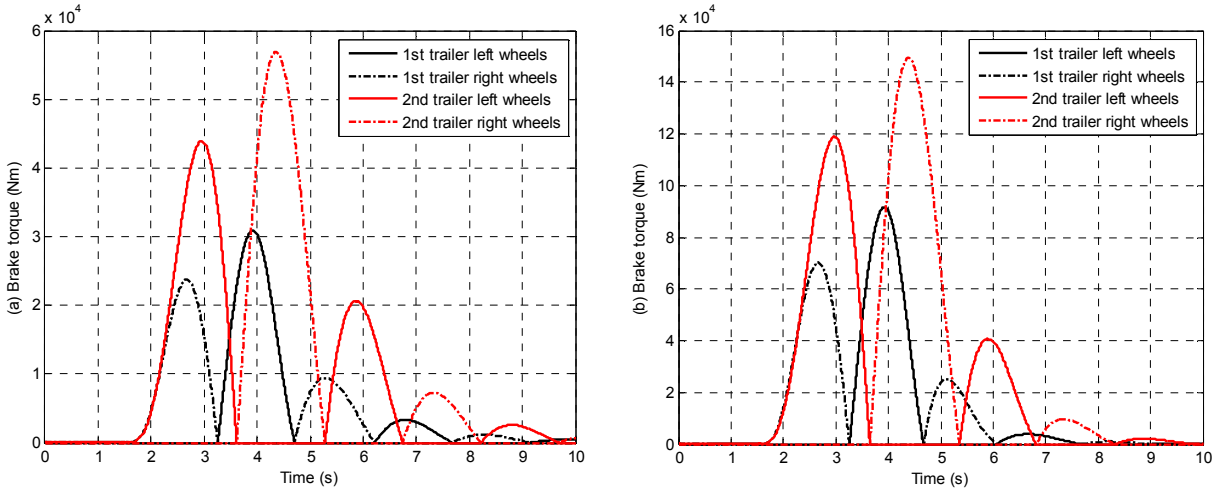

Figure 6.6 Brake torques of the trailer left and right wheels of the MTAHV with the TDB under the low and high lateral acceleration maneuvers: (a) $a_{y1\_ax} = 0.1$ g, and (b) $a_{y1\_ax} = 0.3$ g

6.4.2 MTAHV with Coordinated ATS, TDB and ARC

Figure 6.7(a) shows the side-slip angles of the trailer front, middle and rear tires, and Figure 6.7(b) the steering angles of the trailer front and rear axles of the MTAHV with coordinated ATS, TDB, and ARC under the low lateral acceleration maneuver. The side-slip angle based allocation algorithms sets the upper and lower bounds (0.14 rad or 8 deg) for the trailer front and rear wheel side-slip angles. The side-slip angles of the front wheels have approximately opposite values to that of the rear tires, e.g. $\alpha_4 \approx -\alpha_6$ and $\alpha_7 \approx -\alpha_9$. Since no steering actuated for the wheels on the axle 5 and axle 8, the side-slip angles of these wheels have smaller absolute values than those of the wheels on the front and rear axles. More severe RA suppression on the 2nd semitrailer calls for more steering and causes the tire side-slip angle saturation. The steering angles of the front tires are symmetric to those of the rear tires for the same semitrailer with respect to the time axis. The symmetry of the side-slip angles are diluted by the passive side-slip angles, especially for those of the 1st semitrailer.

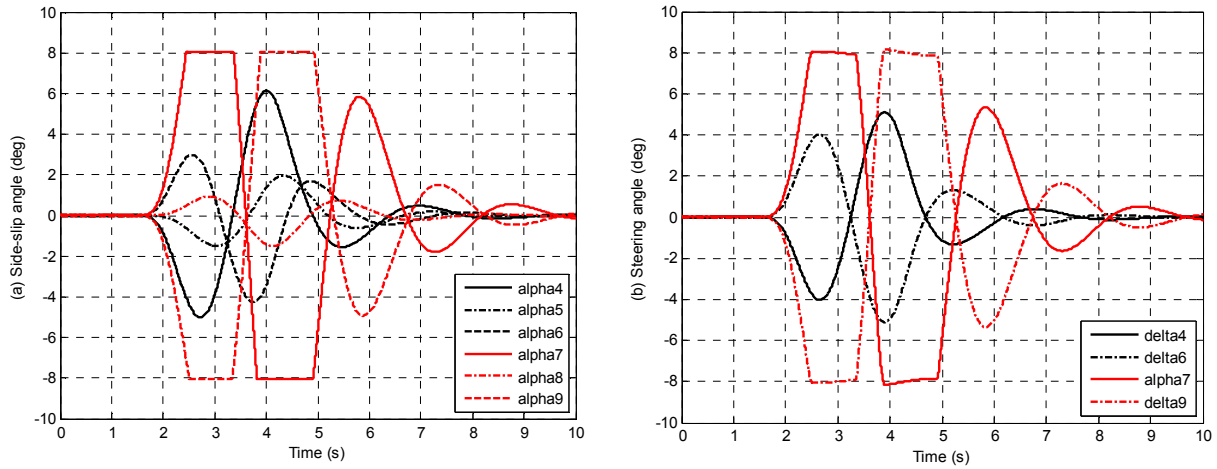

Figure 6.7 Trailer dynamic responses under the low lateral acceleration SCSLA maneuver: (a) side-slip angle, and (b) steering angle

Figure 6.8(a) shows the allocation of the yaw moments between the ATS and TDB actuators under the low lateral acceleration SCSLA maneuver. The side-slip angle threshold sets a boundary, within which the yaw moments are ascribed to the ATS and outside of which allocated to the TDB. The summation of the ATS and TDB portions makes up the total yaw moments, showing a seamless transition from one actuator to the other. Comparing the zones enclosed by the black curves and red curves with the time axis declares that the ATS is the main player under the low-g maneuver. Figure 6.8(b) shows the brake torques of the left and right wheels of the 1st and 2nd semitrailers, realizing the yaw moments $M_{z3.TDB}$ (red curves in Figure 6.8(a)). The ATS takes over the full amount of the yaw moment required for the 1st semitrailer, and for the TDB, there is no yaw moment required for the 1st semitrailer under the low-g maneuver.

Figure 6.9(a) shows the roll angles of the MTAHV integrated with ATS and TDB with/without ARC, and Figure 6.9(b) those of the baseline MTAHV under the low-g SCSLA maneuver. The coordinated ATS and TDB without ARC has increased (worsen) the roll angle of the 1st semitrailer by 40 percent; and thus coordination of the ARC with other ASSs is essential for roll dynamics.

The coordinated ATS, TDB and ARC have improved the roll dynamics significantly, especially, on the tractor unit.

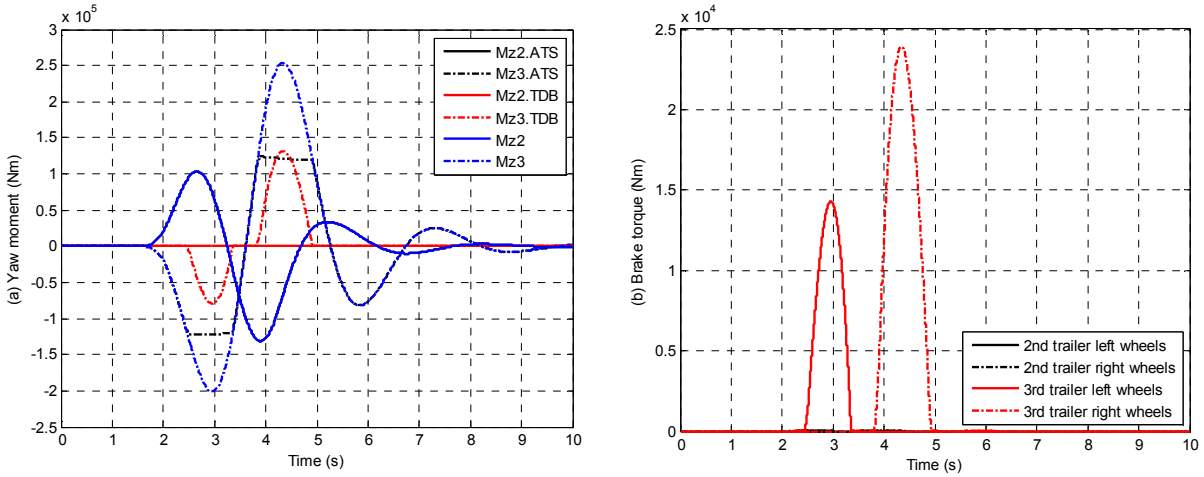

Figure 6.8 Under the low-g maneuver: (a) yaw moment allocation, and (b) Brake torques of the trailer front and rear wheels

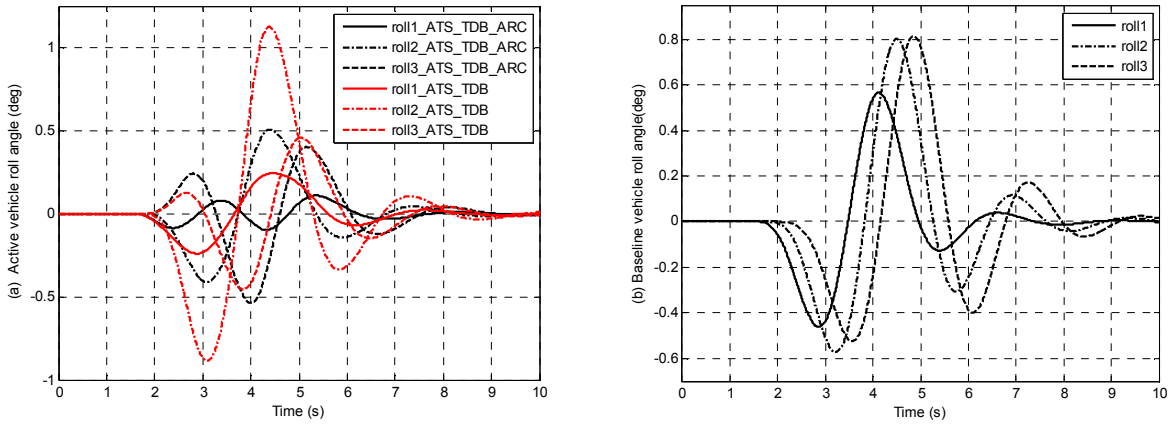

Figure 6.9 Roll angle responses under the low-g SCSLA maneuver: (a) MTAHV integrated with ATS and TDB with/without ARC, and (b) baseline MTAHV

Figure 6.10(a) shows the lateral accelerations of the MATHV with coordinated ATS, TDB and ARC and those of the baseline MTAHV, and Figure 6.10(b) those of the MTAHV with coordinated ATS, TDB and with/without ARC under the low-g SCSLA maneuver. The coordinated ATS, TDB and ARC have improved lateral dynamic performance significantly. Enhancing the lateral dynamics by the ARC is not evident as on the roll dynamics.

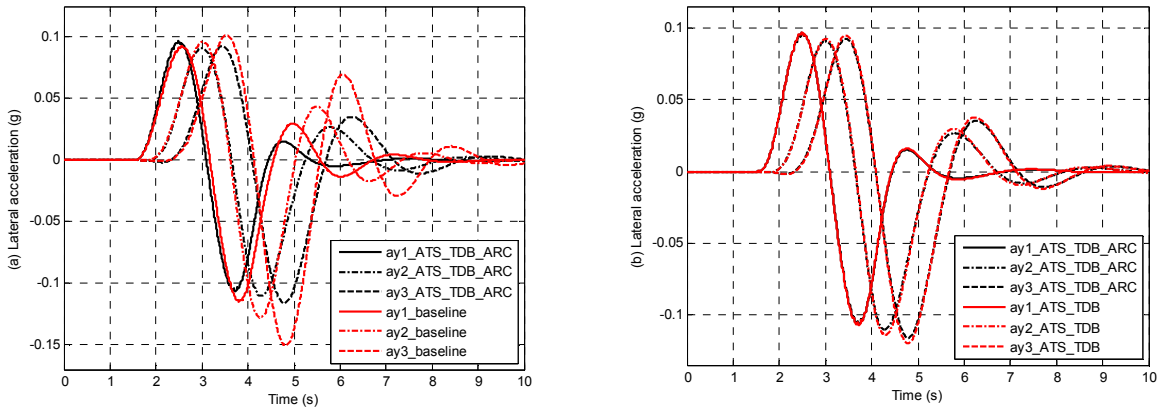

Figure 6.10 Lateral accelerations under the low-g SCSLA maneuver: (a) baseline MTAHV and MTAHV with coordinated ATS, TDB and ARC, and (b) MTAHV coordinated with ATS and TDB with/without ARC

Compared with the low-g maneuver case, the MTAHV under the high-g SCSLA maneuver demonstrates the following common features: 1) the front and rear wheel steer angles of a semitrailer are symmetric with respect to the time axis, 2) the symmetry of the side-slips are diluted by the passive side-slip angles, 3) the yaw moments are allocated to the ATS and TDB, with the former as the primary and the latter the secondary player, and transit seamlessly from the primary to the secondary, 4) the coordination of the ARC with other ASSs is essential for roll dynamics, and minor for improving lateral dynamics, 5) the coordination of the ATS and the TDB has major impact (positive or negative) on roll dynamics, and 6) the coordination of the ATS, TDB and the ARC improves the lateral and roll dynamics significantly.

6.4.3 Impact of the TDB on the Longitudinal Dynamics

Figure 6.11 shows the longitudinal speeds of the MTAHV with the TDB and the coordinated control under the low- and high-g SCSLA maneuvers. The impact of the TDB on the longitudinal dynamics increases in the following sequence: the coordinated control under the low-g maneuver, the TDB under the low-g maneuver, the coordinated control under the high-g maneuver, and the

TDB under the high-g maneuver. With the proposed coordinated control strategy, the adverse impact of the TDB has been greatly reduced.

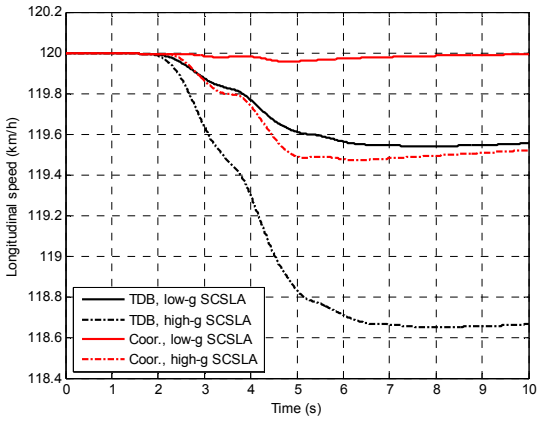

Figure 6.11 Longitudinal speeds of the MTAHV with the TDB and the coordinated control under the low- and high-g maneuvers

6.4.4 Yaw moment allocation

The side-slip angle based yaw moment allocation algorithm is the essence and core of the coordinated control. Figure 6.12 shows the yaw moment (absolute value) time integration allocation in terms of the lateral acceleration amplitude of the SCSLA maneuver. For both the 1st semitrailer in Figure 6.12(a) and the 2nd semitrailer in Figure 6.12(b), the total yaw moment time integration equals the summation of the yaw moment time integrations allocated to the ATS and to the TDB, showing seamless transitions from one actuator to the other. Due to more severe rearward amplification suppression required, the total yaw moment time integration of the 2nd semitrailer is around two times of that of the 1st semitrailer in the lateral acceleration amplitude range considered. Due to relatively low requirement of the yaw moment on the 1st semitrailer, the ATS dominates throughout the amplitude range, and the TDB starts to kick in when the amplitude becomes 0.15g or greater. For the 2nd semitrailer, the TDB kicks in much earlier at an amplitude

of 0.05g, with a much larger raising slope than that of the ATS. When the amplitude is 0.2g or larger, the TDB becomes dominant over the ATS.

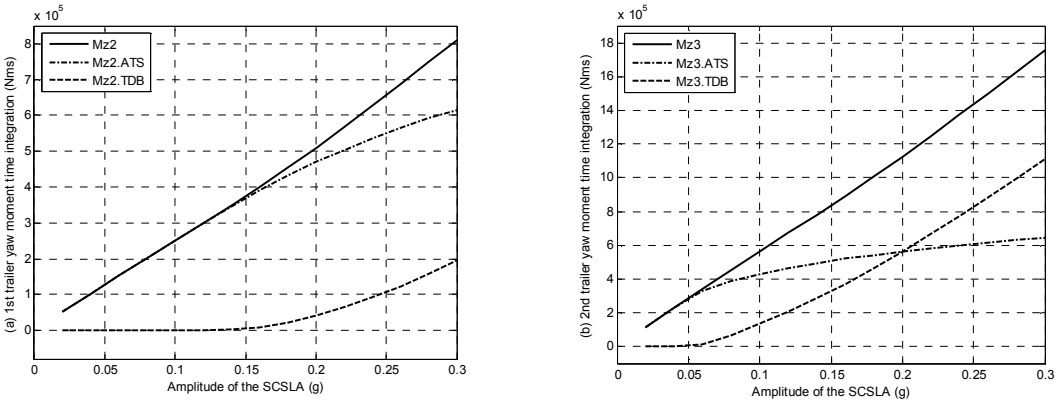

Figure 6.12 Yaw moment (absolute value) time integration allocation in terms of the lateral acceleration amplitude of the SCSLA maneuver: (a) 1st semitrailer, and (b) 2nd semitrailer

Figure 6.13 shows the yaw moment (absolute value) time integration ratios of the ATS and TDB of the 1st and 2nd semitrailers. The ATS ratios decrease and the TDB ratios increase with the increase of the lateral acceleration amplitudes for both semitrailers. At a given lateral acceleration amplitude, the yaw moment (absolute value) time integration ratio for the ATS or TDB is calculated with the corresponding allocated yaw moment (absolute value) time integration divided by the total yaw moment (absolute value) time integration.

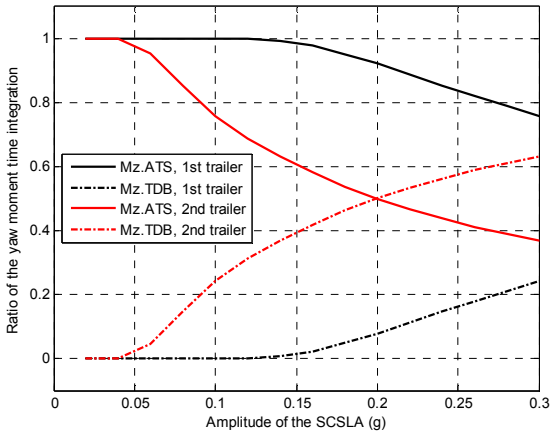

Figure 6.13 Yaw moment time integration ratios with respect to the lateral acceleration amplitude of the SCSLA maneuver

6.5 Summary

This chapter presents a coordinated control strategy for active safety systems of multi-trailer articulated heavy vehicles. Three vehicle models of a B-train double, namely, the linear yaw-plane model, linear yaw-roll model, and the nonlinear EoM yaw-roll model are formulated. A sliding mode control based lateral preview driver model 'drives' the virtual MTAHV. A high level direct moment controller based on the linear yaw-roll model determines the virtual moments to stabilize the yaw and roll dynamics. A side-slip angle based allocation algorithm distributes the roll moments to the ARC actuators, and the yaw moments to the ATS and the TDB actuators, achieving a seamless transition from one actuator to the other. The allocated moments are realized with the ARC, ATS and TDB actuators. The coordinated control system is optimized using the parallel genetic algorithm to achieve an optimal trade-off performance of high-speed maneuverability, lateral and roll stability.

Simulation results show that the ATS is effective but not sufficient in stabilizing the yaw dynamics of the MTAHV in low to medium lateral acceleration range, and fails to stabilize the vehicle at high lateral acceleration operation. The TDB is effective and sufficient to stabilize the vehicle yaw dynamics at low to high lateral acceleration operations. The coordinated ATS and TDB improves the lateral dynamics significantly at low to high lateral acceleration operations. Compared with the TDB, the impact of the coordinated ATS and TDB is much less on the longitudinal dynamics. The coordinated ATS and TDB affect the roll dynamics significantly. The ARC has minor improvement on the lateral dynamics and is essential to improve the roll dynamics.

Chapter 7 On Robust Controllers for Active Steering Systems of Articulated Heavy Vehicles

7.1 Introduction

Active steering systems (ASSs) have been investigated to improve maneuverability (Rangavajhula and Tsao, 2008 and Cheng et al, 2011), enhance lateral stability (Islam et al, 2012, Kharrazi et al, 2012, Ding et al, 2013), and achieve a better trade-off between the aforementioned conflicting measures (He and Islam, 2012) of AHVs. The majority of studies in this field is built on the LQR technique (Maciejowski, 1989) without adequate consideration of the controller robustness.

The AHVs with ASSs usually experience uncertainties, e.g., the variations of the forward speed, road adhesion coefficient, trailer payload (Wang and Tomizuka, 2000), road roughness, wind gusts, and the braking/accelerating forces (Yin et al, 2010). The deterministically determined optimal solutions may be meaningless (Palkovics and El-Gindy, 1996 and Busch and Bestle, 2014). In the reality, an ASS should be designed with an acceptable level of robustness under various operating conditions.

The H_∞ technique has become a powerful tool in handling robustness issue since its invention in the 1980s (Doyle, 1985 and Doyle, 1987). The H_∞ technique treats the model uncertainties, un-modeled dynamics, and the exogenous disturbances in a systematic manner (Skogestad and Postlethwaite, 2001). It has received recognition and still is a hot topic in the single unit vehicle dynamics (Gao et al, 1995, Yin et al, 2010 and Doumiati et al, 2013), AHV lateral stability (Palkovics et al, 1994) and the automated lane guidance (Wang and Tomizuka, 2000). Compared

to the single unit vehicle dynamic control, the ASS controllers based on the H_∞ technique for AHVs, have not received enough consideration.

Besides the H_∞ technique, the sliding mode control (SMC) technique also demonstrates good robustness and invariant properties (Utkin et al, 1999). Since its origination in the former Soviet Union in 1930s (Utkin et al, 1999) and spread to the western world with a historic review paper (Utkin, 1977), the SMC technique has received wide recognition in multiple engineering fields (Habibi and Richards, 1992, Lin et al, 2002, Fernandes and Alcalde, 2007), and applications in the automotive engineering (Mao and Lu, 2008) and the AHV dynamics (Oreh et al, 2014).

The lateral dynamics of AHVs, and the rearward amplification (RA) in particular, demonstrates the frequency-dependent property (Aurell and Winkler, 1995). The majority of studies on the lateral dynamics of AHVs (Palkovics and El-Gindy, 1996, Miege and Cebon, 2005, Cheng and Cebon, 2008, He et al, 2010, Islam et al, 2012, Huang et al, 2012, Ding et al, 2012) focus on the performance measures evaluated mainly in the time-domain. However, as pointed out by Aurell and Winkler (1995), the time-domain performance measures of the RA provide only composite information under a specific maneuver; for the complete RA information of an AHV in a frequency range of interest, the frequency-domain measures are preferred.

To address this issue, Zhu and He (2015) proposed a novel automated frequency response measurement method (AFRM) for acquiring the frequency domain RA measures for AHVs. With the AFRM, a repetitive frequency measurement using the sine waves of various frequencies and amplitudes is assigned to a computer in a way that the signal generation, model simulation, and the frequency response measurement can be conducted in the real-time and on-line manners. Most importantly, the AFRM makes the frequency-domain optimization of AHV dynamics achievable.

This chapter intends to examine the robustness of different ASS controllers. The steering

angles of the tractor rear wheels and the semitrailer wheels are manipulated to improve the directional performance of the tractor/semitrailer combination. To this end, a three degrees of freedom (DOF) linear yaw-plane tractor/semitrailer model is applied to design the controllers using the SMC and MS techniques; a three DOF nonlinear yaw plane model is utilized to devise the controller based on the nonlinear sliding mode control (NSMC) method; the performances of the controllers are assessed using the co-simulations in the time- and frequency-domain through the integration of the controllers designed in the Matlab/Simulink and a nonlinear tractor/semitrailer model developed in TruckSim. The performance measure of the tractor/semitrailer with the active steering system in the frequency-domain is acquired using the AFRM and the controllers are optimized using a genetic algorithm (GA) in a way that the rearward amplification (RA) ratio remains in the vicinity of 1.0 for an optimal trade-off between the high-speed maneuverability and stability in a frequency range of interest. The controllers are also evaluated using simulations in the time-domain at low and high lateral accelerations operations. In the case of simulations in the time-domain, a robustness index is defined to quantify the robustness in terms of the performance measure of the AHV with different active steering controllers.

Subsection 7.2 describes the active steering controllers designed in the Matlab/Simulink software using the SMC, NSMC and MS techniques. The active steering controllers designed in the Matlab/Simulink and the nonlinear tractor/semitrailer model developed in TruckSim are integrated for co-simulation. Subsection 7.3 examines the robustness of the active steering controllers based on the SMC, NSMC, MS and LQR techniques by analyzing the simulation results in the time- and the frequency-domain. Finally, conclusions are drawn in Subsection 7.4.

7.2. Active Steering Controllers Design

To improve the high-speed maneuverability and lateral stability of the tractor/semitrailer combination, the following performance measures are minimized: 1) the state variables of the yaw-plane models; 2) the lateral accelerations of the tractor and semitrailer; and 3) the difference between the rearward amplification ratio and the value of 1.0. The first two requirements are for enhancing the high-speed stability and the third one for the trade-off between the high-speed maneuverability and the lateral stability. Three robust controllers, namely, the SMC, NSMC and the MS, are designed to achieve robust performance measures of the maneuverability and stability subject to parameter uncertainties and un-modeled dynamics. The LQR-based active steering controller similar to the one reported in (He and Islam, 2012) is also devised as a baseline design for the benchmark study. The tractor front wheel steering angle input is treated as and exogenous disturbance; and the active steering angles of the tractor rear wheels and the semitrailer wheels are treated as control variables.

7.2.1 Controller based on the Sliding Mode Control Technique

The first robust controller is designed using the sliding mode control (SMC) technique (Utkin et al, 1999). Removing the exogenous disturbance term of driver, the linear yaw-plane model of the tractor/semitrailer combination expressed previously in Chapter 3 is rewritten as

$$\dot{\mathbf{x}} = \mathbf{A}\mathbf{x} + \mathbf{B}\mathbf{u} \tag{7.1}$$

where $\mathbf{u} = \begin{bmatrix} \delta_2 & \delta_3 \end{bmatrix}^T$ denotes the control variable vector, and $\mathbf{x} = \begin{bmatrix} \psi_1 & \Delta\dot{\psi} & \beta_1 & \Delta\psi \end{bmatrix}^T$ the state variable vector. The system is time-invariant, and the pair $(\mathbf{A}, \mathbf{B})$ is controllable, and $rank(\mathbf{B}) = m$ ($m = \dim(\mathbf{u})$). To fulfill the control design, the state equation should be so arranged that matrix $\mathbf{B}$ can be partitioned as $\mathbf{B} = \begin{bmatrix} \mathbf{B}_1^T & \mathbf{B}_2^T \end{bmatrix}^T$ with $rank(\mathbf{B}_2) = m$, which requires rearranging the state variable

vector as $\mathbf{x} = \begin{bmatrix} \Delta\psi & \dot{\psi}_1 & \Delta\dot{\psi} & \beta_1 \end{bmatrix}^T$. After the rearrangement (the re-arranged state equation is still represented with the pair ($\mathbf{A}, \mathbf{B}$) for brevity), a transformation matrix can be formed on the partitioned input matrices as

$$\mathbf{T} = \begin{bmatrix} \mathbf{I}_{n-m} & -\mathbf{B}_1\mathbf{B}_2^{-1} \\ \mathbf{0} & \mathbf{B}_2^{-1} \end{bmatrix} \tag{7.2}$$

The transformations are made as $\begin{bmatrix} \mathbf{x}_1 \\ \mathbf{x}_2 \end{bmatrix} = \mathbf{T}\mathbf{x}$, $\begin{bmatrix} \mathbf{A}_{11} & \mathbf{A}_{12} \\ \mathbf{A}_{21} & \mathbf{A}_{22} \end{bmatrix} = \mathbf{T}\mathbf{A}\mathbf{T}^{-1}$, $\mathbf{T}\mathbf{B} = \begin{bmatrix} \mathbf{0} \\ \mathbf{I}_{m\times m} \end{bmatrix}$ and the system expressed in Equation (7.1) is transformed into the regular form (Utkin et al, 1999) as

$$\begin{aligned} \dot{\mathbf{x}}_1 &= \mathbf{A}_{11}\mathbf{x}_1 + \mathbf{A}_{12}\mathbf{x}_2 \\ \dot{\mathbf{x}}_2 &= \mathbf{A}_{21}\mathbf{x}_1 + \mathbf{A}_{22}\mathbf{x}_2 + \mathbf{u} \end{aligned} \tag{7.3}$$

The 1st subsystem in Equation (7.3) can be stabilized by using the pole placement technique (Nise, 2011) to determine a feedback law $\mathbf{x}_2 = -\mathbf{K}_0\mathbf{x}_1$. Thus, a sliding surface can be obtained for the original system as

$$\mathbf{s} = \begin{bmatrix} \mathbf{K}_0 & \mathbf{I}_{m\times m} \end{bmatrix}\mathbf{T}^{-1}\mathbf{x} = \mathbf{G}\mathbf{x} \tag{7.4}$$

A control law that continuously minimizes the Lyapunov function candidate $V = \frac{1}{2}\mathbf{s}^T\mathbf{s}$ can be obtained (Utkin et al, 1999) as

$$\mathbf{u} = -\left(\alpha|\mathbf{x}| + \delta\right) sign(\mathbf{s}) \tag{7.5}$$

where α and δ are positive design parameters, $|\mathbf{x}| = \sum_{i=1}^{n} |x_i|$ (where $n = \dim(\mathbf{x})$), and $sign(\mathbf{s}) = \begin{bmatrix} sign(s_1) & \cdots & sign(s_m) \end{bmatrix}$. The sign function Equation (7.5) can be replaced with a saturation

function $sat(s_i)=\begin{cases} s_i & |s_i/\varepsilon_T|<1 \\ \text{sgn}(s_i) & |s_i/\varepsilon_T|\geq 1 \end{cases}, i=1,2,\cdots,m$ to eliminate chattering with $\varepsilon_T>0$ denoting the boundary thickness.

7.2.2 Controller based on the Nonlinear Sliding Mode Control Technique

The nonlinear sliding mode control (NSMC) technique presented by Slotine and Li (1991) is a nonlinear model based controller. The NSMC controller designed in this section is based on a yaw-plane model with the lateral tire forces realized using nonlinear lookup tables. The three DOF nonlinear yaw plane model of the tractor/semitrailer combination presented in Chapter 3 is applied to design the so-called NSMC controller. The state equation of the nonlinear yaw-plane model is decomposed into

$$\dot{\mathbf{x}}(t)=\mathbf{A}_{nl}\mathbf{x}(t)+\mathbf{B}_{nd}F_1+\mathbf{B}_{nc}\mathbf{u}_F \tag{7.6}$$

where $\mathbf{B}_{nd}=\mathbf{B}_{nl}(:,1)$ (1^{st} column of $\mathbf{B}_{nl}$) is the disturbance input matrix, $\mathbf{B}_{nc}=\mathbf{B}_{nl}(:,2:3)$ (2^{nd} and 3^{rd} columns of $\mathbf{B}_{nl}$) the control input matrix, and $\mathbf{u}_F=[F_2 \quad F_3]^T$ the control vector, the lateral tire forces of the tractor front wheels F_1, tractor rear wheels F_2 and the semitrailer wheels F_3, are calculated, the same as Equation (3.10), as

$$F_i=D_i\sin\left(C_i\arctan\left\{B_i\alpha_i-E_i\left[B_i\alpha_i-\arctan\left(B_i\alpha_i\right)\right]\right\}\right), i=1,2,3 \tag{7.7}$$

where B_i, C_i, D_i, and E_i are the magic formula (Pacejka, 2005) parameters tuned to match the responses of the nonlinear yaw-plane model with those of the TruckSim model. Dropping out the disturbance term, the state space equation for the NSMC controller design is given as

$$\dot{\mathbf{x}}(t)=\mathbf{A}_{nl}\mathbf{x}(t)+\mathbf{B}_{nc}\mathbf{u}_F \tag{7.8}$$

The SMC controller is designed using the same method presented in Section 7.2.1 to determine the lateral forces generated by the tractor rear wheels and the semitrailer wheels as

$$\mathbf{u}_F = -\left(\alpha_F \left|\mathbf{x}\right| + \delta_F\right) sign\left(\mathbf{s}_F\right) \tag{7.9}$$

where α_F and δ_F are positive design variables and $\mathbf{s}_F$ the sliding surface built similarly to that in Equation (7.4). Since the lateral tire forces are calculated by using the magic formula in Equation (7.7), i.e., given a side-slip angle, the lateral tire force can be determined. On the other hand, to realize the lateral tire force demanded by the SMC controller, a side-slip angle is derived in an inversed magic formula, which can be achieved using a look-up table based on the tuned magic formula.

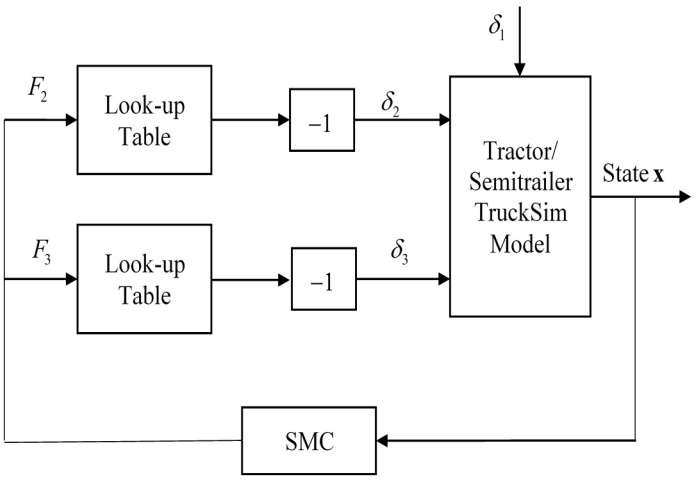

Figure 7.1 Schematic representation of the TruckSim model with the NSMC Controller

The side-slip angles derived from the look-up tables fulfill the 'extra' portion of the side-slip angle of tires from active steering in the kinematical relationships (Zhu and He, 2015) as

$$\alpha_2 = \overbrace{\beta_1 - \left(\frac{b_{12}}{U_1}\right)\dot{\psi}_1}^{state\ contributed} + \overbrace{\left(-\delta_2\right)}^{steering\ contributed},\ \alpha_3 = \overbrace{\beta_1 - \Delta\psi - \left(\frac{l_{c21} + b_{23} + l_{c1}}{U_1}\right)\dot{\psi}_1 - \left(\frac{l_{c21} + b_{23}}{U_2}\right)\Delta\dot{\psi}}^{state\ contributed} + \overbrace{\left(-\delta_3\right)}^{steering\ contributed} \tag{7.10}$$

The total side-slip angles are contributed from: 1) the state variables, and 2) the active steering angles. Removing the state-contributed portion from the side-slip angles, the required active steering angles by the SMC controller can be determined. Considering the nonlinear property of the look-up tables, we entitle the active steering controller NSMC. The schematic diagram of the closed-loop system with the TruckSim model and the NSMC controller is shown in Figure 7.1.

7.2.3 Controller based on the Mu-Synthesis Technique

The active steering controller is based on the Mu-Synthesis (MS) technique. The MS is one of the commonly used H_∞ controllers, which iteratively solves a mixed sensitivity problem for optimal solution in a frequency range of interest (Skogestad and Postlethwaite, 2001). The uncertain parameters are selected using the frequency domain parametric sensitivity analysis (Gu et al, 2013) from the groups describing the vehicle kinematics, tire dynamics and the vehicle inertia properties based on the two criteria: 1) the parameter is most sensitive, and 2) the nominal value of the parameter is the most difficult to obtain.

The model scaling/normalization makes the model analysis and the controller design much simpler (Skogestad and Postlethwaite, 2001). The scaled/normalized variables have their (absolute) values in the range of (0, 1). The variables, such as the exogenous disturbance, control input and the output, are normalized with the corresponding expected magnitudes. With the linear yaw-plane model of the tractor/semitrailer combination in Chapter 3, a scaled linear yaw-plane model is given as

$$\begin{cases} \dot{\mathbf{x}} = \mathbf{A}\mathbf{x} + \mathbf{B}\mathbf{U}_{\max}\bar{\mathbf{u}} \\ \bar{\mathbf{y}} = \mathbf{Y}_{\max}^{-1}\mathbf{C}\mathbf{x} + \mathbf{Y}_{\max}^{-1}\mathbf{D}\mathbf{U}_{\max}\bar{\mathbf{u}} \end{cases} \tag{7.11}$$

Where $\bar{\mathbf{u}} = \begin{bmatrix} \bar{\delta}_1 & \bar{\delta}_2 & \bar{\delta}_3 \end{bmatrix}^T$ denotes the scaled input vector, $\bar{\mathbf{y}} = \begin{bmatrix} \bar{a}_{y1} & \bar{a}_{y2} \end{bmatrix}^T$ the scaled output vector, $\mathbf{U}_{\max} = diag\left(\begin{bmatrix} \delta_{1\max} & \delta_{2\max} & \delta_{3\max} \end{bmatrix}\right)$ and $\mathbf{Y}_{\max} = diag\left(\begin{bmatrix} a_{y1\max} & a_{y2\max} \end{bmatrix}\right)$ the scaling matrices. Open-loop simulations indicate that the tractor/semitrailer combination starts to roll over at the tractor front wheel steering angle of 0.04 radian, which causes the tractor and semitrailer to produce the lateral acceleration of 0.5g ($4.9\ m/s^2$). The expected maximum steering angle for the tractor rear wheels and the semitrailer wheels is 0.1 radian. Hence, the scaling matrices are selected as $\mathbf{U}_{\max} = diag\left(\begin{bmatrix} 0.04 & 0.1 & 0.1 \end{bmatrix}\right)$ and $\mathbf{Y}_{\max} = diag\left(\begin{bmatrix} 4.9 & 4.9 \end{bmatrix}\right)$.

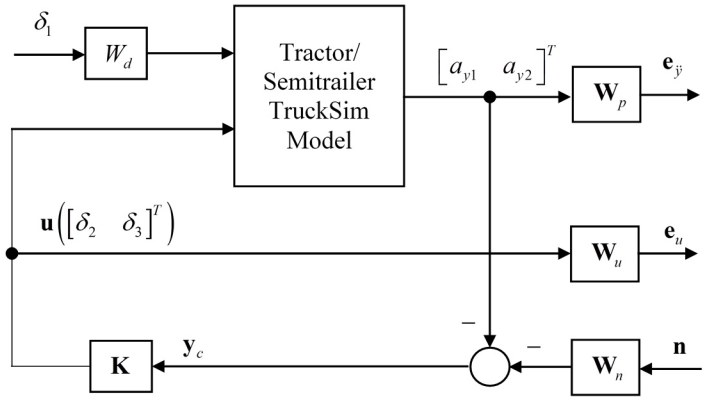

Figure 7.2 The Single DOF control structure with the frequency weighting functions

Since the RA ratio of the tractor/semitrailer without the active steering system is greater than 1.0 at low to the crossover frequency (Islam et al, 2015), the objective of the MS controller design is to restrict the lateral acceleration of the semitrailer and force the RA ratio to approach 1.0. This is a disturbance attenuation problem and may be solved using the single DOF control (Skogestad and Postlethwaite, 2001 and Gu et al, 2013) as shown in Figure 7.2. The exogenous disturbance δ_1 is weighted by the frequency function W_d , the output $\begin{bmatrix} a_{y1} & a_{y2} \end{bmatrix}^T$ by $\mathbf{W}_p$, the control input $\begin{bmatrix} \delta_2 & \delta_3 \end{bmatrix}^T$ by $\mathbf{W}_u$, and the measurement noise $\mathbf{n}$ by $\mathbf{W}_n$. A multi-input and multi-output MS

controller $\mathbf{K}$ may be obtained to minimize the weighted control input $\mathbf{e}_u$ and the weighted output $\mathbf{e}_y$. The RA characteristics of the tractor/semitrailer with the MS active steering controller can be manipulated by appropriate selection of the design parameters of the frequency weighting functions (Skogestad and Postlethwaite, 2001).

The frequency weighting functions are selected following the fundamental principles (Gu et al, 2013): 1) an integral-shape high-gain low-pass filter weights the controlled output for accurate reference tracking; 2) a high-pass filter limits the control input at high frequencies and at the closed-loop bandwidth frequency. Thus, the weighting functions for the MS active steering controller are selected as

$$\begin{cases} W_d = k_{wd},\ \mathbf{W}_n = diag\left(\left[\begin{array}{cc} k_{wn1}\dfrac{n_{wn1}s+1}{d_{wn1}s+1} & k_{wn2}\dfrac{n_{wn2}s+1}{d_{wn2}s+1}\end{array}\right]\right) \\ \mathbf{W}_p = diag\left(\left[\begin{array}{cc} \dfrac{s/M_1+w_{b1}}{s+w_{b1}A_1} & \dfrac{s/M_2+w_{b2}}{s+w_{b2}A_2}\end{array}\right]\right),\ \mathbf{W}_u = diag\left(\left[\begin{array}{cc} k_{wu1}\dfrac{(1/N_1)s+1}{Q_1 s+1} & k_{wu2}\dfrac{(1/N_2)s+1}{Q_2 s+1}\end{array}\right]\right) \end{cases} \tag{7.12}$$

where d_{wn1}, d_{wn2}, k_{wd}, k_{wn1}, k_{wn2}, k_{wu1}, k_{wu2}, n_{wn1}, n_{wn2}, w_{b1}, w_{b2}, A_1, A_2, M_1, M_2, N_1, N_2, Q_1, Q_2 are the design parameters tuned using the trail-and-error method for ideal performance.

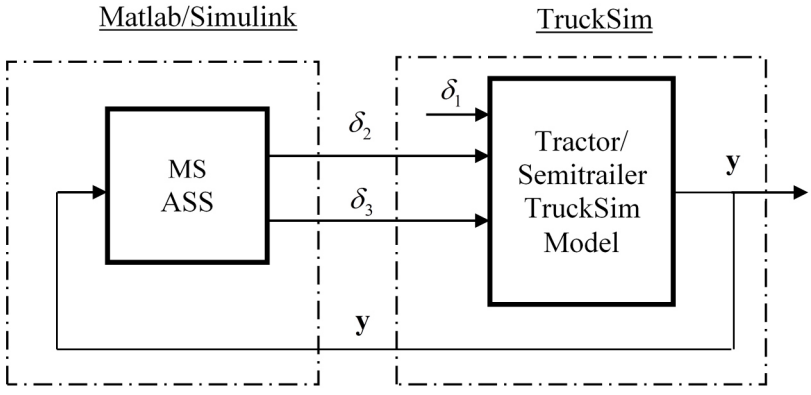

Figure 7.3 Structure of the TruckSim Model integrated with the MS controller

The structure of the MS controller is shown in Figure 7.3, integrated with the tractor/semitrailer model developed in TruckSim.

7.2.4 Design Variable Tuning Using the Frequency-Domain Design Optimization

The RA ratio in lateral acceleration is an important indicator of roll-over tendency for the semitrailer. The RA frequency function of the tractor/semitrailer provides complete information in a frequency range of interest. For an optimum trade-off between the high-speed maneuverability and stability, the RA frequency function should be restricted in the vicinity of 1.0. The design criterion for the frequency-domain design optimization may be chosen as

$$\min_{0\le f\le f_u} obj = RMS\left\{RA(f)-1\right\}, \textit{ with respect to } X_{ASS} \tag{7.13}$$

where X_{ASS} is the design variable vector of the active steering controller to be optimized. Note that RMS stands for the root mean square operation. For the SMC and NSMC based controllers, the X_{ASS} involves the closed-loop poles and the SMC gains. For the MS controller, the design parameters consist of the parameters of the frequency weighting functions. The frequency upper bound f_u is chosen from somewhere close to the crossover frequency using the with trail-and-error method. The tractor/semitrailer is excited with the multi-cycle sinewave steering input (MCSSI) in the continuous mode (Zhu et al, 2016). The RA frequency function $RA(f)$ is acquired using the AFRM (Zhu and He, 2015), and the fitness value is calculated using Equation (7.13). The genetic algorithm is utilized to search the optimal design variable vector to minimize the fitness value.

7.3 Simulation Result Analysis and Discussion

The active steering controllers are evaluated using the simulation results in the time-domain achieved under a low lateral acceleration Single Cycle Sinewave Lateral Acceleration (SCSLA)

maneuver specified in SAE J2179 (SAE, 1993 and Zhu et al, 2016) with the forward speed of 88 km/h, and under a high lateral acceleration double lane change maneuver (Zhu and He, 2016). The driver model built in TruckSim is employed to 'drive' the tractor/semitrailer combination with the active steering controllers. The active steering controllers are also examined with the simulation results in the frequency-domain acquired under the continuous Multi-cycle Sinewave Steer Input (MCSSI) maneuver (Zhu et al, 2016) using the AFRM technique.

7.3.1 Simulation Results under the SCSLA Maneuver

Figure 7.4 shows the desired trajectory to be tracked by the tractor CG under the SCSLA maneuver. Figure 7.5 shows the time histories of lateral accelerations of the TST with the active steering controllers based on the LQR, SMC, NSMC, and the MS techniques under the simulated SCSLA maneuver. Compared with the result of the passive TST provided in Chapter 3, the active steering controllers have the vehicle unit lateral accelerations reduced, especially that of the semitrailer. The RA ratios of all active steering controllers approach 1.0 under the simulated SCSLA maneuver. Almost an identical RA ratio has been achieved by all the controllers. It is difficult to differentiate the controllers under such a low lateral acceleration maneuver.

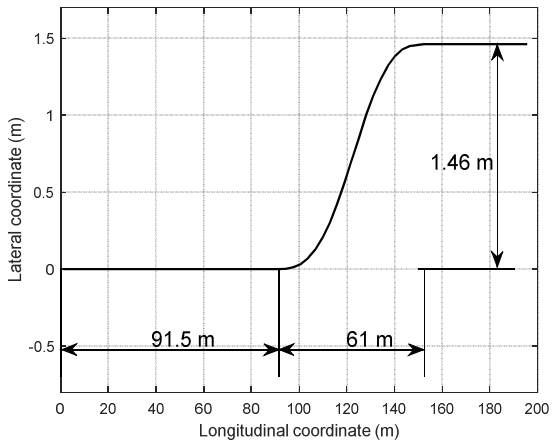

Figure 7.4 Desired trajectory tracked by the tractor CG under the SCSLA maneuver

Figure 7.6 shows the time histories of the active steering angles of the tractor rear wheels and the semitrailer wheels demanded by the different controllers under the SCSLA maneuver. The performance measure representing the energy consumed by the steering actuators on the tractor rear axle and on that of the semitrailer axles can be calculated as $\frac{1}{2}\sum_{k=1}^{\infty}\delta_2^2(k)$ and $\frac{1}{2}\sum_{k=1}^{\infty}\delta_3^2(k)$ (k is the sampling index), respectively. Figure 7.7 illustrates the energy consumption measure corresponding to the controllers of the LQR, SMC, NSMC, and the MS under the SCSLA maneuver. It is indicate that in terms of the energy consumption, the SMC controller is the most efficient, and the MS the least efficient.

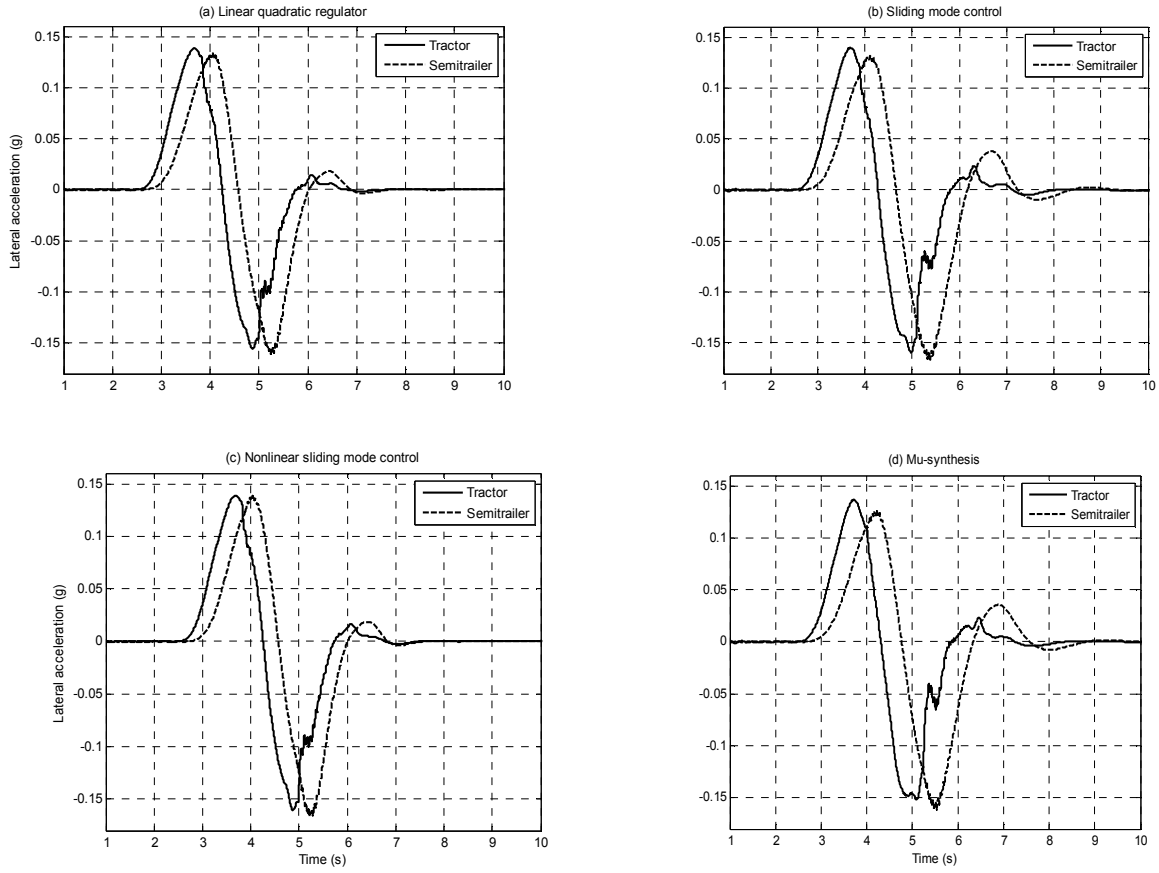

Figure 7.5 Time-histories of the lateral accelerations under the SCSLA maneuver of 88 km/h for the TST with different ASS controllers: (a) LQR, (b) SMC, (c) NSMC and (d) MS

The main feature of the MS controller different from all other controllers is the phase-shift which makes the control command asynchronous with the system output measurements. This creates an issue regarding applying the AFRM. When measuring the frequency response using the AFRM, the vehicle is excited by the continuous mode MCSSI. In the case of without phase-shift, the control effort induced over one sine wave cycle does not affect other cycles of the system. Thus, the input signal may has a zero initial value when starting a new cycle, which makes the AFRM technique applicable. The phase-shift makes the AFRM inapplicable. The phase-shift may be caused by frequency weighting without considering the phase response.

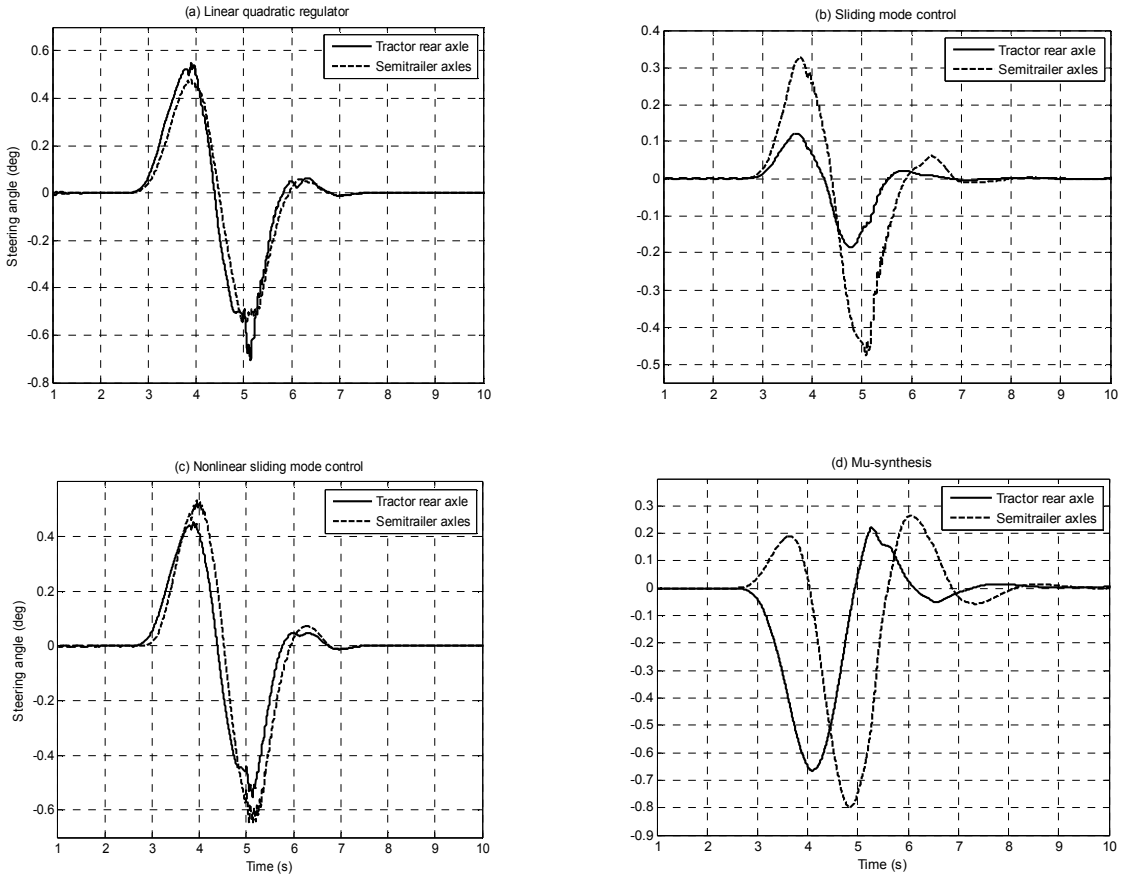

Figure 7.6 Time histories of the active steering angles of the tractor rear wheels and the semitrailer wheels under the SCSLA maneuver demanded by the controllers of: (a) LQR, (b) SMC, (c) NSMC, and (d) MS

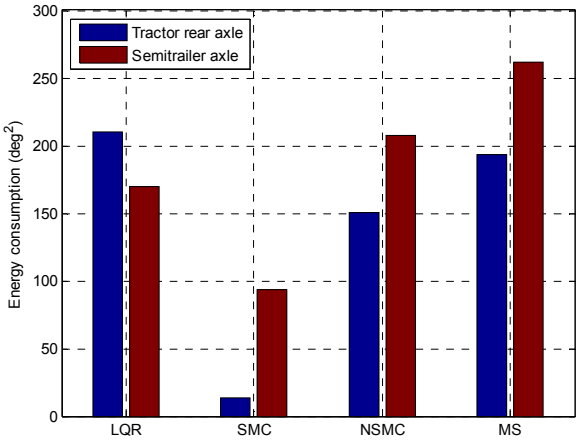

Figure 7.7 Energy consumption measure of the active steering system under the SCSLA maneuver with the controllers of the LQR, SMC, NSMC, and the MS

7.3.2 Simulation Results based on the Frequency Responses

The frequency response of the TST with the active steering controllers of the LQR, SMC, and the NSMC are acquired using the AFRM technique. The amplitude of the MCSSI input is restricted to avoid exciting the nonlinear dynamics of the TST. Figure 7.8 shows the RA frequency responses in lateral acceleration of the passive TST and the TST with the active steering controllers of the LQR, SMC, and the NSMC. The active steering controllers greatly improve the directional performance of the TST by keeping the RA ratio close to 1.0 within the frequency range of 0~0.6 Hz. Within the high frequency range of 0.6~1.0 Hz, the active steering controllers of the SMC and the NSMC outperform the LQR. For the passive TST, within the low frequency range, the RA is higher than that of the TST with active steering controllers, but at the high frequency the RA is lower than that of the TST with ASS. Figure 7.8 shows that among the four cases, the SMC controller exhibit the highest robustness over the frequency range of 0~1.0 Hz.

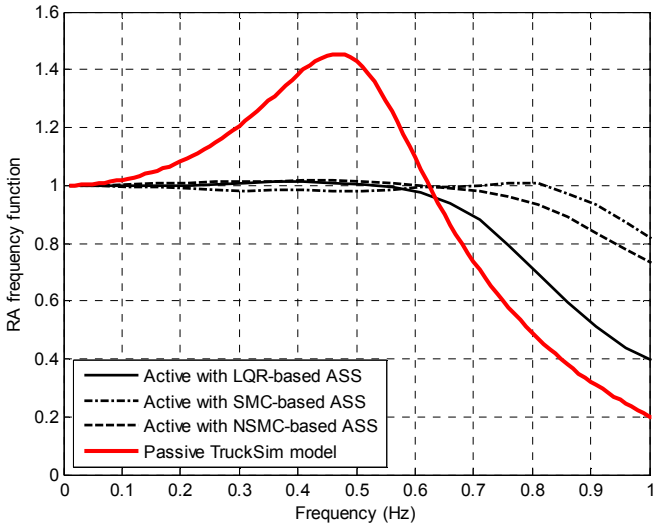

Figure 7.8 RA frequency response functions in lateral acceleration of the passive TST and the TST with the active steering controllers of the LQR, SMC and the NSMC

7.3.3 Simulation Results under the High Lateral Acceleration Maneuver

The robustness of the directional performance of the TST with the ASS controllers is examined under a simulated double lane change (DLC) meanouver. The tractor CG follows the desired trajectory shown in Figure 7.9 at a constant forward speed of 88 km/h. Three parametric uncertainty cases are studied: 1) the uncertain semitrailer sprung mass, 2) the uncertain longitudinal semitrailer CG position, and 3) the uncertain vertical semitrailer CG position. To assess the robustness of the controllers, a robustness index is introduced. For a total of n ($n = 20$ in this research) uncertain cases in a given case study, the maximum (max), mean (mn), and minimum (min) values of the responses at a specific time instant may be obtained. By connecting all max-, mn-, and min-points, respectively, three curves can be obtained, representing the upper-bound, mean, and the lower-bound of the responses of the n uncertain cases. The robustness index is defined as the reciprocal of the area enclosed by the upper- and lower-bound curves for a specific performance measure. If the performance measrue is the lateral acceleration of a vehicle unit, the

robustness index has a unit of s^2/mt . Thus, the robustness index in the lateral acceleration of the tractor with the LQR controller is given as

$$R_{a_{y1\_lqr}} = \frac{1}{\int_0^{\infty} \left(a_{y1\_lqr\_\max}(t) - a_{y1\_lqr\_\min}(t) \right) dt} \tag{7.14}$$

where $a_{y1\_lqr\_\max}$ and $a_{y1\_lqr\_\min}$ denote the upper- and lower-bound of the tractor lateral acceleration responses in a case study with the LQR controller. All other robustness indices of the TST with the ASS controllers can be similarly defined.

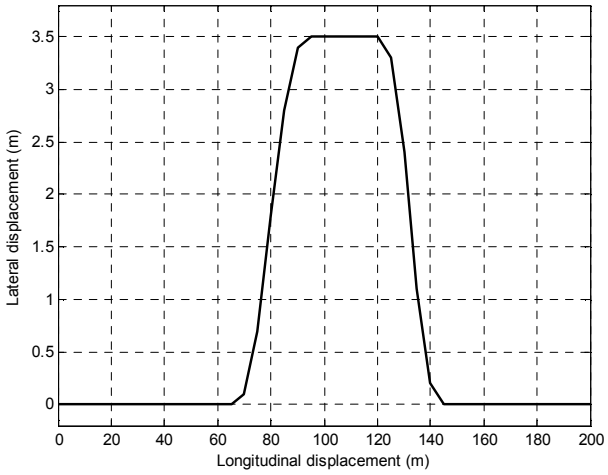

Figure 7.9 Target trajectory to be followed by the CG of the tractor under the DLC maneuver

7.3.3.1 Case Study on the Uncertain Semitrailer Sprung Mass

With the trailer sprung mass (including payload) varied from 0.5 to 2 times of the nominal value, i.e., $0.5m_{2nom} \le m_{2.u} \le 2m_{2nom}$, the upper-, mean- and lower-bound responses in the lateral accelerations and the active steering angles of the TST with the LQR controller can be achieved, and the resulting respnses are shown in Figure 7.10. It shows that the LQR controller does not exhibit good robustness to the semitrailer sprung mass variation.

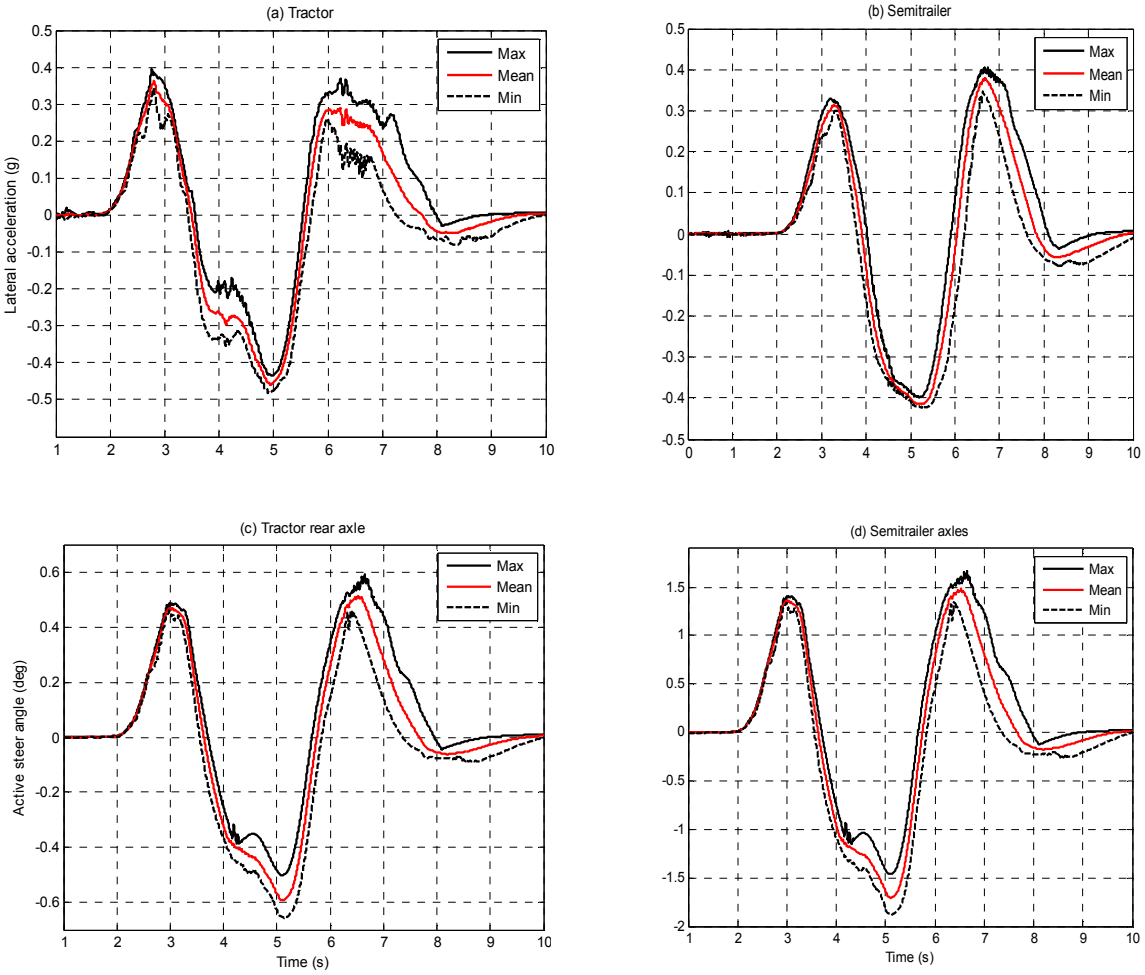

Figure 7.10 Responses of the TST with the LQR controller subject to the trailer sprung mass uncertainty: (a) tractor lateral acceleration, (b) semitrailer lateral acceleration, (c) tractor rear axle wheel steering angle, and (d) semitrailer axle wheel steering angle

Figures 7.11, 7.12, and 7.13 show the upper-, mean- and lower-bound curves of the lateral accelerations and active steering angles of the TST with the controllers of SMC, NSMC and MS, respectively. The corresponding robustness indices are listed in Table 7.1, and ploted in Figure 7.14. Among all the controllers considered, the responses of the NSMC are most noisiest, while the responses of the MS are smoothest. The SMC controller is most robust in the tractor lateral acceleration, followed by the MS, NSMC and the LQR; the SMC, MS and the NSMC improve the

robustness in the tractor lateral acceleration over that of the LQR by 93.22%, 77.3%, and 67.72%, respectively. Simliarly, the MS is most robust in the semitrailer lateral acceleration, followed by the SMC, NSMC, and the LQR; the MS, SMC, and the NSMC improve the robustness in the semitrailer lateral acceleration over that of the LQR by 122.51%, 118.91%, and 7.01%, respectively. The MS controller is most robust in the tractor rear wheel steering angle, followed by the SMC, NSMC, and the LQR. In terms of the semitrailer wheel steering angle, the MS is most robust, followed by the LQR, SMC, and the NSMC.

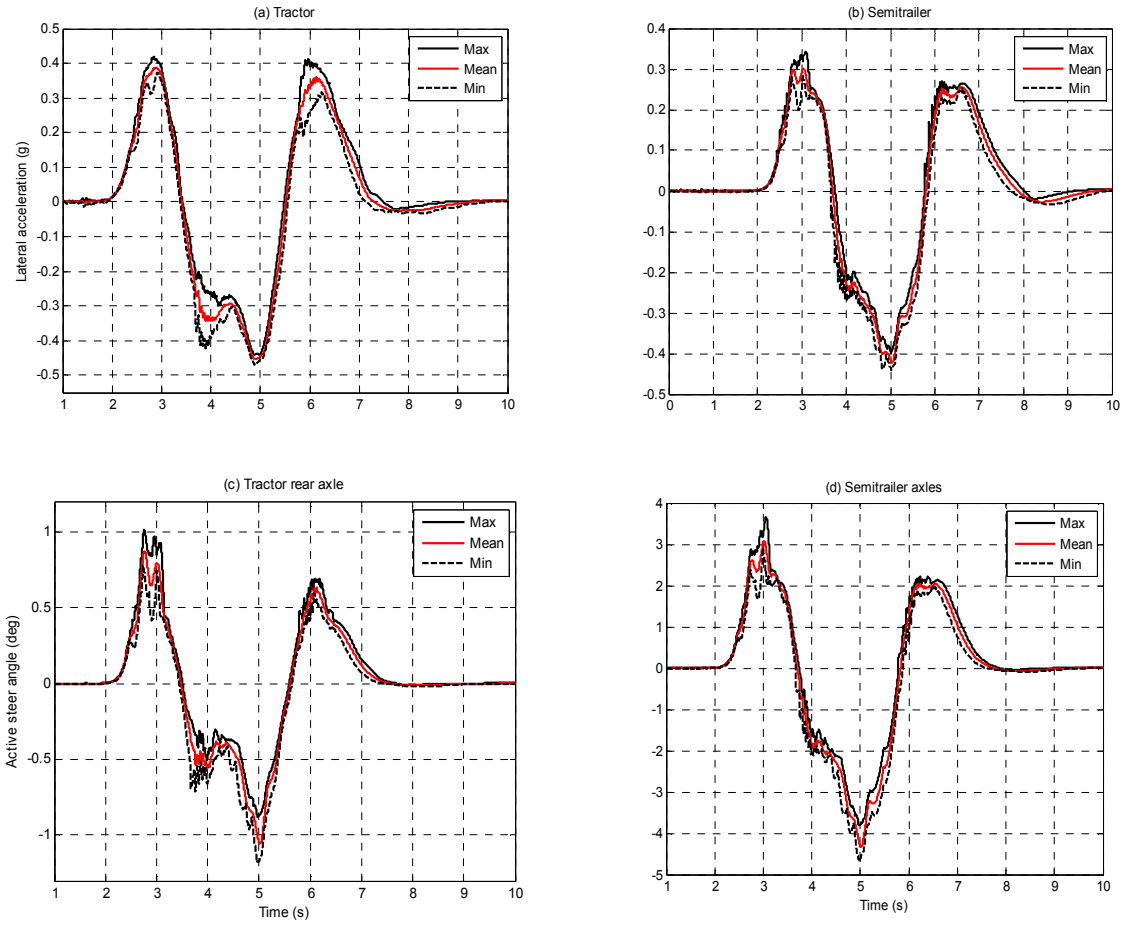

Figure 7.11 Responses of the TST with the SMC controller subject to the semitrailer sprung mass uncertainty: (a) tractor lateral acceleration, (b) semitrailer lateral acceleration, (c) tractor rear wheel steering angle, and (d) semitrailer wheel steering angle

Table 7.1 Robustness indices of the TSTs with the ASS controllers subject to semitrailer sprung mass uncertainty

	LQR	SMC		NSMC		MS	
	* R_{idx}	* R_{idx}	# R_{imp}	* R_{idx}	# R_{imp}	* R_{idx}	# R_{imp}
$R_{a_{y1}}$	1.2728	2.4593	93.22%	2.1348	67.72%	2.2569	77.32%
$R_{a_{y2}}$	1.4045	3.0746	118.91%	1.5030	7.01%	3.1252	122.51%
R_{δ_2}	1.0380	1.2149	17.04%	1.1716	12.87%	1.5322	47.61%
R_{δ_3}	0.3733	0.3567	-4.45%	0.2154	-42.30%	0.8113	117.33%

* R_{idx} is the robustness index defined in Equation (7.14)

R_{imp} is the relative improvement of the robustness over that of the LQR controller

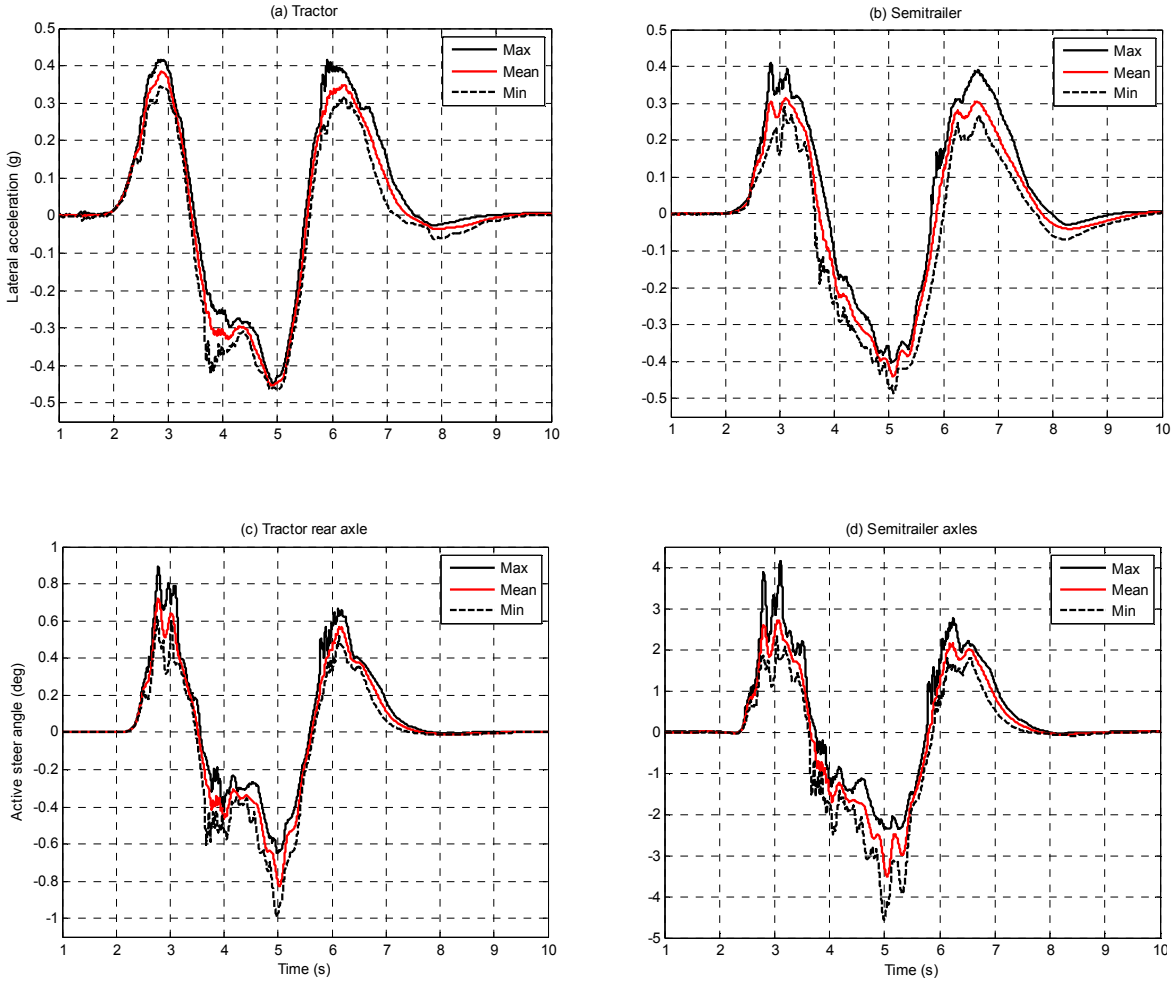

Figure 7.12 Responses of the TST with the NSMC controller subject to the semitrailer sprung mass uncertainty: (a) tractor lateral acceleration, (b) semitrailer lateral acceleration, (c) tractor rear wheel steering angle, and (d) semitrailer wheel steering angle

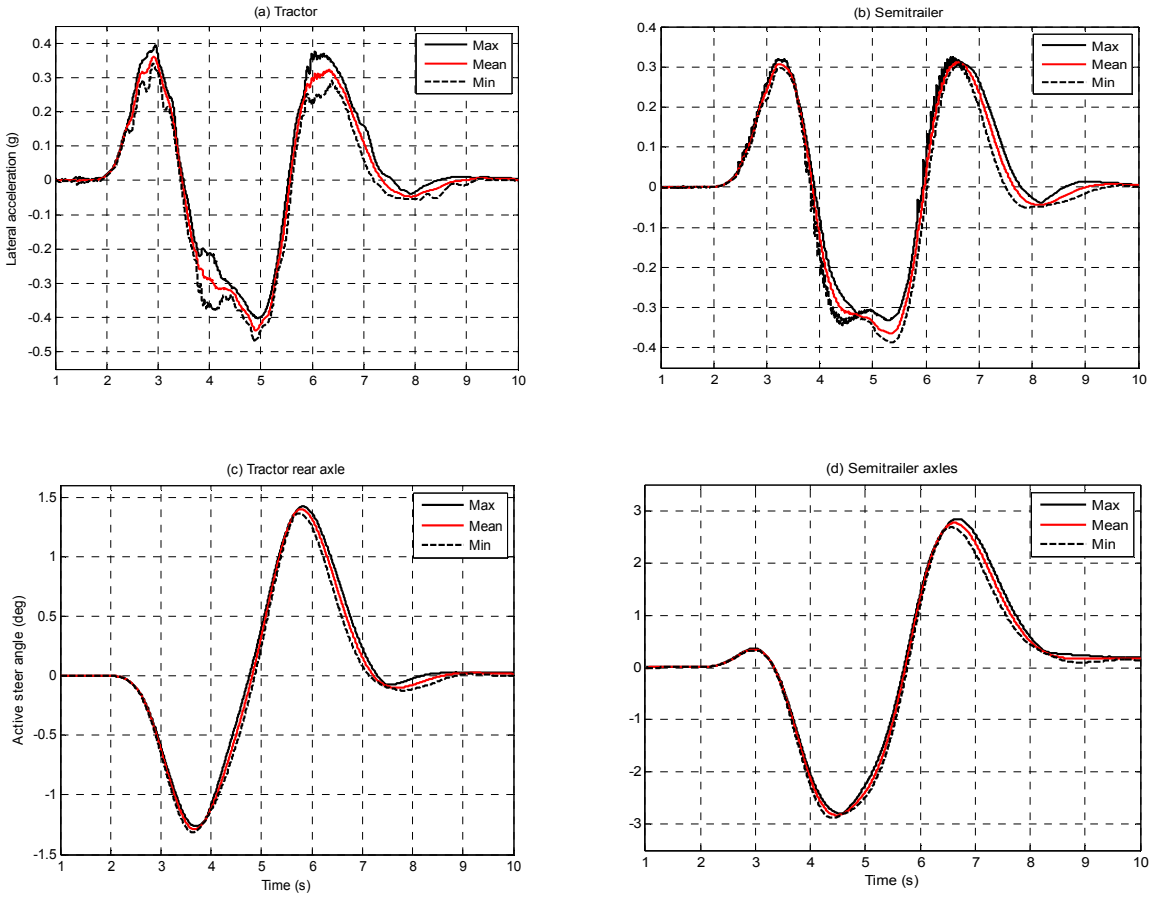

Figure 7.13 Responses of the TST with the MS controller subject to the semitrailer sprung mass uncertainty: (a) tractor lateral acceleration, (b) semitrailer lateral acceleration, (c) tractor rear wheel steering angle, and (d) semitrailer wheel steering angle

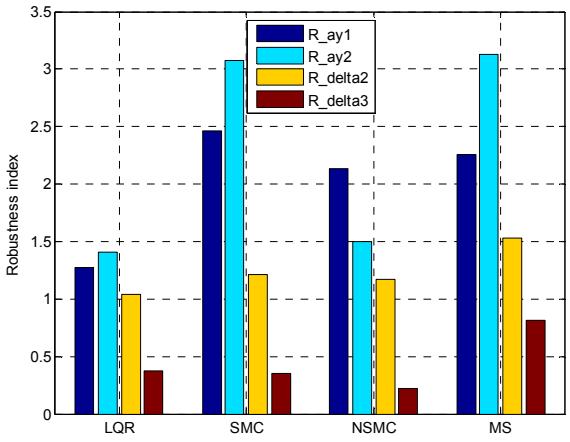

Figure 7.14 Robustness indices of the TST with different controllers subject to the semitrailer sprung mass uncertainty

7.3.3.2 Case Study on the Uncertain Semitrailer CG Longitudinal Position

The robustness of the directional performance of the TST with different active steering controllers is examined under the simulated DLC maneuver subjet to the variation of the semitrailer CG longitudinal position in the range of 0.4 to 1.25 times of the nominal value $\left(0.4l_{21nom} \le l_{21} \le 1.25l_{21nom}\right)$. The robustness indices of the lateral acceleration and the steering angles of the tractor rear wheels and the semitrailer wheels demanded by the LQR, SMC, NSMC, and the MS are listed in Table 7.2 and shown in Figure 7.15.

Compared with the indices shown in Figure 7.14, those seen in Figure 7.15 are lower. This implies that the active steering controllers are more sensitive to the variation of the semitrailer CG longitudinal position than to the change of the semitrailer sprung mass. Furthermore, subject to the variation of the semitrailer CG longitudinal position, the simulation results confirm that the MS controller is the most robust, whereas the LQR is the least robust; in between, the SMC and the NSMC exhibit comparable robustness. The SMC, NSMC and the MS improves the robustness in the tractor lateral acceleration by 51.58%, 58.78%, and 60.13%, and in the semitrailer lateral acceleration by 6.93%, -7.51% and 22.26%, respectively, with respect to the corresponding indices of the LQR controller.

Table 7.2 Robustness indices of the TST with different ASS controllers subject to the variation of trailer CG longitudinal position

	LQR	SMC		NSMC		MS	
	* R_{idx}	* R_{idx}	# R_{imp}	* R_{idx}	# R_{imp}	* R_{idx}	# R_{imp}
$R_{a_{y1}}$	0.9574	1.4512	51.58%	1.5202	58.78%	1.5331	60.13%
$R_{a_{y2}}$	1.2444	1.3307	6.93%	1.1509	-7.51%	1.5214	22.26%
R_{δ_2}	0.5134	0.6330	23.29%	0.5752	12.04%	0.9036	76.00%
R_{δ_3}	0.1824	0.2507	37.44%	0.1364	-25.22%	0.2374	30.15%

* R_{idx} is the robustness index defined in Equation (7.14)

R_{imp} is the relative improvement of the robustness over that of the LQR controller

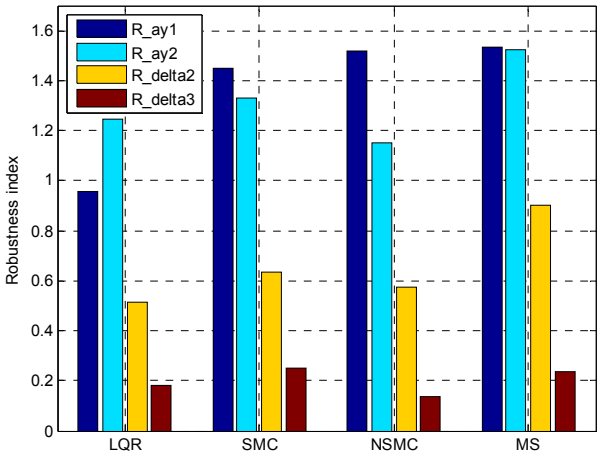

Figure 7.15 Robustness indices of the TST with different ASS controllers subject to the variation of the semitrailer CG longitudinal position

7.3.3.3 Case Study on the Uncertain Semitrailer CG Vertical Position

The robustness of the active steering controllers is evaluated under the simulated DLC maneuver subject to the variation of the semitrailer CG vertical position in the range of 1 to 2 times of the nominal value, i.e., $h_{CGnom} \le h_{CG} \le 2h_{CGnom}$. The resulting robustness indices are listed in Table 7.3 and plotted in Figures 7.16 and 7.17. Compared with the other parametric uncertainties considered, the active steering controllers are more robust to the uncertainty of the semitrailer CG vertical position.

The results disclose a phenomenon that the LQR and MS controllers outperform the SMC and the NSMC controllers. In terms of the steer angles of the tractor rear wheels and the semitrailer wheels, the SMC and NSMC controllers are not sensitive to the variation of the semitrailer CG vertical position. This observation may be interpreted by the fact that the semitrailer CG vertical position mainly affect the inertia properties of the roll dynamics of the semitrailer; and the coupling of the roll dynamics and the yaw dynamics of the TST is loose. The SMC and NSMC controllers work on the full states of the yaw-plane models which are least affected by the roll dynamics-

related parametric uncertainty. However, the LQR and MS controllers are designed considering the vehicle units' lateral accelerations, which are dependent on the roll dynamics of the TST. The MS controller has the robustness index increased by 21.12% in the tractor acceleration, decreased by 22.23% in the semitrailer lateral acceleration, increased by 39.29% in the tractor rear wheel steering angle, and increased by 45.29% in the semitrailer wheel steering angle, with respect to the corresponding robustness indices of the LQR controller.

Table 7.3 Robustness indices of the TST with different ASS controllers subject to the variation of trailer CG vertical position

	LQR	SMC		NSMC		MS	
	* R_{idx}	* R_{idx}	# R_{imp}	* R_{idx}	# R_{imp}	* R_{idx}	# R_{imp}
$R_{a_{y1}}$	4.8055	3.3703	-29.86%	3.8163	-20.58%	5.8206	21.12%
$R_{a_{y2}}$	5.3614	1.9484	-63.66%	2.4276	-54.72%	4.1696	-22.23%
R_{δ_2}	3.0907	811.8262	261.67	652.8228	210.22	4.3049	39.29%
R_{δ_3}	1.1038	299.7797	270.59	111.4278	99.95	1.6108	45.93%

* R_{idx} is the robustness index defined in Equation (16)

R_{imp} is the relative improvement of the robustness over that of the LQR controller

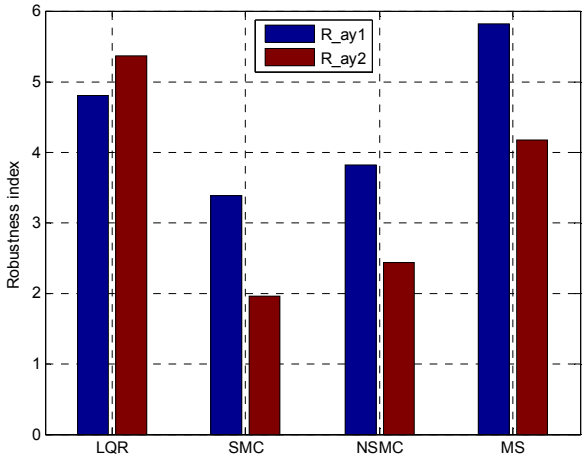

Figure 7.16 Robustness indices in the lateral accelerations of the vehicle units of the TST with different ASS controllers subject to the variation of the semitrailer CG vertical position

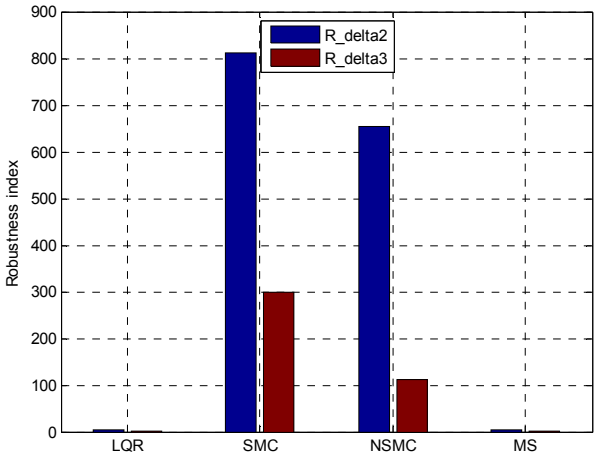

Figure 7.17 Robustness indices in the steer angles of the tractor rear wheels and the semitrailer wheels of the TST with different active steering controllers subject to the variation of the semitrailer CG vertical position

7.4 Conclusions

Three robust active steering system controllers, namely, the SMC, NSMC and the MS, have been studied for improving the high-speed maneuverability and stability of AHVs. To evaluate the robustness of the ASS controllers, co-simulations are conducted by integrating the ASS controllers designed in Matlab/Simulink software and a nonlinear tractor/semitrailer model developed in TruckSim package. The MS-based controller differs from the others by introducing phase-shift into the control command, which makes the AFRM inapplicable. With the AFRM, the design variables of the controllers based on the LQR, SMC, and the NSMC techniques are optimized by using a genetic algorithm for the optimal trade-off between the high-speed maneuverability and the stability in a frequency range of interest. A robustness index has been defined to quantify the robust performance of the ASS controllers based on the LQR, SMC, NSMC and the MS techniques under a high lateral acceleration maneuver.

The simulation results show that it is hard to differentiate the ASS controllers under a low lateral

acceleration maneuver. Under a high lateral acceleration maneuver, the ASS controllers demonstrate different robustness to the parametric uncertainties. Amongst the uncertainties considered, the ASS controllers are the most robust to the uncertainty of the semitrailer CG vertical position and the least robust to the variation of the semitrailer CG longitudinal position. Amongst all the ASS controllers investigated, the MS is the most robust to the uncertainties of the semitrailer sprung mass and the semitrailer CG longitudinal position. Subject to the uncertainty of the semitrailer CG vertical position, the robustness of the LQR and MS based controllers is comparable, and these controllers outperform the SMC and NSMC based controllers.

Chapter 8 An Investigation of Test Maneuvers for Determining Rearward Amplification of Multi-trailer Articulated Heavy Vehicles

8.1 Introduction

Rearward amplification (RA) ratio has been utilized to quantify the obstacle avoidance capability of articulated heavy vehicles (AHVs) since the 1970s (Ervin et al, 1978, Winkler et al, 1992). The RA ratio, defined as the gain of the lateral motion of the rearmost unit and that of the leading unit (Ervin and Guy, 1986, Winkler et al, 1992, Fancher and Winkler, 1992, Woodrooffe and Milliken, 2007 and Wang and He, 2015), describes the tendency of the last trailer to swing out of line or roll over under obstacle avoidance maneuvers (Winkler et al, 1992). AHVs having a lower value of the RA face less risk of rollover under obstacle avoidance maneuvers (Fancher and Winkler, 1992, Woodrooffe and Milliken, 2007). The accident involvement rate is directly associated with the level of RA ratios (Winkler et al, 1992).

The research on the RA can be traced back to the later 1970s. Since then various ad hoc procedures and scenarios have been developed to test the RA measure of AHVs (Ervin et al, 1978, Ervin and Guy, 1986, Winkler et al, 1986, Fancher and Winkler, 1992, Winkler et al, 1992, Winkler et al, 1993). After two decades accumulation of knowledge and experience, there came two milestone events: 1) the Society of Automotive Engineers issued SAE-J2179 in 1993 (SAE-J2179, 1993), setting the single cycle sine wave lateral acceleration input (SCSLA) as the recommended practice, and 2) the International Organization for Standardization released ISO-14791 in 2000 (ISO-14791, 2000), proposing the single cycle sine wave steer input (SCSSI), the SCSLA and

the pseudo random steer input (PRSI) as standard maneuvers for evaluating the RA measure of multi-trailer articulated heavy vehicles (MTAHVs).

Zhu and He (2015) proposed a method for determining the RA measure of AHVs using the automated frequency response measuring (AFRM) technique. With the AFRM technique, a repetitive frequency measurement using sine waves with various frequencies and amplitudes can be assigned to a computer in a way that signal generation, model simulation, and frequency response measurement can be conducted in real-time, and thus an accurate RA frequency function can be achieved.

When determining the RA, one has the time- and frequency-domain maneuvers available. The frequency-domain maneuvers provide a complete RA frequency function of AHVs in a frequency range of interest. The time-domain maneuvers yield composite information of the AHV at a specified frequency. The RA measure under one maneuver differs from that under another (Aurell and Winkler, 1995). Even with the time-domain maneuvers, the result of the SCSLA does not match that of the SCSSI. Wang and He (2015) attributed this disparity to the transient response effect and attempted to minimize it by using the so-called multi-cycle sine wave steer input (MCSSI).

This chapter focuses on identifying the root causes of the disparity and mismatch of the RA measures derived from different testing maneuvers. Various maneuvers, including the SCSSI, MCSSI, and SCSLA in the time-domain as well as the PRSI and the AFRM procedures in the frequency-domain are considered. The factors causing the disparity and mismatch are identified using numerical simulation in the time-domain, and the identified causes are further proved and interpreted using the results derived from the simulated maneuvers in the frequency-domain. Through the simulation and data analysis process, a testing maneuver will be determined, which

bears the strengths of the aforementioned testing maneuvers. A nonlinear yaw-roll model for a B-train double is constructed in TruckSim in order to acquire the RA measures under various simulated testing maneuvers. The resulting data sets are processed in the Matlab/Simulink.

8.2 Vehicle Modeling and Test Maneuvers

8.2.1 TruckSim Model

The B-train double model is constructed in TruckSim to simulate the directional performance of the vehicle under a specified testing maneuver. As shown in Figure 8.1, the configuration of the B-train double is defined as "*S_SS+SSS+SSS*", where "*S*" indicates a solid axle, an underscore "_" a separation of the axle groups, a "+" a fifth-wheel connecting two vehicle units. Thus, as the configuration indicated, the B-train double consists of a 3 solid-axle tractor having one front axle and two rear axles, and two semitrailers each having one tridem axle group.

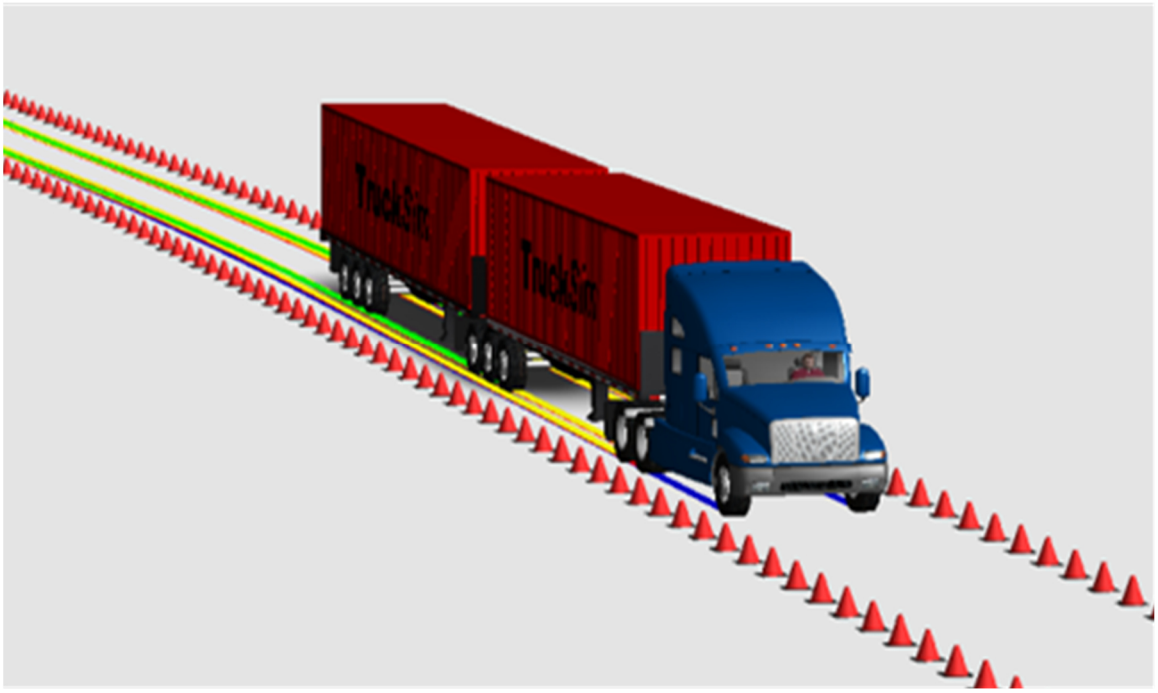

Figure 8.1 TruckSim model of the B-train double

In the TruckSim model, the nonlinear dynamics of the pneumatic tires, suspension systems and the mechanical joints are taken into account. For the nonlinear vehicle model, the motions considered are as follows. Each sprung mass is considered as a rigid body with six DOF, namely lateral, longitudinal, vertical, pitch, roll and yaw motions. The fifth-wheel is modeled as a ball-joint, about which roll, yaw, and pitch motions are allowed. Each axle (group) is treated as a beam axle which can roll and bounce with respect to the sprung mass to which it is attached. Each wheel is modeled with a spinning DOF. Thus, the B-train double is represented by the nonlinear TruckSim model with thirty-eight DOF.

8.2.2 Test Maneuvers for Determining RA

The RA is an effective performance measure to assess the lateral stability of AHVs. The high-speed stability of AHVs may be characterized using the RA measures either in yaw rate or in lateral acceleration gain of the rearmost trailing unit to that of the leading unit under a lane-change maneuver. To measure the RA of multi-unit combination vehicles or articulated buses, the ISO-14791 recommends three test maneuvers, namely, 1) pseudo-random steer input (PRSI), 2) single cycle sine wave steer input (SCSSI), and 3) single cycle sine-wave lateral acceleration (SCSLA). The time-domain test maneuvers, the SCSSI and SCSLA, provide a composite RA gain at a specific frequency; and the frequency-domain test maneuver, the PRSI, provides complete information of RA in a frequency range of interest (Aurell and Koppenaal, 1998). With the PRSI test maneuver, the frequency response functions are obtained using the Fourier transform after the response data of all frequency contents has been recorded, and thus suitable for off-line applications.

The AFRM technique discussed in Chapter 4 may also be applied to obtain the RA frequency function of MTAHVs. With the AFRM technique, steer signal generation, vehicle excitation, and

RA frequency function acquisition are conducted automatically at a given frequency. All the relevant processes should be completed before the frequency being updated. Thus, the AFRM technique is suitable for on-line and real-time applications, and appropriate for frequency-domain design optimization of MTAHVs. For detailed information of the AFRM technique, readers are referred to Zhu and He (2015).

8.3. Tractor Lateral Acceleration Kinematic Analysis and Driver's Characteristics

8.3.1 Kinematic Analysis

MTAHVs are usually modeled with multiple interconnected rigid bodies. Each body may be viewed as a lumped mass at the center of gravity (CG). Depending on the level of details considered, a single (e.g., in a yaw-plane model) or multiple bodies (e.g., in a yaw-roll model) are utilized to describe a vehicle unit. In either way, the RA of a MTAHV may be defined as the ratio of the lateral acceleration or yaw rate measured at the whole mass CG of the rearmost unit to that of the leading unit measured at the whole mass CG (Islam et al, 2015). In the SCSLA test, a desired trajectory is predefined for the CG or the front axle center of the leading unit in a kinematic relationship (Preston-Thomas and E-Gindy, 1995, and ISO-14791, 2000). In practice, the front axle center of the tractor is usually pursued by human drivers and driver models (MacAdam, 1981 and He et al, 2016) in conducting lane-change maneuvers. While considering the low-speed maneuverability of a MTAHV, the low-speed off-tracking (a performance measure), defined as the maximum radial offset between the trajectories of the tractor front axle center and that of the rearmost trailer axle center (He et al, 2015), may be used.

Defining the RA measure in the lateral acceleration at the front axle roll center may bring some benefits. It not only ensures convenience and consistency in the modeling for maneuverability and stability investigation, but also removes the influence of the roll and yaw dynamics of the vehicle

concerned on the RA measure. The lateral acceleration at the front axle roll center can be calculated based on the lateral acceleration at the tractor CG and other relative states of the vehicle unit. Given the lateral acceleration at the whole mass CG of the tractor a_{y1_CG}, and assuming that the roll axis is parallel to the ground surface, the lateral acceleration at the tractor front axle roll center can be determined as

$$a_{y1\_ax} = a_{y1\_CG} + \frac{m_{s1}}{m_1}\left(h_{r1} - h_{s1}\right)\ddot{\phi}_1 + a_{11}\ddot{\psi} \tag{8.1}$$

where a_{11} denotes the longitudinal distance from the whole mass CG of the tractor to its front axle center, a_{y1_ax} the lateral acceleration at tractor front axle roll center, h_{r1} the height of roll center measured from the ground, h_{s1} the height of the tractor sprung mass CG measured from the ground, m_{s1} the tractor sprung mass, m_1 the tractor whole mass, ϕ_1 the roll angle of the tractor sprung mass, ψ_1 the yaw angle of the tractor unit. The 2nd and 3rd terms at the right hand side of Equation (8.1) are contributed by the roll- and yaw-motion, respectively.

The comparison of the individual lateral acceleration terms achieved under a MCSSI maneuver at forward speed of 110km/h is shown in Figure 8.2. The summation of the first two terms forms the lateral acceleration at the roll center under the tractor whole mass CG, which bears the influence of the roll dynamics. The lateral accelerations at the whole mass CG, at the roll center under the tractor whole mass CG and at the tractor front axle roll center are shown in Figure 8.3. The yaw motion introduces phase lead into the lateral acceleration at the tractor front axle roll center.

To maintain consistency throughout the chapter, the RA ratio is defined as the gain of the lateral acceleration at the whole mass CG of the 2nd semitrailer to that of the lateral acceleration at the tractor front axle roll center as proposed by Fancher and Winkler (1992).

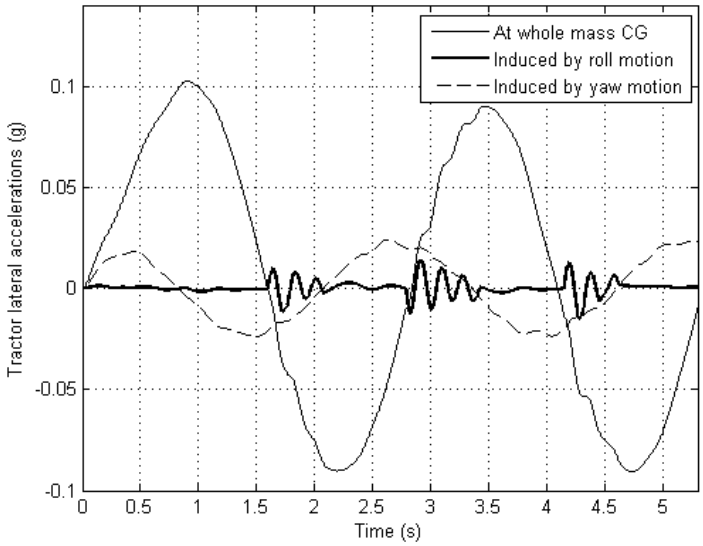

Figure 8.2 Time histories of the lateral acceleration at the whole mass CG, that contributed by the roll motion and that induced by the yaw motion of the B-train double TruckSim model under a MCSSI maneuver at the forward velocity of 110km/h

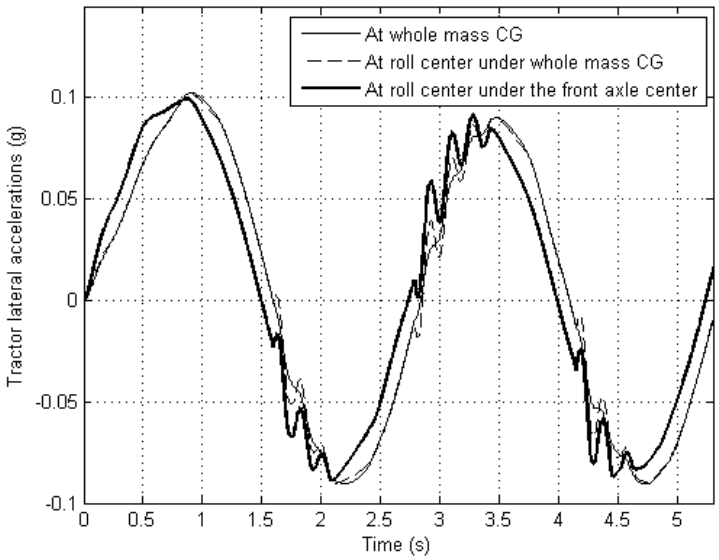

Figure 8.3 Time histories of lateral accelerations at the whole mass CG, at the roll center under the whole mass CG, and the at the tractor front axle roll center of the B-train double TruckSim model under a MCSSI maneuver at the forward velocity of 110km/h

8.3.2 Driver's Characteristics

When utilizing the McAdam preview driver model provided in the TruckSim software to 'drive' the virtual MTAHV, the driver's characteristics, related to the preview time and time lag, and may affect the combined performance of the driver-vehicle system. The target trajectory of the tractor front axle roll center is defined by the kinematic relationship (Preston-Thomas and E-Gindy, 1995, ISO-14791, 2000, and MacAdam and Hagan, 2002), the same as Equation (6.14), as

$$Y = \frac{\overline{a}_{y1\_ax}}{(2\pi f)^2}\left[2\pi f \frac{X}{U} - \sin\left(2\pi f \frac{X}{U}\right)\right] \tag{8.2}$$

where $\overline{a}_{y1\_ax}$ denotes the amplitude of the single cycle sine wave lateral acceleration input (SCSLA), f denotes the frequency of the SCSLA in Hz, U the forward speed of the vehicle (m/s), X the longitudinal position, and Y the lateral position. The effect of the parameters of the driver model, preview time and time lag, and their influence on the XY trajectory of the tractor front axle roll center, and the lateral accelerations at the whole mass CG and at the tractor front axle roll center are considered.

8.3.2.1 Influence of the Preview Time

With $f = 0.4$ Hz, $\overline{a}_{y1\_ax} = 0.15$ g, and $U = 110$ km/h, time lag $\tau_d = 0$ s and preview time T_p varying from 0.1 to 1.5s, the target and XY trajectories of the tractor front axle roll center are shown in Figure 8.4. The lateral accelerations at the tractor whole mass CG and at the tractor front axle roll center are shown in Figures 8.5 and 8.6, respectively. The response speed of the XY trajectory gradually decreases following the growth of the preview time. The lateral accelerations grow following the speed up of the responses of the XY trajectory, and demonstrate high-frequency vibration when the lateral accelerations overpass 0.15g in magnitude.

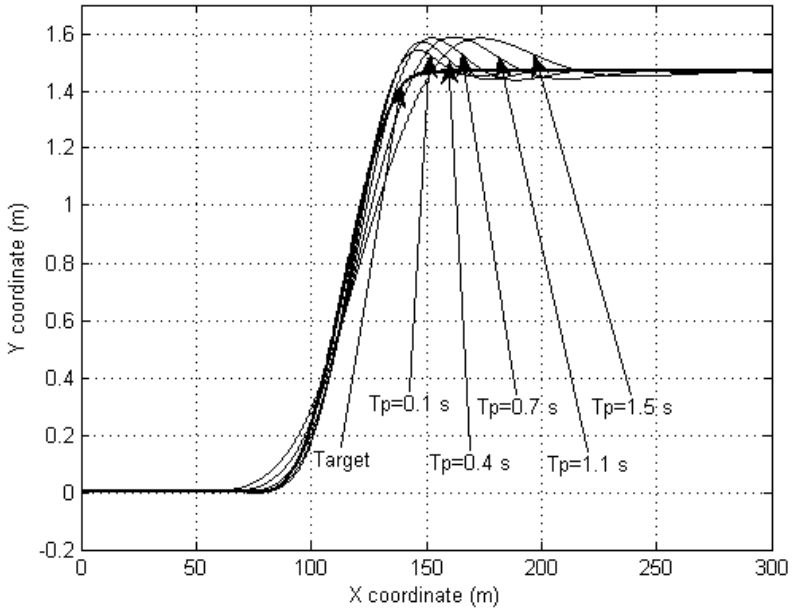

Figure 8.4 Target and XY trajectories of the tractor front axle roll center under the single sine wave lateral acceleration test at forward velocity 110 km/h and driver's time lag $\tau_d = 0$ s and preview time T_p varied from 0.1 to 1.5s

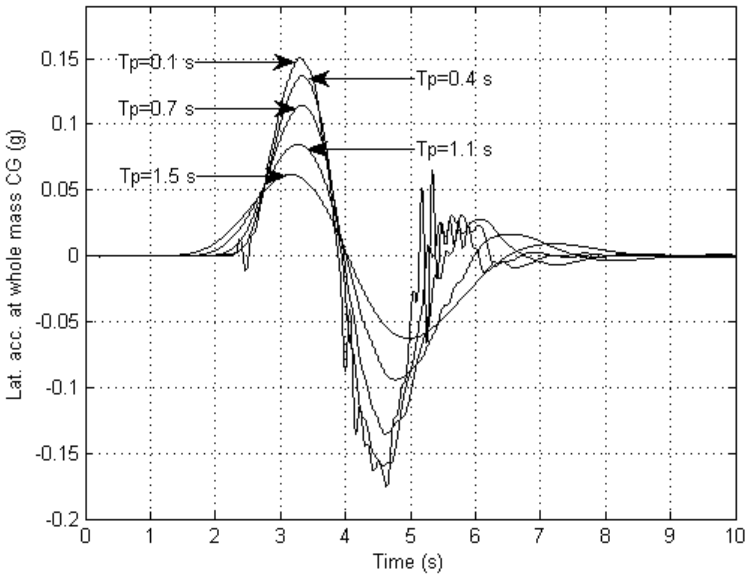

Figure 8.5 Lateral accelerations at the tractor whole mass CG under the SCSLA test at forward speed of 110 km/h and driver's time lag $\tau_d = 0$ s and preview time T_p varied from 0.1 to 1.5s

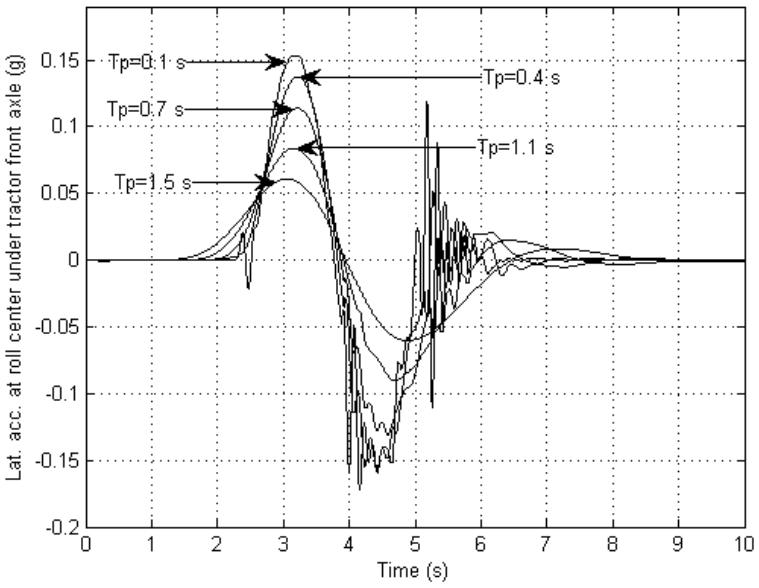

Figure 8.6 Lateral accelerations at the tractor front axle roll center under the SCSLA test at forward speed of 110 km/h and driver's time lag $\tau_d = 0$ s and preview time T_p varied from 0.1 to 1.5s

The filtering effect of the roll dynamics is clearly shown when the lateral acceleration at the whole mass CG reaches a high level in amplitude. Since the roll dynamics has been removed from the lateral acceleration at the tractor front axle roll center, thus higher amplitude of vibration can be expected. The influence of the preview time of the driver model is significant. To achieve the designated single cycle lateral acceleration specified in the kinematic equation (8.2), the preview time has to be carefully manipulated.

8.3.2.2 Influence of the Time Lag

The influence of the time lag of the driver model on the response of the tractor is shown in Figures 8.7 through 8.9. As shown in Figure 8.7, the influence of the time lag varied from 0 to 0.05s on the XY trajectory of the tractor front axle roll center is not apparent, but evident on the lateral accelerations at the tractor front axle roll center and the tractor whole mass CG. Increasing the

time lag may cause instability of the tractor. As shown in Figures 8.8 and 8.9, when the time lag reaches 0.05s the lateral accelerations start to vibrate when the lateral acceleration sine-wave completes a full cycle. Further increasing the time lag would amplify the vibration and lead to yaw instability. The amount of time lag can be sustained without loss of stability may be related to the length of preview time: the longer the preview time, the longer time lag can be tolerated before loss of stability. Furthermore, the influence of the time lag on the lateral acceleration at the front axle roll center is more evident than that at the tractor whole mass CG due to lack of filtering effect of the roll dynamics.

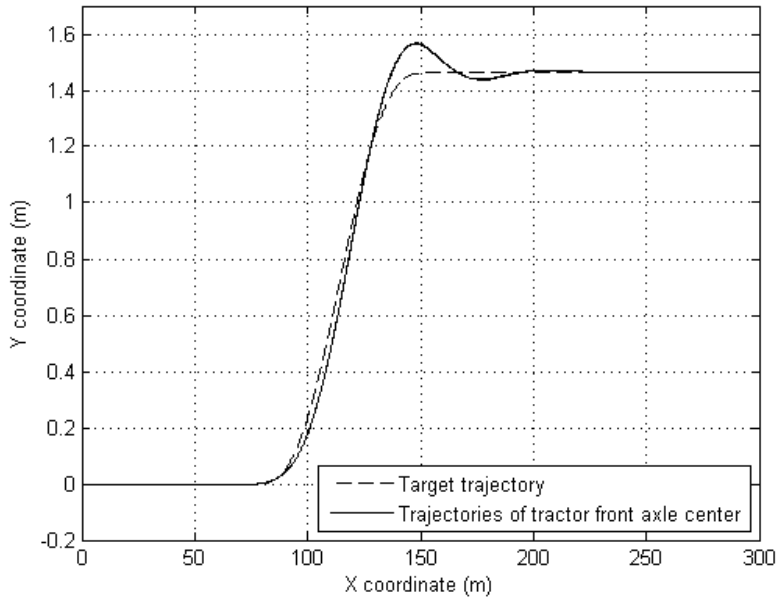

Figure 8.7 Target and XY trajectory of the tractor front axle center under the SCSLA test at the forward speed of 110 km/h and driver's time lag τ_d varied from 0 to 0.05 s with preview time $T_p = 0.4$ s

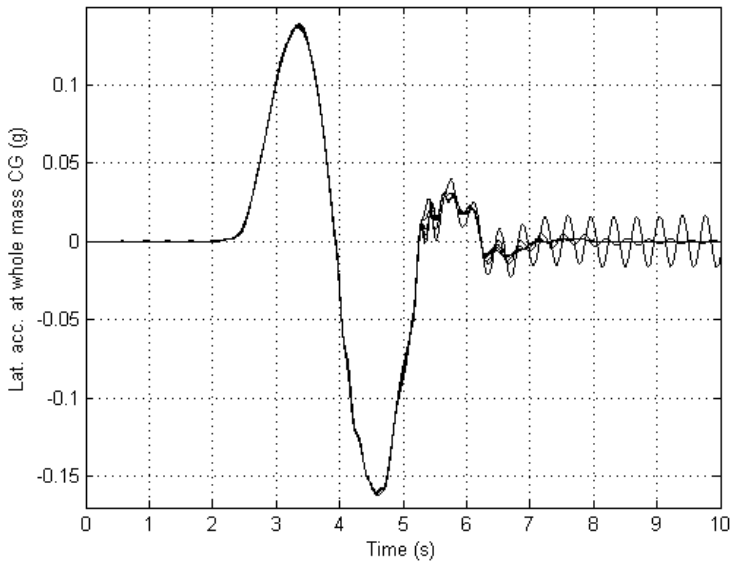

Figure 8.8 Time histories of lateral accelerations at the tractor whole mass CG under the SCSLA maneuver at forward speed of 110 km/h and driver's time lag τ_d varied from 0 to 0.05s with preview time $T_p = 0.4s$

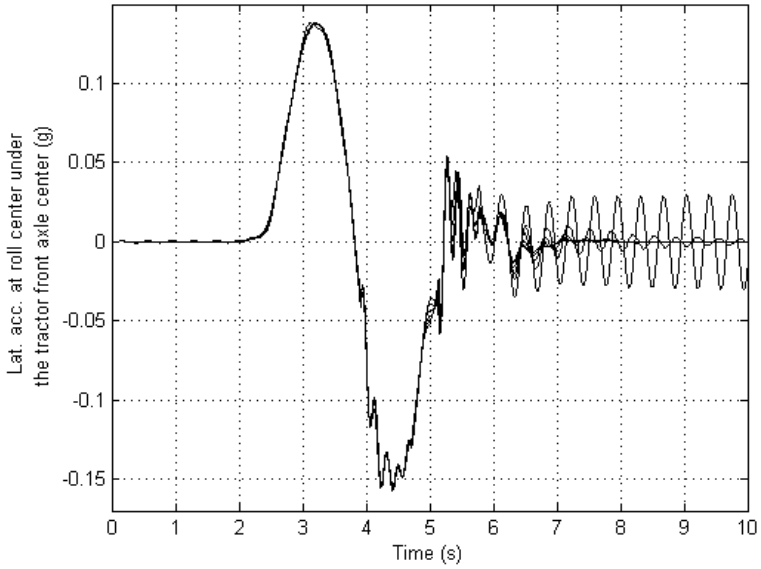

Figure 8.9 Time histories of lateral acceleration at the tractor front axle roll center under the SCSLA maneuver at forward speed of 110 km/h and driver's time lag τ_d varied from 0 to 0.05s with preview time $T_p = 0.4s$

8.4 RA Measures of the B-Train Double

In the following section of this chapter, the forward speed of the B-train double is assumed constant at 110km/h. The following test maneuvers are used to to determine the RA: 1) SCSSI, 2) SCSLA, 3) MCSSI, 4) pseudo-random binary sequence (PRBS) steer input, 5) PRSI; and 6) AFRM. The RA frequency functions from different test maneuvers are compared; and the disparity and mismatch are identified, interpreted and minimized in the time- and frequencey-domain approaches.

8.4.1 RA Frequency Functions with the MCSSI and the AFRM

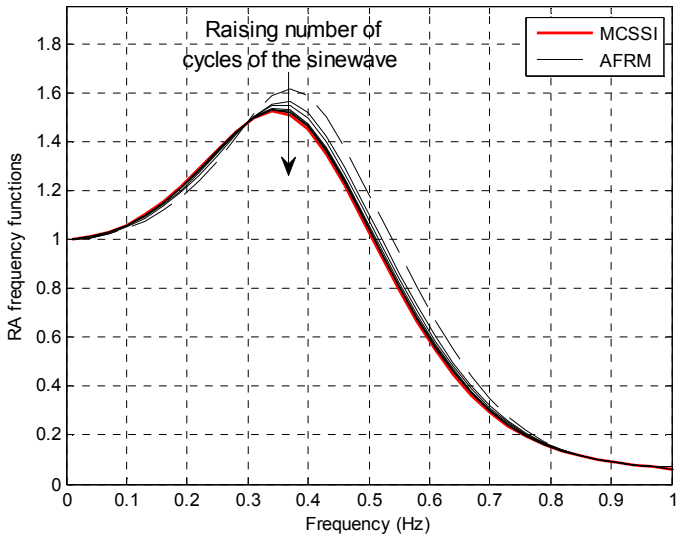

Figure 8.10 RA frequency functions of the B-train double obtained with the MCSSI and the AFRM of different number of cycles

A simple way to acquire the RA frequency function is the MCSSI (Wang and He, 2015). Following the increment of the number of cycles of the sine-wave steer input, the RA frequency functions gradually converge to the red curve in Figure 8.10. With enough number of cycles and frequency instants in the frequency range of interest, the MCSSI RA frequency function provides a precise

and complete frequency response information. The MCSSI RA frequency function is employed as a referrence when genenerating RA frequency functions using all other maneuvers.

The RA frequency functions obtained with the AFRM maneuver are also shown in Figure 8.10. In the AFRM maneuver, the steer input consists of sine waves organized in frequency sequence. The number of cycles of the sine wave steer input is manipulated. Following the growth of the number of cycles, the RA frequency function reduces in peak value and gradually converges to the MCSSI RA frequency function when the number of cycles approching 5 which is deemed as the appropriate cycle number for the AFRM maneuver.

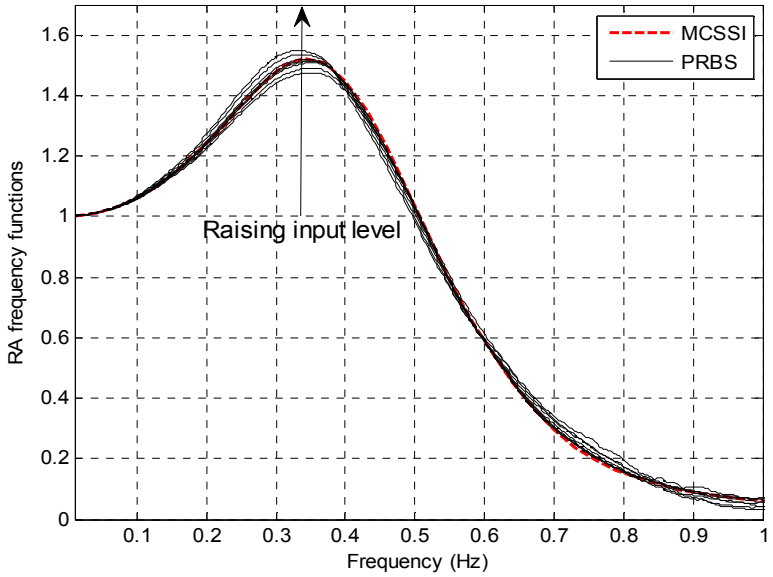

Figure 8.11 RA frequency functions of the B-train double obtained with the MCSSI and the PRBS steer input of varying input level

The RA frequency functions obtained with the PRBS steer test are shown in Figure 8.11 with the MCSSI frequency function. The RA frequency function can be manipulated by adjusting the PRBS level, frequency band and the test length to achieve excellent match with the MCSSI frequency function. The manipulability of the PRBS RA frequency function may have something

to do with inherent nonlinear characteristics of the vehicle, such as deadzone or backlash. A higher level of steer input may better overcome such nonlinear characteristics.

Figure 8.12 compares the RA frequency functions derived under the MCSSI, AFRM, and PRBS test maneuvers. The coherence functions between the PRBS steer input and the output data, i.e., the lateral accelerations at the tractor front axle roll center and at the 2nd trailer whole mass CG, are shown in Figure 8.13, indicating strong confidence on the RA frequency function based on the PRBS maneuver. To quantatively compare the RA frequency functions based on different test maneuvers in the frequency-domain, the respectively RA values at five individual frequencies in Figure 8.13 are listed in Table 8.1. It is shown that with the RA measures based on the MCSSI as references, the maximum relative error is only 3.4%, showing an excellent agreement achieved by the three maneuvers.

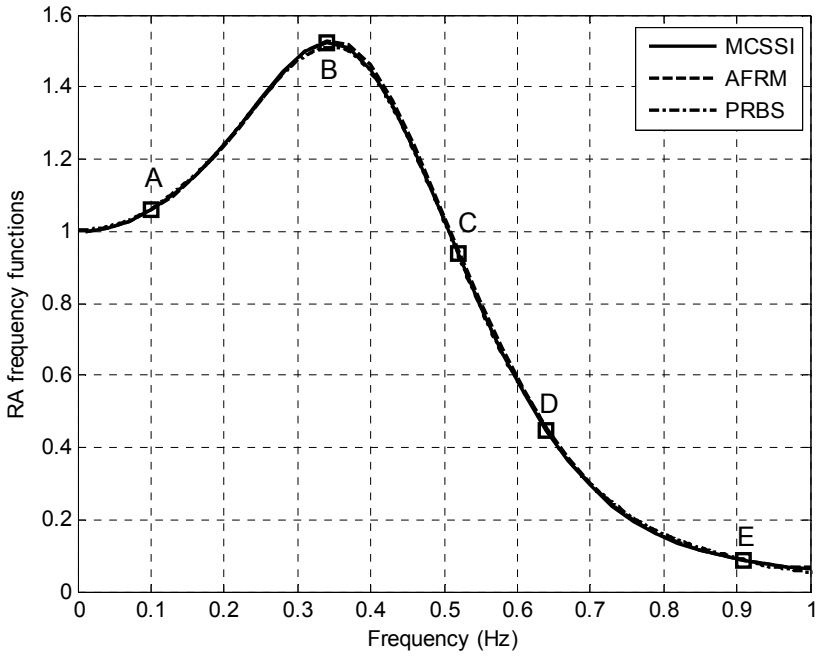

Figure 8.12 RA frequency functions of the B-train double obtained under the MCSSI, the AFRM and the PRBS steer test maneuvers

Table 8.1 RA frequency function values and relative errors for the selected points in Figure 8.12

Methods		MCSSI	AFRM		PRBS	
Point	Frequency (Hz)	RA	RA	Relative error*	RA	Relative error#
A	0.10	1.059	1.058	-0.10%	1.061	0.19%
B	0.34	1.524	1.529	0.33%	1.509	-0.98%
C	0.52	0.936	0.947	1.17%	0.929	-0.75%
D	0.64	0.449	0.457	1.78%	0.453	0.89%
E	0.91	0.087	0.087	0%	0.090	3.40%

* The relative error is defined as the ratio of the difference between the RA values based on the AFRM test and the MCSSI test to that based on the MCSSI test.
# the relative error is defined as the ratio of the difference between the RA values based on the PRBS test and the MCSSI test to that based on the MCSSI test.

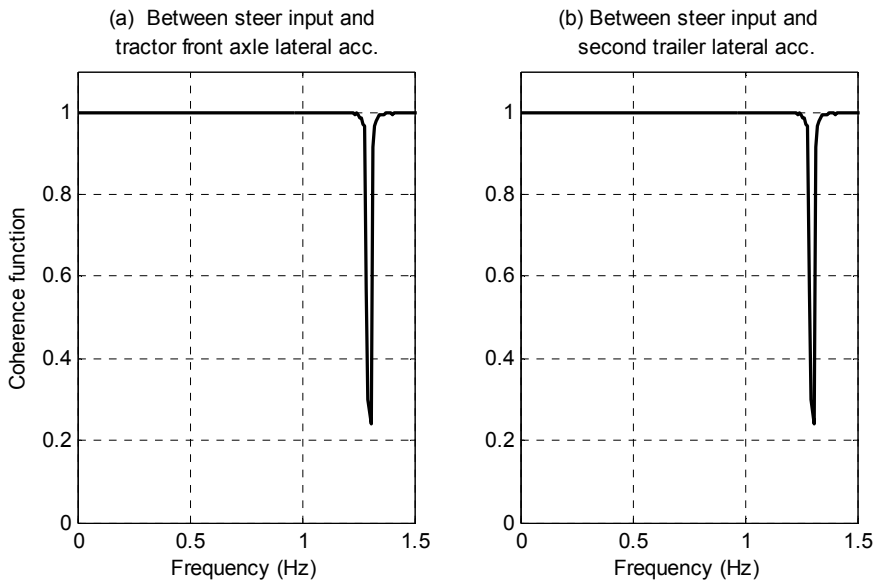

Figure 8.13 Coherence functions between: (a) the PRBS steer input and the lateral acceleration at the tractor front axle roll center, and (b) the PRBS steer input and the lateral acceleration at the 2nd trailer whole mass CG

Among the three maneuvers, the MCSSI is straightforward, purely manual and inefficient. The AFRM is an automated version of the MCSSI; the steer input consists of pure sine waves organized in a frequency series; steer input generation, vehicle excitation, output spectral analyis are carried out in a synchronized fashion on single frequency basis; and the AFRM is suitable for on-line and real-time operations and thus appropriate for frequency-domain design optimization. In the PRBS

maneuver, steer input generation, vehicle excitation, output spectral analysis are conducted in separate stages; the PRBS maneuver is not suitable for on-line operation; and this maneuver has the numerious factors to consider, such as the frequency band, the time length, and the input level.

Figure 8.14 shows the RA frequency functions achieved under the PRSI and the MCSSI maneuvers. Compared with the result based on the PRBS, the RA frequency function based on the PRSI has larger difference from that based on the MCSSI. This may be partially caused by the random variation of the PRSI input level. Uneven distribution of power spectral density of the PRSI in the frequency range of interest may also play a role, i.e., the RA frequency function demonstrates less accuracy in the arrea where there is less spectral power distributed. This problem may be easily solved when using the MCSSI or the AFRM maneuvers where the steer input level and its power spectral density can be adjusted and distributed as desired.

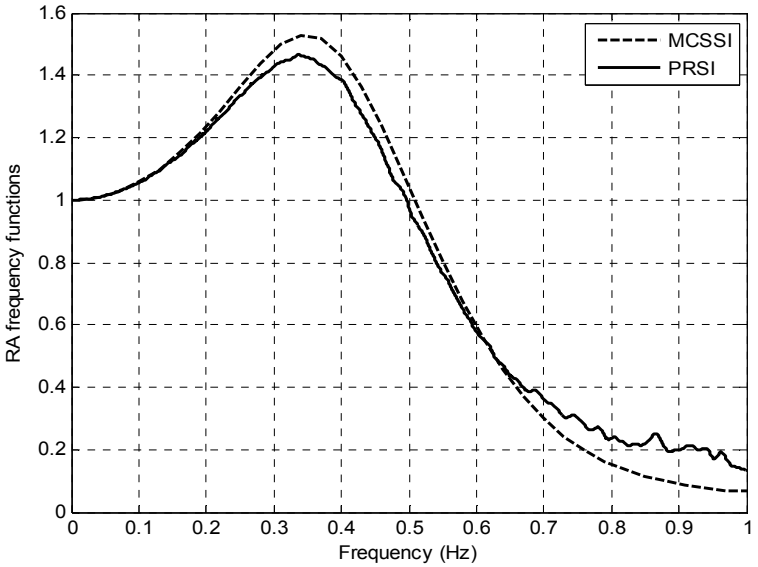

Figure 8.14 RA frequency functions obtained with the pseudo-random steer input and the MCSSI

8.4.2 Single Cycle Sine Wave Steer Input (SCSSI) Test Maneuver

As recommanded by ISO 14791, when applying the SCSSI maneuver, the frequencies selected should be at least 0.1Hz away from each other and no frequency picked in the vincinity of the

maximum RA ratio. Referred to Figure 8.12, the frequencies are selected as 0.01, 0.1, 0.2, …, 0.9 and 1 Hz to cover the frequency range of interest. Figure 8.15 shows the RA frequency functions obtained under the SCSSI, MCSSI, AFRM and the single-cycle AFRM maneuvers. Note that the so called single-cycle AFRM maneuver means that at each frequency, only one cycle of sine wave steer input is offered, and this special AFRM case is essential an automated version of the SCSSI maneuver.

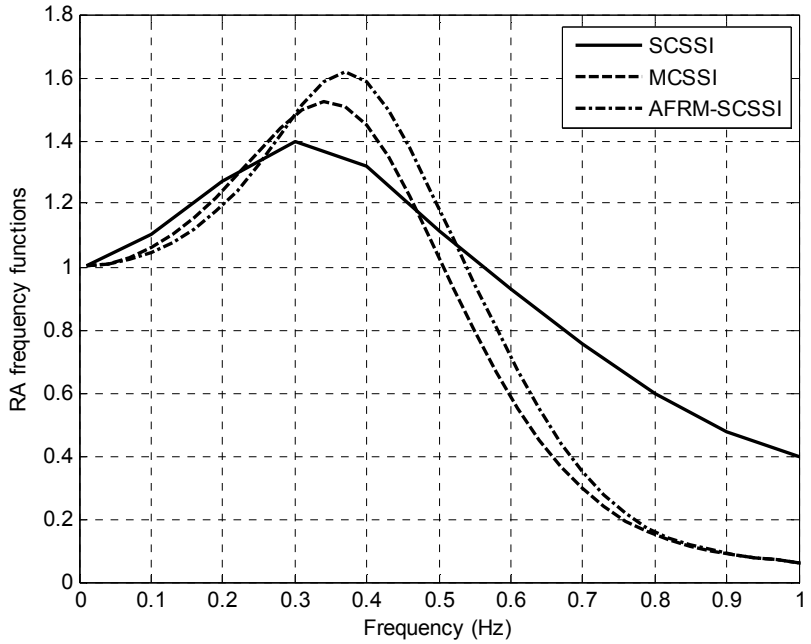

Figure 8.15 Comparison of the RA frequency functions obtained the MCSSI, SCSSI, and the single-cycle AFRM maneuvers

Compared with the RA frequency function based on the single-cycle AFRM, the RA frequency function based on the SCSSI maneuver has larger discranpancy from that based on the MCSSI. Wang and He (2016) attibute this phenomenon to transient response effect. The transient response is frequency dependent, and is more evdient at high frequencies. Therefore, the 2nd trailer has more severe transient tresponse than the tractor which may be related to rearward amplification. Figure

8.16 shows the transient lateral accelerations at the tractor front axle roll center and at the whole mass CG of the 2nd trailer.

There are two major factors affecting the transient characteristics: the *excitation mode* and the number of cycles of the sine wave. The excitation mode is defined as the way of handling the sine waves at individual frequencies to excite the vehicle. There are two excitation modes: namely, *continuous mode* and *intermittent mode*. In the continuous mode, the sine wave steer inputs are organized in a frequency sequence from low to high without intermittence between frequencies. In the intermittent mode, the vehicle is excited as many times as the number of frequency instants. Between frequency instants, there is a intermittence during which the input and the output data can be processed and the RA frequency function value may be calculated.

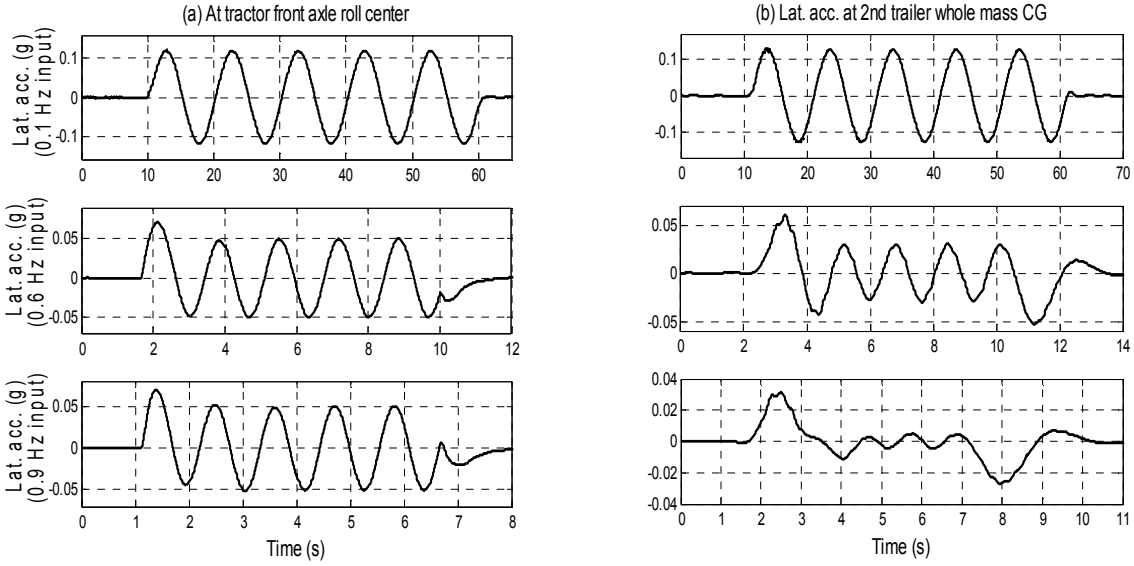

Figure 8.16 Transient lateral acceleration responses with the variation of frequency: (a) at tractor front axle roll center, and (b) at 2nd trailer whole mass CG

The single-cycle AFRM maneuver uses the continuous mode and the SCSSI procedure uses the intermittent mode. Figure 8.17 shows the AFRM and the SCSSI in the conitinuous and intermittent mode, respectively. Comparatively, the excitation mode has more significant

influence on the RA frequency function than the number of cycles. Improving RA frequency function by selecting proper exitation mode is shown in Figure 8.15, i.e., the RA frequency function obtained with continous AFRM is much closer than that of the intermittent SCSSI to that of the MCSSI. The impact of transient characteristis on the RA frequncy function can be attenuated by selecting the continuous mode and/or increasing the number of cycles. The MCSSI attenuates transient by increasing the number of cycles in the intimittent mode. Attenuating the transient response of the AFRM in the contiunuous mode is shown in Figure 8.10. Eliminating the transient-induced discranpancy is possible when the continous mode is applied and the number of cycles of sine-wave is large enough.

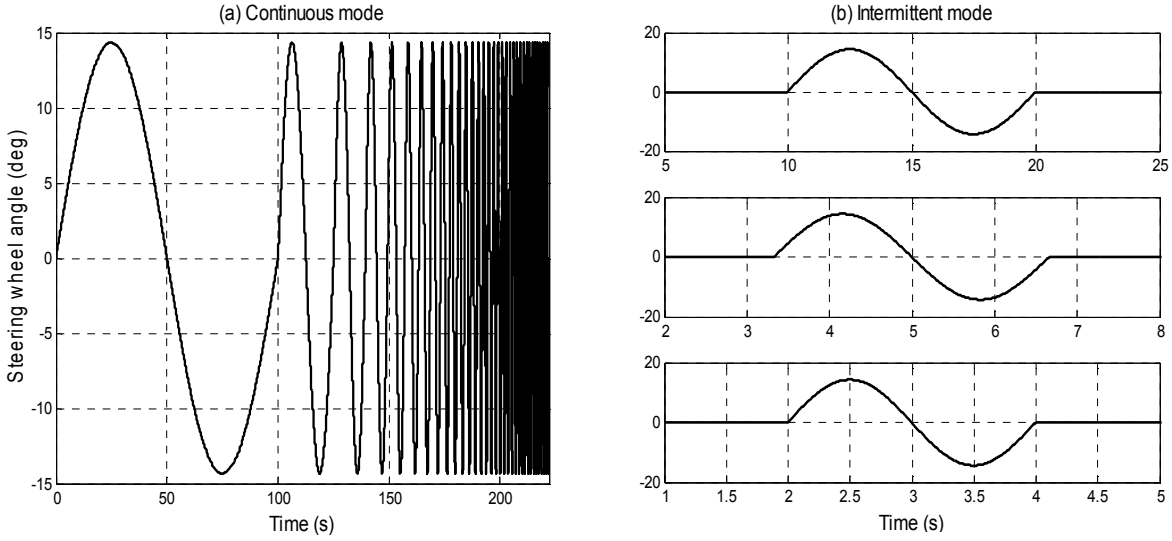

Figure 8.17 Excitation modes of AFRM and SCSSI: (a) continuous mode, and (b) intermittent mode

8.4.3 Single Cycle Sine Wave Lateral Acceleration (SCSLA) Input Maneuver

In the SCSLA maneuver, the amplitude of the lateral acceleration at the tractor front axle roll center is 0.15g (g is the gravational acceleration); and the frequency of the SCSLA is chosen from 0.1 to 0.7 Hz with 0.05 Hz interval. At each frequency instant, the XY trajectory of the tractor

front axle roll center is governed by Equation (8.2), which forms target trajectory of the SLC maneuvers.

The driver model plays an imperative role in trajectory tracking. As discussed in Section 8.3.2, the time lag (τ_d) affects the tracking performance with a limited effect, but influences the lateral stability significantly, and is set to zero for simplicity. The preview time (T_p) affects not only the tracking performance, but also the lateral stability of the vehicle. At each frequency instant, the preview time is carefully manipulated to achieve a trade-off of the tracking performance and the lateral stability. The lateral acceleration at the tractor front axle roll-center shall achieve a peak absolute value close to 0.15g, and the XY trajectory shall remain within $\pm 150mm$ tolerance of the target trajectory (SAE-J2179, 1993, and ISO-14791, 2000).

The RA frequency functions obtained under the SCSLA, SCSSI and MCSSI maneuvers are shown in Figure 8.18. The RA frequency functions based on the SCSLA and SCSSI maneuvers are comparable, and the results derived from the two maneuvers are different from that based on the MCSSI procedure. The tranisent effect has partially intepreted the disparity among the results of different maneuvers in the time-response perspective in Section 8.4.2. It has been proved by the MCSSI and the AFRM methods that given a proper excitation mode and enough number of input cycles, the RA measures in the time-domain can match the RA frequency function in the frequency-domain excellently. This prediction is also applicable to the (multiple-cycle) sine-wave lateral acceleration maneuver.

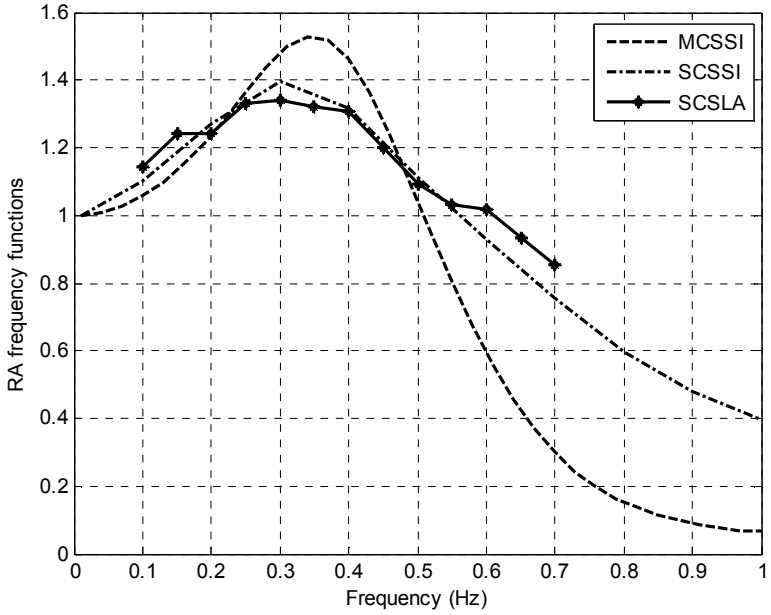

Figure 8.18 RA frequency functions obtained under the SCSLA, SCSSI and MCSSI maneuvers

8.4.4 Frequency-Perspective Intepretation of the Disparity

To inteprete the disparity of the RA frequency function based on the SCSSI maneuver from that obtained using the frequency-domain maneuvers, spectral analysis is conducted on the sine-wave steer input. Figure 8.19 shows the power spectral density of the 0.5 Hz sine-wave of 1, 3 and 5 cycles. The power spectral density is more narrowly concentrated on the center frequency following the increment of the number of cycles. A single cycle sine wave consists of a preceding quiescent period, a sine cycle and a following quiescent period (Aurell and Winkler, 1995). The power spectral density of the SCSSI is distributed on a frequency range in the vincinity of the center frequency. Thus the SCSSI is 'intepreted' by the vehicle as a weighted average of multiple frequency components instead of a pure sine wave. This explains why the RA functions based on the SCSSI and SCSLA maneuver deviate from that based on the MCSSI procedure as shown in Figure 8.19. It is observed that if more cycles are applied, less frequency components will be induced and the singal can better present itself in the frequency perspective.

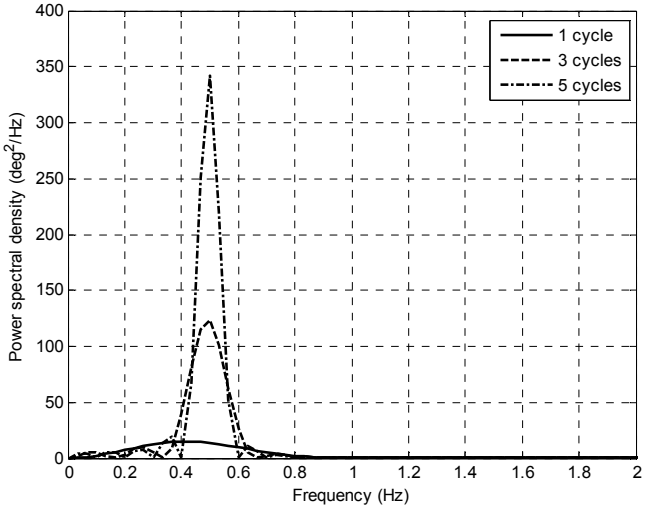

Figure 8.19 Power spectral density of sine wave steer inputs with varying number of cycles

The quiescent periods have significant impact on the RA frequency functions. Improving the RA frequency functions by selecting the contiunuous mode is the way of removing the quiescent periods from the steer input. Forthermore, increasing the number of cycles, the power spectral density can be made concentrated on the center frequency. In these perspectives, the AFRM, gathering all strengths of the time- and frequency-domain methods, appropriate excitation mode and variable number of cycles, has achieved identical match with the MCSSI maneuver in the time-domain and the PRBS procedure in the frequency-domain.

8.5 Summary

This chapter investigates various test maneuvers for determining rearward amplification (RA) frequency functions of multi-trailer articulated heavy vehicles (MTAHVs). The time-domain maneuvers, e.g., single cycle sine-wave steer input (SCSSI), single cycle sine-wave lateral acceleration input (SCSLA) and the multi-cycle sine-wave steer input (MCSSI), as well as the frequency-domain maneuvers, e.g., pseudo-random steer input (PRSI), automated frequency response measurement (AFRM), and pseudo-random binary sequence steer input (PRBS), are

considered. The research focus is on identifying the root casue of the disparity or mismatch among the test maneuvers.

The following insightful findings have been achieved. In the time-domain maneuvers, the excitation mode, defined as the way of handling the sine waves at individual frequencies to excite the vehicle, plays an imperative role. The excitation mode and the number of cycles of sine wave are the primary and the secondary factors affecting the RA frequency functions determined in time-domain. By using proper excitation mode and enough number of cycles, excellent match between the RA frequency functions achieved in the frequency-domain and the time-domain maneuvers has been achieved.

With frequency-domain response analysis, it has been proved that a SCSSI consists of a preceding quiescent period, a complete sine cycle, and a following queiscent period, all of which contribute to its frequequcy spectrum. The power spectral density of a SCSSI is a weighted average of multiple frequency contents distributed in the vincinity of the center frequency. The single cycle sine wave inputs intends to smooth the RA frequency functions, creating a so-called single-cycle effect.

Minimizing the single-cycle effect has resulted in an evolutionary process from the SCSSI, the MCSSI to the AFRM. Bearing the strengths of the time- and frequency-domain methods and using appropriate excitation mode and variable number of cycles, the AFRM has achieved excellent match with the MCSSI in the time-domain and with the PRBS in the frequency-domain.

Chapter 9 Conclusions

This thesis proposes a coordinated control strategy (CCS) for multitrailer articulated heavy vehicle (MTAHV) active safety systems (ASSs). To fulfill the CCS, an automated frequency response measuring technique (AFRM) has been introduced which not only solves the long-term disparity and mismatch issues faced by the relevant standards (SAE-J2179, 1993 and ISO-14791, 2000) governing the practice of determining rearward amplification (RA), an unique feature of articulated heavy vehicles (AHVs), but also extends the design optimization of ASSs of MTAHVs traditionally in time-domain to frequency-domain. A unified driver model considering the dynamic features of single unit vehicles and multi-unit vehicles has been presented to investigate the interactions of the MTAHV, coordinated control system, and driver using closed-loop simulations under various operating conditions.

9.1 Coordinated Control of Active Safety Systems

The coordinated control system (CCS) consists of subsystems of active trailer steering (ATS), trailer differential braking (TDB) and active roll control (ARC). The CCS is designed in a modular, hierarchical, and multilevel approach: 1) at the upper level, a controller is designed to determine direct yaw/roll moments to stabilize the MTAHV; 2) at the intermediate level, an allocator is designed to distribute the moments to individual actuators; and 3) at the lower level, the actuators for the subsystems of the ATS, TDB and ARC realize the allocated moments. The control module, allocator module, and the realization module are designed independently in such a way that re-design or modification of one without affecting the others, which facilitates the future modification and functionality expansion of the CCS.

The upper level controller is a linear quadratic regulator (LQR) built on a ten degrees of freedom (DOF) linear yaw-roll MTAHV model, which minimizes a quadratic performance index formulated on the performance measures of the yaw and roll dynamics and the control variables. The allocator module distributes the direct roll moment to the ARC actuators, considering the rotating mechanisms around the corresponding roll axles between the sprung and unsprung masses of the vehicle units. The allocator assigns the direct yaw moments to the ATS and TDB actuators using a side-slip angle based nonlinear programing allocation algorithm in such a way that the yaw moments are allocated to the ATS up to its linear limit before applying the TDB to restrict the adverse impact on the longitudinal dynamics. The realization module implements the functions of the ATS, TDB, and ARC.

To achieve an optimal overall performance of high-speed maneuverability, yaw and roll stability of the MTAHV, a parallel genetic algorithm is implemented to optimize the upper-level controller, minimizing a performance index formulated on the time-domain performance measures of the yaw and roll dynamics using the cross differential gap (CDG) technique in order to achieve optimal parameters including the design variables of the direct yaw/roll moment controller and the unified driver model.

9.2 Unified Lateral Preview Driver Model

The unified lateral preview driver model is proposed for road vehicles of single or multi-unit using the SMC technique to accommodate parametric uncertainties, un-modeled dynamics, and various operating conditions that MTAHVs inevitably face. By selecting appropriate values of the relevant model parameters, the proposed driver model determines the steering angle considering the motion cues from both the leading and trailing units. The unified driver model is designed with two modes, namely, stability- and path-following oriented, which may be used to simulate the driving

performance of a MTAHV driver under a high-speed evasive and a low-speed path-following maneuver, respectively. The numerical simulations demonstrates the applicability and effectiveness of the proposed driver model.

9.3 Automated Frequency Response Measuring Technique

To acquire more comprehensive information of dynamic responses of MTAHVs in the frequency-domain, an automated frequency response measurement technique (AFRM) is introduced. With the AFRM, active safety systems (ASSs) of MTAHVs can be designed and optimized not only in the time-domain but also in the frequency-domain. The investigation of the test maneuvers for MTAHVs using the time-domain maneuvers, such as the single cycle sine-wave steer input (SCSSI), single cycle sine-wave lateral acceleration (SCSLA), and multiple cycle sine-wave steer input (MCSSI), as well as the frequency-domain maneuvers, such as the pseudo-random steer input (PRSI) and pseudo-random binary sequence (PRBS) steer input, discloses that the AFRM technique bears the strengths of the time- and frequency-domain methods. With appropriate excitation mode and variable number of cycles, the AFRM technique achieves excellent match with the MCSSI in the time-domain and the PRBS in the frequency-domain in acquiring the frequency functions of the rearward amplification of MTAHVs. Furthermore, with the aid of the AFRM technique, the robust active steering systems for a tractor/semitrailer combination, such as the SMC based and the nonlinear SMC based active steering systems, have been optimized for optimal overall performance of high-speed maneuverability and stability in a frequency band of interest.

9.4 Potential Applications of the CCS Strategy, Driver Model, and AFRM Technique

Firstly, the proposed CCS for ASSs of MTAHVs may be directly applied by practice engineers to the chassis systems design of MTAHVs. With the proposed CCS, the active safety subsystems,

i.e., ATS, TDB and ARC compensate each other, restricting adverse impact and enhancing overall performance. The stability and maneuverability of MTAHVs may be improved significantly, and the accident involvement rate of the MTAHVs may be reduced considerably by using the CCS system. The potential benefits induced by promoted application of MTAHVs on economy and environment could be enormous. Secondly, the proposed unified driver model may be easily adopted by autonomous vehicle (single unit or multiunit) manufacturers fulfilling autonomous driving tasks, accommodating parametric uncertainties, un-modeled dynamics and various operating conditions that road vehicles inevitably face. Thirdly, the introducing the AFRM technique into the AHV dynamics not only solves the issues faced by the relevant standards (SAE-J2179 and ISO-14791), i.e., disparity or mismatch between the rearward amplification (RA) measures of the time-domain and frequency-domain methods, but also pushes the design optimization of active safety systems of MTAHVs from traditionally in time-domain to frequency-domain for more comprehensive performance evaluation.

9.5 Future Work

MTAHVs have large sizes and complex configurations, and face inevitably parametric uncertainties and un-modeled dynamics in their modeling. Rearward amplification is an important dynamic feature of MTAHVs, which is forward-speed and frequency dependent. With these concerns in mind, a robust coordinated control of MTAHVs based on the H-infinity technique, considering the ATS, TDB, and ARC will be designed and optimized in a speed range and a frequency band of interest with the aid of the AFRM technique in the future work. Compared with the current CCS, the newly designed CCS will bear the following changes: 1) a H-infinity based upper-level direct yaw/roll moment controller will replace the current LQR base direct yaw/roll moment controller to accommodate parametric uncertainties and un-modeled dynamics; 2) the

implementation of the realization module will be investigated, considering the ATS, TDB and the ARC systems dynamics.

References

Acarman, T. and Ozguner, U., 2003, Rollover Prevention for Heavy Trucks using Frequency Shaped Sliding Mode Control. Proceedings of 2003 IEEE Conference on Control Applications, pp. 7-12

Adams T., Dan Kleinmaier, D., Marach, A., Helfrich, G., Levine, J., and Bittner, J., 2012, Longer Combination Vehicles: An Estimation of Their Benefits and Public Perception of Their Use, Technical Report Documentation Page

Alberding, M.B., Tjønnås, J., and Johansen, T.A., 2014, Integration of vehicle yaw stabilisation and rollover prevention through nonlinear hierarchical control allocation. Vehicle System Dynamics, 52(12), pp. 1607-1621

Aurell, J., and Edund, S., 1989, The Influence of Steered Axles on the Dynamic Stability of Heavy Vehicle, SAE paper NO: 892498

Aurell, J. and Koppenaal, J., 1998, Simplified procedure for determining lateral stability of heavy vehicle combinations, Proceedings of the Fourth International Symposium on Heavy Vehicle Weights and Dimensions, Queensland, Australia

Aurell J, Winkler CB. 1995, Standard test procedures for the lateral stability of heavy vehicle combinations, Road Transport Technology. Vol. 4, University of Michigan Transportation Research Institution, Ann Arbor, pp. 463-471

Azad, N. L., Khajepour, A. and McPhee, J., 2006, An Active Control Device Based on Differential Braking for Articulated Steer Vehicles, SAE International, Technical Paper 2006-01-3568

Bakker, E., Nyborg, L. and Pacejka, H.B. 1987, Tyre modelling for use in vehicle dynamics studies. Society of Automotive Engineers, Warrendale, PA

Barbarisi, O., Palmieri, G., Scala, S., Glielmo, L., 2009, "LTV-MPC for yaw rate control and side slip control with dynamically constrained differential braking", European Journal of Control, 15(3-4), pp. 468–479

Bienkowski, B.N., and Walton, C.M., 2011, The Economic Efficiency of Allowing Long Combination Vehicles in Texas. Research Report SWUTC/11/476660-00077-1

Binder and Khajepour, 2014, Optimal Control Allocation for Coordinated Suspension Control. 2014 American Control Conference (ACC), June 4-6, 2014. Portland, Oregon, USA

Bouteldja, M. and Cerezo, V. 2011, Jackknifing Warning for Articulated Vehicles Based on A Detection and Prediction System, the 3rd International Conference on Road Safety and Simulation, Indianapolis, USA

Bozeman, A. H. and Drench, K. F., 1998, Multi-trailers on the Road. Fifth International Symposium on Heavy Vehicle Weights and Dimensions. pp. 87-106, Queensland, Australia

Busch, J. and Bestle, D., 2014, Optimisation of lateral car dynamics taking into account parameter uncertainties, Vehicle System Dynamics: International Journal of Vehicle Mechanics and Mobility, 52(2), pp. 166-185

CDT, 1984, Longer Combination Vehicles Operational Test, California Department of Transportation, March, 1984, pp. 1-57

Chen, B.C. and Peng, H., 2005, Rollover Warning for Articulated Heavy Vehicles Based on A Time-to-Rollover Metric. ASME Journal of Dynamic Systems, Measurement and Control, 27, pp. 406-414

Chen, L.K. and Hsu, J. Y. 2008, Investigation of jackknife prevention in an articulated scaled vehicle, Vehicle Systems Dynamics, 46, Supplement, pp. 765-777

Chen, L. K. and Shieh, Y. A., 2010, Jackknife prevention for articulated vehicles using model reference adaptive control, Proceedings of Institute of Mechanical Engineering, 225, Part D: Journal of Automobile Engineering, pp. 28-42

Cheng, C., 2009, Enhancing safety of actively-steered articulated vehicles. PhD Dissertation, University of Cambridge, Cambridge, England

Cheng, J. F. and Cebon, D. 2008, Improving roll stability of articulated vehicles using active semi-trailer steering, Vehicle Systems Dynamics, 46, Supplement, pp. 373-388

Cheng, J. F. and Huang, H. C., 2011, Effects of Roadway Geometric Features on Low-Speed Turning Manoeuvres of Large Vehicles, International Journal of Pavement Research and Technology, 4(6), pp. 373-383

Cheng, C., Roebuck, R., Odhams, A. and Cebon, D., 2011, High-speed optimal steering of a tractor-semitrailer, Vehicle Systems Dynamics, 49(4), pp. 561-593

Chung, T. and Yi, K., 2006, Design and Evaluation of Side Slip Angle-Based Vehicle Stability Control Scheme on a Virtual Test Track. IEEE Transactions on Control Systems Technology, 14(2), 224-234

CTAA, 2010, California Truck Accident Attorney, http://www.esteybomberger.com/truck_accident.html, (Accessed on July 18, 2013)

CTSWS, 2000, Comprehensive Truck Size and Weight Study, Final Report, U. S. Department of Transportation, http://www.fhwa.dot.gov/reports/tswstudy/index.htm, (Accessed on May 23, 2011)

Ding, X. and He, Y., 2011, Design and Evaluation of Active Trailer Steering Systems of Long Combination Vehicles Using Driver-Software-in-the-Loop Simulations, submitted to SAE 2012 Congress, Detroit, USA, Manuscript, ID: 12AE-0039

Ding, X. and He, Y., 2012, An Investigation of Driver Models for Closed-loop Dynamic Stability Analysis of Articulated Vehicles. Proceedings of 4th International Conference on Mechanical Engineering and Mechanics, Suzhou, China, pp. 768-772

Ding, X. and He, Y., 2012a, Numerical simulation and analysis of closed-loop driver/articulated vehicle dynamic systems. SAE Int. J. Commer. 5(1), pp. 111-118

Ding, X., He, Y., Ren, J. and Sun, T., 2012, A Comparative Study of Control Algorithms for Active Trailer Steering Systems of Articulated Heavy Vehicles, 2012 American Control Conference, Montreal, Manuscript ID: 1090

Ding, X., Mikaric, S. and He, Y. 2013, Design of an active trailer-steering system for multi-trailer articulated heavy vehicles using real-time simulations, Proceedings of the Institution of Mechanical Engineers, Part D: Journal of Automobile Engineering, 227, pp. 643-655

Doyle, J.C., 1985, Structured uncertainty in control system design. Proceedings of the 24 IEEE Conference on Decision and Control, pp. 260-265

Doyle, J.C., 1987, A review of μ: for case studies in robust control. Proceedings of 10th IFAC World Congress, Munich, Germany, pp. 395-402

Doyle, J.C. and Stein, G., 1979, Robustness with Observers, IEEE Transactions on Automatic Control, 24(4), pp. 607-611

Doumiati, M., Sename, O., Dugard, L., Martinez, J., Gaspar, P. and Szabo, Z., 2013, Integrated vehicle dynamics control via coordination of active front steering and rear braking, European Journal of Control. 19(2), pp. 121-143

Du, H., and Zhang, N., 2008, Robust stability control of vehicle rollover subject to actuator time delay, Proceedings of Institute of Mechanical Engineers, Part I: Journal of Systems and Control Engineering, 222, pp. 163-174

Edgar, J., 2004, Development of performance standards for Australia heavy vehicles, Proceedings of the 8th International Symposium on Heavy Vehicle Weights and Dimensions, South Africa, March 14-18

Eills, J.R., 1969, Vehicle dynamics. Business Books Limited, London

Eisele, D.D. and Peng, H., 2000, Vehicle Dynamics Control with Rollover Prevention for Articulated Heavy Trucks, Proceedings of 5th International Symposium on Advanced Vehicle Control

El-Gindy, M., Mrad, N. and Tong, N., 2001, Sensitivity of rearward amplification control of a tractor/full trailer to tyre cornering stiffness variable, Proc. IMechE, Part D: Journal of Automobile Engineering, 215, pp. 579-588

Elwell, M. and Kimbrough, S., 1993, An Advanced Braking and Stability Controller for Tow-Vehicle and Trailer Combinations. SAE 931878. Seventh International Pacific Conference and Exposition on Automotive Engineering, Phoenix, AZ. November 15-19

Erkert, T. W., Sessions, J. and Layton, R. D., 1989, A Method for Determining Offtracking of Multiple Unit Vehicle Combinations, Journal of Forest Engineering, 1(1), pp. 9-16

Ervin, R.D., Fancher, P.S., Gillespie, T.D., Winkler, C.B. and Wolfe, A. 1978, Ad Hoc Study of Certain Safety-Related Aspects of Double-Bottom Tankers. Final Report, Sponsored by Michigan State Office of Highway Safety Planning, Contract No. MPA-78-002A. Highway Safety Research Institute, University of Michigan, Report No. UM-HSRI-78-18

Ervin, R.D., and Guy, Y., 1986, Influence of Weights and Dimensions on the Stability and Control of Heavy-Duty Trucks in Canada. Final Report, Sponsored by Canroad Transportation

Research Corporation. University of Michigan Transportation Research Institute, Report No. UMTRI-86-35

Ervin, R. and MacAdam, C., 1982, The dynamic response of multiply-articulated truck combinations to steering input, SAE Technical Paper 820973

Ervin, R.D., Nisonger, R.L., MacAdam, C.C. and Fancher, P.S., 1983, Influence of size and weight variables on the stability and control properties of heavy trucks, final Report, University of Michigan Transportation Research Institute (UMTRI), Contract No. FH-11-9577, Report No. UMTRI-83-10

Ervin, R. Winkler, C.B. Fancher, P.S. Hagan, M. Krishnaswami, V. Zhang H. and Bogard, S., 1998, Two active systems for enhancing dynamic stability in heavy truck operations, final Report, University of Michigan Transportation Research Institute (UMTRI), Contract No. DTNH22-95-H-07002, Report No. UMTRI-98-39

Fancher, P., 1982, The transient directional response of full trailers. SAE Technical Paper 821259

Fancher, P. S., Segel, L., Winker, C. B. and Ervin, R. D., 1984, Tracking and Stability of Multi-Unit Truck-Combinations, final Report, MYMA Project Number 9165

Fancher, P.S., and Winkler, C.B., 1992, A Methodology for Measuring Rearward Amplification, Third International Symposium on Heavy Vehicle Weights and Dimensions. Queens College, Cambridge, United Kingdom, June 28 – July 2

Fancher P.S. and Winkler C.B., 2007, Directional performance issues in evaluation and design of articulated heavy vehicles. Vehicle System Dynamics, 45(7-8), pp. 607-647

Fancher, P.S., Winker, C.B., Ervin, R. and Zhang, H., 1998, Using braking to control the lateral motions of full trailers. Vehicle System Dynamics, 28, pp.462-478

Fernandes, A. A. & Alcalde, V.H. C., 2007, Serious Compensation Using Variable Structure and Lyapunov Function Controls for Stabilization Multimachine Power System. Mediterranean Conference on Control and Automation, MED

Fletcher, C., Manzie, C. and Good, M., 2006, Trailer steering: an Australian research perspective and application for by-wire control. Ninth International Symposium on Heavy Vehicle Weighs and Dimensions. June 18-22. Penn State College, Pennsylvania

Fukao, T., Miyasaka, S., Mori, K., Adachi, N., and Osuka, K., 2004, Active Steering Systems, Based on Model Reference Adaptive Nonlinear Control, Vehicle System Dynamics, 42(5), pp. 301-318

Gao, X., Mcvey, B.D., and Tokar, R.L., 1995, Robust controller design of four wheel steering systems using μ synthesis technique, Proceedings of the 34th Conference on Decision and Control, New Orleans, LA

Gillespie, T.D., 1992, Fundamentals of Vehicle Dynamics. Society of Automotive Engineers

Gloth, G. and Sinapius, M., 2004, Analysis of swept-sine runs during modal identification, Mechanical Systems and Signal Processing, 18, pp. 1421-1441

Gu, D.W., Petkov, P. H. and Konstantinov, M. M., 2013, Robust Control Design with Matlab, Second Edition, Springer-Verlag London

Gu, Y. and Yang, G. H., 2011, LMI Optimization Approach on Robustness and H_∞ Control Analysis via Disturbance-Observer-Based Control of Uncertain Systems, Proceedings of 2011 Chinese Control and Decision Conference, pp. 4150-4154

Habibi, S. R. & Richards, R. J., 1992, Sliding mode control of an electrically powered industrial robot. IEE Proceedings D: Control Theory and Applications, 139(2), pp. 207-225

Hac, A., Fulk, D. and Chen, H., 2009, Stability and Control Consideration of Vehicle-Trailer Combination, SAE International Journal of Passenger Cars-Mechanical Systems, 1(1), pp. 925-937

Hancock, M. J., Williams, R. A., Gordon, T. J., & Best M. C., 2005, A comparison of braking and differential control of road vehicle yaw-sideslip dynamics, Proceedings of the Institution of Mechanical Engineers, Part D: Journal of Automobile Engineering, 219(3), pp. 309-327

Hata, N., Hasegawa, S., Takahashi, S., Ito, K., and Fujishiro, T., 1989, A Control Method for 4WS Truck to Suppress Excursion of a Body Rear Overhang (SAE Paper No. 892521). SAE Trans., 98(2), pp. 754-760

He, Y., 2008, Design Synthesis of Mechatronic Vehicles with Coordinated Control Systems, Vehicle System Dynamics, 46, Supplement, pp. 923-936

He, J., Crolla, D.A., Levesley, M.C., and Manning, W.J., 2006, Coordination of active steering, driveline, and braking for integrated vehicle dynamics control. Proc. IMechE Part D: J. Automobile Engineering, 20, pp. 1401-1421

He, Y. and Islam, M., 2012, An automated design method for active trailer steering systems of articulated heavy vehicles, Transactions of ASME, Journal of Mechanical Design, 134 (041002), pp. 1-15

He, Y., Islam, M. and Oberoi, D., 2013, An automated design synthesis method for multi-trailer articulated heavy vehicles, Int. J. Vehicle Performance, 1(2), pp. 183-204

He, Y., Islam, M.M. and Webster, T., 2010, An Integrated Design Method for Articulated Heavy Vehicles with Active Trailer Steering Systems, SAE International Journal of Passenger Cars-Mechanical Systems, 119(6), pp. 158-174

He, Y., Islam, M.M., Zhu, S., and Hu, T., 2016, Directional Performance Optimization of Multi-Trailer Articulated Heavy Vehicles with Trailer Lateral Dynamic Control Systems. Proc. IMechE, Part D: Journal of Automobile Engineering, ID JAUTTO-15-0122

He, Y., McPhee, J., 2007, A Review of Automated Design Synthesis Approaches for Virtual Development of Ground Vehicle Suspensions, SAE International, Technical Paper 07AC-40

HeiBing, B., Ersoy, M., (Eds.), 2011, Chassis Handbook, Fundamentals, Driving Dynamics, Components, Mechatronics, Perspectives. Vieveg+Teubner Verlag | Springer Fachmedien Wiesbaden Gmbh

Hibbeler, R.C., 2007, Engineering Mechanics Dynamics. 11th Edition in SI Units, Prentice Hall Pearson Education South Asia Pte Limited

Horiuchi S, Yuhara N, 2000, An analytical approach to the prediction of handling qualities of vehicles with advanced steering control system using multi-input driver model. Transactions of the ASME, Journal of Dynamic Systems, Measurement, and Control. 122(3), pp. 497-490

Huang, H. H., Yedavalli, R. K. and Guenther, D. A., 2012, Active roll control for rollover prevention of heavy articulated vehicles with multiple-rollover –index minimization. Vehicle Systems Dynamics, 50(3), pp. 471-493

Imine, H., Fridman, L.M. and Madani, T., 2012, Steering Control for Rollover Avoidance of Heavy Vehicles, IEEE Transactions on Vehicular Technology, 61(8), pp. 3499-2509

International Organization for Standardization, 2000, "Road vehicles – Heavy commercial vehicle combinations and articulated buses – Lateral stability test methods", ISO14791:2000(E), Geneva: International Organization for Standardization; 2000

Islam, M.M., 2013, Parallel Design Optimization of Multitrailer Articulated Heavy Vehicles with Active Safety Systems. PhD thesis. University of Ontario Institute of Technology, Oshawa, Canada

Islam, M.M., Ding, X. and He, Y., 2012, A closed-loop dynamic simulation-based design method for articulated heavy vehicles with active trailer steering systems, Vehicle System Dynamics, 50(5), pp.675-697

Islam, M.M. and He, Y., 2008, Stability Optimization of Articulated Frame Steer Vehicles. CATS 2008

Islam, M. M., and He, Y., 2011, An Optimal Preview Controller for Active Trailer Steering Systems of Articulated Heavy Vehicles, SAE 2011 World Congress, Paper No: 2011-01-0983, Detroit, MI, USA

Islam, M. and He, Y., 2013, A parallel design optimization method for articulated heavy vehicles with active safety systems, Int. J. Heavy Vehicle Systems, 20(4), pp. 327-341

Islam, M.M., He, Y., and Hu, T., 2013, A design optimization method for multi-trailer articulated heavy vehicles with active safety systems. Proceedings of 23rd International Symposium on Dynamic of Vehicles on Roads and Tracks (CD), Qingdao, China, 10 pages

Islam, M., He, Y., Zhu, S. and Wang, Q., 2015, A comparative study of multi-trailer articulated heavy vehicle models, Proc of IMechE Part D: J Automobile Engineering, 229(9), pp. 1200-1228

Islam, M. M., He, Y. and Webster, T., (2010), Automated Design Synthesis of Articulated Heavy Vehicles with Active Trailer Steering Systems, Proceedings of ASME IDETC/CIE 2010, Paper No: DETC2010-28160, Montreal, Canada

Islam, M. M., He, Y., and Webster, T., 2010a, A Compound Lateral Position Deviation Preview Controller for Active Trailer Steering Systems of Articulated Heavy Vehicles, Proceedings of CSME Forum 2010(CD), Victoria, BC, Canada

Islam, M., He, Y., Zhu, S. and Wang, Q., 2015, A comparative study of multi-trailer articulated heavy vehicle models, Proc of IMechE Part D: J Automobile Engineering, 229(9), pp. 1200-1228

Islam, M.M., Mikaric, S., He, Y. and Hu, T., 2012, Parallel design optimization of articulated heavy vehicles with active safety systems. Proceedings of the FISITA 2012 World Automotive Congress, Beijing, China, pp. 1563-1575

ISO-14791, 2000, International Organization for Standardization. Road vehicles – Heavy commercial vehicle combinations and articulated buses – Lateral stability test methods. ISO-14791:2000(E), Geneva: International Organization for Standardization

Jason, B. N., Awad, W., Robles, J., Kononov, J. and Pinkerton, B., 1998, Truck Accidents at Freeway Ramps: Data Analysis and High-Risk Site Identification, Journal of Transportation and Statics, 1, pp.75-92

Jazar, R.N., 2011, Advanced Dynamics Rigid Body, Multibody, and Aerospace Applications. John Willey & Sons, Inc., Hoboken, New Jersey

Jo, J. S., You, S. H., Joeng, J. Y., Lee, K. I., and Yi, K. 2008, Vehicle Stability Control System for Enhancing Steerablity, Lateral Stability, and Roll Stability, International Journal of Automotive Technology, 9(5), pp. 571-576

Jujnovich B., and Cebon D., 2002, Comparative performance of semi-trailer steering systems. Proceedings of the 7th International Symposium on Heavy Vehicle Weight and Dimensions, Delft, the Netherlands

Jujnovich, B. and Cebon, D., 2013, Path-Following Steering Control for Articulated Vehicles, Journal of Dynamic Systems, Measurement, and Control, 135, 031006

Kamnik, R., Boettiger, F. and Hunt, K., 2003, Roll dynamics and lateral load transfer estimation in articulated heavy freight vehicles. Proceedings of Institute of Mechanical Engineers, 217, Part D: Journal of Automobile Engineering, pp.985-997

Kang, X. and Deng, W., 2007, Vehicle-trailer handling dynamics and stability control — an engineering review, SAE Technical Paper 2007-01-0822

Kharrazi, S., 2012, Steering Based Lateral Performance Control of Long Heavy Vehicle Combinations, PhD thesis, Chalmers University of Technology, Gothenburg, Sweden

Kharrazi, S., Fredriksson, J. and Lidberg, M., 2010, Lateral Stability Control of a Long Heavy Vehicle Combination by Active Steering of the Towed Units, 13th International IEEE Annual Conference on Intelligent Transportation Systems, Madeira Island, Portugal, pp. 168-173

Kharazi, S., Lidherg, M. Roebuck, R., Fredriksson J. and Odhams, A., 2012, Implementation of active steering on longer combination vehicles for enhanced lateral performance. Vehicle System Dynamics, 50(12), pp. 1949-1970

Kharazi, S., Lidherg, M. and Fredriksson, J., 2013, A generic controller for improving lateral performance of heavy vehicle combinations. Proc. IMechE Part D: J Automobile Engineering, 227(5), pp. 619-642

Kortum, W., 1993, Review of multibody computer codes for vehicle system dynamics, Vehicle System Dynamics Supplement, 22, pp. 3-26

Lam, C.P., 1988, Comparison of Simulation and Test Results for Various Truck Combination Configurations, International Symposium on Heavy Vehicle Weights and Dimensions, Kelowna, British Columbia, Canada, pp. 315-335

LCVP, 2011, Long combination vehicle program review. Accessed on Nov. 14, 2013 at http://www.mto.gov.on.ca/english/trucks/LCV-Pilot-Program-Review-Mar-1-2011-Final.pdf

Lin, R.C., 1994, An Investigation of Active Roll Control for Heavy Vehicle Suspensions. PhD thesis, University of Cambridge, Cambridge, England

Lin, R.C., Cebon, D. and Cole, D.J., 1996, Active Roll Control of Articulated Vehicles, Vehicle System Dynamics, 26, pp. 17-43

Lin, F. J., Lin C. H. & Shen, P. H., 2002, Variable Structure Control for Linear Synchronous Motor Using Recurrent Fuzzy Neural Network. IECON Proceedings (Industrial Electronics Conference), 3, 2108-2113

Liu, Z., 2007, Characterisation of optimal human driver model and stability of a tractor-semitrailer vehicle system with time delay. Mechanical Systems and Signal Processing, 21, pp. 2080-2098

MacAdam, C. C., 1980, An Optimal Preview Control for Linear Systems. Journal of Dynamic Systems, Measurement and Control, 188(102)

MacAdam, C. C., 1981, Application of a Preview Control for Simulation of Closed-loop Automobile Driving. IEEE Transactions on Systems, Man, and Cybernetics, SMC-11(6), pp. 393-399

MacAdam, C. C., 2003, Understanding and Modeling the Human Driver. Vehicle System Dynamics, 40(1-3), pp. 101-134

MacAdam, C. and Hagan, M., 2002, A simple differential brake control algorithm for attenuating rearward amplification in doubles and triples combination vehicles, Vehicle System Dynamics Supplement, 37, pp.234-245

MacAdam, C.C., Hagan, M., Fancher, P., Winkler, C., Ervin, R., Zhou, J. and Bogard, S., 2000, Rearward Amplification Suppression. UMTRI-2000-47. DTFM61-96-C-00038

Maciejowski, J.M., 1989, Multivariable feedback design, Addison Wesley

Mao, X. and Lu, K., 2008, Research on the nonlinear governor of diesel engine with variable structure control theory. 2008 IEEE International Conference on Robotics, Automation and Mechanics, pp. 537-542

MathWorks, 2014, Measuring Frequency Response Using a Spectrum Analyzer, MathWorks Documentation Center, http://www.mathworks.com/help/stateflow/ug/frequency-response-measurement-with-a-spectrum-analyzer.html (April 18, 2014)

MSC, 2014, Mechanical Simulation Corporation, TruckSim Options. https://www.carsim.com/products/trucksim/packages.php (April 8, 2014)

Menhour, L., Lechner, D., and Charara, A., 2010, Sliding Mode Control to Design a Driver Model for Vehicle Steering: Experimental Validation and Stability Evaluation of Sideslip Motion. 6th IFAC Symposium Advances in Automotive Control, July 12-14, Munich, Germany

Miege, A.J.P. and Cebon, D., 2005, Optimal roll control of an articulated vehicle: theory and model validation. Vehicle System Dynamics, 43(12), pp. 867-893

Minaker, B.P., and Rieveley, R.J. 2010, Automatic generation of the nonholonomic equations of motion for vehicle stability analysis. Vehicle System Dynamics, 48:9, 1043-1063

Minaker, B., and Rieveley, R. J., 2013, EoM user guide. University of Windsor, Windsor, Ontario, Canada

Mokhiamar, O. & Abe, M. 2002, Active wheel steering and yaw moment control combination to maximize stability as well as vehicle responsiveness during quick lane change for active vehicle handling safety, Proceedings of the Institution of Mechanical Engineers, Part D: Journal of Automobile Engineering, 216(2), pp. 115-124

Nagl, P. 2007, Long Combination Vehicles for Asia and the Pacific Region: Some Economic Implications, UNESCAP Working Paper

Nise, N.S., 2011, Control Systems Engineering, 6th Edition, John Wiley and Sons, Inc.

Notsu, I., Takahashi, S., and Watanabe, Y., 1991, Investigation into Turning Behaviour of Semi-Trailer with Additional Trailer Wheel Steering-A Control Method for Trailer Wheel Steering to Minimize Trailer Rear Overhang Swing in Short Turns, SAE Paper No. 912570

NTC, 2005, Rules for the Assessment of Potential Performance-Based Standards. Discussion Paper. National Transport Commission, Australia

NRTC, 2001, Definition of Potential Performance Measures and Initial Standards, Prepared for National Road Transport Commission by ARRB Transport Research Ltd., Report, Melbourne, Victoria, Australia

Oberoi, D. and He, Y., (2011), "Simulation-Based Design Synthesis of Articulated Heavy Vehicle for Improving Manoeuvrability and Stability", Proceedings of 4th International Conference on Mechanical Engineering and Mechanics, Suzhou, China, pp. 193-197

Oberoi, D., Islam, M. M., and He, Y., (2011), "Design Optimization of Articulated Heavy Vehicles Using Genetic Algorithms and Multibody Vehicle Model", Proceedings of 23rd Canadian Congress of Applied Mechanics, Vancouver, BC, Canada

Odhams, A. M. C., Roebuck, R. L., Jujnovich, B. A., and Cebon, D. 2010, Active steering of a tractor semitrailer, Proc. IMechE Vol. 225 Part D: J. Automobile Engineering, pp. 847-869

Ogata, K., 2010, *Modern Control Engineering.* Fifth Edition, Prentice Hall, New Jersey, USA

OLCV, 2009, Ontario LCV Pilot Program Conditions, http:www.mto.gov.on.ca/english/trucks/lcv/lcvconditions.pdf, (April 17, 2009)

Oreh, S.H.T., Kazemi, R. and Azadi, S., 2014, A sliding-mode controller for directional control of articulated heavy vehicles. Proceedings of the Institute of Mechanical Engineers Part D: Journal of Automobile Engineering, 228(3) pp. 245-262

Oudghiri, M., Chadli, M. and Jajjaji, A., (2007), Vehicle Yaw Control Using a Robust H_∞ Observer-Based Fuzzy Controller Design, Proceedings of 46th IEEE Conference on Decision and Control, New Orleans, USA

Pacejka, H. 2005, Tyre and vehicle dynamics. SAE International, Warrendale, USA

Palkovics, L. and El-Gindy, M., 1996, Examination of different control strategies of heavy-vehicle performance. Journal of Dynamic Systems, Measurement, and Control, 118, pp. 489-498

Palkovics, L. and Fries, A., 2001, Intelligent electronic systems in commercial vehicles for enhanced traffic safety, Vehicle Systems Dynamics, Vol. 35(4/5), pp. 227-289

Palkovics, L., Ilosvai, L. and Semsey, A., 1994, the self-steering behaviour of a tractor-semitrailer at high-speed and its control to improve lateral stability. Heavy Vehicle Systems, International journal of vehicle design, 1(3), 304-323

Palkovics, L., Semsey, A., and Gerum, E., 1999, Rollover Prevention System for Commercial Vehicles-Additional Sensorless Function of the Electronic Brake System, Vehicle System Dynamics, 32(4/5), pp. 285-297

Peng H, 2002, Evaluation of driver assistance systems – a human centered approach. Proceeding of the International Symposium on Advanced Vehicle Control. University of Michigan, Ann Arbor, USA

Percy, A. and Spark, I., 2012, A numerical control algorithm for a B-double truck-trailer with steerable trailer wheels and active hitch angles, Proceedings of the Institution of Mechanical Engineers, Part D: Journal of Automobile Engineering, 227, pp. 899-904

Percy, A. and Spark, I., 2012a, A numerical control algorithm for a B-double truck-trailer with steerable trailer wheels and active hitch angles. Part 2: Reversing, Proceedings of the Institution of Mechanical Engineers, Part D: Journal of Automobile Engineering, 226, pp. 289-300

Petersen, E., Neuhaus, D., Glabe, K., Koschorek, R. and Reich, T., 1998, Vehicle Stability Control for Trucks and Buses. Reprinted from: Electronics for Trucks and Buses (SP-1401) SAE 982782. International Truck and Bus Meeting and Exposition. Indianapolis, IN. November 16 -18

Plochl, M., and Edelmann, J., 2007, Driver models in automobile dynamics application. Vehicle System Dynamics, 45(7-8), pp. 699-741

Preston-Thomas, J., and E-Gindy, M., 1995, Path Compliance in Lane-Change Tests Designed to Evaluate Rearward Amplification, Road transport technology—4. University of Michigan Transportation Research Institute, Ann Arbor, 1995

Printelon, R., Guillaume, P., Rolain, Y., Schoukens, J. and Van hamme, H., 1994, Parametric identification of transfer functions in the frequency domain-a survey, IEEE Transactions on Automatic Control, (39)11, pp. 2245-2259

Rangavajhula, K. and Tsao, H.S.J., 2007, Active trailer steering control of an articulated system with a tractor and three full trailers for tractor-track following. Int J Heavy Veh Systems, 14(3), pp. 271-293

Rangavajhula, K. and Tsao, H. S. J., 2008, Command steering of trailers and command-steering-based optimal control of an articulated system for tractor-track following, Proceedings of Institute of Mechanical Engineers, 222, Part D: Journal of Automobile Engineering, pp. 935-954

SAE-J2179, 1993, Society of Automotive Engineers. A test for evaluating the rearward amplification of multi-articulated vehicles. SAE Recommended Practice J2179, Warrendale, USA; 1993

Sampson, D. J. M. 2000, Active Roll Control of Articulated Heavy Vehicles. PHD thesis, University of Cambridge, Cambridge, England, United Kingdom

Sampson, D. J. M., 2002, Active roll control of articulated heavy vehicles, Technical Report CUED/C-Mech/TR 82

Sampson D.J.M. and Cebon, D., 1998, An investigation of roll control system design for articulated heavy vehicles. Proceedings of the International Symposium on Advanced Vehicle Control (AVEC'98), Japan, pp. 311-316

Schofield, B., Hagglund, T. and Rantzer, A., 2006, Vehicle Dynamics Control and Controller Allocation for Rollover Prevention. Proceedings of the 2006 IEEE International Conference on Control Applications Munich, Germany, October 4-6

Schofield, B, and Hagglund, T., 2008, Optimal Control Allocation in Vehicle Dynamics Control for Rollover Mitigation. 2008 American Control Conference Westin Seattle Hotel, Seattle, Washington, USA, June 11-13, 2008

Shamim, R., Islam, M. M., and He, Y., (2011), A Comparative Study of Active Control Strategies for Improving Lateral Stability of Car-Trailer Systems, SAE 2011World Congress, Paper NO: 2011-01-0959, Detroit, MI, USA

Skogestad, S. and Postlethwaite, I., 2001, Multivariable Feedback Control Analysis and Design, 2nd Edition, John Wiley & Sons

Slotine J.E., 1984, Sliding controller design for nonlinear system. International Journal of Control. 40(2), pp. 421-434

Slotine, J. E. and Li, W. 1991, Applied Nonlinear Control. Prentice Hall, New Jersey

Stevenson, B., Ridley, P., 2005, Automated Vehicle Stability Control for Articulated Vehicles, Proceedings of the Australasian Conference on Robotics and Automation, 5 - 7 December 5-7, New South Wales, Australia

Sulaiman, S., Samin, P.M., Jamaluddin, H., Rahman, R.A. and Burhaumudin, M.S., 2012, Groundhook Control of Semi-Active Suspension for Heavy Vehicle, International Journal of Research in Engineering and Technology, 1(3), pp. 2277-4378

Tabatabaei Oreh, S. H., Kazemi, R., Azadi, S., 2012, A new desired articulation angle for directional control of articulated vehicles, Proc IMechE Part K: J Multi-body Dynamics, 226(4) pp. 298-314

Tabatabaei Oreh, S. H., Kazemi, R., Azadi, S. and Zahedi, A., 2012a, A New Method for Directional Control of Tractor Semi-trailer, Australian Journal of Basic and Applied Sciences, 6(12), pp: 396-409

Tagesson, K., Sundstrom, P., Laine, L. and Dela, N., 2009, Real-time Performance of Control Allocation for Actuator Coordination in Heavy Vehicles. Intelligent Vehicles Symposium, 2009 IEEE. pp 685-690

Taheri, S., 2014, Steering Control Characteristics of Human Driver Coupled with an Articulated Commercial Vehicle, PhD thesis, Concordia University, Montreal, Canada

Tanka, K. and Takahiro, K., 1997, Design of a Stable Fuzzy Controller for an Articulated Vehicle, IEEE Transactions on Systems, Man, and Cybernetics-Part B: Cybernetics, 27(3), pp. 552-558

Tavasoli, A., and Naraghi, M., 2013, An Optimized Multi-Stage Scheme to Coordinate Steering and Braking. IJST. Transactions of Mechanical Engineering, Vol. 37, No. M2, pp. 161-174

Ungoren, A.Y., and Peng, H., 2005, An adaptive lateral preview driver model. Vehicle System Dynamics, 43(4), pp. 245-259

USDT, 2005, Report to Congress on the Large Truck Crash Causation Study, U.S. Department of Transportation, and Federal Motor Carrier Safety Administration

Utkin, V. 1977, Variable structure systems with sliding mode. IEEE Transactions on Automatic Control, 22(2), pp. 212-222

Utkin, V., Guldner, J. and Shi, J., 1999, Sliding mode control in electromechanical systems, Taylor and Francis

VehicleSim, 2011, The VehicleSim Steering Controller Technical Memo. Mechanical Simulation Corporation, Michigan, USA

Wang Q, He Y, 2015, Design and validation of active trailer steering systems for multi-trailer articulated heavy vehicles considering driver-vehicle-controller interactions. International Journal of Vehicle Performance, 2(1), pp. 58-84

Wang, Q. and He, Y., 2016, A Study on Single Lane Change Maneuvers for Determining Rearward Amplification of Multitrailer Articulated Heavy Vehicles with Active Trailer Steering Systems, Vehicle System Dynamics, 54(1), pp. 102-123

Wang, J., and Longoria, R.G., 2006, Coordinated Vehicle Dynamics Control with Control Distribution. Proceedings of the 2006 American Control Conference Minneapolis, Minnesota, USA. June 14-16

Wang, J.Y. and Tomizuka, M., 2000, Dynamic analysis and robust steering controller design for automated lane guidance of heavy-duty vehicles, Asian Journal of Control, 2(3), pp.140-154

Winkler, C., 2001, Rollover of heavy commercial vehicles, UMTRI Research Review, 31(2001), pp. 1-17

Winkler, C.B., Bogard, S.E., Ervin, R.D., Horsman, A., Blower, D., Mink, C. and Karanihas, S. 1993, Evaluation of innovative converter dollies, Contract no. DTFH61-89-C-00081, U.S. DOT, Federal Highway Administration

Winkler, C.B., Fancher P.S., Bareket Z., Bogard S., Johnson G., Karamihas, S. and Mink C. 1992, Heavy vehicle size and weight – test procedures for minimum safety performance standards. Final technical report, NHTSA, US DOT, contract DTNH22-87-D17174, University of Michigan Transportation Research Institute, Report No. UMTRI-92-13

Winkler, C., Fancher, P., Carsten, O., Mathew, A. and Dill, P., 1986, Improving the dynamic performance of multitrailer vehicles: a study of innovative dollies, final Report, University of Michigan Transportation Research Institute (UMTRI), FWHA Contract No. DTFH61-84-C-00026, Report No. UMRI-86-26

Winkler C.B., Fancher P.S., Carsten O., A. Mathew A., and Dill, P., 1986, Improving the dynamic performance of multitrailer vehicles: a study of innovative dollies, final Report, University of Michigan Transportation Research Institute (UMTRI), FWHA Contract No. DTFH61-84-C-00026, Report No. UMRI-86-26

Winkler, D., Fancher, P. and MacAdam, C., 1983, Parametric analysis of heavy duty truck dynamic stability, Volume I – Technical Report, Transportation Research Institute, University of Michigan

Wong, J.Y., 2008, Theory of ground vehicles. John Willey

Woodrooffe J., Ash, L., 2001, Economic efficiency of long combination transport vehicle in Alberta. Woodrooffe and Associates, Report, Canada, pp. 1-30

Woodrooffe, J., Anderson D. and Lloyd Ash L., 2004, The Influence of Policy on Crash Rate of Long Combination Vehicles. Proceedings of 8th International Symposium on Heavy Vehicle Weights and Dimensions

Woodrooffe, J., and Milliken P., 2007, Safety Analysis of a Double & Triple Carrying Loaded Containers. Report Prepared for Saskatchewan Highways and Transportation

Wu, D. H., and Lin, J. H., (2003), "Analysis of Dynamic Lateral Response for a Multi-Axle-Steering Tractor and Trailer", International Journal of Heavy Vehicle Systems, 10(4), 281-294

Yang X, 1999, A closed-loop driver/vehicle directional dynamics predictor. PhD thesis, Concordia University, Canada

Yang, X., Rakheja, S., and Stiharu, I., 2001, Adapting an articulated vehicle to its drivers. Transaction of the ASME Journal of Mechanical Design, 123, pp. 132-140

Yang, X., Rakheja, S., and Stiharu, I., 2002, Structure of the driver model for articulated vehicles. Heavy Vehicle Systems, International Journal of Vehicle Design, 9(1), pp. 27-51

Yim, S., J., Yoon, J. Y., Cho, W. K., and Yi, K. S., 2011, An Investigation on Rollover Prevention Systems:, Unified Chassis Control versus Electronic Stability Control with Active Anti-roll Bar, Proceedings of the Institution of Mechanical Engineers, Part D: Journal of Automobile Engineering, 225, pp. 1-14

Yin, G.D., Chen, N., Wang, J.X. and Chen, J.S., 2010, Robust control for 4WS vehicles considering a varying tire-road friction coefficient, International Journal of Automotive Technology, 11(1), pp. 33-40

Young KD, Utkin VI, Özgùner Ù, 1999, A control engineer's guide to sliding mode control. IEEE Transactions on Control Systems Technology. 7(3), pp. 328-342

Zhou, S. and Zhang, S., 2012, Jackknife Control on Tractor Semi-trailer during High Speed Curve Driving, Sensors & Transducers Journal, 16, Special Issue, pp. 277-284

Zhu S, He Y, 2016, A driver-adaptive stability control strategy for sport utility vehicles. Under review, Vehicle System Dynamics. Manuscript ID: NVSD-2015-0156

Zhu, S., He, Y. and Ren, J., 2016, Modeling and Validation of the Lateral Dynamics of Multi-Trailer Articulated Heavy Vehicles for Active Safety Systems Design and Optimization. To be submitted to Vehicle System Dynamics.

Zhu, S. and He, Y., 2016. A Unified Lateral Preview Driver Model for Road Vehicles. Under review, Vehicle System Dynamics. Manuscript ID: NVSD-2016-0243

Zhu, S. and He, Y., 2015. Articulated Heavy Vehicle Lateral Dynamic Analysis Using an Automated Frequency Response Measuring Technique. International Journal of Vehicle Performance, 2(1), pp. 30 - 57

Zhu, S., Ni, Z., and He, Y., 2016, An Investigation of Test Maneuvers for Determining Rearward Amplification of Articulated Heavy Vehicles. To be submitted to Vehicle System Dynamics

Zong, C., Zhu, T., Wang, C. and Liu, H., 2011, Multi-objective Stability Control Algorithm of Heavy Tractor Semi-trailer Based on Differential Braking, CHINESE JOURNAL OF MECHANICAL ENGINEERING, 25(1), pp. 88-97

Appendix A System Matrices and Parameters of the Tractor/Semitrailer Models

The system matrices of the 3-DOF linear yaw-plane model of the tractor/semitrailer shown in Equations (3.7) and (3.8) are given as

$$\mathbf{M}=\begin{bmatrix} -m_2\left(l_{c1}+l_{c21}\right) & -m_2 l_{c21} & \left(m_1+m_2\right)U_1 & 0 \\ I_{zz1}+m_2 l_{c1}\left(l_{c1}+l_{c21}\right) & m_2 l_{c1} l_{c21} & -m_2 l_{c1} U_1 & 0 \\ I_{zz2}+m_2 l_{c21}\left(l_{c1}+l_{c21}\right) & I_{zz2}+m_2 l_{c21}^2 & -m_2 l_{c21} U_1 & 0 \\ 0 & 0 & 0 & 1 \end{bmatrix},$$

$\mathbf{P}\in\mathbf{R}^{4\times 4}$, and the non-zero elements of matrix $\mathbf{P}$ are given as

$$P(1,1)=\frac{\left(l_{c21}+b_{23}+l_{c1}\right)C_{r23}-C_{f11}a_{11}+C_{r12}b_{12}}{U_1}-\left(m_1+m_2\right)U_1,\ P(1,2)=\frac{\left(l_{c21}+b_{23}\right)C_{r23}}{U_1},$$

$$P(1,3)=-\left(C_{f11}+C_{r12}+C_{r23}\right),\ P(1,4)=C_{r23},\ \ P(2,1)=m_2 l_{c1}U_1-\frac{\left(l_{c1}+b_{23}+l_{c21}\right)C_{r23}l_{c1}+C_{f11}a_{11}^2+C_{r12}b_{12}^2}{U_1},$$

$$P(2,2)=-\frac{\left(l_{c21}+b_{23}\right)C_{r23}l_{c1}}{U_1},\ P(2,3)=C_{r12}b_{12}-C_{f11}a_{11}+C_{r23}l_{c1},\ P(2,4)=-C_{r23}l_{c1}\ ,$$

$$P(3,1)=m_2 l_{c21}U_1-\frac{\left(l_{c21}+b_{23}+l_{c1}\right)C_{r23}\left(l_{c21}+b_{23}\right)}{U_1},\ P(3,2)=-\frac{\left(l_{c21}+b_{23}\right)^2 C_{r23}}{U_1},\ P(3,3)=\left(l_{c21}+b_{23}\right)C_{r23},$$

$$P(3,4)=-\left(l_{c21}+b_{23}\right)C_{r23},\ P(4,2)=1.\ \mathbf{H}_1=\begin{bmatrix} C_{f11} \\ C_{f11}a_{11} \\ 0 \\ 0 \end{bmatrix},\ \mathbf{H}_2=\begin{bmatrix} C_{r12} \\ -C_{r12}b_{12} \\ 0 \\ 0 \end{bmatrix}\ \text{and}\ \mathbf{H}_3=\begin{bmatrix} C_{r23} \\ -C_{r23}l_{c1} \\ -C_{r23}\left(l_{c21}+b_{23}\right) \\ 0 \end{bmatrix}.$$

$$\mathbf{C}=\begin{bmatrix} U_1\mathbf{A}(3,:)+\begin{bmatrix}U_1 & 0 & 0 & 0\end{bmatrix} \\ -\left(l_{c21}+l_{c1}\right)\mathbf{A}(1,:)-l_{c21}\mathbf{A}(2,:)+U_1\mathbf{A}(3,:)+\begin{bmatrix}U_1 & 0 & 0 & 0\end{bmatrix} \end{bmatrix},$$

$$\mathbf{D}_1 = \begin{bmatrix} U_1\mathbf{B}_1(3,:) \\ -(l_{c21}+l_{c1})\mathbf{B}_1(1,:) - l_{c21}\mathbf{B}_1(2,:) + U_1\mathbf{B}_1(3,:) \end{bmatrix},\ \mathbf{D}_2 = \begin{bmatrix} U_1\mathbf{B}_2(3,:) \\ -(l_{c21}+l_{c1})\mathbf{B}_2(1,:) - l_{c21}\mathbf{B}_2(2,:) + U_1\mathbf{B}_2(3,:) \end{bmatrix},$$

$$\mathbf{D}_3 = \begin{bmatrix} U_1\mathbf{B}_3(3,:) \\ -(l_{c21}+l_{c1})\mathbf{B}_3(1,:) - l_{c21}\mathbf{B}_3(2,:) + U_1\mathbf{B}_3(3,:) \end{bmatrix}, \text{ where } A(i,:), i=1,2,3 \text{ means the } i^{th} \text{ row of matrix } \mathbf{A},$$

$\mathbf{B}_j(i,:),\ j=1,2,3,\ i=1,2,3$ denotes the i^{th} row of matrix $\mathbf{B}_j$.

The system matrices of the nonlinear yaw-plane model of the tractor/semitrailer in Equation (9) are given as

$$\mathbf{C}_{nl} = \begin{bmatrix} U_1\mathbf{A}_{nl}(3,:) + [U_1 \quad 0 \quad 0 \quad 0] \\ -(l_{c21}+l_{c1})\mathbf{A}_{nl}(1,:) - l_{c21}\mathbf{A}_{nl}(2,:) + U_1\mathbf{A}_{nl}(3,:) + [U_1 \quad 0 \quad 0 \quad 0] \end{bmatrix},$$

$$\mathbf{D}_{nl} = \begin{bmatrix} U_1\mathbf{B}_{nl}(3,:) \\ -(l_{c21}+l_{c1})\mathbf{B}_{nl}(1,:) - l_{c21}\mathbf{B}_{nl}(2,:) + U_1\mathbf{B}_{nl}(3,:) \end{bmatrix},\ \mathbf{H}_{nl} = \begin{bmatrix} a_{11} & -b_{12} & -l_{c1} \\ 0 & 0 & -b_{23}-l_{c21} \\ 0 & 0 & 0 \\ 1 & 1 & 1 \end{bmatrix},$$

$$\mathbf{M}_{nl} = \begin{bmatrix} 0 & 0 & 0 & 1 \\ -(l_{c1}+l_{c21})m_2 & -l_{c21}m_2 & (m_1+m_2)U_1 & 0 \\ I_{zz1}+l_{c1}(l_{c1}+l_{c21})m_2 & l_{c1}l_{c21}m_2 & -l_{c1}m_2U_1 & 0 \\ I_{zz2}+l_{c21}(l_{c1}+l_{c21})m_2 & I_{zz2}+l_{c21}^2m_2 & -l_{c21}m_2U_1 & 0 \end{bmatrix},\ \mathbf{P}_{nl} = \begin{bmatrix} 0 & 0 & 1 & 0 \\ 0 & -(m_1U_1+m_2U_2) & 0 & 0 \\ 0 & l_{c1}m_2U_2 & 0 & 0 \\ 0 & l_{c21}m_2U_2 & 0 & 0 \end{bmatrix}, .$$

The system parameters of the tractor/semitrailer combination are listed in Table A1.

Table A1 System parameters of the tractor/semitrailer combination

Symbol	Description	Nominal Value
a_{11}	Longitudinal distance between tractor front axle and tractor CG (m)	1.115
b_{12}	Longitudinal distance between tractor rear axle and tractor CG (m)	2.585
b_{23}	Longitudinal distance between trailer CG and trailer axle (m)	4.507
F_i	Lateral tire force of the i^{th} axle, $i=1,2,3$ (N)	
F_{y1}	Lateral coupling force at fifth-wheel (N)	
I_{zz1}	Yaw mass moment of inertia of tractor ($kg.m^2$)	20,616
I_{zz2}	Yaw mass moment of inertia of trailer ($kg.m^2$)	113,580
l_{c1}	Longitudinal distance between tractor CG and fifth wheel (m)	1.959
l_{c21}	Longitudinal distance between trailer CG and fifth wheel (m)	5.493
m_1	Tractor total mass (kg)	6,525
m_2	Trailer total mass (kg)	11,665

U_1	Tractor's forward speed (m/s)	
U_2	Trailer's forward speed (m/s)	
y_1	Lateral position of the tractor (m)	
y_2	Lateral position of the trailer (m)	
α_1	Equivalent side-slip angle of tires on the 1st axle of tractor (rad)	
α_2	Equivalent side-slip angle of tires on the 2nd axle of tractor (rad)	
α_3	Equivalent side-slip angle of tires on the axle of trailer (rad)	
β_1	Side-slip angle at tractor center of gravity (CG) (rad)	
β_2	Side-slip angle at trailer CG (rad)	
δ_{1f}	Equivalent steer angle of tractor front wheels(rad)	
δ_2	Equivalent steer angle of tractor rear wheels(rad)	
δ_3	Equivalent steer angle of trailer wheels(rad)	
ψ_1	Tractor yaw angle(rad)	
ψ_2	Trailer yaw angle(rad)	
$\Delta\psi$	Articulation angle between the tractor and semitrailer unit (rad)	

Appendix B Notation and Nominal Values of the Parameters of the B-Train Double Models

Symbol	Description	Nominal Value
α_1	Side slip angle of the tires of the tractor front axle (rad)	
α_{1l}	Side slip angle of the left tire of the tractor front axle (rad)	
α_{1r}	Side slip angle of the right tire of the tractor front axle (rad)	
α_2	Side slip angle of the tires of the tractor 1st rear axle (rad)	
α_{2l}	Side slip angle of the left tire of the tractor 1st rear axle (rad)	
α_{2r}	Side slip angle of the right tire of the tractor 1st rear axle (rad)	
α_3	Side slip angle of the tires of the tractor 2nd rear axle (rad)	
α_{3l}	Side slip angle of the left tire of the tractor 2nd rear axle (rad)	
α_{3r}	Side slip angle of the right tire of the tractor 2nd rear axle (rad)	
α_4	Side slip angle of the tires of the 1st semitrailer front axle (rad)	
α_{4l}	Side slip angle of the left tire of the 1st semitrailer front axle (rad)	
α_{4r}	Side slip angle of the right tire of the 1st semitrailer front axle (rad)	
α_5	Side slip angle of the tires of the 1st semitrailer middle axle (rad)	
α_{5l}	Side slip angle of the left tire of the 1st semitrailer middle axle (rad)	
α_{5r}	Side slip angle of the right tire of the 1st semitrailer middle axle (rad)	
α_6	Side slip angle of the tires of the 1st semitrailer rear axle (rad)	
α_{6l}	Side slip angle of the left tire of the 1st semitrailer rear axle (rad)	
α_{6r}	Side slip angle of the right tire of the 1st semitrailer rear axle (rad)	
α_7	Side slip angle of the tires of the 2nd semitrailer front axle (rad)	
α_{7l}	Side slip angle of the left tire of the 2nd semitrailer front axle (rad)	
α_{7r}	Side slip angle of the right tire of the 2nd semitrailer front axle (rad)	
α_8	Side slip angle of the tires of the 2nd semitrailer middle axle (rad)	
α_{8l}	Side slip angle of the left tire of the 2nd semitrailer middle axle (rad)	
α_{8r}	Side slip angle of the right tire of the 2nd semitrailer middle axle (rad)	
α_9	Side slip angle of the tires of the 2nd semitrailer rear axle (rad)	
α_{9l}	Side slip angle of the left tire of the 2nd semitrailer rear axle (rad)	
α_{9r}	Side slip angle of the right tire of the 2nd semitrailer rear axle (rad)	
β_1	Side slip angle at the whole mass CG of the tractor (rad)	

β_2	Side slip angle at the whole mass CG of the 1st semitrailer (rad)	
β_3	Side slip angle at the whole mass CG of the 2nd semitrailer (rad)	
β_{s1}	Side slip angle at the sprung mass CG of the tractor (rad)	
β_{s2}	Side slip angle at the sprung mass CG of the 1st semitrailer (rad)	
β_{s3}	Side slip angle at the sprung mass CG of the 2nd semitrailer (rad)	
δ_{11}	Front wheel steer angle of the tractor (rad)	
δ_4	Steer angle of the 1st semitrailer front axle (rad)	
δ_5	Steer angle of the 1st semitrailer middle axle (rad)	
δ_6	Steer angle of the 1st semitrailer rear axle (rad)	
δ_7	Steer angle of the 2nd semitrailer front axle (rad)	
δ_8	Steer angle of the 2nd semitrailer middle axle (rad)	
δ_9	Steering angle of the 2nd semitrailer rear axle (rad)	
$\dot{\psi}_1$	Yaw rate of the whole mass of the tractor (rad/s)	
$\dot{\psi}_2$	Yaw rate of the whole mass of the 1st semitrailer (rad/s)	
$\dot{\psi}_3$	Yaw rate of the whole mass of the 2nd semitrailer (rad/s)	
ϕ_1	Roll angle of the sprung mass of the tractor about its roll axis (rad)	
ϕ_2	Roll angle of the sprung mass of the 1st semitrailer about its roll axis (rad)	
ϕ_3	Roll angle of the sprung mass of the 2nd semitrailer about its roll axis (rad)	
ϕ_{t1}	Roll angle of the unsprung mass of the tractor about its roll axis (rad)	
ϕ_{t2}	Roll angle of the unsprung mass of the 1st semitrailer about its roll axis (rad)	
ϕ_{t3}	Roll angle of the unsprung mass of the 2nd semitrailer about its roll axis (rad)	
σ_i	Longitudinal slip ratio of the i^{th} wheel, $i = 1l, 1r, 2l, 2r, \cdots, 9l, 9r$	
a_{11}	Longitudinal distance between the whole mass CG of the tractor and its front axle (m)	1.999
a_{11s}	Longitudinal distance between the tractor sprung mass CG and its front axle (m)	1.384
a_{11u}	Longitudinal distance between the tractor unsprung mass CG and its front axle (m)	3.988
a_2	Longitudinal distance between the whole mass CG of the 1st semitrailer and the 1st coupling point (m)	6.973
a_{2s}	Longitudinal distance between the 1st semitrailer sprung mass CG and the 1st coupling point (m)	6.385
a_{2u}	Uncertain longitudinal distance between the 1st coupling point and the whole mass CG of the 1st semitrailer (m)	
a_3	Longitudinal distance between the whole mass CG of the 2nd semitrailer and the 2nd coupling point (m)	6.973
a_{3s}	Longitudinal distance between the 2nd semitrailer sprung mass CG and the 2nd coupling point (m)	6.385

$a_{3.u}$	Uncertain longitudinal distance between the 2nd coupling point and the whole mass CG of the 2nd semitrailer (m)	
a_{x1}	Longitudinal acceleration at the whole mass CG of the tractor $\left(m/\mathrm{s}^2\right)$	
a_{x2}	Longitudinal acceleration at the whole mass CG of the 1st semitrailer $\left(m/\mathrm{s}^2\right)$	
a_{x2}	Longitudinal acceleration at the whole mass CG of the 2nd semitrailer $\left(m/\mathrm{s}^2\right)$	
a_{y1}	Lateral acceleration at the whole mass CG of the tractor $\left(m/\mathrm{s}^2\right)$	
a_{y2}	Lateral acceleration at the whole mass CG of the 1st semitrailer $\left(m/\mathrm{s}^2\right)$	
a_{y3}	Lateral acceleration at the whole mass CG of the 2nd semitrailer $\left(m/\mathrm{s}^2\right)$	
a_{y1s}	Lateral acceleration at the sprung mass CG of the tractor $\left(m/\mathrm{s}^2\right)$	
a_{y2s}	Lateral acceleration at the sprung mass CG of the 1st semitrailer $\left(m/\mathrm{s}^2\right)$	
a_{y3s}	Lateral acceleration at the sprung mass CG of the 2nd semitrailer $\left(m/\mathrm{s}^2\right)$	
b_{12}	Longitudinal distance between the tractor whole mass CG and its 1st rear axle (m)	3.001
b_{12s}	Longitudinal distance between the tractor sprung mass CG and its 1st rear axle (m)	3.616
b_{12u}	Longitudinal distance between the tractor unsprung mass CG and its 1st rear axle (m)	1.012
b_{13}	Longitudinal distance between the tractor whole mass CG and its 2nd rear axle (m)	4.271
b_{13s}	Longitudinal distance between the tractor sprung mass CG and its 2nd rear axle (m)	4.886
b_{13u}	Longitudinal distance between the tractor unsprung mass CG and its 2nd rear axle (m)	2.282
b_{24}	Longitudinal distance between the 1st semitrailer whole mass CG and its front axle (m)	3.257
b_{24s}	Longitudinal distance between the 1st semitrailer sprung mass CG and its front axle (m)	3.85
b_{24u}	Longitudinal distance between the 1st semitrailer unsprung mass CG and its front axle (m)	
b_{25}	Longitudinal distance between the whole mass CG of the 1st semitrailer and its middle axle (m)	4.527
b_{25s}	Longitudinal distance between the 1st sprung mass CG and its middle axle (m)	5.12
b_{26}	Longitudinal distance between the whole mass CG of the 1st semitrailer and its rear axle (m)	5.797
b_{26s}	Longitudinal distance between the sprung mass CG of the 1st semitrailer and its rear axle (m)	6.39

b_{37}	Longitudinal distance between the whole mass CG of the 2nd semitrailer and its front axle (m)	3.257
b_{37s}	Longitudinal distance between the 2nd sprung mass CG of the 2nd semitrailer and its front axle (m)	3.85
b_{38}	Longitudinal distance between the whole mass CG of the 2nd semitrailer and its middle axle (m)	4.527
b_{38s}	Longitudinal distance between the 2nd sprung mass CG and its middle axle (m)	5.12
b_{39}	Longitudinal distance between the whole mass CG of the 2nd semitrailer and its rear axle (m)	5.797
b_{39s}	Longitudinal distance between the 2nd sprung mass CG of the 2nd semitrailer and its rear axle (m)	6.39
C_1	Combined cornering stiffness of the tires of the tractor front axle (N/rad)	424,000
C_2	Combined cornering stiffness of the tires of the 1st rear axle of the tractor (N/rad)	420,200
C_3	Combined cornering stiffness of the tires of the 2nd rear axle of the tractor (N/rad)	420,200
C_4	Combined cornering stiffness of the tires of the front axle of the 1st semitrailer (N/rad)	581,900
C_5	Combined cornering stiffness of the tires of the middle axle of the 1st semitrailer (N/rad)	581,900
C_6	Combined cornering stiffness of the tires of the rear axle of the 1st semitrailer (N/rad)	581,900
C_7	Combined cornering stiffness of the tires of the front axle of the 2nd semitrailer (N/rad)	346,500
C_8	Combined cornering stiffness of the tires of the middle axle of the 2nd semitrailer (N/rad)	346,500
C_9	Combined cornering stiffness of the tires of the rear axle of the 2nd semitrailer (N/rad)	346,500
C_{s1}	Combined longitudinal slip coefficient of the tires on the tractor front axle	170,000
C_{s2}	Combined longitudinal slip coefficient of the tires on the 1st rear axle of the tractor	180,000
C_{s3}	Combined longitudinal slip coefficient of the tires on the 2nd rear axle of the tractor	180,000
C_{s4}	Combined longitudinal slip coefficient of the tires on the 1st semitrailer front axle	290,000
C_{s5}	Combined longitudinal slip coefficient of the tires on the 1st semitrailer middle axle	290,000
C_{s6}	Combined longitudinal slip coefficient of the tires on the 1st semitrailer rear axle	290,000
C_{s7}	Combined longitudinal slip coefficient of the tires on the 2nd semitrailer front axle	190,000
C_{s8}	Combined longitudinal slip coefficient of the tires on the 2nd semitrailer middle axle	190,000
C_{s9}	Combined longitudinal slip coefficient of the tires on the 2nd semitrailer rear axle	190,000
d_{11}	Track width of the tractor front axle (m)	1.98
d_1	Track width of the tractor rear axles (m)	1.65

d_2	Track width of the 1st semitrailer (m)	1.65
d_3	Track width of the 2nd semitrailer (m)	1.65
d_x	Longitudinal distance between each axle of the semitrailer (m)	1.27
F_{cx1}	Longitudinal coupling force at the 1st coupling point (N)	
F_{cx2}	Longitudinal coupling force at the 2nd coupling point (N)	
F_{cy1}	Lateral coupling force at the 1st coupling point (N)	
F_{cy2}	Lateral coupling force at the 2nd coupling point (N)	
F_{xi}	Longitudinal force of the tires on the i^{th} $(i=1,2,\cdots,9)$ axle (N)	
F_{yi}	Lateral force of the tires on the i^{th} $(i=1,2,\cdots,9)$ axle (N)	
F_{zi}	Normal force of the i^{th} $(i=1l,1\mathrm{r},2l,\cdots,9r)$ tire (N)	
f_r	Longitudinal resistance coefficient	0.02
h_{c1}	Height of the 1st coupling point measured upwards from the ground (m)	1.1
h_{c2}	Height of the 2nd coupling point measured upwards from the ground (m)	1.1
h_{cg1}	Height of the whole mass CG of the tractor (m)	0.9
h_{cg2}	Height of the whole mass CG of the 1st semitrailer (m)	1.435
h_{cg3}	Height of the whole mass CG of the 2nd semitrailer (m)	1.435
h_{ri}	Height of the roll center of the sprung/unsprung masses of the $i^{th}(i=1,2,3)$ unit measured upwards from the ground (m)	0.705
h_{bi}	Height of the coupling point measured upwards from the roll center of the $i^{th}(i=1,2,3)$ unit (m)	0.395
h_{s1}	Height of the sprung mass CG of the tractor measured upwards from the ground (m)	1.019
h_{s2}	Height of the sprung mass CG of the 1st semitrailer measured upwards from the ground (m)	1.555
h_{s3}	Height of the sprung mass CG of the 2nd semitrailer measured upwards from the ground (m)	1.555
h_{u1}	Height of the tractor unsprung mass CG measured upwards from the ground (m)	0.519
h_{u2}	Height of the 1st semitrailer unsprung mass CG measured upwards from the ground (m)	0.51
h_{u3}	Height of the 2nd semitrailer unsprung mass CG measured upwards from the ground (m)	0.51
I_{sxxi}	Roll moment of inertia of the sprung mass of the $i^{th}(i=1,2,3)$ unit measured about the CG of the sprung mass (kgm^2)	6,879

I_{sxzi}	Yaw-roll product of inertia of the sprung mass of the $i^{th}\ (i=1,2,3)$ unit measured about the CG of the sprung mass $\left(kgm^2\right)$	130
I_{u1xx}	Roll moment of inertia of the unsprung mass of the tractor measured about the CG of the unsprung mass $\left(kgm^2\right)$	867
I_{u2xx}	Roll moment of inertia of the unsprung mass of the 1st semitrailer measured about the CG of the unsprung mass $\left(kgm^2\right)$	798
I_{u3xx}	Roll moment of inertia of the unsprung mass of the 2nd semitrailer measured about the CG of the unsprung mass $\left(kgm^2\right)$	798
I_{u1xz}	Yaw-roll product of inertia of the unsprung mass of the tractor measured about the CG of the unsprung mass $\left(kgm^2\right)$	0
I_{u2xz}	Yaw-roll product of inertia of the unsprung mass of the 1st semitrailer measured about the CG of the unsprung mass $\left(kgm^2\right)$	0
I_{u3xz}	Yaw-roll product of inertia of the unsprung mass of the 2nd semitrailer measured about the CG of the unsprung mass $\left(kgm^2\right)$	0
I_{zz1}	Yaw moment of inertia of the whole mass of the tractor, measured about the whole mass CG $\left(kgm^2\right)$	43,996
I_{zz2}	Yaw moment of inertia of the whole mass of the 1st semitrailer, measured about the whole mass CG $\left(kgm^2\right)$	490,940
I_{zz3}	Yaw moment of inertia of the whole mass of the 2nd semitrailer, measured about the whole mass CG $\left(kgm^2\right)$	490,940
K_{12}	Roll stiffness of the fifthwheel between the tractor and 1st semitrailer $\left(Nm/rad\right)$	550,000
K_{23}	Roll stiffness of the fifthwheel between the 1st and 2nd semitrailers $\left(Nm/rad\right)$	550,000
K_b	Brake gain of each wheel in the tridem wheel groups $\left(Nm/MP_a\right)$	14,286
K_{r1f}	Roll stiffness of the front suspension of the tractor adjusted with the tire vertical stiffness $\left(Nm/rad\right)$	700,000
K_{r1r}	Roll stiffness of the rear suspension group of the tractor adjusted with the tire vertical stiffness $\left(Nm/rad\right)$	1100,000
K_{r2}	Roll stiffness of the suspension (group) of the 1st semitrailer adjusted with the tire vertical stiffness $\left(Nm/rad\right)$	2000,000
K_{r3}	Roll stiffness of the suspension (group) of the 2nd semitrailer adjusted with the tire vertical stiffness $\left(Nm/rad\right)$	2200,000
K_{t1f}	Tire roll stiffness of the tractor front axle $\left(Nm/rad\right)$	900,000
K_{t1r}	Tire roll stiffness of the tractor rear axle $\left(Nm/rad\right)$	1,500,000
K_{t2}	Tire roll stiffness of the axle (group) of the 1st semitrailer $\left(Nm/rad\right)$	6,000,000
K_{t3}	Tire roll stiffness of the axle (group) of the 2nd semitrailer $\left(Nm/rad\right)$	5,200,000

l_{c1}	Longitudinal distance between the whole mass CG of the tractor and the 1st coupling point (m)	3.636
l_{c21}	Longitudinal distance between the whole mass CG of the 1st semitrailer and the 1st coupling point (m)	6.973
l_{c22}	Longitudinal distance between the whole mass CG of the 1st semitrailer and the 2nd coupling point (m)	5.597
l_{c3}	Longitudinal distance between the whole mass CG of the 2nd semitrailer and the 2nd coupling point (m)	6.973
L_{r1f}	Roll damping coefficient of the tractor front suspension (Nms/rad)	50,000
L_{r1r}	Roll damping coefficient of the tractor rear suspension group (Nms/rad)	80,000
L_{r2}	Roll damping coefficient of the 1st semitrailer suspension group (Nms/rad)	120,000
L_{r3}	Roll damping coefficient of the 2nd semitrailer suspension group (Nms/rad)	120,000
m_1	Whole mass of the tractor (kg)	8,258
m_{1s}	Sprung mass of the tractor (kg)	6,308
m_{1u}	Unsprung mass of the tractor (kg)	1,950
m_2	Whole mass of the 1st semitrailer (kg)	17,997
m_{2s}	Sprung mass of the 1st semitrailer (kg)	15,927
m_{2u}	Unsprung mass of the 1st semitrailer (kg)	2,070
$m_{2.u}$	Uncertain whole mass of the 1st semitrailer (kg)	
m_{3s}	Sprung mass of the 2nd semitrailer (kg)	15,927
m_{3u}	Unsprung mass of the 2nd semitrailer (kg)	2,070
$m_{3.u}$	Uncertain whole mass of the 2nd semitrailer (kg)	
$M_{x1f/r}$	External roll moment of the front/rear axle (group) of the tractor (Nm)	
M_{x2}	External roll moment of the 1st semitrailer (Nm)	
M_{x3}	External roll moment of the 2nd semitrailer (Nm)	
M_{y1}	Pitch moment of the tractor sprung mass (Nm)	
M_{z2}	External yaw moment of the 1st semitrailer (Nm)	
M_{z3}	External yaw moment of the 2nd semitrailer (Nm)	
N_{β_1}	Partial derivative of the net tyre yaw moment with respect to the sideslip angle at the whole mass CG of the tractor (Nm/rad)	2208,200
N_{β_2}	Partial derivative of the net tyre yaw moment with respect to the sideslip angle at the whole mass CG of the 1st semitrailer (Nm/rad)	7,902,300
N_{β_3}	Partial derivative of the net tyre yaw moment with respect to the sideslip angle at the whole mass CG of the 2nd semitrailer (Nm/rad)	4,705,500
$N_{\delta_{11}}$	Partial derivative of the net tyre yaw moment with respect to the wheel steer angle of the tractor front axle (Nm/rad)	847,530

N_{δ_4}	Partial derivative of the net tyre yaw moment with respect to the wheel steer angle of the 1st semitrailer front axle (Nm/rad)	-1,895,100
N_{δ_5}	Partial derivative of the net tyre yaw moment with respect to the wheel steer angle of the 1st semitrailer middle axle (Nm/rad)	-2,634,100
N_{δ_6}	Partial derivative of the net tyre yaw moment with respect to the wheel steer angle of the 1st semitrailer rear axle (Nm/rad)	-3,373,100
N_{δ_7}	Partial derivative of the net tyre yaw moment with respect to the wheel steer angle of the 2nd semitrailer front axle (Nm/rad)	-1,128,400
N_{δ_8}	Partial derivative of the net tyre yaw moment with respect to the wheel steer angle of the 2nd semitrailer middle axle (Nm/rad)	-1,568,500
N_{δ_9}	Partial derivative of the net tyre yaw moment with respect to the wheel steer angle of the 2nd semitrailer rear axle (Nm/rad)	-2,008,600
$N_{\dot{\psi}_1}$	Partial derivative of the net tyre yaw moment with respect to the yaw rate at the whole mass CG of the tractor (Nms/rad)	-1,314,400
$N_{\dot{\psi}_2}$	Partial derivative of the net tyre yaw moment with respect to the yaw rate at the whole mass CG of the 1st semitrailer (Nms/rad)	-3,764,800
$N_{\dot{\psi}_3}$	Partial derivative of the net tyre yaw moment with respect to the yaw rate at the whole mass CG of the 2nd semitrailer (Nms/rad)	-2,241,800
p_{a_2}	Relative error from the nominal value of the longitudinal distance a_2	
p_{a_3}	Relative error from the nominal value of the longitudinal distance a_3	
p_{m_2}	Relative error from the nominal value of the whole of the 1st semitrailer	
p_{m_3}	Relative error from the nominal value of the whole of the 2nd semitrailer	
r_w	Effective rolling radius of the semitrailer wheel (m)	0.51
T_d	Drive torque $(N \cdot m)$	
U	Forward speed at the whole mass CG of the unit	
V_i	Lateral speed at the whole mass CG of the i^{th} $(i = 1,2,3)$ unit	
${}^{yp}\vec{V}_i^{\,j}$	Velocity of the i^{th} ($i = 1,2,3$) unit at the j^{th} ($j = 1,2$) coupling point represented in the i^{th} body-fixed coordinate system (m/s) in the yaw-plane model	
${}^{yr}\vec{V}_i^{\,j}$	Velocity of the i^{th} ($i = 1,2,3$) unit at the j^{th} ($j = 1,2$) coupling point represented in the i^{th} body-fixed coordinate system (m/s) in the yaw-roll model	
${}^{yp}_{O}\vec{V}_i^{\,j}$	Inertia coordinate system representation of ${}^{yp}\vec{V}_i^{\,j}$	
${}^{yr}_{O}\vec{V}_i^{\,j}$	Inertia coordinate system representation of ${}^{yr}\vec{V}_i^{\,j}$	
Y_1	Lateral position of the tractor front axle center (m)	
Y_2	Lateral position of the whole mass CG of the 1st semitrailer (m)	
Y_3	Lateral position of the whole mass CG of the 2nd semitrailer (m)	
Y_{β_1}	Partial derivative of the net tyre lateral force with respect to the sideslip angle at the whole mass CG of the tractor (N/rad)	-1,264,400

Y_{β_2}	Partial derivative of the net tyre lateral force with respect to the sideslip angle at the whole mass CG of the 1st semitrailer (N/rad)	-1,745,700
Y_{β_3}	Partial derivative of the net tyre lateral force with respect to the sideslip angle at the whole mass CG of the 2nd semitrailer (N/rad)	-1,039,500
$Y_{\delta_{11}}$	Partial derivative of the net tyre lateral force with respect to the wheel steer angle of the tractor front axle (N/rad)	424,000
Y_{δ_4}	Partial derivative of the net tyre lateral force with respect to the wheel steer angle of the 1st semitrailer front axle (N/rad)	581,900
Y_{δ_5}	Partial derivative of the net tyre lateral force with respect to the wheel steer angle of the 1st semitrailer middle axle (N/rad)	581,900
Y_{δ_6}	Partial derivative of the net tyre lateral force with respect to the wheel steer angle of the 1st semitrailer rear axle (N/rad)	581,900
Y_{δ_7}	Partial derivative of the net tyre lateral force with respect to the wheel steer angle of the 2nd semitrailer front axle (N/rad)	346,500
Y_{δ_8}	Partial derivative of the net tyre lateral force with respect to the wheel steer angle of the 2nd semitrailer middle axle (N/rad)	346,500
Y_{δ_9}	Partial derivative of the net tyre lateral force with respect to the wheel steer angle of the 2nd semitrailer rear axle (N/rad)	346,500
$Y_{\dot{\psi}_1}$	Partial derivative of the net tyre lateral force with respect to the yaw rate at the whole mass CG of the tractor (Ns/rad)	220,820
$Y_{\dot{\psi}_2}$	Partial derivative of the net tyre lateral force with respect to the yaw rate at the whole mass CG of the 1st semitrailer (Ns/rad)	790,230
$Y_{\dot{\psi}_3}$	Partial derivative of the net tyre lateral force with respect to the yaw rate at the whole mass CG of the 2nd semitrailer (Ns/rad)	470,550

Appendix C System Matrices of the Yaw-roll Model of the B-Train Double

The system matrices of the yaw-roll model of the B-train double are given as follows. $\mathbf{M} \in \mathbf{R}^{18\times 18}$, and the nonzero elements of $\mathbf{M}$ are given:

$M(1,2) = I_{sxz1} - l_{c1}m_{s1}(h_{s1} - h_{r1})$, $M(1,3) = -l_{c1}m_1U$, $M(1,4) = -I_{zz1}$, $M(2,1) = L_{r1f} + L_{r1r}$,
$M(2,2) = I_{sxx1} + m_{s1}(h_{s1} - h_{r1})^2 - h_{cr1}m_{s1}(h_{s1} - h_{r1})$, $M(2,3) = m_{s1}U(h_{s1} - h_{r1}) - h_{cr1}m_1U$, $M(2,4) = -I_{sxz1}$,
$M(2,13) = -L_{r1f} - L_{r1r}$, $M(3,1) = L_{r1f} + L_{r1r}$, $M(3,3) = -m_{u1}U(h_{u1} - h_{r1})$, $M(3,4) = I_{u1xz}$,
$M(3,13) = -(L_{r1f} + L_{r1r})$, $M(4,2) = m_{s1}(h_{s1} - h_{r1})$, $M(4,3) = m_1U$, $M(4,6) = m_{s2}(h_{s2} - h_{r2})$, $M(4,7) = m_2U$
, $M(4,10) = m_{s3}(h_{s3} - h_{r3})$, $M(4,11) = m_3U$, $M(5,2) = l_{c21}m_{s1}(h_{s1} - h_{r1})$, $M(5,3) = l_{c21}m_1U$, $M(5,6) = -I_{sxz2}$,
$M(5,8) = I_{zz2}$, $M(5,10) = -l_{c22}m_{s3}(h_{s3} - h_{r3})$, $M(5,11) = -l_{c22}m_3U$, $M(6,2) = h_{cr2}m_{s1}(h_{s1} - h_{r1})$, $M(6,3) = h_{cr2}m_1U$,
$M(6,5) = L_{r2}$, $M(6,6) = I_{xx2} + m_{s2}(h_{s2} - h_{r2})^2$, $M(6,7) = m_{s2}U(h_{s2} - h_{r2})$, $M(6,8) = -I_{sxz2}$,
$M(6,10) = h_{cr3}m_{s3}(h_{s3} - h_{r3})$, $M(6,11) = h_{cr3}m_3U$, $M(6,15) = -L_{r2}$, $M(7,5) = L_{r2}$, $M(7,7) = -m_{u2}U(h_{u2} - h_{r2})$,
$M(7,8) = I_{u2xz}$, $M(7,15) = -L_{r2}$, $M(7,16) = -I_{u2xx} - m_{u2}(h_{u2} - h_{r2})^2$, $M(8,10) = l_{c3}m_{s3}(h_{s3} - h_{r3}) + I_{xz3}$,
$M(8,11) = l_{c3}m_3U$, $M(8,12) = -I_{zz3}$, $M(9,9) = L_{r3}$, $M(9,10) = I_{sxx3} + m_{s3}(h_{s3} - h_{r3})^2 - h_{cr3}m_{s3}(h_{s3} - h_{r3})$,
$M(9,11) = m_{s3}U(h_{s3} - h_{r3}) - h_{cr3}m_3U$, $M(9,12) = -I_{sxz3}$, $M(9,17) = -L_{r3}$, $M(10,9) = -L_{r3}$, $M(10,11) = m_{u3}U(h_{u3} - h_{r3})$,
$M(10,12) = -I_{u3xz}$, $M(10,17) = L_{r3}$, $M(10,18) = I_{u3xx} + m_{u3}(h_{u3} - h_{r3})^2$, $M(11,2) = h_{cr1}$, $M(11,3) = U$, $M(11,4) = -l_{c1}$
, $M(11,6) = -h_{cr2}$, $M(11,7) = -U$, $M(11,8) = -l_{c21}$, $M(12,6) = h_{cr2}$, $M(12,7) = U$, $M(12,8) = -l_{c22}$,
$M(12,10) = -h_{cr3}$, $M(12,11) = -U$, $M(12,12) = -l_{c3}$, $M(13,1) = 1$, $M(14,5) = 1$, $M(15,9) = 1$, $M(16,13) = 1$,
$M(17,15) = 1$, $M(18,17) = 1$.

$\mathbf{N} \in \mathbf{R}^{18\times 18}$, and the nonzero elements of $\mathbf{N}$ are given:

$N(1,3) = N_{\beta_1} + l_{c1}Y_{\beta_1}$, $N(1,4) = N_{\dot{\psi}_1} + l_{c1}Y_{\dot{\psi}_1} - l_{c1}m_1U$, $N(2,1) = (K_{r1f} + K_{r1r} + K_{12}) - m_{s1}g(h_{s1} - h_{r1})$,
$N(2,3) = h_{cr1}Y_{\beta_1}$, $N(2,4) = m_{s1}U(h_{s1} - h_{r1}) + h_{cr1}Y_{\dot{\psi}_1} - h_{cr1}m_1U$, $N(2,5) = -K_{12}$, $N(2,13) = -K_{r1f} - K_{r1r}$,
$N(3,1) = K_{r1f} + K_{r1r}$, $N(3,3) = -h_{r1}Y_{\beta_1}$, $N(3,4) = -h_{r1}Y_{\dot{\psi}_1} - m_{u1}U(h_{u1} - h_{r1})$,
$N(3,13) = m_{u1}g(h_{u1} - h_{r1}) - K_{r1f} - K_{r1r} - K_{t1f} - K_{t1r}$, $N(4,3) = -Y_{\beta_1}$, $N(4,4) = m_1U - Y_{\dot{\psi}_1}$, $N(4,7) = -Y_{\beta_2}$,
$N(4,8) = m_2U - Y_{\dot{\psi}_2}$, $N(4,11) = -Y_{\beta_3}$, $N(4,12) = m_3U - Y_{\dot{\psi}_3}$, $N(5,3) = -l_{c21}Y_{\beta_1}$; $N(5,4) = l_{c21}m_1U - l_{c21}Y_{\dot{\psi}_1}$,
$N(5,7) = -N_{\beta_2}$, $N(5,8) = -N_{\dot{\psi}_2}$, $N(5,11) = l_{c22}Y_{\beta_3}$, $N(5,12) = l_{c22}Y_{\dot{\psi}_3} - l_{c22}m_3U$, $N(6,1) = -K_{12}$, $N(6,3) = -h_{cr2}Y_{\beta_1}$,
$N(6,4) = h_{cr2}m_1U - h_{cr2}Y_{\dot{\psi}_1}$, $N(6,5) = K_{r2} + K_{12} + K_{23} - m_{s2}g(h_{s2} - h_{r2})$, $N(6,8) = m_{s2}U(h_{s2} - h_{r2})$,
$N(6,9) = -K_{23}$, $N(6,11) = -h_{cr3}Y_{\beta_3}$, $N(6,12) = h_{cr3}m_3U - h_{cr3}Y_{\dot{\psi}_3}$, $N(6,15) = -K_{r2}$, $N(7,5) = K_{r2}$,

$N(7,7) = -h_{r2}Y_{\beta_2}$, $N(7,8) = -m_{u2}U(h_{u2} - h_{r2}) - h_{r2}Y_{\psi_2}$, $N(7,15) = m_{u2}g(h_{u2} - h_{r2}) - (K_{r2} + K_{tr2})$,
$N(8,11) = N_{\beta_3} - l_{c3}Y_{\beta_3}$, $N(8,12) = l_{c3}m_3U + N_{\psi_3} - l_{c3}Y_{\psi_3}$, $N(9,5) = -K_{23}$, $N(9,9) = K_{23} + K_{r3} - m_{s3}g(h_{s3} - h_{r3})$,
$N(9,11) = h_{cr3}Y_{\beta_3}$, $N(9,12) = m_{s3}U(h_{s3} - h_{r3}) + h_{cr3}Y_{\psi_3} - h_{cr3}m_3U$, $N(9,17) = -K_{r3}$, $N(10,9) = -K_{r3}$, $N(10,11) = h_{r3}Y_{\beta_3}$,
$N(10,12) = m_{u3}U(h_{u3} - h_{r3}) + h_{r3}Y_{\psi_3}$, $N(10,17) = K_{r3} + K_{t3} - m_{u3}g(h_{u3} - h_{r3})$, $N(11,4) = U$, $N(11,8) = -U$,
$N(12,8) = U$, $N(12,12) = -U$, $N(13,2) = -1$, $N(14,6) = -1$, $N(15,10) = -1$, $N(16,14) = -1$, $N(17,16) = -1$,
$N(18,18) = -1$

$\mathbf{Q} \in \mathbf{R}^{18\times 1}$, and the nonzero elements of $\mathbf{Q}$ are given:

$Q(1,1) = N_{\delta_{1f}} + l_{c1}Y_{\delta_{1f}}$, $Q(2,1) = h_{cr1}Y_{\delta_{1f}}$, $Q(3,1) = -h_{r1}Y_{\delta_{1f}}$, $Q(4,1) = -Y_{\delta_{1f}}$, $Q(5,1) = -l_{c21}Y_{\delta_{1f}}$,
$Q(6,1) = -h_{cr2}Y_{\delta_{1f}}$.

$\mathbf{R} \in \mathbf{R}^{18\times 4}$, and the nonzero elements of $\mathbf{R}$ are given:

$R(2,1) = -1$, $R(2,2) = -1$, $R(3,1) = -1$, $R(3,2) = -1$, $R(6,3) = -1$, $R(7,3) = 1$, $R(9,4) = -1$, $R(10,4) = 1$.

$\mathbf{W} \in \mathbf{R}^{18\times 2}$, and the nonzero elements of $\mathbf{W}$ are $W(5,1) = -1$ and $W(8,2) = 1$.

$$\mathbf{C} = \begin{bmatrix} UA(3,:) + U\mathbf{S}(1,:) \\ UA(7,:) + U\mathbf{S}(2,:) \\ UA(11,:) + U\mathbf{S}(3,:) \\ \mathbf{P} \end{bmatrix}, \quad \mathbf{D} = \begin{bmatrix} U\mathbf{B}(3,:) \\ U\mathbf{B}(7,:) \\ U\mathbf{B}(11,:) \\ \mathbf{0}_{6\times 6} \end{bmatrix} \text{ and } \mathbf{D}_{dd} = \begin{bmatrix} U\mathbf{B}_{dd}(3,:) \\ U\mathbf{B}_{dd}(7,:) \\ U\mathbf{B}_{dd}(11,:) \\ \mathbf{0}_{6\times 1} \end{bmatrix}$$

where $\mathbf{S} \in \mathbf{R}^{3\times 18}$ and its nonzero elements are $\mathbf{S}(1,4) = 1$, $\mathbf{S}(2,8) = 1$, and $\mathbf{S}(3,12) = 1$. $\mathbf{P} \in \mathbf{R}^{6\times 18}$ and its nonzero elements are $\mathbf{P}(1,1) = 1$, $\mathbf{P}(2,13) = 1$, $\mathbf{P}(3,5) = 1$, $\mathbf{P}(4,15) = 1$, $\mathbf{P}(5,9) = 1$ and $\mathbf{P}(6,17) = 1$.

Appendix D System Matrices of the Linear Yaw-plane Model of the B-train Double

The system matrices of the yaw-plane model of the B-train double are given as follows. $\mathbf{J} \in \mathbf{R}^{6\times 6}$, and the zero elements of $\mathbf{J}$ are given:

$J(1,1) = l_{c1}m_1U$, $J(1,2) = I_{zz1}$, $J(2,1) = m_1U$, $J(2,3) = m_2U$, $J(2,5) = m_3U$, $J(3,1) = l_{c21}m_1U$, $J(3,4) = I_{zz2}$, $J(3,5) = -l_{c22}m_3U$, $J(4,5) = -l_{c3}m_3U$, $J(4,6) = I_{zz3}$, $J(5,1) = 1$, $J(5,2) = -\frac{l_{c1}}{U}$, $J(5,3) = -1$, $J(5,4) = -\frac{l_{c21}}{U}$, $J(6,3) = 1$, $J(6,4) = -\frac{l_{c22}}{U}$, $J(6,5) = -1$, $J(6,6) = -\frac{l_{c3}}{U}$.

$\mathbf{K} \in \mathbf{R}^{6\times 6}$, and the nonzero elements of $\mathbf{K}$ are given:

$K(1,1) = -\left(N_{\beta_1} + l_{c1}Y_{\beta_1}\right)$, $K(1,2) = -\left(N_{\dot{\psi}_1} - l_{c1}m_1U + l_{c1}Y_{\dot{\psi}_1}\right)$, $K(2,1) = -Y_{\beta_1}$, $K(2,2) = m_1U - Y_{\dot{\psi}_1}$, $K(2,3) = -Y_{\beta_2}$, $K(2,4) = m_2U - Y_{\dot{\psi}_2}$, $K(2,5) = -Y_{\beta_3}$, $K(2,6) = m_3U - Y_{\dot{\psi}_3}$, $K(3,1) = -l_{c21}Y_{\beta_1}$, $K(3,2) = l_{c21}m_1U - l_{c21}Y_{\dot{\psi}_1}$, $K(3,3) = -N_{\beta_2}$, $K(3,4) = -N_{\dot{\psi}_2}$, $K(3,5) = l_{c22}Y_{\beta_3}$, $K(3,6) = l_{c22}Y_{\dot{\psi}_3} - l_{c22}m_3U$, $K(4,5) = l_{c3}Y_{\beta_3} - N_{\beta_3}$, $K(4,6) = l_{c3}Y_{\dot{\psi}_3} - l_{c3}m_3U - N_{\dot{\psi}_3}$, $K(5,2) = 1$, $K(5,4) = -1$, $K(6,4) = 1$, $K(6,6) = -1$.

$\mathbf{L} \in \mathbf{R}^{6\times 1}$, and the nonzero elements of $\mathbf{L}$ are given:

$L(1,1) = -\left(N_{\delta_{11}} + l_{c1}Y_{\delta_{11}}\right)$, $L(2,1) = -Y_{\delta_{11}}$, $L(3,1) = -l_{c21}Y_{\delta_{11}}$.

$\mathbf{T} \in \mathbf{R}^{6\times 6}$, and its nonzero elements are given:

$T(2,1) = -Y_{\delta_4}$, $T(2,2) = -Y_{\delta_5}$, $T(2,3) = -Y_{\delta_6}$, $T(2,4) = -Y_{\delta_7}$, $T(2,5) = -Y_{\delta_8}$, $T(2,6) = -Y_{\delta_9}$, $T(3,1) = -N_{\delta_4}$, $T(3,2) = -N_{\delta_5}$, $T(3,3) = -N_{\delta_6}$, $T(3,4) = l_{c22}Y_{\delta_7}$, $T(3,5) = l_{c22}Y_{\delta_8}$, $T(3,6) = l_{c22}Y_{\delta_9}$, $T(4,4) = l_{c3}Y_{\delta_7} - N_{\delta_7}$, $T(4,5) = l_{c3}Y_{\delta_8} - N_{\delta_8}$, $T(4,6) = l_{c3}Y_{\delta_9} - N_{\delta_9}$.

$\mathbf{V} \in \mathbf{R}^{6\times 2}$ and its nonzero elements are given:

$V(3,1) = -1$, $V(4,2) = 1$.

Appendix E System Matrices of the Nonlinear Yaw-plane Model of the B-train Double

$$\mathbf{K}_n = \begin{bmatrix} 0 & -l_{c1}m_1U & 0 & 0 & 0 & 0 \\ 0 & -m_1U & 0 & -m_2U & 0 & -m_3U \\ 0 & -l_{c21}m_1U & 0 & 0 & 0 & l_{c22}m_3U \\ 0 & 0 & 0 & 0 & 0 & l_{c3}m_3U \\ 0 & -1 & 0 & 1 & 0 & 0 \\ 0 & 0 & 0 & -1 & 0 & 1 \end{bmatrix}, \quad \mathbf{R}_n = \begin{bmatrix} 0 & 0 \\ 0 & 0 \\ 1 & 0 \\ 0 & 1 \\ 0 & 0 \\ 0 & 0 \end{bmatrix},$$

$$\mathbf{L}_n = \begin{bmatrix} a_{11}+l_{c1} & l_{c1}-b_{12} & l_{c1}-b_{13} & 0 & 0 & 0 & 0 & 0 & 0 \\ 1 & 1 & 1 & 1 & 1 & 1 & 1 & 1 & 1 \\ l_{c21} & l_{c21} & l_{c21} & -b_{24} & -b_{25} & -b_{26} & -l_{c22} & -l_{c22} & -l_{c22} \\ 0 & 0 & 0 & 0 & 0 & 0 & -(b_{37}+l_{c3}) & -(b_{38}+l_{c3}) & -(b_{39}+l_{c3}) \\ 0 & 0 & 0 & 0 & 0 & 0 & 0 & 0 & 0 \\ 0 & 0 & 0 & 0 & 0 & 0 & 0 & 0 & 0 \end{bmatrix}.$$

Appendix F State Variables of the EoM Yaw-roll Model and Resulted Forces and Moments of the B-train Double

State variables of the EoM yaw-roll model of the B-train double are listed in Table F1.

Table F1 State variables of the EoM yaw-roll model of the B-train double

Rigid bodies	Locations and orientations ($\mathbf{p}_i$)	First-order time derivatives ($\dot{\mathbf{p}}_i$)
Tractor sprung mass (B_1)	1: longitudinal position (x_1) 2: lateral position (y_1) 3: vertical position (z_1) 4: roll angle (ϕ_1) 5: pitch angle (θ_1) 6: yaw angle (ψ_1)	37: longitudinal speed ($\dot{x}_1$) 38: lateral speed ($\dot{y}_1$) 39: vertical speed ($\dot{z}_1$) 40: roll rate ($\dot{\phi}_1$) 41: pitch rate ($\dot{\theta}_1$) 42: yaw rate ($\dot{\psi}_1$)
Tractor unsprung mass (B_2)	7: longitudinal position (x_{t1}) 8: lateral position (y_{t1}) 9: vertical position (z_{t1}) 10: roll angle (ϕ_{t1}) 11: pitch angle (θ_{t1}) 12: yaw angle (ψ_{t1})	43: longitudinal speed ($\dot{x}_{t1}$) 44: lateral speed ($\dot{y}_{t1}$) 45: vertical speed ($\dot{z}_{t1}$) 46: roll rate ($\dot{\phi}_{t1}$) 47: pitch rate ($\dot{\theta}_{t1}$) 48: yaw rate ($\dot{\psi}_{t1}$)
1st semitrailer sprung mass (B_3)	13: longitudinal position (x_2) 14: lateral position (y_2) 15: vertical position (z_2) 16: roll angle (ϕ_2) 17: pitch angle (θ_2) 18: yaw angle (ψ_2)	49: longitudinal speed ($\dot{x}_2$) 50: lateral speed ($\dot{y}_2$) 51: vertical speed ($\dot{z}_2$) 52: roll rate ($\dot{\phi}_2$) 53: pitch rate ($\dot{\theta}_2$) 54: yaw rate ($\dot{\psi}_2$)
1st semitrailer unsprung mass (B_4)	19: longitudinal position (x_{t2}) 20: lateral position (y_{t2}) 21: vertical position (z_{t2}) 22: roll angle (ϕ_{t2}) 23: pitch angle (θ_{t2}) 24: yaw angle (ψ_{t2})	55: longitudinal speed ($\dot{x}_{t2}$) 56: lateral speed ($\dot{y}_{t2}$) 57: vertical speed ($\dot{z}_{t2}$) 58: roll rate ($\dot{\phi}_{t2}$) 59: pitch rate ($\dot{\theta}_{t2}$) 60: yaw rate ($\dot{\psi}_{t2}$)
2nd semitrailer sprung mass (B_5)	25: longitudinal position (x_3) 26: lateral position (y_3) 27: vertical position (z_3) 28: roll angle (ϕ_3) 29: pitch angle (θ_3) 30: yaw angle (ψ_3)	61: longitudinal speed ($\dot{x}_3$) 62: lateral speed ($\dot{y}_3$) 63: vertical speed ($\dot{z}_3$) 64: roll rate ($\dot{\phi}_3$) 65: pitch rate ($\dot{\theta}_3$) 66: yaw rate ($\dot{\psi}_3$)
	31: longitudinal position (x_{t3}) 32: lateral position (y_{t3}) 33: vertical position (z_{t3})	67: longitudinal speed ($\dot{x}_{t3}$) 68: lateral speed ($\dot{y}_{t3}$) 69: vertical speed ($\dot{z}_{t3}$)

2nd semitrailer unsprung mass (B_6)	34: roll angle (ϕ_{t3}) 35: pitch angle (θ_{t3}) 36: yaw angle (ψ_{t3})	70: roll rate ($\dot{\phi}_{t3}$) 71: pitch rate ($\dot{\theta}_{t3}$) 72: yaw rate ($\dot{\psi}_{t3}$)

Complete list of the state variables employed for the tire model and the resulted forces and moments to the EoM yaw-roll model are illustrated in Table F2.

Table F2 Complete list of the state variables for the tire model and the resulted forces and moments to the EoM model

Rigid bodies	State variables	External forces (moments)
Tractor unsprung mass (B_2)	43: longitudinal speed ($\dot{x}_{t1}$) 44: lateral speed ($\dot{y}_{t1}$) 46: roll rate ($\dot{\phi}_{t1}$) 48: yaw rate ($\dot{\psi}_{t1}$)	43: longitudinal force (F_{xt1}) 44: lateral force (F_{yt1}) 46: roll moment (M_{xt1}) 48: yaw moment (M_{zt1})
1st trailer unsprung mass (B_4)	55: longitudinal speed ($\dot{x}_{t2}$) 56: lateral speed ($\dot{y}_{t2}$) 58: roll rate ($\dot{\phi}_{t2}$) 60: yaw rate ($\dot{\psi}_{t2}$)	55: longitudinal force (F_{xt2}) 56: lateral force (F_{yt2}) 58: roll moment (M_{xt2}) 60: yaw moment (M_{zt2})
2nd trailer unsprung mass (B_6)	67: longitudinal speed ($\dot{x}_{t3}$) 68: lateral speed ($\dot{y}_{t3}$) 70: roll rate ($\dot{\phi}_{t3}$) 72: yaw rate ($\dot{\psi}_{t3}$)	67: longitudinal force (F_{xt3}) 68: lateral force (F_{yt3}) 70: roll moment (M_{xt3}) 72: yaw moment (M_{zt3})

Appendix G Matrices of the Augmented Linear Yaw-plane Model for the SMC-Based Preview Driver Model Design

The process matrix $\mathbf{A}_d \in \mathbf{R}^{12\times 12}$ and its nonzero elements are given as

$A_d(1,2)=u_1$, $A_d(1,3)=1$, $A_d(1,4)=a_{11}$, $A_d(2,4)=1$, $A_d(3,3)=A_p(1,1)$, $A_d(3,4)=A_p(1,2)u_1$,
$A_d(3,7)=A_p(1,3)$, $A_d(3,8)=A_p(1,4)u_1$, $A_d(3,11)=A_p(1,5)$, $A_d(3,12)=A_p(1,6)u_1$, $A_d(4,3)=A_p(2,1)/u_1$,
$A_d(4,4)=A_p(2,2)$, $A_d(4,7)=A_p(2,3)/u_2$, $A_d(4,8)=A_p(2,4)$, $A_d(4,11)=A_p(2,5)/u_3$,
$A_d(4,12)=A_p(2,6)$, $A_d(5,6)=u_2$, $A_d(5,7)=1$, $A_d(6,8)=1$, $A_d(7,3)=A_p(3,1)$, $A_d(7,4)=A_p(3,2)u_2$,
$A_d(7,7)=A_p(3,3)$,
$A_d(7,8)=A_p(3,4)u_2$, $A_d(7,11)=A_p(3,5)$, $A_d(7,12)=A_p(3,6)u_2$, $A_d(8,3)=A_p(4,1)/u_1$,
$A_d(8,4)=A_p(4,2)$, $A_d(8,7)=A_p(4,3)/u_2$, $A_d(8,8)=A_p(4,4)$, $A_d(8,11)=A_p(4,5)/u_3$,
$A_d(8,12)=A_p(4,6)$, $A_d(9,10)=u_3$, $A_d(9,11)=1$, $A_d(10,12)=1$, $A_d(11,3)=A_p(5,1)$, $A_d(11,4)=A_p(5,2)u_3$,
$A_d(11,7)=A_p(5,3)$, $A_d(11,8)=A_p(5,4)u_3$, $A_d(11,11)=A_p(5,5)$, $A_d(11,12)=A_p(5,6)u_3$,
$A_d(12,3)=A_p(6,1)/u_1$, $A_d(12,4)=A_p(6,2)$, $A_d(12,7)=A_p(6,3)/u_2$, $A_d(12,8)=A_p(6,4)$,
$A_d(12,11)=A_p(6,5)/u_3$, $A_d(12,12)=A_p(6,6)$.

$\mathbf{B}_d=\begin{bmatrix}0 & 0 & C_p(1)u_1 & C_p(2) & 0 & 0 & C_p(3)u_2 & C_p(4) & 0 & 0 & C_p(5)u_3 & C_p(6)\end{bmatrix}^T$ and

$$\mathbf{C}_d=\begin{bmatrix}1&0&0&0&0&0&0&0&0&0&0&0\\0&0&0&0&1&0&0&0&0&0&0&0\\0&0&0&0&0&0&0&0&1&0&0&0\end{bmatrix}.$$